



**HAL**  
open science

## Photothermal studies on cryoprotectant media

Allen Mathew

► **To cite this version:**

Allen Mathew. Photothermal studies on cryoprotectant media. Other. Université du Littoral Côte d'Opale, 2018. English. NNT : 2018DUNK0478 . tel-01990789

**HAL Id: tel-01990789**

**<https://theses.hal.science/tel-01990789>**

Submitted on 23 Jan 2019

**HAL** is a multi-disciplinary open access archive for the deposit and dissemination of scientific research documents, whether they are published or not. The documents may come from teaching and research institutions in France or abroad, or from public or private research centers.

L'archive ouverte pluridisciplinaire **HAL**, est destinée au dépôt et à la diffusion de documents scientifiques de niveau recherche, publiés ou non, émanant des établissements d'enseignement et de recherche français ou étrangers, des laboratoires publics ou privés.

---

# PHOTOTHERMAL STUDIES ON CRYOPROTECTANT MEDIA

---

## ÉTUDES PHOTOTHERMIQUES DE MILIEUX CRYOPROTECTEURS

---

### THESIS

*submitted to*

L'UNIVERSITÉ DU LITTORAL CÔTE D'OPALE

*for the award of the degree of*

**Doctor of Philosophy in Physics**

*by*

**Allen MATHEW**

Defended on 11 July 2018 before the board of examiners:

---

|                                |   |              |
|--------------------------------|---|--------------|
| <b>Gilles TESSIER</b>          | Professor<br>Sorbonne Université, Paris 6   | Rapporteur   |
| <b>Nicolae Dorin DADARLAT</b>  | Professor<br>INCDTIM, Cluj-Napoca, Romania  | Rapporteur   |
| <b>Sophie DUQUESNE</b>         | Professor<br>Unité Matériaux et Transformations,<br>École Nationale Supérieure de Chimie de Lille | Examinatrice |
| <b>Anne BAUDOT</b>             | Maître de conférences (Supervisor)<br>Université Paris Descartes, Paris V                         | Examinatrice |
| <b>Fabrice GOUTIER</b>         | Maître de conférences (Supervisor)<br>Université du Littoral Côte d'Opale                         | Examinateur  |
| <b>Abdelhak HADJ SAHARAOUI</b> | Professor (Director of Thesis)<br>Université du Littoral Côte d'Opale                             | Examinateur  |

Unité de Dynamique et Structure des Matériaux Moléculaires



---

## Acknowledgment

---

I would like to use this opportunity to express my gratitude to all those who have helped me during the time of my PhD research.

I thank Dr. Abdelhak Hadj Sahraoui (professor, ULCO Dunkerque), director of UDSMM laboratory (Unite de Dynamique et Structure des Materiaux Moleculaires) as well as my thesis and Dr. Fabrice GOUTIER (maître de conférences, ULCO Dunkerque), co-director of my thesis for providing all support and guidance throughout my thesis.

Equally I want to thank my second director of thesis, Dr. Gérard LOUIS (professor), Université Paris Descartes and co-director Dr. Anne BOUDUT (Maitre de conférences), Université Paris Descartes for their full support, guidance and result interpretation from Paris and providing me facilities to do experiments in their laboratory. Thanks for the warm and hearty welcome given by both whenever I visited Paris.

Dr. Abdelhak is a great person of knowledge, experience, generosity and humbleness. I am happy to be a part of his group. I am thankful to him for giving me vacations to visit my family in India and for all the timely advices and help.

Fabrice was my daily supervisor who helped me a lot to build the experimental setup and in the advancement of my thesis. It was with the help of Fabrice that I could do all the administrative works in France as I hardly spoke any French while I arrived here. I could learn the true meaning of perseverance, patience and hard work from Fabrice. It was one of the greatest experience in my life to work with him.

I am grateful to all my directors and co-directors for all their support, valuable discussions, corrections and reviews of my thesis manuscript.

I extent my sincere gratitude to all the jury members, Dr. Gilles TESSIER (Professor, Institut de la Vision, Sorbonne Université (Paris 6), Paris) and Dr. Nicolae Dorin DADARLAT (Professor, INCDTIM Cluj-Napoca, Romania) as rapporteurs and Dr. Sophie DUQUESNE (Professor, École Nationale Supérieure de Chimie de Lille, Unité Matériaux et Transformations (UMET) - UMR-CNRS 8207, Lille) as examiner, for kindly accepting to evaluate my

---

thesis and to come for my PhD defense.

A big thanks to Maju KURIAKOSE and his adorable family. They made me felt that I have a second home in Dunkerque.

Any experimental work cannot be done without the help of a well-trained technician and that role was perfectly handled by Mr. Benoit ESCORNE. I thank Benoit for his expertise.

I thank Abdelaziz Ellass, engineer who worked alongside, for all his help and experimental support.

We have been helped by the CEDIL industries for manufacturing our cells. I extend my sincere gratitude for their technical support.

I would like to thank Dr. Christ GLORIEUX (professor, Katholieke Universiteit (KU) Leuven, Belgium) for providing the metallic coating on my pyroelectric sensors and for his valuable advices.

In the third year of my PhD I got the position of ATER in ULCO. I thank Dr. Abdelhak for supporting my candidature for the ATER. Also I would like to thank Dr. Arnaud CUISSET for allotting my classes without affecting my research schedule much.

As I was not a good French speaker I was in constant need of help for teaching. I am grateful to Stephane LONGUEMART, Michael DEPRIESTER, Sylvain DELENCLOS and Corinne KOLINSKY for explaining and practising the practical works with me. Stephane and Michael have helped me by sharing their scientific experiences during the time of difficulties in research.

Also I would like to thank all my lab colleagues, Prof. Abdelylah DAOUDI, Philippe HUS, Yahia BOUSSOUALEM, Mathieu BARDOUX, Jan LEYS, Benoit DUPONCHEL, Alejandro SEGOVIA MERA, Karim TAOUTI, Dharmendra Pratap SINGH, Eliane BSAIBESS, Kiril KONDRATENKO, Said BELLAFKIH, Elie BADINE and everyone from the UDSMM group in Calais for their support and comradeship. Many of us are from different nationalities and I thank each and every one for sharing their exotic cuisine and gifts from their homeland.

I would like to thank Cedric BRAY for explaining the practical works in mechanics. I thank the lab assistants Pierre in Dunkerque and Wilfred in Calais for doing all the arrangements for the practical classes.

I would like to thank our secretaries Veronique and Virginie for all the administrative help and delicious homemade cookies and cakes.

I love to thank my friends from other laboratories : Leila, Alla, Serena, Paul Praveen, Eleonore, Isabelle, Eddy, Sara, Raya, Jihane, Pamela, Sohaib, Aziz, Ferdaous and Tong for their friendship and support.

I am really fortunate to have many friends outside my workplace. They are Elvira, Grace, Zoser, Melody, Ruth, Dorin, Adrien, Mathilde, Magali, Xin and Feng. I am always grateful to all of them for making my PhD life memorable.

The person who inspired me a lot is Dr. Vinoy THOMAS, Assistant professor, Christian College, Chengannur, India. I thank him for all the inspirations and advices.

Equally I want to thank Dr. Joice THOMAS, KU leuven, Belgium and his family for all the

---

advices and support during the course of my academic life.

My family always extended their full support, love, care and acceptance throughout my life. I am fortunate to be born as the son of Mrs. Anu MATHEW and Mr. Mathew ABRAHAM. It's not possible to explain here how much I value that in my life. I believe that all the good things I have got in my life are because of the good deeds of my father and mother. It was difficult for me to accept the death of my grandfather who was one of the greatest support in my life. I appreciate all the things they have done for me. My heartfelt gratitude to them for their care and prayers.

The person whom I always care the most is my loving brother Paven Thomas MATHEW, PhD researcher in Dublin, Ireland. There is no words to express how much I appreciate him in my life. I am always proud about the little and great achievements he had. I wish him the best to finish his Phd with great success and thanks a lot to be an amazing brother.

I thank my best friends Aravind and Nikil from India for all their support. Also I thank my very good friends Jijo, Manchester University, UK and Ramu, KIT, Germany for providing the articles that I couldn't access.

I am richly blessed by God to have a loving family, amazing friends and excellent professors in my life. I thank God wholeheartedly for all the blessings showered upon me and for the courage and wisdom given to finish my PhD successfully.

Finally I would like to extend my sincere gratitude to all who have helped me directly or indirectly during the course of my research life in France. I am extremely sorry if I miss any names.

Allen

11-July-2018, Dunkerque



*The woods are lovely, dark and deep,  
But I have promises to keep,  
And miles to go before I sleep,  
And miles to go before I sleep.*

ROBERT FROST



*Dedicated to my papa, mama and  
brother*



---

# Contents

---

|   |             |
|---|-------------|
| <b>Acknowledgment</b>   | <b>i</b>    |
| <b>Résumé</b>   | <b>xiii</b> |
| <b>Introduction</b>   | <b>1</b>    |
| <b>1 Cryoprotectants and Glassy State</b>   | <b>5</b>    |
| 1.1 Cryoprotectants . . . . .   | 6           |
| 1.2 Vitrification . . . . .   | 9           |
| 1.3 Glassy State of a Material . . . . .  | 10          |
| 1.4 Theoretical Models of Glass Dynamics . . . . .  | 13          |
| 1.5 Glass Transition Study . . . . .  | 14          |
| 1.6 The Photo Pyroelectric Technique . . . . .  | 15          |
| <b>2 Theory of Heat Transfer and Photo Pyroelectric Technique</b>   | <b>19</b>   |
| 2.1 Heat Diffusion Equation and Solution . . . . .  | 19          |
| 2.2 PPE Configurations for Thermal Properties Measurement . . . . .   | 20          |
| 2.3 Temperature Fields for Different Layers of FPPE Configuration with Semi<br>Transparent Sensor . . . . . | 23          |
| 2.3.1 Expression of the PPE Signal in FPPE Configuration with Semi Trans-<br>parent Sensor . . . . .        | 25          |
| 2.3.2 Expression of the PPE Signal in FPPE Configuration with Opaque Sensor                                 | 27          |
| 2.4 Determination of Thermal Parameters at Ambient Temperature . . . . .                                    | 29          |
| 2.4.1 FPPE Configuration with Semi Transparent Sensor . . . . .   | 30          |
| 2.4.2 FPPE Configuration with Opaque Sensor . . . . .   | 30          |
| 2.5 Summary . . . . .   | 31          |

|           |  |           |
|-----------|--|-----------|
| <b>3</b>  | <b>Experimental Setup and Photo Pyroelectric Measurements at Ambient Temperature</b> | <b>33</b> |
| 3.1       | Experimental Setup . . . . .   | 33        |
| 3.1.1     | PPE Cell . . . . .   | 34        |
| 3.1.1.1   | Cell Design . . . . .  | 34        |
| 3.1.1.2   | Pyroelectric Sensors Used for Measurement . . . . .                                  | 36        |
| 3.1.1.3   | Temperature Measurement . . . . .  | 36        |
| 3.1.2     | Illumination and Temperature Controller . . . . .                                    | 38        |
| 3.1.3     | Data Acquisition . . . . .   | 39        |
| 3.1.4     | Ground Loop . . . . .  | 40        |
| 3.1.5     | Sample Preparation . . . . .   | 40        |
| 3.1.6     | Low Temperature Experiments . . . . .  | 41        |
| 3.2       | Effusivity Measurements at Ambient Temperature . . . . .                             | 41        |
| 3.2.1     | Characterization of Pyro Electric Sensors (Effusivity and Diffusivity) . . . . .     | 41        |
| 3.2.2     | Pure Samples . . . . .   | 44        |
| 3.2.3     | Binary Mixtures and Molecular Association . . . . .                                  | 47        |
| 3.3       | Summary . . . . .  | 50        |
| <b>4</b>  | <b>Low Temperature Photo Pyroelectric Measurements: Results and Discussion</b>       | <b>51</b> |
| 4.1       | Low Temperature PPE: Theory . . . . .  | 51        |
| 4.1.1     | Simulation of PPE Signal in the $\alpha$ Relaxation Region . . . . .                 | 51        |
| 4.1.2     | Determination of Effusivity from PPE Signal . . . . .                                | 54        |
| 4.1.3     | Determination of the Relaxation Time . . . . .                                       | 54        |
| 4.1.3.1   | Choosing the Model For Relaxation Time . . . . .                                     | 55        |
| 4.1.3.2   | Estimation of Model Parameters for Relaxation Time . . . . .                         | 57        |
| 4.1.4     | Fragility . . . . .  | 58        |
| 4.2       | Low Temperature PPE: Results and Discussion . . . . .                                | 60        |
| 4.2.1     | Pure Glycerol . . . . .  | 61        |
| 4.2.1.1   | Results at 22Hz . . . . .  | 61        |
| 4.2.1.1.1 | Estimation of Parameters: $\alpha, \beta, E_\infty, \Delta E$ . . . . .              | 62        |
| 4.2.1.1.2 | Choosing the Model for Relaxation Time . . . . .                                     | 63        |
| 4.2.1.1.3 | Estimation of Model Parameters for Relaxation Time . . . . .                         | 65        |
| 4.2.1.1.4 | 7-Parameter Fit . . . . .  | 66        |
| 4.2.1.1.5 | Fragility and Dyre-Olsen Index . . . . .   | 69        |
| 4.2.1.2   | Other Frequencies . . . . .  | 69        |
| 4.2.2     | Pure 1,2 Propanediol . . . . .   | 72        |
| 4.2.3     | Binary Mixtures . . . . .  | 75        |
| 4.2.3.1   | 90 wt% Glycerol-Water Mixture . . . . .  | 77        |
| 4.2.3.1.1 | Estimation of Parameters: $\alpha, \beta, E_\infty, \Delta E$ . . . . .              | 78        |

|  |   |            |
|--|---|------------|
| 4.2.3.1.2  | Choosing the Model for Relaxation Time . . . . .                  | 78         |
| 4.2.3.1.3  | Estimation of Model Parameters for Relaxation Time                | 81         |
| 4.2.3.1.4  | 7-Parameter Fit . . . . .   | 82         |
| 4.2.3.1.5  | Fragility and Dyre-Olsen Index . . . . .                          | 84         |
| 4.2.3.2  | 80 wt% Glycerol-Water Mixture . . . . .                           | 84         |
| 4.2.3.3  | 70 wt% Glycerol-Water Mixture . . . . .                           | 86         |
| 4.2.3.4  | 93.13 wt% 1,2 Propanediol-Water Mixture . . . . .                 | 88         |
| 4.2.3.5  | 70 wt% 1,2 Propanediol-Water Mixture . . . . .                    | 90         |
| 4.2.4  | Classical and New Fragility . . . . .                             | 93         |
| 4.2.5  | Individual Frequency Relaxation . . . . .                         | 95         |
| 4.3  | Viscosity Measurements . . . . .                                  | 99         |
| 4.3.1  | Viscosity Study on Glycerol and Binary Solutions . . . . .        | 99         |
| 4.3.2  | Viscosity Study on 1,2 Propanediol and Binary Solutions . . . . . | 103        |
| 4.4  | Differential Scanning Calorimetry Measurement . . . . .           | 107        |
| 4.5  | Summary . . . . .   | 111        |
| <b>Discussion, General Conclusion and Future Outlook</b> |   | <b>113</b> |
| 4.6  | Discussion . . . . .  | 113        |
| 4.7  | Conclusion . . . . .  | 117        |
| 4.8  | Future Outlook . . . . .  | 118        |
| <b>Bibliography</b>                                      |   | <b>118</b> |



---

## Résumé

---

L'objectif principal de cette thèse est la mise en place d'un banc expérimental basé sur la technique photo pyroélectrique (PPE) pour étudier les propriétés thermiques des matériaux de -180 °C à l'ambient. L'étude des propriétés thermiques des matériaux est très importante pour améliorer leurs utilisations dans différents domaines (capteurs de température, conducteurs thermiques, isolants, etc...) et pour comprendre leur comportement lorsqu'ils sont soumis à des variations de température. Ce sont les propriétés thermiques des matériaux qui déterminent leur comportement en présence d'une onde thermique ou dans un champ de température.

Les techniques photothermiques sont considérées comme des outils efficaces pour l'étude des propriétés thermiques des matériaux. Elles sont basées sur la détection et l'analyse d'un gradient de température créé suite à l'absorption par l'échantillon de l'énergie d'une radiation d'intensité modulée (faisceau laser par exemple). Parmi celles-ci, la technique photo pyroélectrique (PPE) joue un rôle important dans la caractérisation thermique des matériaux. Dans cette technique la variation de température est détectée en utilisant un matériau pyroélectrique comme capteur.

Les capteurs pyroélectriques sont généralement des lames découpées de manière à ce que les champs de polarisation permanents soient orientés dans une direction orthogonale par rapport à la surface du transducteur comme le montre la figure 1. Ils sont une sous-classe des matériaux ferroélectriques, qui satisfont à certaines exigences cristallographiques, telles que l'absence de centre de symétrie dans le réseau cristallin et un seul axe de symétrie de rotation. Ils présentent une polarisation macroscopique dépendant de la température. Cette polarisation diminue avec l'augmentation de la température comme le montre la figure 2 et disparaît à une température particulière appelée température de Curie. Au-delà de la température de Curie, le cristal est en phase paraélectrique.

Les matériaux pyroélectriques ont la capacité de générer une tension temporaire due au changement de la polarisation électrique en raison du changement de flux thermique provoqué par la modulation de la source lumineuse. Cette propriété est appelée effet pyroélectrique.

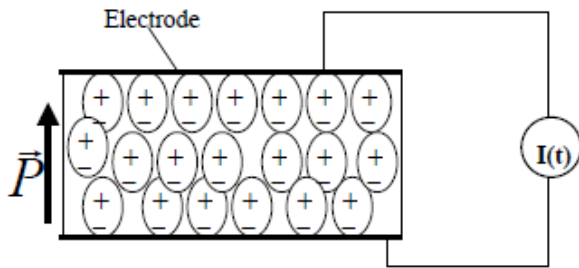


FIGURE 1 – Schéma d'un matériau pyroélectrique recouvert d'électrodes opaques

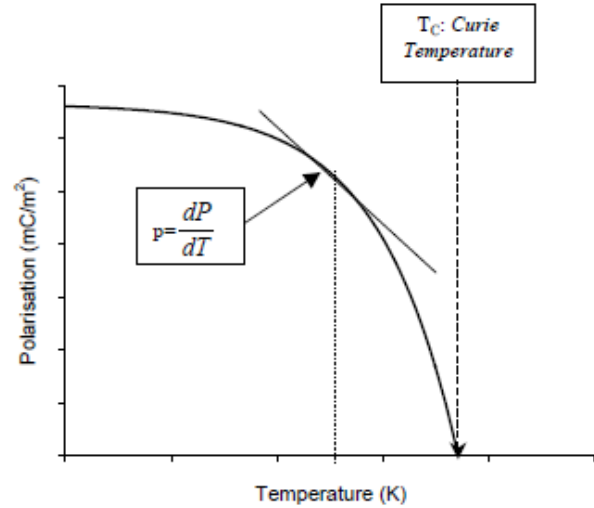


FIGURE 2 – Variation de la polarisation d'un matériau ferroélectrique par rapport à la température

La pente de la courbe de la figure 2 donne le coefficient pyroélectrique. Aucun matériau n'est pyroélectrique au-dessus de la température de Curie. La tension générée par un matériau pyroélectrique est fonction du changement de température. Les matériaux pyroélectriques peuvent être utilisés comme capteurs pour étudier les propriétés thermiques de matériaux solides ou liquides sur une large plage de température (15K à 400K). L'avantage d'une sensibilité élevée, d'une large bande passante (généralement du mHz à plusieurs kHz), d'un rapport signal sur bruit élevé et de la simplicité de mise en œuvre ont incité les chercheurs à utiliser largement la PPE.

L'étude des propriétés thermiques est indispensable dans le domaine de la cryoconservation.

La cryoconservation consiste à préserver des cellules ou des tissus vivants à très basses températures pour une utilisation future ou des études ultérieures. A une température cryogénique, les activités biologiques dans les cellules vivantes sont ralenties de façon drastique et les cellules peuvent donc être durablement conservées. Mais les cellules biologiques contiennent beaucoup d'eau qui se transforme en glace en-dessous de 0 °C. Les procédures de cryoconservation cherchent donc à éviter ou à contrôler les risques de cristallisation de l'eau.

Lorsque la glace se forme à l'intérieur des cellules biologiques, elle provoque des dommages irréversibles au niveau de la paroi cellulaire et des structures internes (à cause de l'expansion du volume). Lorsqu'elle se forme autour des cellules, elle les expose à différentes contraintes pouvant les endommager : il peut y avoir rupture des cellules, apparition de lésions liées à la surconcentration de la solution non congelée, et contraction cellulaire létale liée à la déshydratation excessive des cellules par effet osmotique.

La nature propose différentes façons de préserver la vie dans des conditions de froid extrême. Certains organismes tolèrent la formation de glace. La grenouille des bois (*Rana sylvatica*) par exemple peut survivre à un gel important de ses fluides corporels pendant la saison

hivernale. Il en est de même pour l'organisme multicellulaire microscopique appelé l'ourson d'eau (Tardigrada). D'autres restent en surfusion. Ainsi, les poissons polaires et les insectes terrestres synthétisent des protéines antigél et des glycoprotéines antigél qui permettent la surfusion de leurs fluides corporels en-dessous de la température de congélation.

Comme dans la nature, les procédés développés par les cryobiologistes utilisent des molécules antigél appelées cryoprotecteurs (CPA) qui protègent les cellules contre les dommages causés par le gel ou empêchent la formation de glace. Deux types de cryoprotecteurs sont à distinguer selon leur capacité à pénétrer ou non dans la cellule. Les CPA pénétrants peuvent intégrer le volume intracellulaire et agir dans le cytoplasme. Les CPA non pénétrants ne peuvent pas traverser les membranes cellulaires et agissent dans l'environnement extracellulaire, participant à l'équilibre osmotique. Tous sont très solubles dans l'eau. Ils ont une bonne affinité avec elle et sont liés aux molécules d'eau par des liaisons hydrogène. Leur action dépend de leur proportion en solution. Ils sont biocompatibles, mais deviennent chimiquement toxiques à partir d'une certaine concentration. Le glycérol et le 1,2 propanediol sont des polyalcools qui font partie des CPA pénétrants.

Dans les applications cliniques, deux stratégies sont développées en cryobiologie pour préserver les systèmes biologiques : soit la cristallisation de l'eau est contrôlée à l'extérieur des cellules en appliquant un protocole de refroidissement lent spécifique au type de cellules, en présence d'une faible quantité de cryoprotecteur ; soit la formation de glace est totalement évitée pendant le refroidissement et le réchauffement suivant par application de vitesses de variation de la température très élevées, en présence d'une grande quantité de cryoprotecteur. Cette dernière stratégie, appelée vitrification, est développée pour des systèmes biologiques complexes contenant plusieurs types de cellules, comme les organes par exemple qui sont des structures complexes et fonctionnelles.

Le processus de vitrification permet de former, en-dessous de la température de transition vitreuse  $T_g$ , un état solide amorphe appelé verre, sans aucune structure cristalline. L'état vitreux est caractérisé par une viscosité élevée de l'ordre de  $10^{13}$  poises au  $T_g$  (à titre de comparaison, la viscosité de l'eau est inférieure à 0,1 poise à son point de fusion). L'eau pure peut être vitrifiée, mais ce n'est possible que pour des très faibles volumes (de l'ordre du  $\mu\text{m}^3$ ) par application de vitesses de refroidissement ultra-rapides de l'ordre de  $10^7$  °C  $\text{min}^{-1}$ . Dans la pratique, en cryobiologie, la vitrification nécessite de grandes vitesses de refroidissement et la présence d'une concentration élevée de CPA (généralement trois à quatre fois plus élevée qu'en congélation lente). Pour obtenir une vitesse de refroidissement élevée dans l'échantillon biologique, sa taille doit être petite. La présence de CPA abaisse la vitesse de refroidissement requise, permettant ainsi une plus grande taille d'échantillon. Cependant, une concentration trop élevée de CPA conduit à une toxicité nuisible pour le système biologique. Il convient donc de trouver le bon compromis et le choix des cryoprotecteurs est déterminant.

En cryobiologie, une vitrification réussie signifie que la glace ne se forme ni au refroidissement, ni au réchauffement suivant, et que les fractures dans l'état vitreux sont évitées. En

effet, comme dans les verres minéraux à température ambiante, les solutions aqueuses vitrifiées peuvent se fracturer à cause de contraintes thermomécaniques. Une propriété importante du verre est donc son paramètre de fragilité ( $m$ ). Les verres dits « forts » ont une structure qui est peu sensible au changement de température alors que celle des verres dits « fragiles » évolue avec la température. Le paramètre de fragilité est utile dans la sélection des CPA pour la cryoconservation.

Dans ce travail de thèse, nous avons utilisé la PPE pour étudier l'évolution des propriétés thermiques de plusieurs cryoprotecteurs (glycérol, 1,2 propanediol) purs ou en solutions aqueuses au voisinage de la transition vitreuse. Nous avons déterminé leur température de transition vitreuse  $T_g$  et leur paramètre de fragilité.

Au voisinage de la transition vitreuse, les liquides présentent une propriété caractéristique de dépendance en fréquence de la capacité calorifique. La PPE permet de mesurer et d'étudier cette propriété directement. La relaxation associée à la vitrification est appelée relaxation  $\alpha$ .

La figure 3 montre l'évolution de la partie réelle et de la partie imaginaire de la capacité calorifique en fonction de la fréquence au voisinage de la transition vitreuse.

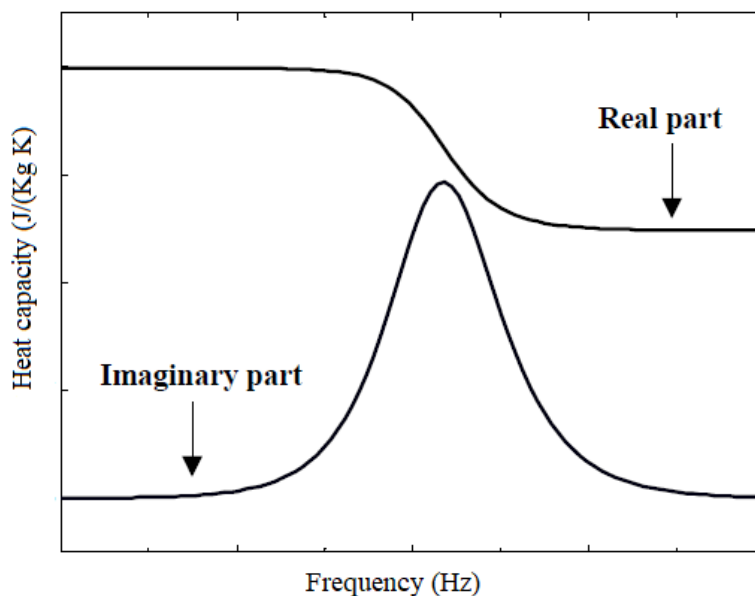


FIGURE 3 – Parties réelles et imaginaires de la capacité calorifique en fonction de la fréquence

Ces phénomènes de relaxation peuvent être aussi étudiés à travers l'un ou l'autre des paramètres thermiques des matériaux tels que l'effusivité thermique, la diffusivité thermique ou la conductivité thermique. La technique PPE dans ses différentes configurations permet ces études. Les figures 4, 5 et 6 montrent ces différentes configurations : la configuration arrière (BPPE), la configuration avant (FPPE) avec électrodes opaques et la configuration avant avec une électrode transparente.

Nous avons choisi d'effectuer cette étude à travers l'effusivité thermique (en  $W s^{1/2} m^{-2} K^{-1}$ )

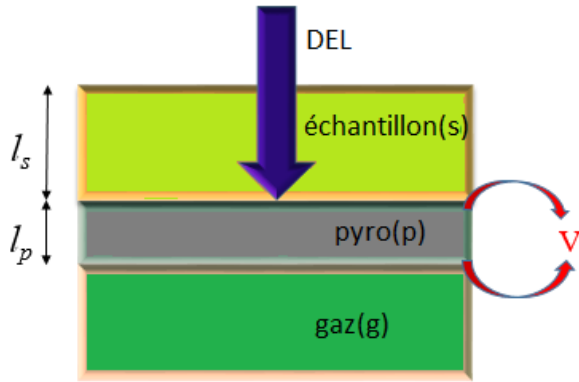


FIGURE 4 – **BPPE pour échantillon transparent** : La chaleur est générée à l'interface échantillon / pyro et diffuse à la fois vers l'échantillon et vers le capteur pyro

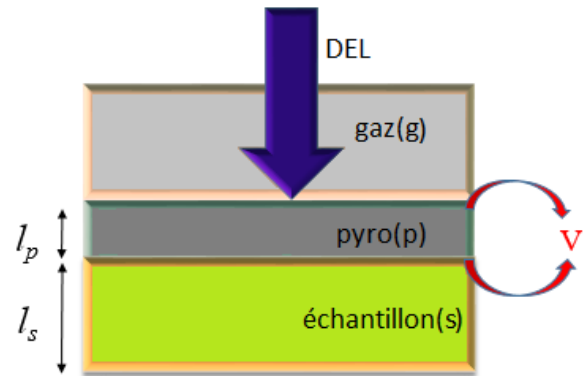


FIGURE 5 – **FPPE** : La chaleur est générée à l'interface gaz / pyro et diffuse à travers le capteur pyro, traverse l'interface pyro / échantillon et atteint l'échantillon

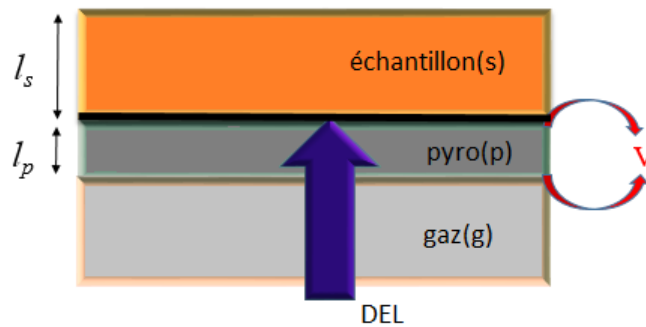


FIGURE 6 – **FPPE avec capteur pyroélectrique semi-transparent** : La chaleur est produite à l'interface échantillon / pyro et diffuse à la fois dans le capteur pyro et dans l'échantillon

reliée à la capacité calorifique par la relation :

$$e = \sqrt{\rho c k} \quad (1)$$

où,  $\rho$  est la masse volumique en  $kg\ m^{-3}$

$c$  est la capacité calorifique en  $J\ kg^{-1}\ K^{-1}$

$k$  est la conductivité thermique en  $W\ m^{-1}\ K^{-1}$

L'effusivité décrit la facilité avec laquelle un matériau échange de la chaleur.

La diffusivité thermique a également été mesurée en utilisant la PPE. La diffusivité thermique, exprimée en  $m^2\ s^{-1}$ , est donnée par :

$$\alpha = k/\rho c \quad (2)$$

Elle décrit avec quelle facilité les ondes thermiques peuvent diffuser à travers le matériau.

Un nouveau banc de mesure à basses températures basé sur la technique PPE a été déve-

loppé et mis en place au laboratoire dans le cadre de cette thèse. La figure 7 montre un schéma simplifié de ce banc qui permet de travailler dans les différentes configurations. Dans ce travail, nous avons utilisé la configuration FPPE pour déterminer l'effusivité et la diffusivité des fluides étudiés. Toutes les expériences à température ambiante ont été réalisées à l'aide d'un capteur pyroélectrique à base de tantalate de lithium ( $LiTaO_3$ ) de 300 micromètres d'épaisseur, de surface  $30 \times 30 \text{ mm}^2$  et recouvert d'or sur les deux faces. Pour les études à basse température, le  $LiTaO_3$  a une épaisseur de 500 micromètre et une surface de  $30 \times 30 \text{ mm}^2$ . Ce dernier est semi-transparent avec un côté recouvert d'or et l'autre côté recouvert d'oxyde d'indium et d'étain (ITO).

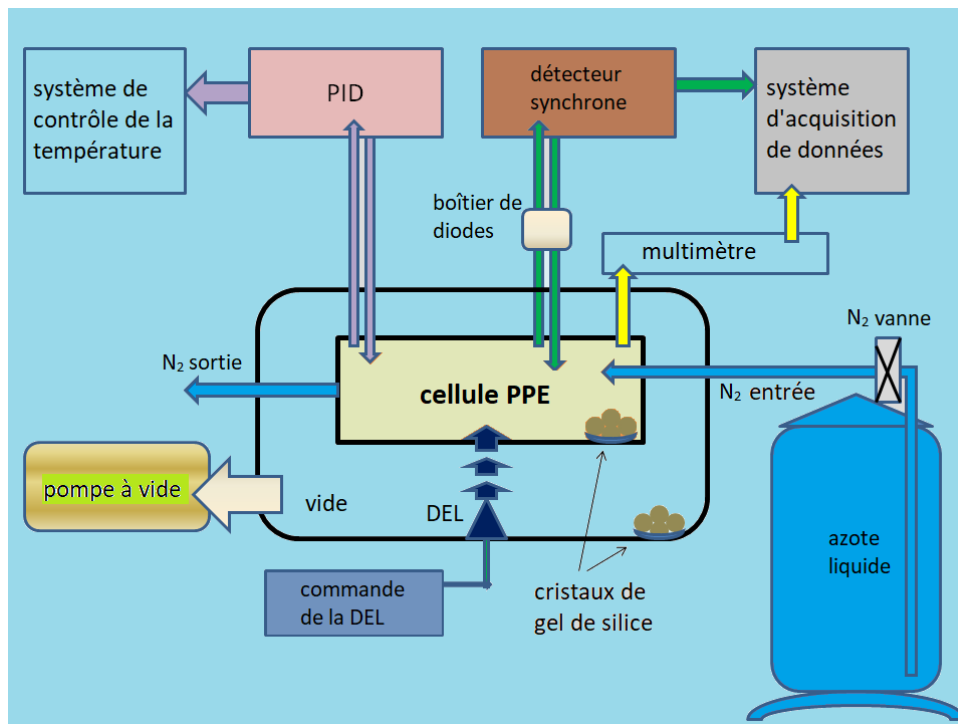


FIGURE 7 – Section transversale simplifiée de notre configuration PPE et du système de contrôle de température et d'acquisition de données

Le capteur pyroélectrique ainsi que les échantillons sont placés dans une cellule maintenue à pression atmosphérique (cellule PPE). La température de cette cellule est contrôlée par un collier chauffant et par circulation d'azote liquide. La figure 8 montre une représentation schématique de la cellule (réalisée en aluminium) avec deux chambres, A et B. La chambre A contient le capteur pyroélectrique et l'échantillon et la chambre B permet la circulation de l'azote liquide. Des vannes d'entrée et de sortie pour l'azote liquide sont raccordées à la chambre B. Il est nécessaire d'avoir deux chambres séparées pour isoler le capteur et l'échantillon du flux d'azote liquide.

La cellule PPE est entourée par le vide afin de l'isoler des phénomènes de convection extérieurs. Les fuites aux basses températures ont été détectées en analysant le niveau de vide. Les mesures de température ont été effectuées à l'aide de capteurs Pt1000 en montage quatre fils en

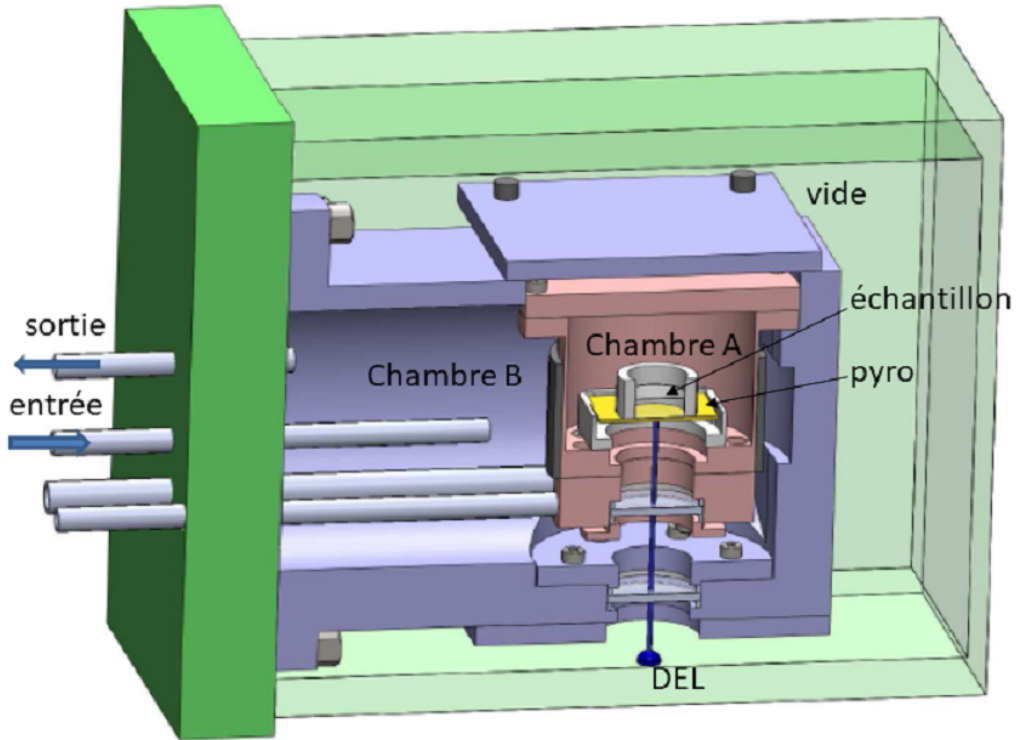


FIGURE 8 – Représentation schématique de la cellule PPE

utilisant deux multimètres : un Keithley 3706 et un Keithley 2700. Ces températures sont les paramètres d'entrée de différents régulateurs PID qui étaient utilisés pour maintenir constante la température des différents circuits électroniques et de la DEL. Tous les pilotages ont été effectués à l'aide de programmes LABVIEW. Le signal pyroélectrique a été mesuré par un détecteur synchrone de marque Signal Recovery (modèle 7124). Toutes les mesures pyroélectriques à température ambiante ont été effectuées en mode tension avec des réglages automatiques pour la sensibilité, le gain AC et la constante de temps. Les mesures aux basses températures ont été effectuées en mode courant avec des réglages manuels pour ces paramètres. La longueur des câbles a été optimisée afin d'éviter le bruit électronique et des blindages électromagnétiques ont été mis en place.

### Mesures à température ambiante

La mise en place d'un nouvel instrument nécessite une calibration à l'aide d'échantillons dont les caractéristiques sont connues, par exemple du glycérol ou du 1,2 propanediol. Avant d'étudier ces échantillons, il était nécessaire de caractériser les capteurs pyroélectriques. De l'eau pure a été utilisée dans la procédure de normalisation pour déterminer l'effusivité et la diffusivité des capteurs pyroélectriques. Pour cela, nous avons utilisé la configuration FPPE dans laquelle l'expression du signal PPE est donnée par :

$$\Gamma(f, T) = 1 - (1 + R_{sp}) e^{-\sigma_p l_p} \quad (3)$$

où  $\sigma_p$  est le nombre d'onde complexe donné par :

$$\sigma_p = (1 + i) \frac{1}{\mu_p} \quad (4)$$

où,  $\mu_p$  est la longueur de diffusion thermique du capteur (normalement exprimée en  $\mu m$ ).

et  $R_{sp} = \frac{b_{sp}-1}{b_{sp}+1}$  où  $b_{sp} = \frac{e_s}{e_p}$  avec  $e_s$  et  $e_p$  les effusivités respectives de l'échantillon et du capteur.

La figure 9 montre l'évolution de l'amplitude et de la phase normalisées du signal PPE en fonction de la fréquence, obtenue pour un tantalate de  $300 \mu m$  d'épaisseur. Le substrat utilisé dans la procédure de normalisation est de l'eau. Une procédure d'ajustement numérique a été utilisée pour déterminer la diffusivité et l'effusivité du tantalate. La même démarche a été utilisée pour la mesure des paramètres thermiques de deux autre capteurs (tableaux 1 et 2). Les valeurs obtenues sont en bon accord avec les données de la littérature.

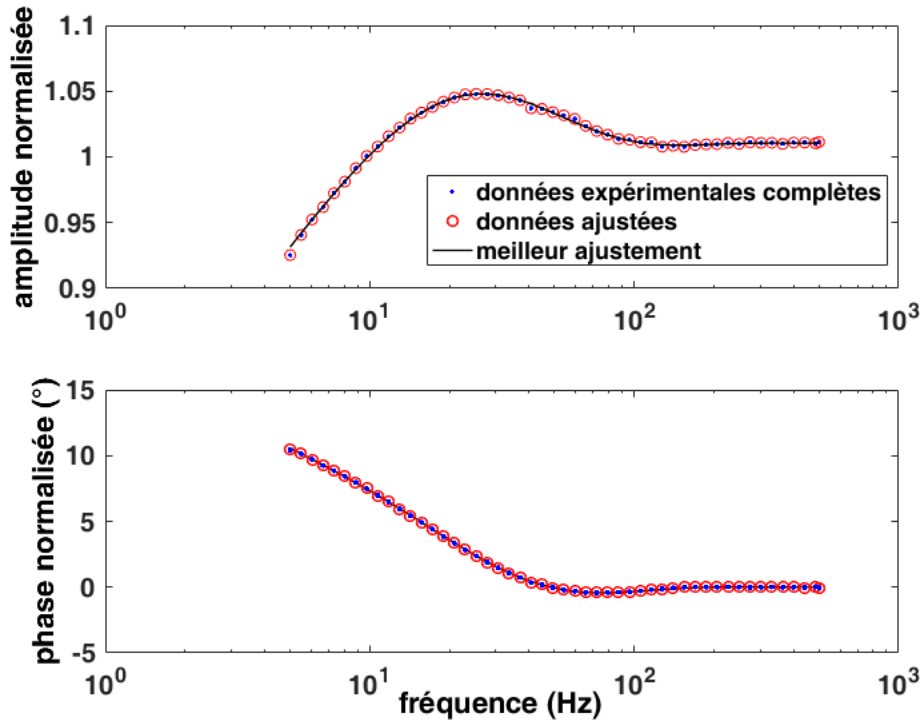


FIGURE 9 – Amplitude et phase normalisées du signal PPE pour le  $LiTaO_3$  ( $300 \mu m$  d'épaisseur avec des électrodes Or-Or)

| Effusivité ( $W s^{1/2} m^{-2} K^{-1}$ ) |               |                         |
|--|---------------|-------------------------|
| Matériau (T ambiante)                    | Ce travail    | Littérature             |
| $LiTaO_3$ ( $300 \mu m$ )                | $4214 \pm 11$ | 3777 [103], 3743 [107], |
| $LiTaO_3$ ( $500 \mu m$ )                | $3857 \pm 8$  | 3750 [110], 3575 [112]  |
| PZT ( $500 \mu m$ )                      | $1710 \pm 8$  | $1733 \pm 42$ [101]     |

TABEAU 1 – Effusivités obtenues pour différents capteurs en utilisant l'eau comme étalon

| Matériau (T ambiante)    | Diffusivité ( $m^2 s^{-1}$ ) |                                       |
|--------------------------|------------------------------|---------------------------------------|
|                          | Ce travail                   | Littérature                           |
| $LiTaO_3$ (300 $\mu m$ ) | $(13.83 \pm 0.04) e-7$       | $12.46 e-7$ [107], $12.47 e-7$ [110], |
| $LiTaO_3$ (500 $\mu m$ ) | $(14.66 \pm 0.03) e-7$       | $13.67 e-7$ [112]                     |
| PZT (500 $\mu m$ )       | $(4.36 \pm 0.02) e-7$        | $(3.51 \pm 0.15) e-7$ [101]           |

TABLEAU 2 – Diffusivités obtenues pour différents capteurs en utilisant l’eau comme étalon

Nous avons utilisé le capteur pyroélectrique ainsi caractérisé pour mesurer l’effusivité thermique du glycérol et du 1,2 propanediol. Les figure 10 et 11 montrent le meilleur ajustement numérique de l’amplitude et de la phase normalisées du signal PPE obtenu respectivement pour le glycérol et le 1,2 propanediol.

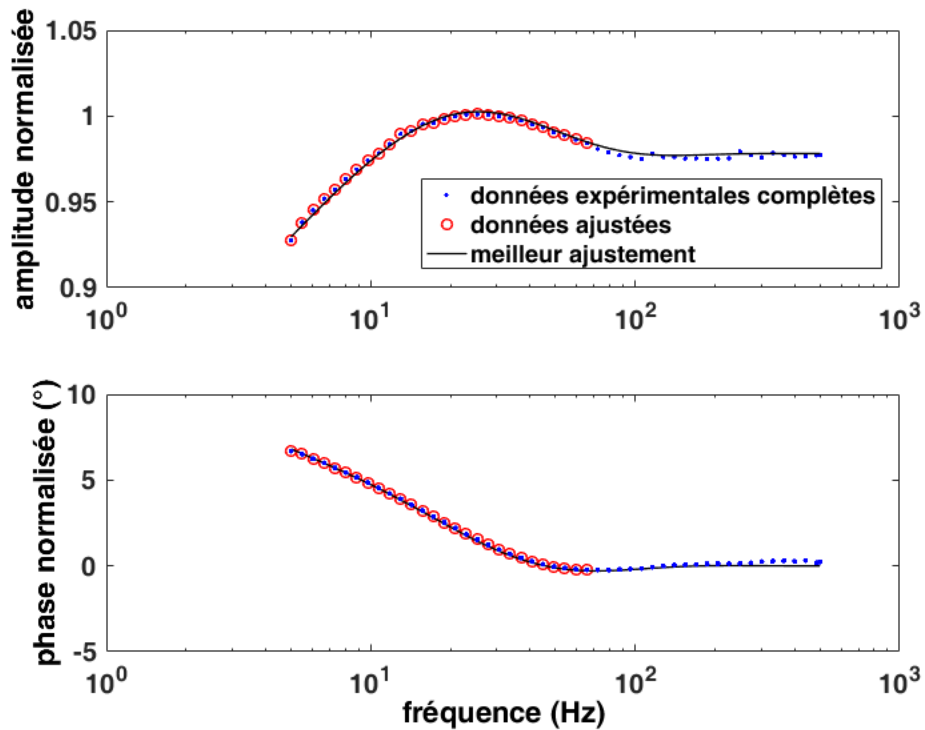


FIGURE 10 – Ajustement numérique de l’amplitude et de la phase normalisées du signal PPE pour le glycérol (capteur :  $LiTaO_3$  de 300  $\mu m$ )

Les tableaux 3 et 4 montrent les résultats que nous avons obtenus comparés avec les données de la littérature. Nous observons un bon accord entre valeurs comparées.

| Effusivité ( $W s^{1/2} m^{-2} K^{-1}$ ) |             |
|--|-------------|
| Ce travail ( $LiTaO_3$ )                 | $958 \pm 7$ |
| Ce travail (PZT)                         | $935 \pm 6$ |
| a  | 924         |
| b  | 897         |
| c  | 933         |
| d  | 945         |
| e  | 943         |
| f  | 912         |

TABLEAU 3 – Comparaison des valeurs obtenues pour l’effusivité du glycérol pur avec la littérature, a : [121], b : [107], c : [112], d : [122], e : [93], f : [123].

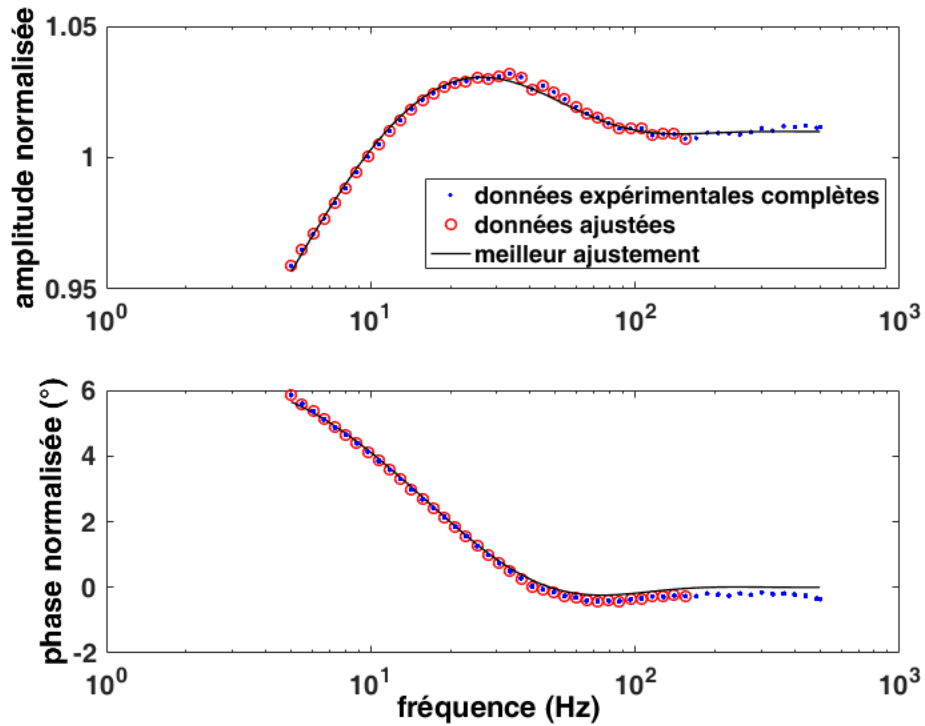


FIGURE 11 – Ajustement numérique de l’amplitude et de la phase normalisées du signal PPE pour le 1,2 propanediol pur (capteur :  $LiTaO_3$  de  $300 \mu m$ )

| Effusivité ( $W s^{1/2} m^{-2} K^{-1}$ ) |              |
|--|--------------|
| Ce travail                               | $768 \pm 5$  |
| a  | $732 \pm 51$ |
| b  | 721          |

TABLEAU 4 – Comparaison de l’effusivité du 1,2 propanediol avec la littérature, a : [123], b : [121]

### Association moléculaire

L’effusivité thermique a été utilisée pour étudier la force de l’interaction moléculaire dans les liquides binaires. Les liquides peuvent être divisés en deux classes, les liquides normaux

et les liquides associés. Les deux ont des propriétés très différentes. Cette différence de propriétés est due aux forces d'association qui jouent un rôle important dans la détermination des propriétés internes des molécules telles que la forme et la distribution électronique.

Des solutions aqueuses des deux CPA ont été préparées à des concentrations différentes allant de 10 % en masse à 90 % en masse. L'effusivité thermique de ces solutions a été déterminée à l'aide de la configuration FPPE. L'évolution de l'effusivité en fonction de la concentration molaire en glycérol est montrée sur la figure 12.

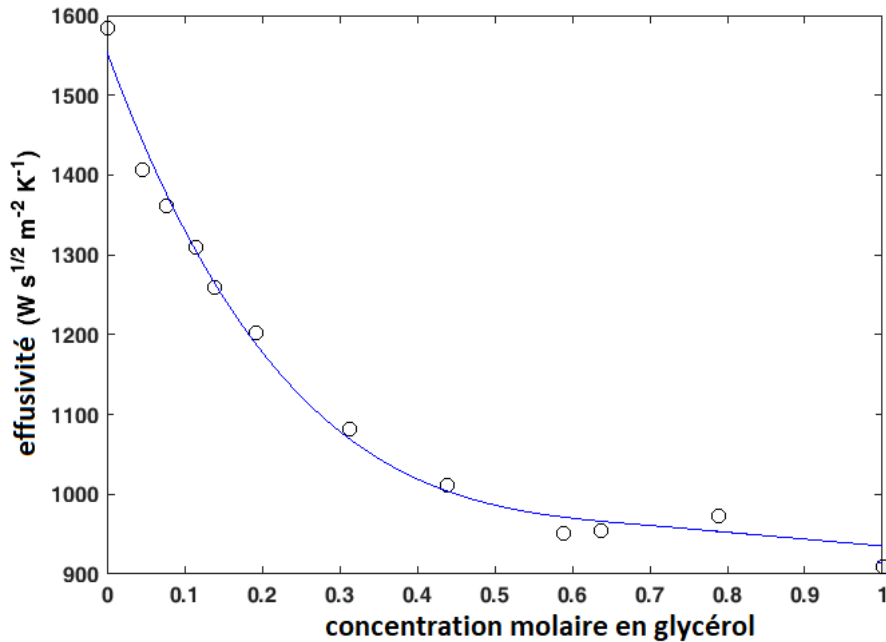


FIGURE 12 – Effusivité des solutions binaires glycérol-eau

L'association moléculaire a été étudiée en calculant la quantité,  $\Delta e/e$ , appelée «écart relatif» et définie comme  $(e_{exp} - e_{theor})/e_{theor}$ , où  $e_{theor}$  a été calculée à l'aide de l'équation  $(pourcentage\ molaire_{CPA})(e_{CPA}) + (pourcentage\ molaire_{eau})(e_{eau})$ . L'écart relatif est une grandeur sans dimension et est une mesure de la déviation de l'effusivité par rapport à la linéarité.

Pour étudier l'association moléculaire dans le mélange eau-glycerol, l'évolution de l'écart relatif, mentionné plus haut, est tracé en fonction de la concentration molaire de glycérol, comme indiqué sur la figure 13. Pour les mélanges binaires non associatifs, l'écart relatif présente un comportement linéaire lorsqu'il est représenté en fonction de la concentration. La déviation par rapport à la linéarité montre une association moléculaire.

De même, des solutions aqueuses de 1,2 propanediol ont également été étudiées. L'évolution de l'effusivité en fonction de la concentration molaire en glycérol est montrée sur la figure 14.

La figure 15 montre le courbe d'écart relatif en fonction de la concentration molaire de 1,2 propanediol.

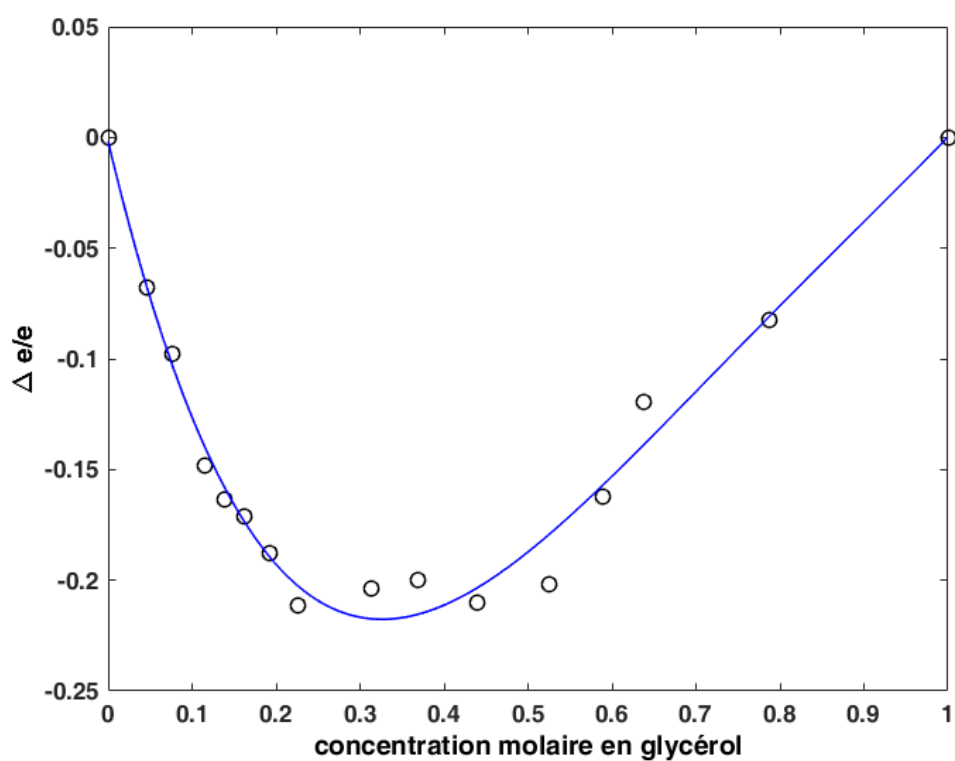


FIGURE 13 – Écart relatif de l'effusivité des solutions binaires glycérol-eau

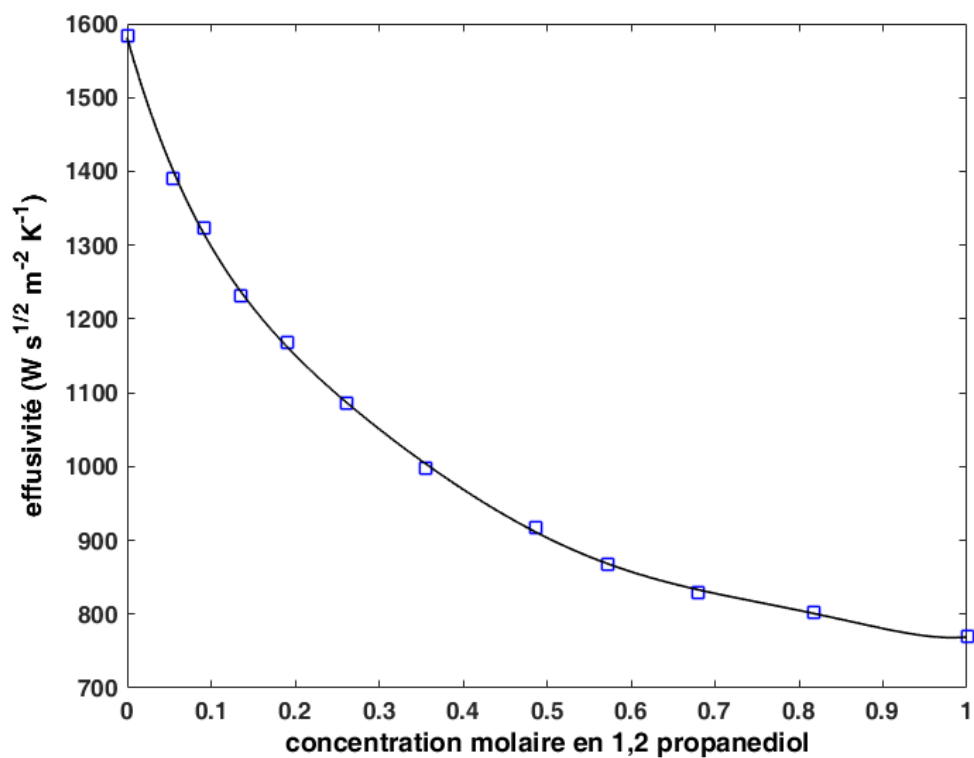


FIGURE 14 – Effusivité des solutions binaires 1,2 propanediol-eau

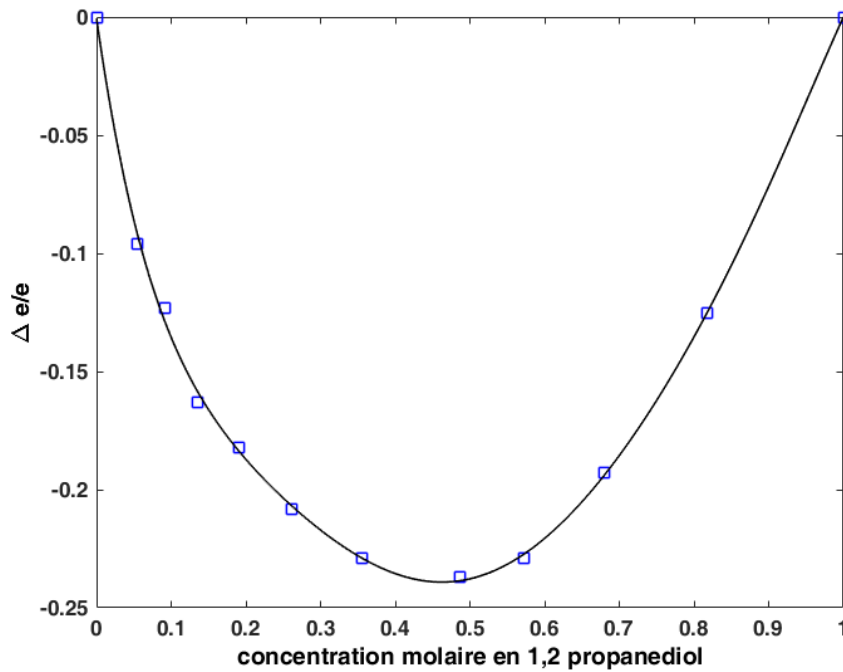


FIGURE 15 – Écart relatif de l'effusivité des solutions binaires 1,2 propanediol-eau

Les deux figures (13 et 15) montrent que le processus d'association moléculaire s'est produit dans les deux mélanges binaires glycérol-eau et 1,2 propanediol-eau. Par conséquent, nous avons utilisé la mesure de l'effusivité thermique comme une technique appropriée pour détecter l'association moléculaire dans les liquides binaires.

## Mesures aux basses températures

### Détermination du temps de relaxation $\tau$

Dans le quatrième chapitre de la thèse, nous nous sommes intéressés à l'évolution de la capacité calorifique de liquides cryoprotectants au voisinage de la relaxation alpha. Cette étude a été effectuée à travers la mesure de l'effusivité thermique de ces liquides dont le carré est proportionnel à la capacité calorifique ( $e^2 = \rho ck$ ).

La dépendance en fréquence de la capacité calorifique des liquides vitrifiables est complexe. Elle peut être décrite par le modèle empirique d'Havriliak-Negami (HN) qui est donné par l'expression :

$$c(\omega, T) = c_\infty + \left[ \frac{c_0 - c_\infty}{\left(1 + (i\omega\tau)^\alpha\right)^\beta} \right] \quad (5)$$

où  $\omega$  est la fréquence angulaire,  $\omega = 2\pi\nu$ ,  $\nu$  est la fréquence de modulation.  $c_0$  et  $c_\infty$  sont des constantes.  $\alpha$  et  $\beta$  sont compris entre 0 et 1.  $\tau$  est le temps de relaxation. Il dépend de la température.

La relation entre l'effusivité thermique et la capacité calorifique ( $e^2 = \rho ck$ ) permet de

réécrire l'équation 5 sous la forme :

$$e^2(\omega, T) = e_\infty^2 + \left[ \frac{e_0^2 - e_\infty^2}{(1 + (i\omega\tau)^\alpha)^\beta} \right] \quad (6)$$

Dans cette équation, la dépendance en température de  $\tau$  peut être décrite par différents modèles théoriques comme les lois de Vogel Fulcher Tamman (VFT), Bässler-Avramov (BA), Waterton-Mauro (WM ou MYEGA), Critical-like (Crit), etc. Trouver le modèle approprié pour un liquide donné n'est pas aisé. Il est possible d'essayer chacun des modèles et de vérifier sa validité, mais cela est fastidieux lorsqu'il s'agit d'étudier un grand nombre d'échantillons. Par conséquent, nous avons utilisé un protocole pour déterminer le bon modèle qui décrit l'évolution de  $\tau$  en fonction de la température.

Ce protocole est basé sur l'utilisation d'une représentation complexe plane telle que le tracé Cole-Cole ou le tracé Wicket. Pour une écriture aisée, nous simplifions l'équation 6 en remplaçant  $e^2$  par  $E$  :

$$E(\omega, T) = E_\infty + \left[ \frac{E_0 - E_\infty}{(1 + (i\omega\tau)^\alpha)^\beta} \right] \quad (7)$$

Ainsi, le carré de l'effusivité complexe peut être écrit sous la forme  $E(\omega, T) = E' + iE''$  ( $E'$  est la partie réelle de  $e^2$  et  $E''$  est la partie imaginaire de  $e^2$ ). La partie réelle ( $E'$ ) est appelée module de stockage et la partie imaginaire ( $E''$ ) est appelée module de perte. Pour le graphique de Wicket, nous considérons une autre quantité, appelée facteur de perte, défini comme  $\tan \delta = \frac{E''}{E'}$ . Dans le tracé Wicket, le facteur de perte est représenté en fonction du module de stockage, ( $\frac{E''}{E'} = f(E')$ ).

Par ajustement numérique du graphe Wicket à l'aide de l'équation 7, les quatre paramètres  $\alpha$ ,  $\beta$ ,  $E_0$  et  $(E_0 - E_\infty)$  noté  $\Delta E$  peuvent être déterminés. En utilisant ces paramètres,  $\tau$  est déterminé à l'aide de l'expression suivante, obtenue à partir de l'équation 7.

$$\tau(T) = -i \frac{\exp(\ln(\exp(\ln((E_0 - E_\infty)/(E(\omega, T) - E_\infty))/\beta) - 1)/\alpha)}{\omega} \quad (8)$$

Nous appelons cette méthode "méthode directe".

À partir du  $\tau$  ainsi calculé, l'énergie d'activation est obtenue en utilisant l'équation :

$$\Delta E_a(T) = RT \ln\left(\frac{\tau(T)}{\tau_\infty}\right) \quad (9)$$

Ensuite, à partir de l'énergie d'activation, l'indice de Dyre-Olsen  $I_{DO}$  peut être déterminé en utilisant l'équation :

$$I_{DO}(T) = - \frac{d \ln \Delta E_a(T)}{d(\ln T)} \quad (10)$$

L'analyse de  $I_{DO}$  est importante pour tester la validité de différents modèles définissant la

dépendance en température de  $\tau$  dans le cas des liquides vitrifiables ultravisqueux de faible poids moléculaire. Ceci est réalisé en considérant l'évolution en fonction de la température de l'inverse de l'indice de Dyre-Olsen ( $I_{DO}^{-1}$ ).  $I_{DO}^{-1}$  qui est calculé pour chaque modèle comme suit :

$$\frac{1}{I_{DO}} = \begin{cases} \left(\frac{1}{T_0}\right) T - 1 & \text{pour VFT} \\ \frac{1}{D-1} & \text{pour BA} \\ \left(\frac{1}{C}\right) T & \text{pour WM} \\ \left(\frac{1}{\phi}\right) T - \frac{T_C}{\phi} & \text{pour Crit} \end{cases} \quad (11)$$

L'équation 11, montre que l'inverse de l'indice de Dyre Olsen est linéaire, de la forme,  $I_{DO}^{-1} = mT + c$ . La valeur de "c" définit le modèle pour  $\tau$  :  $c = 1$  pour le modèle VFT,  $c = 0$  pour le modèle WM (MYEGA) et  $c = -T_C/\phi$  pour le modèle critique. Pour le modèle BA  $I_{DO}^{-1}$  atteint une valeur constante de  $1/(D-1)$ . Ainsi, il est donc possible de déterminer le modèle qui décrit la dépendance en température de  $\tau$  à partir de l'évolution en température de  $I_{DO}^{-1}$ .

Une simulation de l'évolution en température de  $I_{DO}$  et  $I_{DO}^{-1}$  pour différents modèles est montrée dans la figure 16 [132].

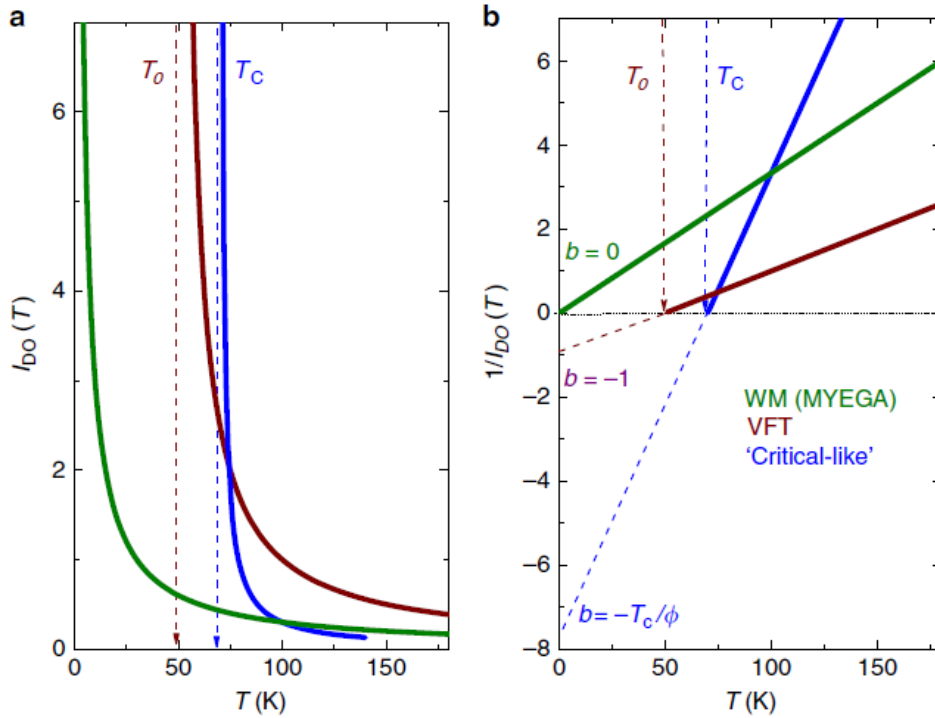


FIGURE 16 – Évolution en fonction de la température de  $I_{DO}$  (a) et  $I_{DO}^{-1}$  (b) pour différentes équations montrant le comportement de  $\tau(T)$ . L'équation BA donne une ligne horizontale qui est omise ici. Figure reproduite d'après la littérature [132].

Si le modèle ainsi déterminé est par exemple le modèle VFT, on peut introduire ce modèle dans l'équation 7 et effectuer un ajustement numérique sur l'évolution en température des

parties réelles et imaginaires du carré de l'effusivité et déterminer les sept paramètres. Nous appelons cette méthode "ajustement à 7 paramètres". La démarche est identique dans le cas des autres modèles

### Température de transition vitreuse et fragilité

Deux paramètres importants interviennent dans l'études des CPA, la température de la transition vitreuse qui est par convention la température pour laquelle  $\tau = 100$  s et la fragilité  $m$  (paramètre sans dimension) qui rend compte de la sensibilité de la structure au changement de la température. La fragilité est calculée à partir de  $\tau(T)$  en utilisant l'équation suivante :

$$m = \left( \frac{d \log(\tau)}{d(T_g/T)} \right)_{T=T_g} \quad (12)$$

Une autre définition de la fragilité a été proposée par Martinez-Garcia et al. [53, 132]. Il s'agit du rapport entre l'enthalpie d'activation et l'énergie d'activation au  $T_g$ , donné par :

$$M = I_{DO}(T_g) = \left. \frac{d \ln \Delta E_a(T)}{d(T_g/T)} \right|_{T=T_g} = \frac{\Delta H_a(T_g)}{\Delta E_a(T_g)} - 1 \quad (13)$$

A partir des équations 10, 12 et 13, la relation suivante entre  $m$  et  $M$  peut être déduite :

$$m = C(1 + M) = C(1 + I_{DO}(T_g)) = C \frac{\Delta H_a(T_g)}{\Delta E_a(T_g)} \quad (14)$$

où  $C$  est une constante :  $C = 2 - \log(\tau_\infty)$  qui peut prendre des valeurs comprises entre 13 et 18.

L'évolution en fonction de la température du rapport entre l'enthalpie et l'énergie d'activation apparente peut être étudiée parallèlement à l'évolution de  $\log(\tau)$  en fonction de  $T_g/T$  (courbe d'OLUA). Cela permet une comparaison entre la fragilité classique,  $m$  et la nouvelle fragilité,  $M$ . Un exemple est montré à la figure 17.

Pour l'ensemble des liquides que nous avons étudiés dans ce travail, le protocole mentionné ci-dessus a été utilisé pour déterminer leur  $T_g$  et leur fragilité  $m$ . La section suivante synthétise les résultats obtenus et la comparaison avec les données de la littérature.

### Résultats des mesures aux basses températures

Le glycérol, le 1,2 propanediol et leurs mélanges binaires avec de l'eau ont été étudiés à l'aide de ce protocole. Pour cette étude, la configuration FPPE avec capteur pyroélectrique semi-transparent a été utilisée. Les échantillons ont été placés dans la cellule PPE et refroidis à  $-196$  °C à une vitesse de  $6$  °C  $\text{min}^{-1}$  et ensuite soumis à une élévation de température à une vitesse d'environ  $1$  °C  $\text{min}^{-1}$ . L'acquisition des données a été effectuée pendant la phase de chauffage. A partir du signal PPE obtenu, les parties réelle et imaginaire de l'effusivité carrée ont été calculées et utilisées pour tracer le diagramme de Wicket à partir duquel  $\tau$ , l'énergie d'activation et  $I_{DO}^{-1}$  ont été déterminés. Le modèle décrivant  $\tau(T)$  a été obtenu pour chaque matériau à partir de l'évolution en température de  $I_{DO}^{-1}$ . Ensuite, en utilisant l'ajustement à 7 paramètres, tous les paramètres ont été déterminés. Les valeurs de  $T_g$ ,  $m$  et  $M$  de tous les

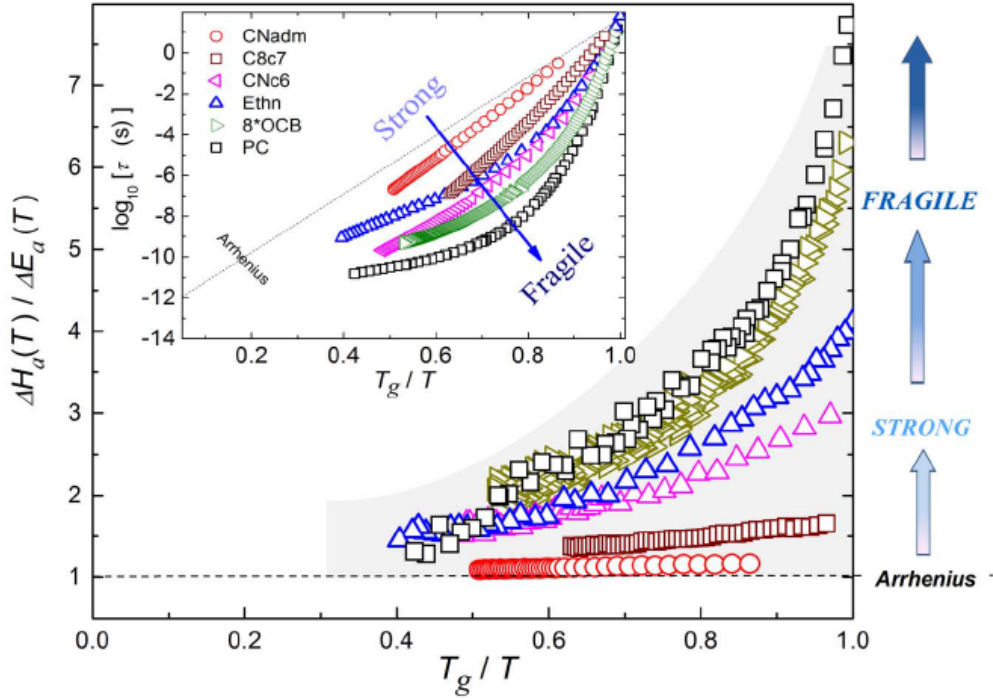


FIGURE 17 – Évolution du rapport entre l’enthalpie d’activation apparente et l’énergie pour quelques systèmes vitrifiables. Figure issue de la littérature [53].

échantillons ont été calculés et comparés avec les données de la littérature.

### Résultats obtenus pour le glycérol pur

La figure 18 montre l’évolution de l’amplitude et la phase normalisées du signal PPE en fonction de la température pour le glycérol pur. La mesure a été réalisée à une fréquence fixe de 22 Hz..

La relaxation est observée à la fois sur l’amplitude et la phase du signal comme prévu par les simulations que nous avons effectuées. L’amplitude diminue et la phase montre un pic au moment de la relaxation  $\alpha$ . Le point d’inflexion sur l’amplitude apparaît à la même température que le pic sur la phase du signal. A partir de l’amplitude et la phase du signal, nous avons calculé l’effusivité au carré du glycérol pur en fonction de la température à l’aide de l’équation suivante :

$$\Gamma(f, T) = \frac{1}{1 + b_{sp}} = \frac{1}{1 + \frac{e_s}{e_p}} \quad (15)$$

où  $e_s$  et  $e_p$  sont les effusivités respectives de l’échantillon et du capteur.

En utilisant les parties réelles et imaginaires, le diagramme de Wicket a été tracé. Une procédure d’ajustement numérique de ce tracé (figure 19) a été utilisée pour déterminer les valeurs des quatre paramètres :  $\alpha$ ,  $\beta$ ,  $E_0$  et  $\Delta E$  (tableau 5).

| Fréquence (Hz) | $\alpha$ | $\beta$ | $E_\infty$ | $\Delta E$ |
|----------------|----------|---------|------------|------------|
| 22             | 1        | 0.52    | 212920     | 146570     |

TABLEAU 5 – Paramètres pour le glycérol pur en utilisant le modèle d’Havriliak-Negami

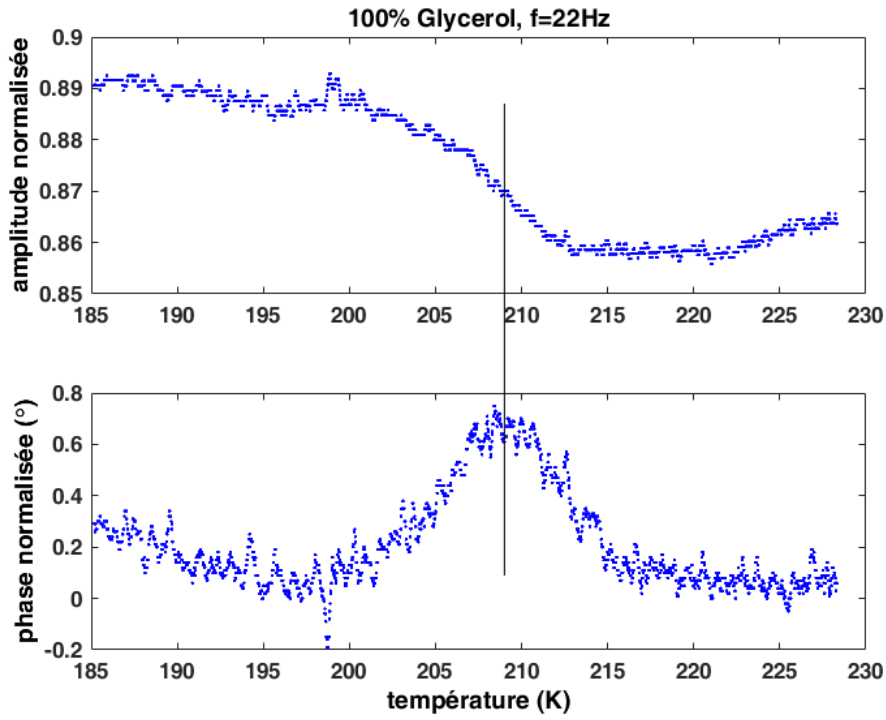


FIGURE 18 – Amplitude et phase normalisées du glycérol pur lors d’un balayage en température à une fréquence fixe de 22 Hz en utilisant un capteur  $LiTaO_3$  de  $500 \mu m$  d’épaisseur

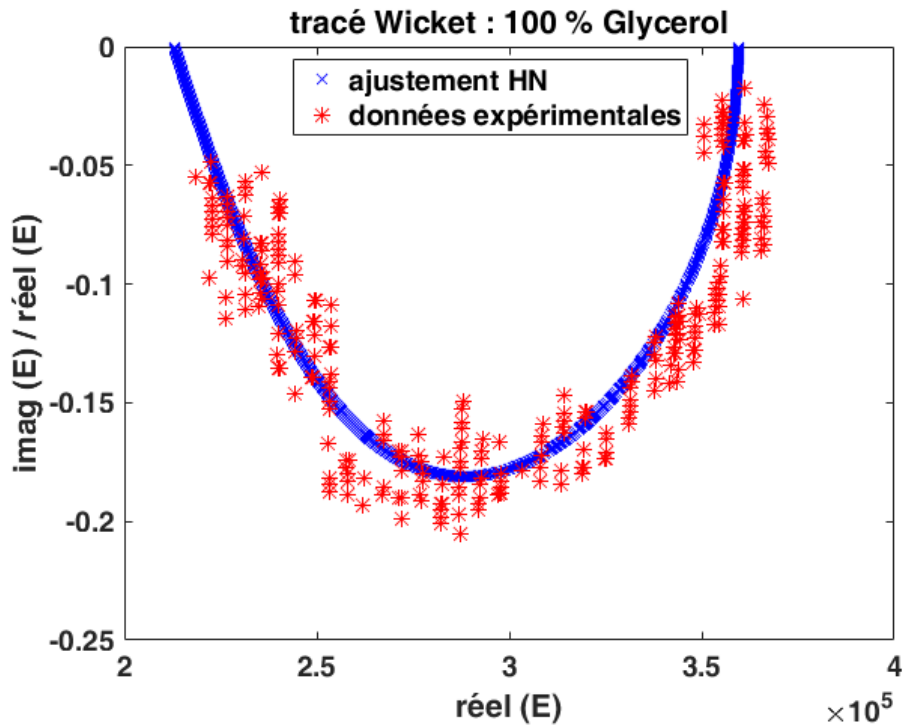


FIGURE 19 – Tracé Wicket ajusté pour le glycérol pur

En utilisant l’équation 9, l’énergie d’activation a été calculée, cela a permis le calcul du  $I_{DO}^{-1}$  et la détermination de la dépendance en température de  $\tau$ . La figure 20 montre l’évolution en

fonction de la température de  $I_{DO}^{-1}$ .

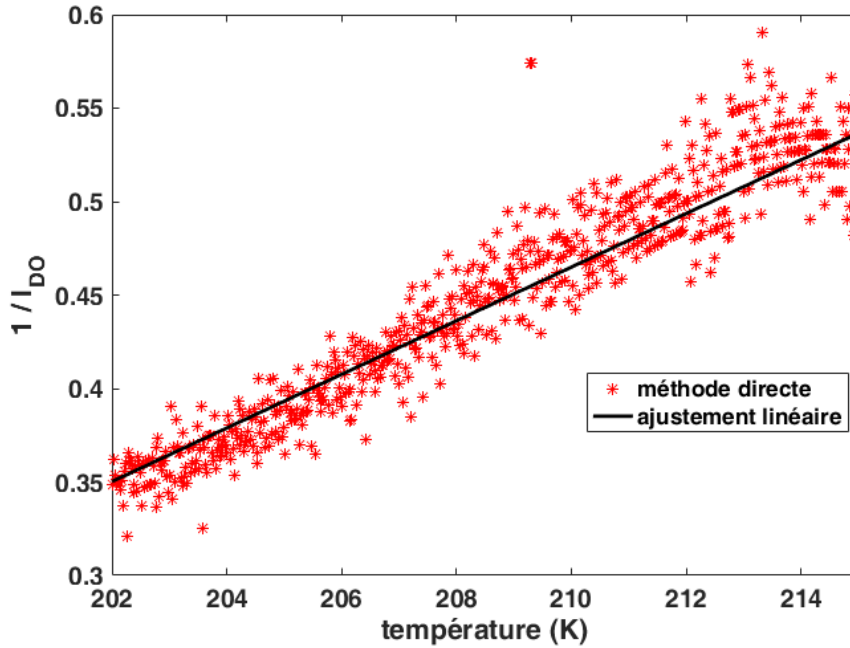


FIGURE 20 – Évolution en température de  $I_{DO}^{-1}$ . L'équation de la régression linéaire est  $I_{DO}^{-1} = 0.01434 T - 2.547$

L'analyse du  $I_{DO}^{-1}$ , a permis de déterminer que l'évolution en température de  $\tau$  suivait la loi VFT :

$$\tau(T) = \tau_{\infty} \exp\left(\frac{D T_0}{T - T_0}\right), \quad D = B/T_0 \quad (16)$$

En reportant l'équation 16 dans l'équation 7, nous avons effectué un "ajustement à 7 paramètres" sur les parties réelle et imaginaire de l'effusivité carrée pour trouver les paramètres  $\alpha$ ,  $\beta$ ,  $E_0$ ,  $\Delta E$ ,  $T_0$ ,  $B$  et  $\tau_0$ . La figure 21 montre les parties réelles et imaginaires ajustées de l'effusivité au carré pour le glycérol pur à 22 Hz.

A l'aide des paramètres VFT ainsi obtenus, nous avons calculé le  $T_g$  en utilisant la convention  $T = T_g$  lorsque  $\tau=100$  s et  $m$  en utilisant l'équation 12. Le tableau 6 montre les valeurs de  $T_g$ ,  $m$  et  $M$  pour le glycérol pur (mesure PPE à 22 Hz).

| $T_g$ (K) | $m$   | $M$  |
|-----------|-------|------|
| 193.80    | 65.98 | 3.49 |

TABEAU 6 –  $T_g$ ,  $m$  et  $M$  pour le glycérol pur (expérience PPE à 22 Hz)

Plusieurs mesures ont été menées pour chaque échantillon à des fréquences différentes. Les valeurs du  $T_g$  et de  $m$  ont été déterminés et leur valeur moyenne a été calculée. À partir des résultats ainsi obtenus, une classification des échantillons basée sur les valeurs de  $m$  et  $M$  a été établie (figures 22 et 23).

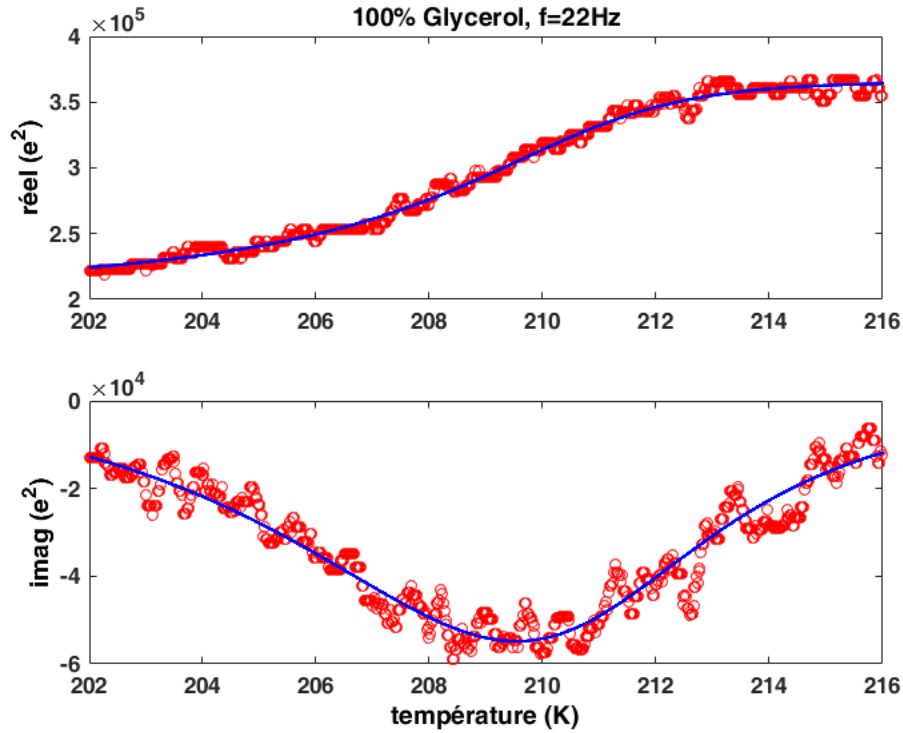


FIGURE 21 – Parties réelles et imaginaires de l’effusivité carrée ajustée par la méthode "d’ajustement à 7 paramètres"

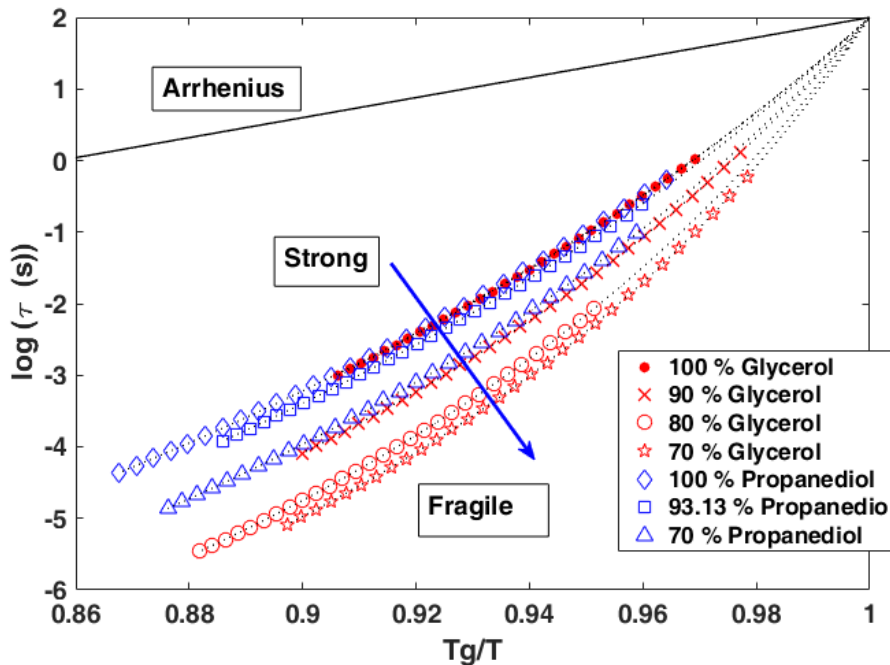


FIGURE 22 – Diagramme d’OLUVA pour classer les échantillons étudiés en fonction de leur fragilité

Des mesures de viscosité et de calorimétrie différentielle à balayage (DSC) ont été effectuées pour certains échantillons et les résultats ont été comparés aux résultats de la PPE. Le

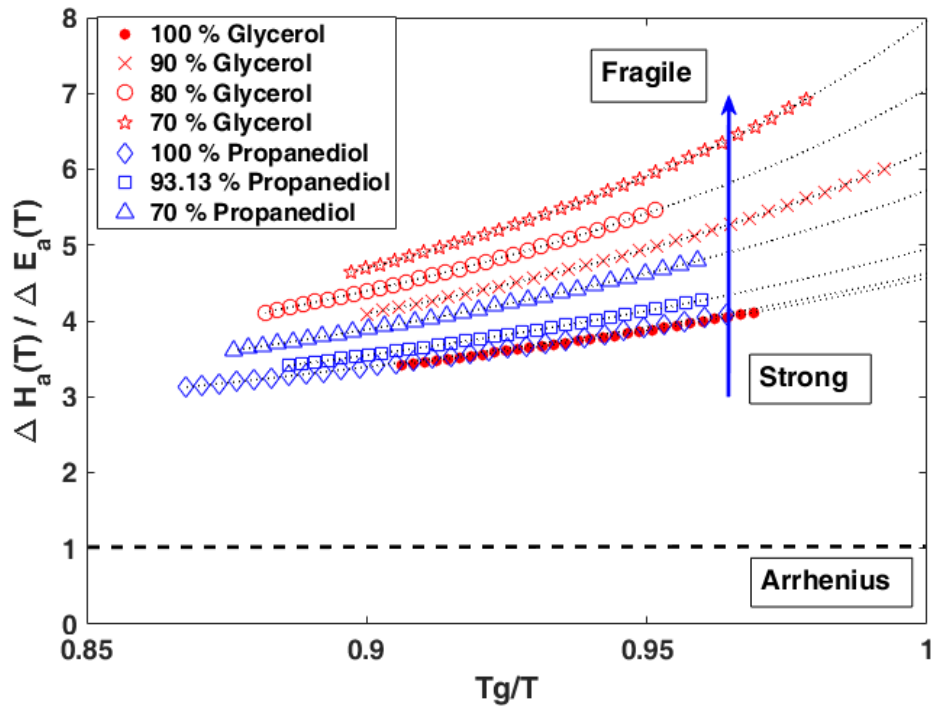


FIGURE 23 – Évolution du rapport entre l’enthalpie d’activation apparente et l’énergie pour tous les échantillons étudiés

tableau 7 montre la comparaison entre les valeurs de  $T_g$  déterminées à partir de la DSC, celles obtenues à l’aide de la PPE, de la viscosité et celles trouvées dans la littérature. Les résultats montrent une bonne correspondance des données obtenues par PPE avec celles obtenues par les autres techniques.

| Échantillon               | $T_g$ (DSC) | $T_g$ (PPE)   | $T_g$ (Viscosité) | $T_g$ (Littérature)        |
|---------------------------|-------------|---------------|-------------------|----------------------------|
| 100 wt% glycerol          | 191.7       | $195 \pm 6$   | 182.5             | $190^1, 191^2$             |
| 90 wt% glycerol           | 182.2       | 193.4         | 174.1             | $181.5^3, 186.0 \pm 0.1^4$ |
| 80 wt% glycerol           | -           | $180 \pm 3$   | 173.6             | $174.0^3, 177.9 \pm 0.2^4$ |
| 70 wt% glycerol           | -           | $183 \pm 5$   | 177.7             | $168.3^3, 171.0 \pm 0.2^4$ |
| 60 wt% glycerol           | -           | -             | 168.9             | $162.1^3, 165.1 \pm 0.1^4$ |
| 50 wt% glycerol           | -           | -             | 166.0             | $160.0 \pm 0.1^4$          |
| 100 wt% 1,2 propanediol   | 169.5       | $173 \pm 3$   | 167.9             | $167^a, 164^b$             |
| 93.13 wt% 1,2 propanediol | 167.8       | $172 \pm 3$   | 167.4             | -                          |
| 90 wt% 1,2 propanediol    | -           | -             | 174.4             | $162.47^c, 165^d$          |
| 80 wt% 1,2 propanediol    | -           | -             | 185.8             | $160.78^c, 164^d$          |
| 70 wt% 1,2 propanediol    | -           | $185.2 \pm 1$ | 167.4             | $160.45^c, 163^d$          |
| 60 wt% 1,2 propanediol    | -           | -             | 182.2             | $161.00^c, 166^d$          |

TABLEAU 7 –  $T_g$  de tous les échantillons obtenus par différentes techniques et comparaison avec les données de la littérature, 1 : [69], 2 : [139], 3 : [97], 4 : [137], a : [69], b : [139], c : [98], d : [96]

De même, m a également été déterminée par DSC, PPE et des mesures de viscosité. Le

tableau 8 montre la comparaison des résultats obtenus pour m avec les données de la littérature.

| Échantillon               | m (DSC) | m (PPE) | m (Viscosité) | m (Littérature)                                       |
|---------------------------|---------|---------|---------------|---|
| 100 wt% glycerol          | 77.1    | 71 ± 20 | 54.5          | 53 <sup>a</sup> , 78 <sup>b</sup> , 52.3 <sup>c</sup> |
| 90 wt% glycerol           | 63.3    | 92      | 60.5          | -   |
| 80 wt% glycerol           | -       | 98 ± 35 | 78.6          | 54.4 <sup>c</sup>                                     |
| 70 wt% glycerol           | -       | 118     | 115.2         | 56.5 <sup>c</sup>                                     |
| 60 wt% glycerol           | -       | -       | 119.5         | 57.3 <sup>c</sup>                                     |
| 50 wt% glycerol           | -       | -       | 124.3         | -   |
| 100 wt% 1,2 propanediol   | 74.5    | 71 ± 16 | 67.4          | 52 <sup>a</sup> , 45 <sup>b</sup>                     |
| 93.13 wt% 1,2 propanediol | 82.9    | 75 ± 12 | 73.0          | -   |
| 90 wt% 1,2 propanediol    | -       | -       | 93.4          | -   |
| 80 wt% 1,2 propanediol    | -       | -       | 149.9         | -   |
| 70 wt% 1,2 propanediol    | -       | 87 ± 16 | 156.1         | -   |
| 60 wt% 1,2 propanediol    | -       | -       | 150.9         | -   |

TABLEAU 8 – Paramètres de fragilité de tous les échantillons obtenus par différentes techniques et comparaison avec les données de la littérature, a : [69], b : [139] , c : [99]

## Conclusion

En utilisant le banc de mesure PPE basses températures nouvellement construit, nous avons déterminé les paramètres de vitrification comme le  $T_g$  et m pour différents échantillons cryoprotecteurs. Ces paramètres ont également été étudiés en utilisant la viscosité et la DSC pour mener une étude en parallèle afin de comparer les résultats obtenus. Ces résultats sont en bon accord les uns avec les autres. La différence entre certains des résultats est due à l'incertitude expérimentale. Elle devrait pouvoir être réduite en réalisant un nombre plus élevé de mesures.



---

## Introduction

---

*Two roads diverged in a wood, and I—  
I took the one less traveled by,  
And that has made all the difference.*

---

ROBERT FROST

Knowing the properties of materials is a key factor for their application in various domains. The properties of any material can be classified into mechanical, thermal and electrical properties. Researchers applied different techniques to study these properties in a deeper level for the betterment of technology. Thermal properties of materials have been studied for many decades. Studying the thermal properties of materials is very important to improve their applications in the development of heat sensors, conductors, insulators etc and to comprehend their behavior when subjected to variation in temperature, for example, thermal expansion. It is the characteristic of a material that defines how it behaves in the presence of a heat wave or in a temperature field. By knowing their thermal properties, we can understand how easily and efficiently they can accept and transfer heat energy through them.

Various techniques are being used for studying the thermal properties of substances. Among them, photothermal methods are considered as efficient tools for this application. Photopyroelectric (PPE) technique is a promising method for thermal characterization of materials. Pyroelectric materials can generate a potential difference when they suffer a change in temperature. The voltage generated by a pyroelectric material is a function of change in temperature. They can be used as sensors to study the thermal properties of other materials. The thermal properties of all materials depend on temperature, i.e, the heat absorbed by a material at, for instance, 100K is different from that at 500K. Therefore, we must study the thermal properties as function of temperature. PPE technique can be easily adopted for this purpose. An efficient pyroelectric material to be used as sensors must be able to generate a signal for a wide range of temperature and must not affect the intrinsic properties of the investigated sample.

Thermal properties study is an inevitable part in the field of cryopreservation, where living cells or tissues are cooled down to sub zero temperatures and preserved for future. Being in a sub zero temperature, the biological activities in living cells are slowed down drastically or completely stopped and the cells can be preserved for future studies or application. In this process it is very important to avoid or control the chances of ice formation by the water present in the cells or tissues. When ice formation is prevented, the resulting mixture ends up in the form of a glass. Ice formation can happen during cooling and thawing process. The rate of cooling and thawing is one of the main factor that affects the crystallization in cells which depends on their thermal properties. Various techniques are applied in the field of cryopreservation to limit freeze damage. To understand the effect of rate of cooling and thawing on the living cells it is crucial to study their thermal properties at sub zero temperature.

In cryopreservation techniques, substances called cryoprotectants (CPAs) are used to limit ice formation during the process. These CPAs mix with the tissues and act as a protection against freeze damages. There are different CPAs used in the industry. The rates of cooling and thawing vary according to CPAs. The type and concentration of CPAs depend on the type of cells or tissues. A higher concentration of CPAs prevents ice formation more efficiently but increases the risk of toxicity, which eventually damages the cells. So it is crucial to study their thermal properties and effect of concentration to enhance their performance in cryopreservation.

When cooling a liquid, it can solidify either into a crystalline solid or into an amorphous solid also known as glass. Glassy state has been studied for decades to get a profound understanding of the glass dynamics. Dielectric measurements, Differential Scanning Calorimetry (DSC), Nuclear Magnetic Resonance (NMR) spectroscopy, light scattering spectroscopy, photothermal techniques etc have been used for this study, providing significant progress in development of new theories to explain the glassy state. Despite these progresses, the glass dynamics is not fully understood. So our aim is to study the glassy state with the help of PPE technique to have a better comprehension. Heat capacity of glass formers shows a characteristic feature of frequency dependence. PPE technique is an efficient tool to study the frequency dependence of heat capacity.

Our area of interest is to study the thermal properties of CPAs using PPE technique. Considering the high sensitivity, better accuracy, easy installation and other advantages of PPE technique, we decided to build a PPE instrument to study the thermal properties of the glass forming liquids at low temperature. Although PPE was used widely for thermal characterization at ambient and high temperatures, the low temperature studies were not common. This work mainly focuses on the development, installation and calibration of a new low temperature PPE instrument in the UDSMM laboratory and the use of PPE to find the glass parameters like glass transition temperature ( $T_g$ ) and fragility ( $m$ ) of CPAs like glycerol and 1,2 propanediol and their aqueous solutions. Very little information is available on these parameters of their aqueous solutions. Therefore, we have studied the pure CPAs and their aqueous solutions us-

ing PPE method and determined their  $T_g$  and  $m$ . It is always good to compare the results among different techniques and this was done using viscosity and DSC measurements. These results have been compared with the results from PPE.

The manuscript contains four chapters. The first chapter discusses about cryopreservation, cryoprotectants, vitrification, glassy state and PPE technique. Vitrification is an efficient and widely used cryopreservation technique. This chapter also briefs about the common thermal properties determination techniques and some theoretical models to explain the glass dynamics.

The second chapter explains the theory of heat transfer through different layers of materials and the PPE technique in detail. There are different experimental models for PPE to study different properties. This chapter explains these models and how to determine the thermal properties of different layers from the PPE signal.

The third chapter describes our main work, which is the development of experimental setup. We have done PPE measurements at ambient temperature and sub zero temperature. Here we elaborated the design, construction and calibration of our instrument and the ambient temperature experiments and results. The samples chosen for the calibration of the instrument are the well known glycerol and 1,2 propanediol (propylene glycol). They are widely used in cryopreservation. The mixtures of glycerol-water and 1,2 propanediol-water at different concentrations were studied at ambient temperature to understand the molecular interactions in these mixtures.

The last chapter explains the glass transition study from the low temperature PPE experiments using Havriliak Negami model. The  $\alpha$  relaxation time ( $\tau$ ) has a dependence on temperature. Many theoretical models were developed to explain its dependence. We talk about a protocol to find the correct model for the temperature dependence of  $\tau$  in chapter four. All samples were studied using this protocol and results are discussed. This chapter also gives a detailed explanation of the viscosity and DSC measurements. The PPE results are compared with viscosity results and literatures.

The manuscript ends with a discussion about new developments in PPE instrumentation and viscosity measurements. Effect of cooling rate on PPE signal and experimental uncertainty are also discussed in this section.



---

## Cryoprotectants and Glassy State

---

Preserving life in extreme conditions is a challenging task. Nature has its own way of life preservation in extreme freezing conditions. The wood frog (*Rana sylvatica*) is an example which can survive extensive freezing of its body fluids during the winter season [1]. Another example is a microscopic multicellular organism called water-bear (*Tardigrada*) [2]. Polar fish and terrestrial insects have evolved antifreeze proteins and antifreeze glycoproteins that permit supercooling of their body fluids below the equilibrium freezing temperature [3]. Researchers were adapting these methods of preservation for the betterment of our day to day life and they call this process as "cryopreservation". Thus cryopreservation can be termed as a technique used to preserve living cells and tissues for a long period of time by cooling it to sub zero temperature thereby limiting biological degradation. It has plenty of practical applications in medicine, biotechnology, agriculture, forestry and biodiversity conservation, with a large potential for biological cells and tissue banking. A lot of studies have been done in cyropreservation for many decades to understand and overcome the challenges involved in the process [4, 5]. In cryobiology it was understood that formation and maintaining a glassy or vitreous state in the living cells during cooling and thawing process is the key factor for cell survival [6]. At very low subzero temperature the biological activity has been slowed down and the cell life can be preserved for a long period of time (months or years). But during freezing, biological cells are exposed to a variety of stresses when ice crystallization occurs, that can lead to rupture of cells or lethal changes in concentration of unfrozen fraction. Contrary to popular belief, injury caused during freezing is not only due to the expansion of water. Water expels all salts while freezing. This exclusion process pushes everything out and forms ice crystals resulting in a high concentration of salts. Both intracellular and extracellular ice formation cause damage. Intracellular ice crystals can damage the cell wall and structure, while the extracellular ice crystals increases the salt concentration to levels that cause damage to the cell (solution effect) or

lead to its lethal contraction by excessive dehydration (by osmotic effect).

Like it is made in nature for the species with cold blood, the procedures developed by cryobiologists use antifreeze molecules called cryoprotectants (CPA). Two strategies are developed in cryobiology to preserve biological systems: either ice crystallization is controlled around the cells by applying a slow cooling protocol specific to the kind of cells, or ice formation is totally avoided during cooling and thawing [4]. The latter one, called vitrification [4, 5], is developed for complex biological systems containing several kinds of cells. In slow-freezing, to ensure the survival of the cell, a delicate balance between extracellular ice formation and cell dehydration must be maintained. It involves optimized and controlled freezing to avoid intracellular ice crystallization. Cells are placed in contact to CPAs prior to slow freezing and outside of the cells, a part of the system vitrifies. Indeed, during freezing, the concentration of solutes in the unfrozen solution increases until the residual solution is sufficiently concentrated to vitrify. Regarding cryobiology, the vitrification process refers to the vitrification of the whole system, without any ice formation. Vitrification needs application of high cooling rates in the presence of higher concentration of CPAs (generally three to four times more than in slow freezing) to form a glass-like solid state, i.e. an amorphous solid, without forming any crystalline structure.

## 1.1 Cryoprotectants

Cryoprotectants (CPAs) are the necessary essential ingredients to protect the cells from freezing damage. CPAs can be defined as any materials added to cells prior to cooling that yields a higher post-thaw survival rate than without its presence. They are compounds that reduce deleterious effects and stress expressed on cells during a cooling to low temperatures.

Two kinds of cryoprotectants are distinguished, according to their capacity to penetrate or not into cell. The penetrating CPAs can integrate the intracellular volume and act within the cytoplasm. The non-penetrating CPAs cannot cross cellular membranes and act in the extracellular environment, participating to the osmotic balance. All of them are very soluble in water. They have a good affinity with it and are bounded to water molecules by hydrogen bonds. Their action depends on their proportion in solution. They are biocompatible, but they become chemically toxic from a certain concentration. The main families are polyalcohols, some polymers, sugars and antifreeze proteins.

When no CPA is used, almost entire water forms ice and cells are crushed into a small volume resulting in their damage, while the presence of CPA results in a larger unfrozen volume. When ice grows, the percentage of CPA present in liquid solution increases as the temperature is lowered. Eventually the cryoprotectant reaches a concentration that cannot be frozen. Growth of ice crystals stops and there is more room for cells to survive between the ice crystals. On further cooling below the glass transition temperature  $T_g$ , the remaining unfrozen liquid pocket solidifies into a glass, permitting storage for practically unlimited periods of time [7]. The cells can survive extracellular freezing by existing inside the glassy solid between the ice crystals.

The volume of unfrozen part at the end of freezing is higher if the initial CPA concentration is higher.

Variation in the survival of cells with cooling rate, for a given warming rate, is illustrated in figure 1.1 [8].

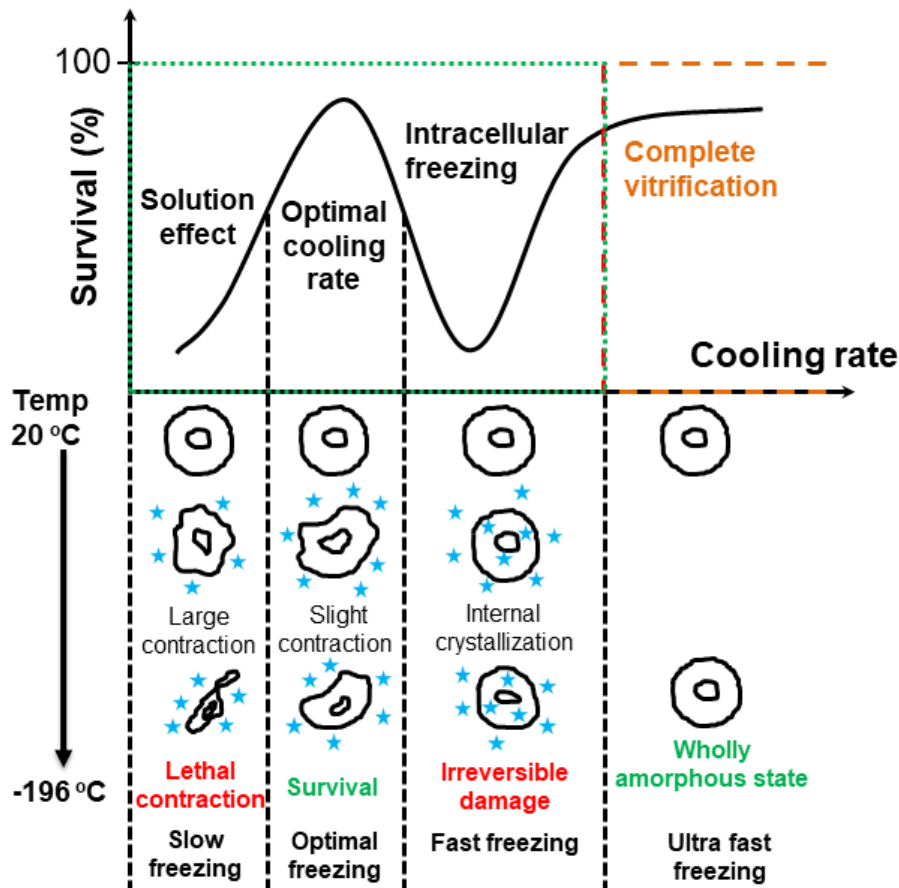


Figure 1.1 – Variation of survival of cells with cooling rates. Figure adapted from literature [8].

We can observe a survival peak at a low cooling rate, which is called classical peak and a second increase of survival at a higher cooling rate. When the cells are subjected to cooling, at a low rate, ice crystals are formed outside the cells. As the temperature is lowered, extracellular salt concentration increases because of the increase in the extracellular ice formation. This leads to an osmotic pressure which promotes the cells to loose water and shrink. Low cooling rates provide more time for the cells to shrink. Too much shrinking kills the cells. An optimal cooling rate can maintain the balance and increase cell survival, as observed at the classical peak. If cooling rate is too fast in comparison with this optimal cooling rate, cells do not have time to dehydrate enough by osmotic effect, that leads intracellular ice crystallization. At very high cooling rates, the time is not enough to form ice inside as well as outside the cells. This

cooling causes vitrification of the system which is seen as the second increase of survival.

Effect of CPA concentration on the survival of cells obtained after a freezing procedure is shown in figure 1.2 [9]. As the CPA concentration increases, the height of the survival peak increases and its position moves to lower cooling rates. This is because the high CPA concentration reduces the extracellular ice formation thereby reducing cell shrinkage. Reduction in cell shrinkage would favor intracellular ice formation but it is prevented by the increased penetrating CPA concentration they contain.

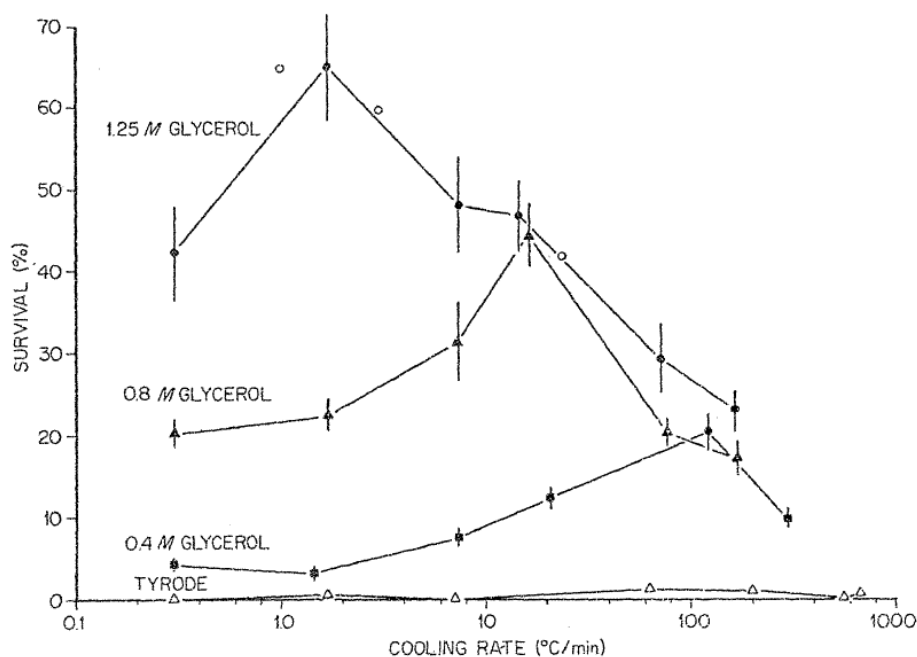


Figure 1.2 – Survival of colony-forming activity of stem cells suspended in Tyrode solution or in the indicated concentrations of glycerol solutions after cooling to  $-196\text{ }^{\circ}\text{C}$  at various rates and rapid warming. Figure reproduced from literature [9].

CPAs are widely used in food [10], medical [11] and pharmaceutical [12] industries. There are natural CPAs found in the fungi, bacteria, plants, insects and polar marine fishes. Sugars have been identified in their bodies which help them to survive the extreme conditions. Trehalose is a sugar which is found in drought-resistant tardigrades surviving high temperatures and the same sugar has been found in some freeze-resistant insect species [13]. High levels of glycerol has been found in over-wintering insect stages [14]. Some insects produce a range of polyols which assist them in cold survival [15]. Some synthesize special anti-freeze proteins [16] that can lower the non-equilibrium freezing points of water without changing the melting point [17]. But using these anti-freeze proteins in clinical cryopreservation has some adverse effects [18]. It can increase freeze damage in some cases [19]. For decades, several studies have been conducted on alcohols, sugars, diols and amides to investigate for their cryoprotective behavior. Cryoprotection of some plants have been done for a century by using sugars [20]. Solutes such as 1,2 propanediol, glycerol, dimethyl sulphoxide (DMSO), ethylene glycol

were found to have a higher cryoprotective behavior in different systems. All of them are penetrating CPAs. Some examples are, using 1,2 propanediol, 60 % survival rate in pronucleate stage embryos has been achieved after thawing and for a 2-cells stage embryos the survival rate was similar for both DMSO and 1,2 propanediol. Human embryos can be cryopreserved successfully by protocols using 1,2 propanediol, DMSO, or glycerol as CPAs [21]. In IVF (In vitro fertilization which is an effective type of assisted reproductive technology to help women become pregnant) technology, 1,2 propanediol is used to preserve human oocytes because it removes water from cell by creating an osmotic gradient. This helps the cytosol, the fluid portion of the cell, to form a glass-like state and avoid crystallization which can crush its membrane. Some amino acids like glutamic acid, glycine, proline, etc [22] also show cryoprotective behavior. Glycerol is a widely used CPA in clinical cryopreservation [23, 24]. The colligative property of glycerol [25] helps to bind with water, leading to an increased viscosity of the body fluids and thus reducing the availability of nucleating sites. By varying the concentration and cooling rate of the glycerol-cell mixture, it is possible to obtain a wholly amorphous state [26].

## 1.2 Vitrification

Vitrification is proposed to be the best way for the cryopreservation of organs [23]. Vitrification process can form an amorphous solid state. Even pure water can be vitrified. But it is possible only at very low volume (of the order of  $\mu m^3$ ) and requires ultrafast cooling rates [27, 28] on the order of  $10^7$  °C  $min^{-1}$  [29]. Cooling rate of  $10^3 - 10^4$  K  $s^{-1}$  under high pressure was used by O. Mishima and Y. Suzuki to vitrify pure water in emulsified form [30]. Glassy water can be prepared by rapid quenching of microscopic samples of water into a cryogenic liquid [31, 32]. A high concentration of CPAs (30-60 w/w CPA-cell) is introduced in vitrification process [5, 33]. Preservation of animal embryos were studied using vitrification at the beginning [34]. Later it was developed for plant cells and tissues [35]. Cryopreservation of whole organs is even more challenging than simple tissues. For vitrifying the whole organ using a realistic cooling rate it is required to introduce high concentration of CPAs [36–38]. Many researchers have worked in whole organ preservation which includes ovaries [39], slices of liver [40], blood vessels [41], kidney [23, 42] etc. Abazari et al. [27] have done studies on cryopreservation of articular cartilage.

In both freezing and vitrification methods, a vitreous mixture of cells and CPAs is obtained but the percentage of vitreous part obtained from freezing method is less compared to that from vitrification. During vitrification, a high concentration of CPAs and fast cooling facilitate the entire volume of the tissue to become a glassy solid. The high CPA concentration leads to toxicity which ultimately hinders the cryopreservation process. We can say, in vitrification three factors must be in balance. One is the size of the sample, second is the cooling and warming rates and lastly the nature of CPAs and their concentration. To achieve a high cooling rate the size of sample must be small. But addition of CPA lowers the required cooling rate

thereby allowing a bigger sample size. Since toxicity is a serious concern due to high CPA concentration in vitrification, researchers investigated different methodologies to overcome this problem. Fahy et al. [5] have proposed some methods to reduce the effective amount of CPAs required for vitrification. They have reported an important way to reduce toxicity is to use a dilute solution of CPAs like glycerol-water, 1,2 propanediol-water etc. Another method is to increase the hydrostatic pressure which in turn elevate the  $T_g$ . Once cooling is done till  $T_g$  the pressure can be released without the danger of crystallization. Another way is to use a mixture of different CPAs (penetrating and non penetrating CPAs).

For glycerol-water mixtures, it was reported that for low concentration, until about 35%(w/w) it is impossible to avoid ice crystallization [37, 43]. G. VIGIER and R. VASSOILLE studied the crystallization in glycerol-water mixtures [44]. They found that for intermediate concentration, between 40% and 60%, after cooling it was possible to obtain a vitreous mixture of cells and glycerol-water solution without ice formation. Above 60%, only an amorphous state was observed which is in agreement with the observations from P. Boutron and A. Kaufmann [26].

Another important observation is the change in the viscosity of the CPA-cell mixture while cooling. G. J. Morris et al. have studied the high viscosity encountered in glycerol solutions while freezing [24]. They determined the viscosity of the residual unfrozen solution encountered during the freezing of glycerol-water and glycerol-water-NaCl solutions at sub-zero temperatures. Their results showed that during the freezing of an aqueous solution of glycerol the viscosity of the freeze concentrated material (unfrozen portion) increases rapidly. It is because of the increase in the concentration of glycerol and reduction in temperature. They have reported that 1,2 propanediol also shows the same trend as glycerol but CPAs like DMSO and methanol show lower viscosity.

CPAs that increase the viscosity while freezing, for instance, glycerol, 1,2 propanediol, sugar etc can cryopreserve the cells like spermatozoa, RBC (Red Blood Cells) and bacteria in an efficient way with application of high cooling rates ( $10-50\text{ }^\circ\text{C min}^{-1}$ ), while CPAs with low viscosity like DMSO and methanol offer poor cryoprotection for these cells [24]. Therefore, it is very important to study the thermal properties and the viscosity of the CPAs and their aqueous solutions to understand their behavior at sub-zero temperatures to determine their potential usability as a CPA in clinical cryopreservation.

### 1.3 Glassy State of a Material

As we said already the ultimate aim in cryopreservation is to obtain a glassy state in the cells and in the solution surrounding cells. Let us see what is a glassy state by considering a material in gaseous form at high temperature. When we lower the temperature, it changes from the gaseous state to liquid state with a reduction in volume. Further lowering of temperature results the liquid to have a transition to solid state when the melting point ( $T_m$ ) is reached. But if we lower the temperature in a faster rate there is a possibility that the liquid bypasses the

solid state and continues to be in a supercooled liquid state until it reaches the glass transition temperature ( $T_g$ ) at which it becomes a glass as shown in figure 1.3.

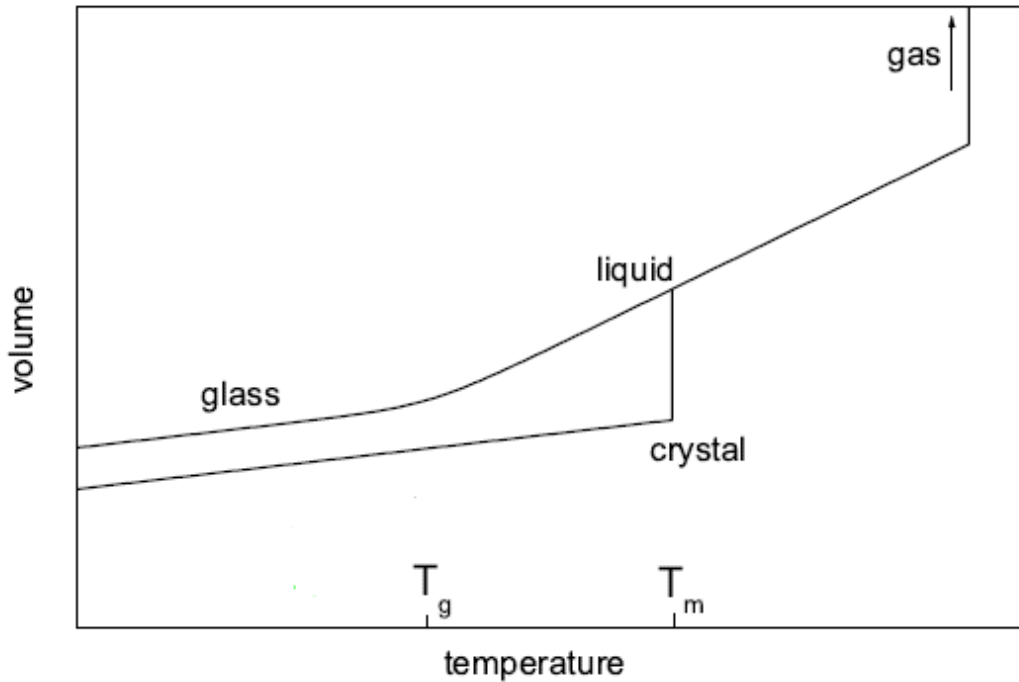


Figure 1.3 – Volume-temperature diagram of different phases at ambient pressure [45]

Therefore a liquid can solidify in two ways: one in a discontinuous way which leads to crystalline solid or in a continuous way which leads to an amorphous solid called glass. A lot of studies have been conducted on the glassy materials to get a better understanding about the physical phenomenon happening at this state of phase. Despite all those contributions in the investigation of glass transition, the phenomenon still remains an unsolved and a challenging problem.

When a liquid vitrifies to glass it exhibits a new, more limited kind of metastability as compared to that of the normal supercooled liquid [46]. In glass transition phenomenon there is a crossover happening from liquid to glass state. There exists a crossover temperature or critical temperature ( $T_c$ ) which is above the  $T_g$ . The changes in the supercooled dynamics occur at  $T_c$ . The Mode Coupling Theory (MCT) developed by Gotze and Sjogren [47] predicts the existence of this critical temperature. Another important prediction of MCT is the existence of different relaxation processes like  $\alpha$  [48] and  $\beta$  [49]. Relaxation associated with solidification is referred to as  $\alpha$  relaxation. Secondary phenomena like  $\beta$  relaxation can also encounter over a wide range of temperatures.

A relaxation time is associated with each phenomenon, i.e,  $\tau_\alpha$  for  $\alpha$  relaxation and  $\tau_\beta$  for  $\beta$  relaxation. The  $\tau_\alpha$  has a very low value (in the order of ps) in the liquid state. But as it goes to supercooled liquid state  $\tau_\alpha$  increases. The glass transition is characterized by a  $\tau_\alpha \approx 100$  sec [48]. ie, the liquid needs more time to readjust its volume to maintain equilibrium. Eventually

molecules will rearrange so slowly that they don't have enough time to sample configurations adequately and the liquid structure appears 'frozen' on the laboratory time scale (minutes) [50]. Therefore, we can say a falling out of equilibrium happens in the fast cooling process.  $\tau_\alpha$  is experimentally accessible at higher temperature while below  $T_g$  it is so high that it is almost impossible for any experiments to access.

A glassy state is also characterized by high viscosity  $\eta$ , of the order of  $10^{12}$  Pa.s (or  $10^{13}$  poise) at  $T_g$  [47, 51]. For comparison, viscosity of water is less than 0.1 poise at its melting point. Viscosity is the internal friction in a liquid during its motion. It is because each layer traverse in different velocities and they glide with respect to each other. In simple words, viscosity is the resistance of a liquid to flow. As the liquid is cooled its viscosity increases and in a dramatic fashion in the supercooled liquid state. This high viscous supercooled liquid behaves as a solid for all practical purposes. Close to  $T_g$  the viscosity is extraordinarily sensitive to temperature.

L. Sjogren and W. Gotze [48] explained about the mechanism behind high viscosity encountered while supercooling. An atom can be trapped to some extent for a moment of time by the surrounding atoms which introduces time dependent potential barriers. This trapping mechanism is called cage effect. These barriers try to hinder the local density fluctuations and increase the viscosity. While supercooled, the cage effect is enhanced and leads to a localization of a cluster of atoms for a long time. Thus the resulting increase in viscosity implies a slowing down on the rearrangement of atoms. They also explain an additional back flow term which induces a hopping over barrier process. This defines the transport of atoms when the cage effect is sufficiently high.

An important model in glass physics is the super-Arrhenius model [52, 53] which explains the viscosity of a supercooled glass former.

$$\eta = \eta_\infty \exp\left(\frac{\Delta E_a(T)}{RT}\right) \quad (1.1)$$

where  $\eta_\infty$  is a constant which is temperature independent, T is the temperature, R is the universal gas constant and  $\Delta E_a(T)$  is the activation energy which is a temperature dependent quantity.

To determine  $\Delta E_a(T)$ , many theories have been proposed such as VFT (Vogel-Fulcher-Tammann) model [52, 54–57], free volume model [58–60], Adam and Gibbs (AG) model [61, 62], Bässler-Avramov (BA) model [63, 64], Waterton-Mauro (MYEGA) model [65, 66], Critical-like (Crit) model [67, 68] etc.

For application in cryobiology, a successful vitrification means that no ice crystallizes on cooling or on warming, and that fracture in the glassy state is avoided. Indeed, as in inorganic glasses at normal temperature, fracture formation might happen in the glassy state of aqueous solutions, because of thermomechanical stresses in fully or partially vitrified systems. Thus, an important property of the glass is its fragility or the steepness index (m). The above models

allow to determine the fragility of the glasses. Based on them, the glasses are classified into strong and fragile glasses. R. Bohmer et al. [69] have studied the relaxations in strong and fragile glasses. The strong glasses do not change their structure with an increase in temperature while fragile glasses have a weak structure that changes with temperature. This fragility plays an important role in classifying CPAs for cryopreservation. A fragile glass former is not an efficient CPA while a strong one provides better cryoprotection [70, 71]. This is because the fragile glass formers have a low resistance to the local structural changes which occur when the temperature is decreased towards the  $T_g$ . Therefore, studying the fragility is as important as determining the  $T_g$  for a better selection of CPAs in cryopreservation.

## 1.4 Theoretical Models of Glass Dynamics

Experimentally the glass transition in a glass former is manifested by a change in its physical parameters like heat capacity [72], dielectric permittivity [73] or shear modulus [73] as shown in figure 1.4. This is observed in the real and imaginary parts of the physical parameters. The real part drops and the imaginary part increases to a maximum value and returns to the original value. The peak in the imaginary part and the point of inflection in the real part are at the same frequency.

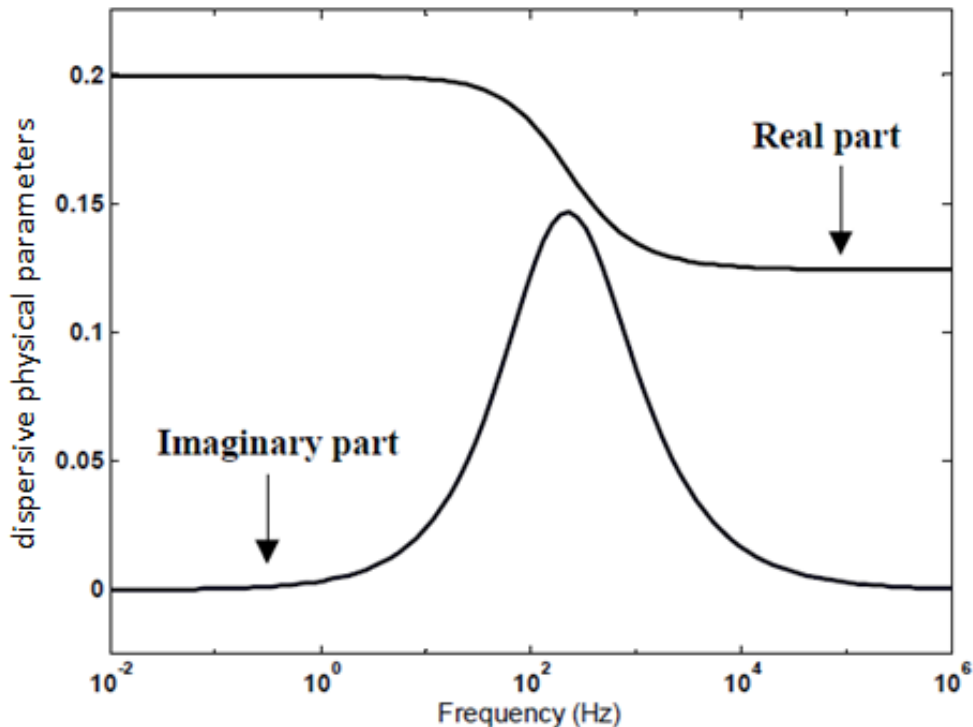


Figure 1.4 – Real and imaginary parts of dispersive physical parameters as function of frequency. Figure reproduced from [74].

The spectroscopic information can be extracted from the signal by a simultaneous fit of

these real and imaginary parts of the relaxation. In the frequency domain there are many semi-empirical functions used for fitting such as Debye, Cole-Cole or Cole-Davidson law [75]. All these are simplified form of the generalized Havriliak-Negami (HN) model [76]. By fitting the physical parameters according to the suitable model, it is possible to determine the aforementioned relaxation time,  $\tau$ .  $\tau$  is a temperature dependent quantity. The temperature dependence of  $\tau$  is explained by different models. For materials that follow VFT law, the  $\tau$  is given by the following equation.

$$\tau = \tau_{\infty} \exp\left(\frac{B}{T - T_0}\right) \quad (1.2)$$

where  $T_0$  is the temperature where the relaxation time diverges. B is a constant with unit K, dependent of  $T_0$ . Equation 1.2 can be written in another form as given by:

$$\tau = \tau_{\infty} \exp\left(\frac{D T_0}{T - T_0}\right) \quad (1.3)$$

where D is a constant, independent of temperature.

## 1.5 Glass Transition Study

Glass transition is associated with a serious change in the entropy, volume, heat capacity, thermal expansivity, compressibility and thermal conductivity of the material. Researchers use different techniques to study the variation in these parameters to understand glass transition in a broader sense.

For instance, researchers use dielectric measurements [77], NMR technique [78], light scattering [79], ultrasonic attenuation [80], Dynamic Scanning Calorimetry (DSC) [81] and modulated DSC [82, 83], Adiabatic Scanning Calorimeter (ASC) [84] and Nonadiabatic Scanning Calorimeter [85], photothermal studies [86–88], viscosity [51, 89, 90] studies etc to study the glass transition dynamics. One of the dynamic quantities of interest is the frequency-dependent specific heat capacity,  $c_p(\nu)$ . It is the linear response of the enthalpy of a system in equilibrium to a small temperature oscillation at a frequency,  $\nu$  [91].

Differential Scanning Calorimetry (DSC) is a widely used technique to measure the temperature and heat flow associated with transitions in materials as a function of time and temperature. DSC is the most widely used thermal analysis technique to study polymers, organic and inorganic materials. When a cooling and heating rate of  $20\text{ }^{\circ}\text{C min}^{-1}$  is used in DSC the onset glass transition occurs at a temperature at which the relaxation time is close to 100 s [92]. Another version of DSC called Modulated DSC (MDSC) was developed which uses a modulation (a sinusoidal ripple) in addition to the traditional DSC mechanism. This improved the DSC results by introducing three extra variables like heating rate, amplitude of modulation and frequency of modulation. MDSC provides better results, faster than DSC.

N. O. Birge and S. R. Nagel [72] developed a specific heat spectroscopy based on non-adiabatic technique to measure  $c_p(\omega)$ , where  $\omega$  is the angular frequency ( $\omega = 2\pi\nu$ ). They studied the glass transition in glycerol. The same technique was used by P. K. Dixon and S. R. Nagel [91] to study the o-Terphenyl mixtures near their glass transition.

In the photothermal section, photo pyroelectric (PPE) technique is a very powerful and simple method to study the thermal properties. One of the main advantage of PPE over other methods is that it can study both static (specific heat capacity) and dynamic (effusivity, diffusivity, thermal conductivity) thermal properties.

Specific heat capacity, thermal conductivity, thermal diffusivity and thermal effusivity define the ability of a material to store and transfer heat. A thorough understanding of these properties is crucial for any process or material which experiences a large or fast gradient in temperature. Studying these parameters provides important information about composition, purity and structure of the material and also their behavior at low temperature.

Although many studies have been reported on glycerol [93, 94] and 1,2 propanediol [95] using different techniques, their binary mixtures with water are not much investigated especially using photothermal techniques. P. Boutron and A. Kaufmann have studied mixtures of water-glycerol-DMSO [26] and water-1,2 propanediol [96] using DSC. C. Gao et al. reported DSC measurements on aqueous solutions of glycerol and 1,2 propanediol and calculated their  $T_g$  [97, 98]. Dielectric measurements have been performed on aqueous solutions of glycerol by S. Sudo et al. [99] and determined their  $T_g$  and  $m$ . We were unable to find other literature data about their fragility. As water is abundantly found in living cells all CPAs must interact with water during cryopreservation process and studying their aqueous solution is necessary to understand their interaction. As fragile glass formers provide weak cryoprotection [70, 71], it is important to study the glass properties of the aqueous solutions of CPAs to understand their performance in cryopreservation. Therefore, we have investigated their aqueous solutions using PPE technique and determined their  $T_g$  and  $m$ . Furthermore, We have performed viscosity measurements on these samples to obtain their  $T_g$  and  $m$  for a comparative study.

## 1.6 The Photo Pyroelectric Technique

When an electromagnetic (EM) wave is absorbed by a material the atoms excited to higher energy states and they lose this energy by either radiative or non-radiative transitions. The latter one results in phonon excitation and produces heat in the material as shown in figure 1.5. This forms the basis of photothermal effects.

In photo pyroelectric (PPE) technique, a temperature variation in the investigating sample is produced using an EM wave (LASER or LED) and is detected using a pyroelectric material as sensor. Pyroelectric sensors are normally thin slabs which are cut so that the permanent polarization fields are oriented in orthogonal direction with respect to the transducer surface as shown in figure 1.6.

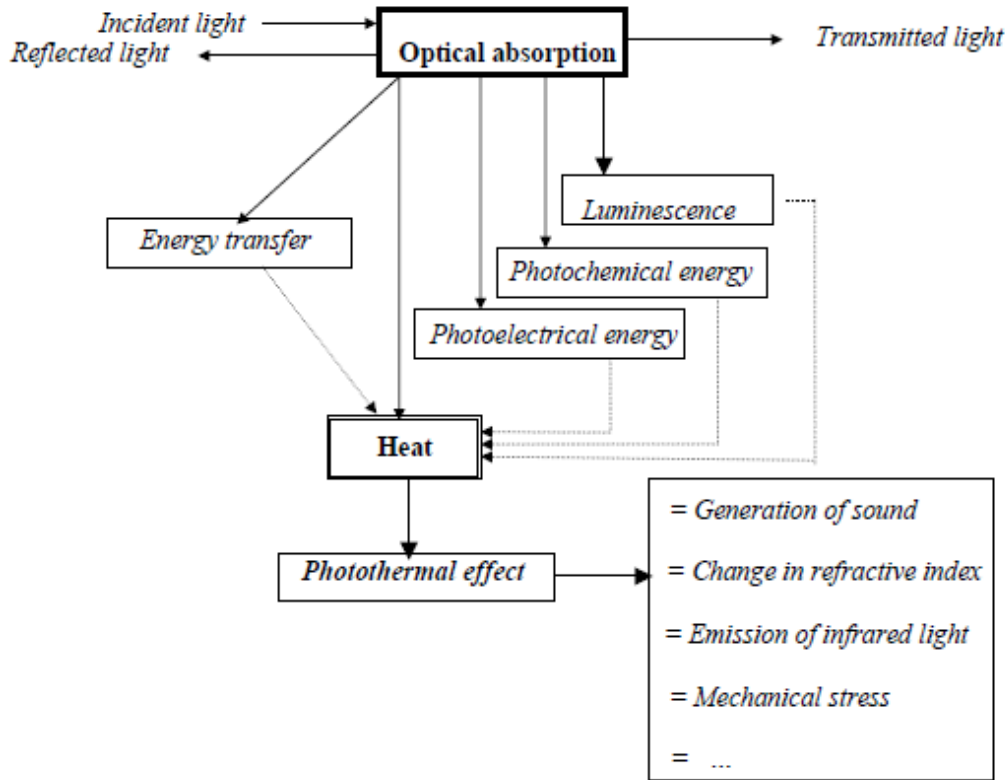


Figure 1.5 – Possible consequences of an EM absorption. Figure reproduced from [74].

Pyroelectricity is a sub-class of ferroelectricity. Even in the absence of an external electric field some low-symmetric crystals show a spontaneous polarization. This property is called ferroelectricity. This is due to the non coincidence of the average positions of positive and negative charges in the crystals. A sub-class of ferroelectric materials which satisfy certain crystallographic requirements, such as no center of symmetry in the crystal lattice and only one rotational symmetry axis, exhibits a macroscopic, temperature dependent polarization.

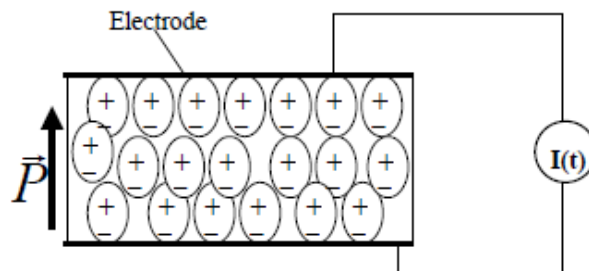


Figure 1.6 – A scheme of pyroelectric material coated with opaque electrodes. Figure reproduced from [74].

This polarization decreases with increasing temperature as shown in figure 1.7 and vanishes at a particular temperature called Curie temperature. Above Curie temperature the crystal is in paraelectric phase.

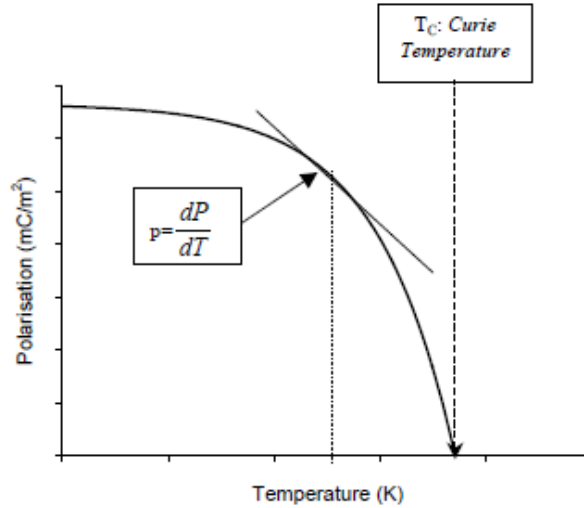


Figure 1.7 – Variation of polarization of a ferroelectric material with respect to temperature. Figure reproduced from [74].

The pyroelectric materials have the ability to generate a temporary voltage due to the change in the electric polarization because of the changing heat flux. This property is called pyroelectric effect. The slope of the curve in figure 1.7 gives the pyroelectric coefficient. No material shows any pyroelectric property above Curie temperature. Another important property is the piezoelectric property which is the generation of a voltage due to the expansion or contraction of the crystal lattice resulting from a mechanical stress. Here a thermal expansion in the crystal lattice has to be considered which adds a secondary effect to the primary pyroelectric effect as shown in figure 1.8.

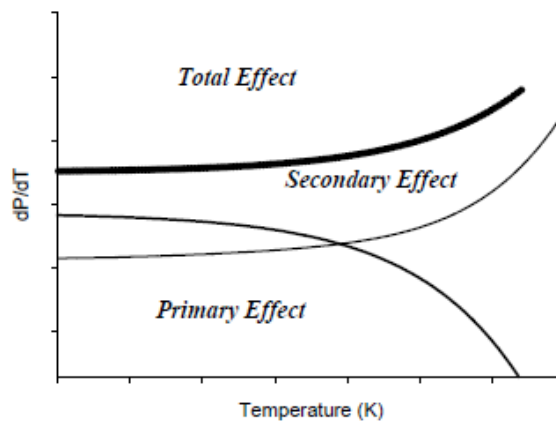


Figure 1.8 – Total effect as a sum of pyroelectric (primary) effect and piezoelectric (secondary) effect. Figure reproduced from [74].

PPE techniques can characterize solids [100], liquids [101] and gases [102] for a wide range of temperature especially from 15K to 400K [103]. The advantage of high sensitivity, large bandwidth (typically mHz to several kHz), high signal to noise ratio and simplicity to implement [104] have attracted researchers to use PPE technique widely. M. Chirtoc and G.

Mihailescu [105] reported the versatility of PPE, since PPE signal depends on both the thermal and the optical properties, non spectroscopic problems like depth profiling [106], investigation of multilayered structures, thermal effusivity, diffusivity and conductivity measurements [107–111] and phase transition [86, 88] can also be analysed. A. Mandelis and M. Zver [104] successfully determined the voltage of the PPE signal generated by a pyroelectric sensor in thermal contact with the sample. Practically, there are mainly two experimental configurations used for different property study, BPPE (back detection photo pyroelectric) [110] and FPPE (front detection photo pyroelectric) [112] configuration. Their details are discussed in the next chapter.

---

# Theory of Heat Transfer and Photo Pyroelectric Technique

---

### Introduction

The process of heat diffusion inside a material is defined by the Fourier law of heat diffusion. By applying the proper boundary condition we can solve the heat diffusion equation and quantitatively explain the process of heat transfer inside a material. We have discussed the basic theory and versatility of PPE technique in the previous chapter. This chapter focuses on the adaptation of PPE technique for the effusivity measurements at ambient temperature. It begins with the heat diffusion process and explains the temperature fields in different layers in a PPE configuration. Also it shows how to extract thermal information from the experimental data.

### 2.1 Heat Diffusion Equation and Solution

In a PPE setup, the sensor and sample layers are stacked together to form a set of 'n' layers. Temperature distribution in different layers can be obtained by solving the heat diffusion equation. Let us consider a modulated heat flux incident on a homogeneous isotropic medium having an infinitesimal volume  $dV$  in a space with dimension  $dx, dy, dz$  in X, Y, Z direction respectively. The heat transfer inside this medium is a diffusion process rather than a wave motion. This is governed by a heat diffusion equation which is obtained by considering the resultant of energy received and released. The three dimensional (3D) "Heat Diffusion Equation" can be written as:

$$\frac{\partial^2 T}{\partial x^2} + \frac{\partial^2 T}{\partial y^2} + \frac{\partial^2 T}{\partial z^2} + \frac{E_g}{k} = \frac{\rho c}{k} \frac{\partial T}{\partial t} \quad (2.1)$$

where, T is the temperature in K

$\rho$  is the density in  $kg\ m^{-3}$

$c$  is the heat capacity in  $J kg^{-1}K^{-1}$

$k$  is the thermal conductivity in  $W m^{-1}K^{-1}$

$E_g$  is the energy generated by the incident heat flux in  $J$ .

Considering the simplicity and easy analytical interpretation, we reduce the 3D case to 1D heat propagation and the 1D approach is considered for all our theoretical and experimental studies. This approach is based on the idea that the heat diffusion happening only in one direction, say  $z$  axis and there is no heat diffusion in  $x$  and  $y$  axes. In practice, this can be achieved by using a spot size larger than the heat diffusion length. The spot size does not have any influence if this condition is satisfied. The 1D heat diffusion equation that we consider is given by:

$$\frac{\partial^2 T}{\partial z^2} + \frac{E_g}{k} = \frac{\rho c}{k} \frac{\partial T}{\partial t} \quad (2.2)$$

Using the boundary conditions for specific practical models, we can find the solution to the 1D heat diffusion equation. This solution provides the temperature fields in each layer which depends on their thermal parameters especially, thermal effusivity and thermal diffusivity. These temperature fields are periodically oscillating due to the modulated heat flux and can be written as a function of angular frequency ( $\omega = 2\pi\nu$ , where  $\nu$  is the modulation frequency) and time ( $t$ ) as given by:

$$T(z, \omega, t) = T_0(z) e^{i\omega t} \quad (2.3)$$

where,  $T_0$  is the peak value of the temperature oscillation. The equation 2.2, which is in the form of partial differential equation, can be solved by the variable separable form.

In PPE technique, the voltage is generated across the pyroelectric sensor (pyro sensor). Once the solution of the 1-D heat diffusion equation provides the temperature variation across the pyroelectric sensor ( $T_p$ ), the PPE voltage generated is given by the expression [113]:

$$V(t) = \frac{i\omega\tau_E p l_p}{\epsilon(1+i\omega)\tau_E} \int_{thickness(l_p)} T_p(z) dz e^{i\omega t} \quad (2.4)$$

where,

$\omega$  is the chopping frequency or  $\omega = 2\pi\nu$

$\tau_E$  is the electrical time constant of the detector

$p$  is the pyroelectric coefficient

$\epsilon$  is the dielectric permittivity of the sensor

$l_p$  is the thickness of the pyroelectric sensor (normally expressed in  $\mu m$ )

## 2.2 PPE Configurations for Thermal Properties Measurement

For any material, the principal thermophysical parameters are heat capacity ( $c$ ) and thermal conductivity ( $k$ ). The properties we study dynamically using a modulated heat wave are effu-

sivity ( $e$ ) and diffusivity ( $\alpha$ ), which can provide the aforementioned principal parameters. The thermal effusivity, expressed in unit,  $Ws^{1/2}m^{-2}K^{-1}$  is given by:

$$e = \sqrt{\rho c k} \quad (2.5)$$

where,

$\rho$  is the density

$c$  is the heat capacity

$k$  is the conductivity

Effusivity describes how easily a material can acquire heat from the surroundings. A material with high effusivity, iron feels colder than a material with lower effusivity, rubber. Thermal conductivity has a slight relaxation depending on frequency and this relaxation can be neglected in comparison with the relaxation of heat capacity [114]. Therefore, studying the relaxation in effusivity provides information about the relaxation of heat capacity of sample.

The thermal diffusivity, expressed in unit,  $m^2 sec^{-1}$  is given by:

$$\alpha = k/\rho c \quad (2.6)$$

which describes how easily heat waves can diffuse through the material. For example, iron has a higher diffusivity than rubber.

Different configurations are used for the effective study of these parameters like BPPE [110] configuration where the pyroelectric sensor is in the rear side of the irradiated sample. This configuration is sensitive to both the effusivity and diffusivity of the sample. Figure 2.1 shows the BPPE configuration for a transparent sample. Another configuration is the FPPE [112] configuration where the pyroelectric sensor is directly irradiated and sample is in contact to its rear surface as shown in figure 2.2. This configuration is sensitive to the effusivity of the sample. Generally, the faces of the pyroelectric sensors are coated with opaque electrodes to absorb the incident light. Dadarlat et al. [113, 115] introduced the idea of a semi transparent pyroelectric sensors with one face coated with transparent electrode, Indium Tin Oxide (ITO). This is presented in the figure 2.3 which is called FPPE configuration with semi transparent pyroelectric sensor. It helps to extend the range of the modulating frequency. To explain this we must discuss about the thermal diffusion length,  $\mu$ , which is the measure of the depth that the heat waves can diffuse inside the material.  $\mu$  is a function of modulation frequency ( $f$ ) and diffusivity ( $\alpha$ ) of the material and is given by:

$$\mu = \sqrt{\frac{\alpha}{\pi f}} \quad (2.7)$$

Therefore, the heat wave penetration in the layers is inversely proportional to the modulating frequency. If  $l$  is the thickness of a layer, the cases, ( $\mu > l$ ) and ( $\mu < l$ ) are termed as 'thermally

thin' and 'thermally thick' respectively in PPE.

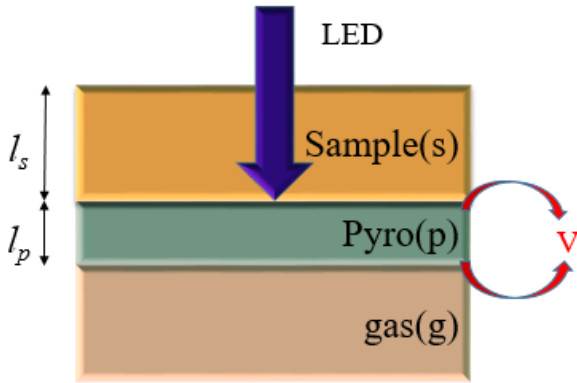


Figure 2.1 – Back photo pyroelectric configuration for a transparent sample (**BPPE**). Heat is generated at the sample/pyro interface and flows to both sample and pyro sensor

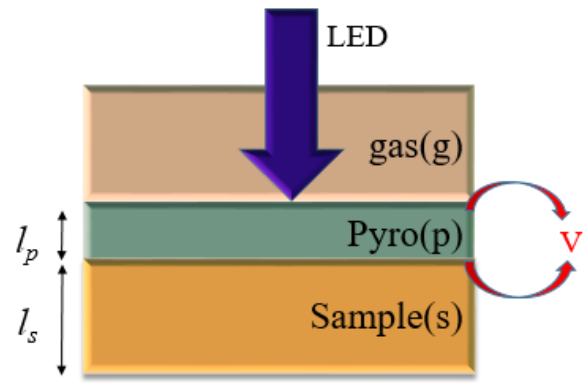


Figure 2.2 – Front photo pyroelectric configuration (**FPPE**). Heat is generated at the gas/pyro interface and flows through the pyro sensor, crosses the pyro/sample interface and reaches the sample

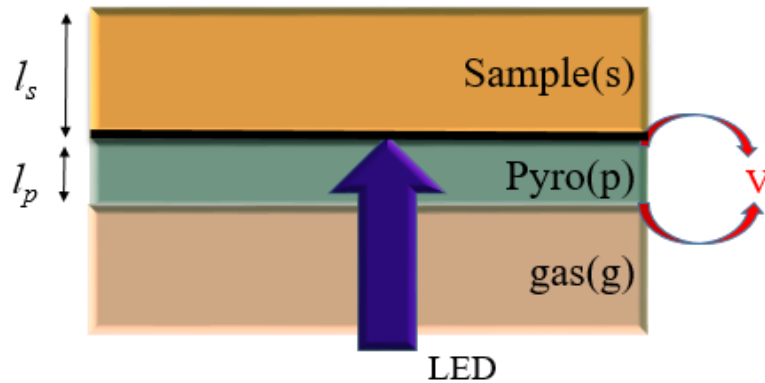


Figure 2.3 – **FPPE configuration with semi transparent sensor**. Heat is produced at the sample/pyro interface and flows to both pyro sensor and sample (like in the case of BPPE with a transparent sample)

For our studies, we used a three layer model in FPPE (figure 2.2) and (figure 2.3) configurations using a pyroelectric sensor, Lithium Tantalate ( $LiTaO_3$ ).

The next section explains the derivation of temperature fields and PPE voltage from a three layer FPPE configuration with a semi transparent sensor used for our experiment.

## 2.3 Temperature Fields for Different Layers of FPPE Configuration with Semi Transparent Sensor

Here we consider a three-layer system in FPPE configuration with layer 2 as semi transparent, where the light is incident at the interface between layer 1 and layer 2 which is made opaque by a metallic coating, as shown in figure 2.4.

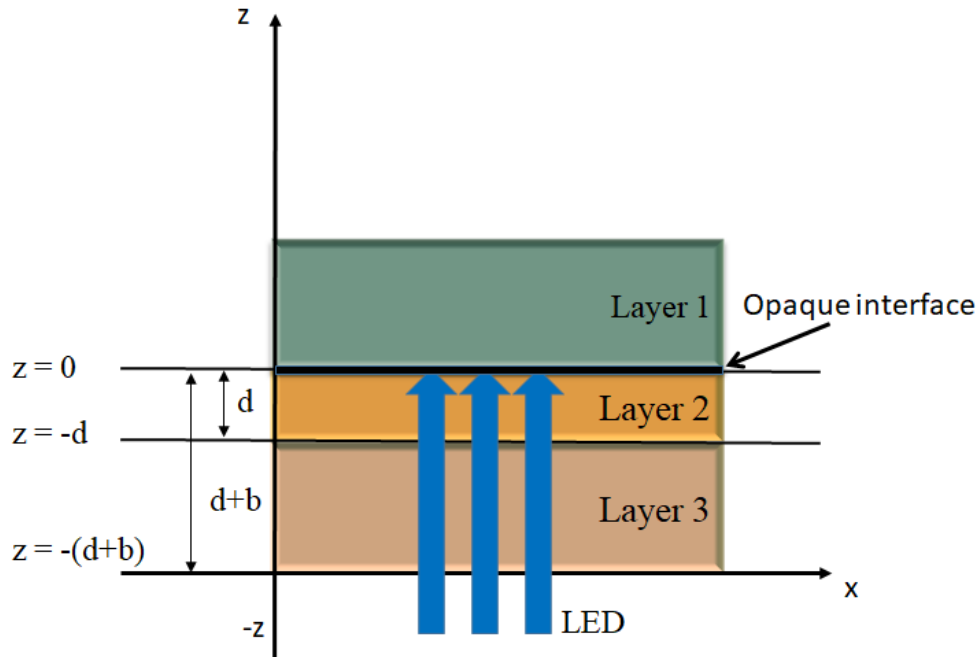


Figure 2.4 – A 3-layer geometry of the FPPE configuration with layer 2 as semi transparent. Heat is generated at the layer1/layer2 interface and flows through layer 1, layer 2 and layer 3

The interface between layer 2 and layer 3 is made transparent and light passes without any absorption. If we consider layer 1 as the sample and layer 2 as the pyroelectric sensor, the light is incident at the pyroelectric sensor-sample (p-s) interface which is made opaque by a gold coating so that all the incident radiation is considered to be absorbed at the interface. To solve the heat equation, we denote the temperature fields in layer 1, layer 2 and layer 3 as  $T_1(z, t)$ ,  $T_2(z, t)$ ,  $T_3(z, t)$  respectively and are given by:

$$T_1(z, t) = (A_1 e^{\sigma_1 z} + B_1 e^{-\sigma_1 z}) e^{i\omega t} \quad (z \geq 0) \quad (2.8)$$

$$T_2(z, t) = (A_2 e^{\sigma_2 z} + B_2 e^{-\sigma_2 z} - E \beta e^{-\beta z} \eta \frac{I_0}{2\kappa}) e^{i\omega t} \quad (0 \geq z \geq -d) \quad (2.9)$$

$$T_3(z, t) = (A_3 e^{\sigma_3 z} + B_3 e^{-\sigma_3 z}) e^{i\omega t} \quad (z \leq -d) \quad (2.10)$$

where, A, B and E are constants which can be determined by solving the equation using proper boundary conditions.

$\beta$  is the optical absorption coefficient

$\eta$  is the efficiency of conversion of absorbed light into heat

$I_0$  is the peak intensity

$\sigma$  is the complex wave number given by:

$$\sigma = (1 + i) \frac{1}{\mu} \quad (2.11)$$

where,  $\mu$  is the thermal diffusion length (normally expressed in  $\mu m$ )

In equation 2.9,  $E \beta e^{-\beta z} \eta \frac{I_0}{2\kappa}$  is called the source term. The constant, E can be solved from equation 2.2 and is given by:  $E = \frac{1}{\beta^2 - \sigma_1^2}$

Therefore, the source term excluding  $e^{-\beta z}$  and  $e^{i\omega t}$  which can be denoted as  $\epsilon$  is given by:

$$\epsilon = \frac{\beta \eta I_0}{2 K_1 (\beta^2 - \sigma_1^2)} \quad (2.12)$$

All unknown coefficients in the equations 2.8, 2.9, 2.10 can be solved by applying the proper boundary conditions. For simplicity, we can assume the coefficient  $A_1$  in equation 2.8 and  $B_3$  in 2.10 equal to zero because the temperature at infinity is zero.

The boundary conditions are given by:

$$1) T_i = T_j$$

$$2) k_i \frac{dT_i}{dz} - k_j \frac{dT_j}{dz} = 0 \quad \text{where, (i,j)=(1,2); (2,3)}$$

which provide four equations given by:

$$T_1 = T_2 \quad k_1 \frac{dT_1}{dz} - k_2 \frac{dT_2}{dz} = 0 \quad (z=0)$$

$$T_2 = T_3 \quad k_2 \frac{dT_2}{dz} - k_3 \frac{dT_3}{dz} = 0 \quad (z=d)$$

Applying these boundary conditions to the equations 2.8 and 2.9 at  $z=0$  gives

$$-b_{12} B_1 - A_2 + B_2 = \frac{-\beta \epsilon}{\sigma_2} \quad (2.13)$$

$$B_1 - A_2 - B_2 = -\epsilon \quad (2.14)$$

Similarly, applying these boundary conditions to the equations 2.9 and 2.10 at  $z=d$  gives

$$A_2 e^{-\sigma_2 d} - B_2 e^{\sigma_2 d} - b_{32} A_3 = \frac{\beta}{\sigma_2} \epsilon e^{-\beta d} \quad (2.15)$$

$$A_2 e^{-\sigma_2 d} + B_2 e^{\sigma_2 d} - A_3 = \epsilon e^{-\beta d} \quad (2.16)$$

where,  $b_{12}$  and  $b_{32}$  are given by:

$$b_{12} = \frac{k_1 \sigma_1}{k_2 \sigma_2} = \frac{e_1}{e_2} \quad (2.17)$$

$$b_{32} = \frac{k_3 \sigma_3}{k_2 \sigma_2} = \frac{e_3}{e_2} \quad (2.18)$$

where,  $e_1, e_2, e_3$  are the effusivities of layer 1, layer 2, layer 3 respectively. The equations 2.13, 2.14, 2.15 and 2.16 can be represented as matrix and solved using Cramer's rule which gives the unknown coefficients,  $B_1, A_2, B_2$  and  $A_3$ . By substituting these coefficients in equations 2.8, 2.9, 2.10, the temperature fields in each layer can be determined as:

$$T_1 = \epsilon \frac{\left[ (1 + b_{32}) \left( \frac{\beta}{\sigma_2} - 1 \right) e^{\sigma_2 d} + (1 - b_{32}) \left( \frac{\beta}{\sigma_2} + 1 \right) e^{-\sigma_2 d} + 2 \left( b_{32} - \frac{\beta}{\sigma_2} \right) e^{-\beta d} \right]}{(1 + b_{12})(1 + b_{32}) e^{\sigma_2 d} - (1 - b_{12})(1 - b_{32}) e^{-\sigma_2 d}} e^{-\sigma_1 z} e^{i\omega t} \quad (2.19)$$

$$T_2 = \epsilon \left[ \frac{\left[ (1 + b_{32}) \left( b_{12} + \frac{\beta}{\sigma_2} \right) e^{\sigma_2 d} + (1 - b_{12}) \left( b_{32} - \frac{\beta}{\sigma_2} \right) e^{-\beta d} \right]}{(1 + b_{12})(1 + b_{32}) e^{\sigma_2 d} - (1 - b_{12})(1 - b_{32}) e^{-\sigma_2 d}} e^{\sigma_2 z} + \frac{\left[ (1 + b_{12}) \left( b_{32} - \frac{\beta}{\sigma_2} \right) e^{-\beta d} + (1 - b_{32}) \left( b_{12} + \frac{\beta}{\sigma_2} \right) e^{-\sigma_2 d} \right]}{(1 + b_{12})(1 + b_{32}) e^{\sigma_2 d} - (1 - b_{12})(1 - b_{32}) e^{-\sigma_2 d}} e^{-\sigma_2 z} - e^{\beta z} \right] e^{i\omega t} \quad (2.20)$$

$$T_3 = \epsilon \frac{\left[ -e^{d(\sigma_2 - \beta)} (1 + b_{12}) \left( 1 + \frac{\beta}{\sigma_2} \right) + e^{-d(\sigma_2 + \beta)} (1 - b_{12}) \left( 1 - \frac{\beta}{\sigma_2} \right) + 2 \left( b_{12} + \frac{\beta}{\sigma_2} \right) \right]}{(1 + b_{12})(1 + b_{32}) e^{\sigma_2 d} - (1 - b_{12})(1 - b_{32}) e^{-\sigma_2 d}} e^{\sigma_3 z} e^{i\omega t} \quad (2.21)$$

Equations 2.19, 2.20 and 2.21 provide the temperature fields in each layer in the FPPE configuration with a semi transparent sensor.

### 2.3.1 Expression of the PPE Signal in FPPE Configuration with Semi Transparent Sensor

If we consider the layer 1, layer 2 and layer 3 as sample (s), pyroelectric sensor (p) and backing (b) respectively as shown in the figure 2.3, then the signal is generated by the layer 2 (pyroelectric sensor). The voltage generated in the layer 2 which is a function of frequency (f) and temperature (T) is given by:

$$V(f, T) = \int_0^{-d} T_2(z) dz \quad (2.22)$$

Solving the above equations, we obtain the complex PPE signal in the form

$$V(f, T) = V_0(f, T) \Gamma(f, T) \quad (2.23)$$

where,  $V_0$  is the instrumental contribution and the factor  $\Gamma$  holds the thermo-optical properties of the sample and other layers. The instrumental factor depends on the electrical time constant,  $\tau_E = RC$  where  $R$  is the input resistance of the measuring instrument and  $C$  is the sum of capacitance of the sensor, connection wires and input capacitance of the instrument.

While calculating  $V$  using the equation 2.22, we consider  $\beta \gg 1$  because of the high absorption at the metallic coating which nullifies some variables like  $e^{-\beta d} \approx 0$  and  $\sigma/\beta \approx 0$  that helps to simplify the calculation. Also we replace  $d$  with  $l_p$  which is the thickness of the pyroelectric sensor. The resulting equation is given by:

$$V = V_0 \frac{\left[ 2 b_{bp} \left( b_{sp} + \frac{\beta_p}{\sigma_p} \right) - (1 + b_{bp}) \left( b_{sp} + \frac{\beta_p}{\sigma_p} \right) \left[ e^{\sigma_p l_p} + R_{bp} e^{-\sigma_p l_p} \right] \right]}{\sigma_p (b_{sp} + 1) (b_{bp} + 1) \left[ e^{\sigma_p l_p} - R_{sp} R_{bp} e^{-\sigma_p l_p} \right]} e^{i\omega t} \quad (2.24)$$

where,  $\beta_p$  is the optical absorption coefficient of the pyroelectric sensor.

$R_{ij}$  represents the reflection coefficient of the thermal waves between two media (i and j where i, j can be any layer 1, 2 or 3):  $R_{ij} = \frac{b_{ij}-1}{b_{ij}+1}$  where  $b_{ij} = \frac{e_i}{e_j}$  [107].

If we consider the layer 3 or backing as air (b=g), then the following approximations can be applied:  $b_{gp} = \frac{e_g}{e_p} \approx 0$  and  $R_{gp} = \frac{b_{gp}-1}{b_{gp}+1} \approx -1$  and the equation 2.24 is simplified as given below:

$$V = V_0 \frac{\left[ \left( b_{sp} + \frac{\beta_p}{\sigma_p} \right) \left[ e^{-2\sigma_p l_p} - 1 \right] \right]}{\sigma_p (b_{sp} + 1) \left[ 1 + R_{sp} e^{-2\sigma_p l_p} \right]} e^{i\omega t} \quad (2.25)$$

## Normalization

A simple normalization step is needed to remove the instrumental factor  $V_0$ . This is done by running the same experiment by replacing the sample with air. Hence the configuration becomes air/sensor/air, ie, (s=g) then  $R_{gp} \approx -1$  and the expression for the voltage is given by:

$$V_n = V_0 \left[ \frac{-\beta_p}{\sigma_p^2} \right] e^{i\omega t} \quad (2.26)$$

Normalization is done by dividing 2.25 by equation 2.26 so that the factor  $V_0 e^{i\omega t}$  vanishes and  $\sigma_p/\beta_p \approx 0$ . Hereafter we consider only the factor  $\Gamma$  for further discussion. Thus the normalized expression for  $\Gamma$  for the sample/sensor/air configuration reduces to the following:

$$\boxed{V(f, T) = \Gamma(f, T) = \frac{1 - e^{-2\sigma_p l_p}}{(1 + b_{sp})[1 + R_{sp} e^{-2\sigma_p l_p}]}} \quad (2.27)$$

## Special Case: Thermally Thick Sensor and Sample

We can further simplify expression 2.27 in the case of a thermally thick sensor ( $\mu_p < l_p$ ) and sample ( $\mu_s < l_s$ ). The normalized expression for  $\Gamma$  for the simplified system (thermally

thick sensor and sample) is given by

$$\Gamma(f, T) = \frac{1}{1 + b_{sp}} = \frac{1}{1 + \frac{e_s}{e_p}} \quad (2.28)$$

Hence by knowing the effusivity of either the sensor or sample, the effusivity of the other can be determined easily. Simulated curve using the equation 2.27 is shown in figure 2.5.

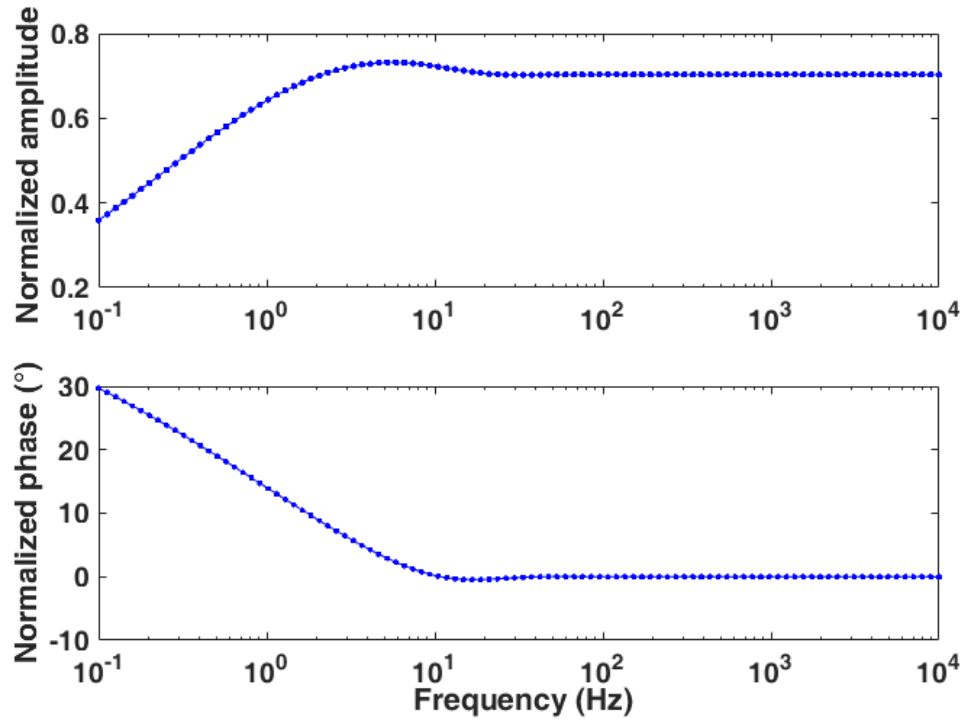


Figure 2.5 – Simulation of normalized amplitude and phase for 300  $\mu\text{m}$   $\text{LiTaO}_3$  for FPPE model with a semi transparent sensor

For the case of a thermally thick sensor and sample, the FPPE configuration with semi transparent sensor shown in figure 2.3 is exactly the same as the BPPE configuration with a transparent sample shown in figure 2.1. In both cases, always the sample-pyro (s-p) interface is illuminated and the heat wave is confined only in the sample and sensor. Therefore, we can use the equation 2.28 for a three-layer BPPE configuration having a transparent sample for the condition of a thermally thick sensor and sample also.

### 2.3.2 Expression of the PPE Signal in FPPE Configuration with Opaque Sensor

A second configuration was also used for the characterization of sensors and samples. This was the FPPE configuration shown in figure 2.2. To solve for the temperature fields and PPE signal, we start from the general expression for a five layer configuration as in figure 2.6.

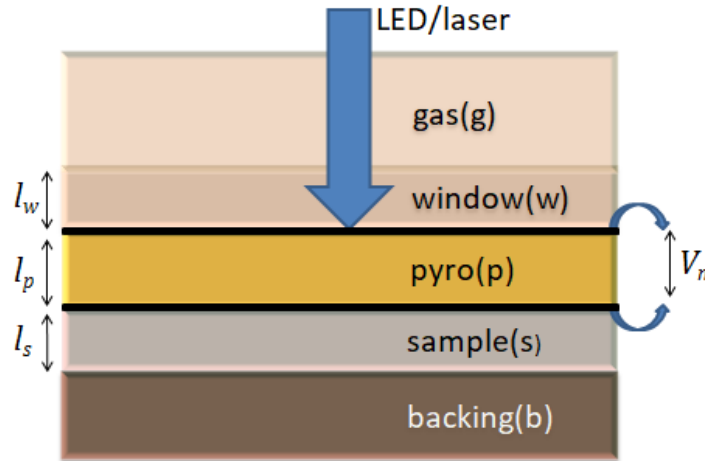


Figure 2.6 – A 5-layer geometry of the FPPE configuration

Here the light is absorbed at the window-sensor (w-p) interface. For that, one can use a pyroelectric sensor with opaque metallic coating at the w-p interface.

The normalized expression for  $\Gamma$  for this configuration is given by [107]:

$$\Gamma(f, T) = \left[ \frac{b_{gp} + 1}{b_{wp} + 1} \right] \times \left[ \frac{1 + R_{sp} e^{-2\sigma_p l_p} - (1 + R_{sp}) e^{-\sigma_p l_p}}{1 + R_{gp} e^{-2\sigma_p l_p} - (1 + R_{gp}) e^{-\sigma_p l_p}} \right] \times \left[ \frac{1 - R_{gp} R_{gp} e^{-2\sigma_p l_p}}{1 - R_{sp} R_{wp} e^{-2\sigma_p l_p}} \right] \quad (2.29)$$

where,

$$R_{ij} = \frac{(b_{ij}-1)}{(b_{ij}+1)}$$

where, i,j= w,p,s refer to front medium (window), pyroelectric sensor and sample respectively.

From equation 2.29, one can obtain the expression of  $\Gamma$  for the FPPE configuration (air/sensor/sample (g-p-s)) shown in figure 2.2. This is done by replacing the window and backing with air ( $w, b \rightarrow g$ ), then  $b_{wp} = b_{gp} \approx 0$  and  $R_{gp} \approx -1$ . Now the normalized expression 2.29 reduces as given below:

$$\Gamma(f, T) = \frac{1 - e^{-\sigma_p l_p} + R_{sp} [e^{-2\sigma_p l_p} - e^{-\sigma_p l_p}]}{1 - R_{sp} e^{-2\sigma_p l_p}} \quad (2.30)$$

### Special Case: Thermally Thick Sensor and Sample

For the special case, when a pyroelectric sensor being thermally thick ( $\mu_p < l_p$ ), the term  $e^{-2\sigma_p l_p} \approx 0$  and the normalized expression 2.30 reduces to

$$\Gamma(f, T) = 1 - (1 + R_{sp}) e^{-\sigma_p l_p} \quad (2.31)$$

The amplitude and phase of the PPE signal hold information about the effusivity and diffusivity of the sensor and also the effusivity of the sample. An analysis of equation 2.31 indicates

that the thermal diffusivity of the sample (contained in  $\sigma_p$ ) can be directly measured by performing a frequency scan of the amplitude and/or the phase of the PPE signal. A simulation of the normalized amplitude and phase using the equation 2.30 and 2.31 is shown in figure 2.7.

We can observe the difference in the profiles of amplitude and phase from both equations at low frequencies. The equation 2.31 can be used above a certain frequency from where both equations provide the same result. Below this frequency, the thermally thick case is not valid.

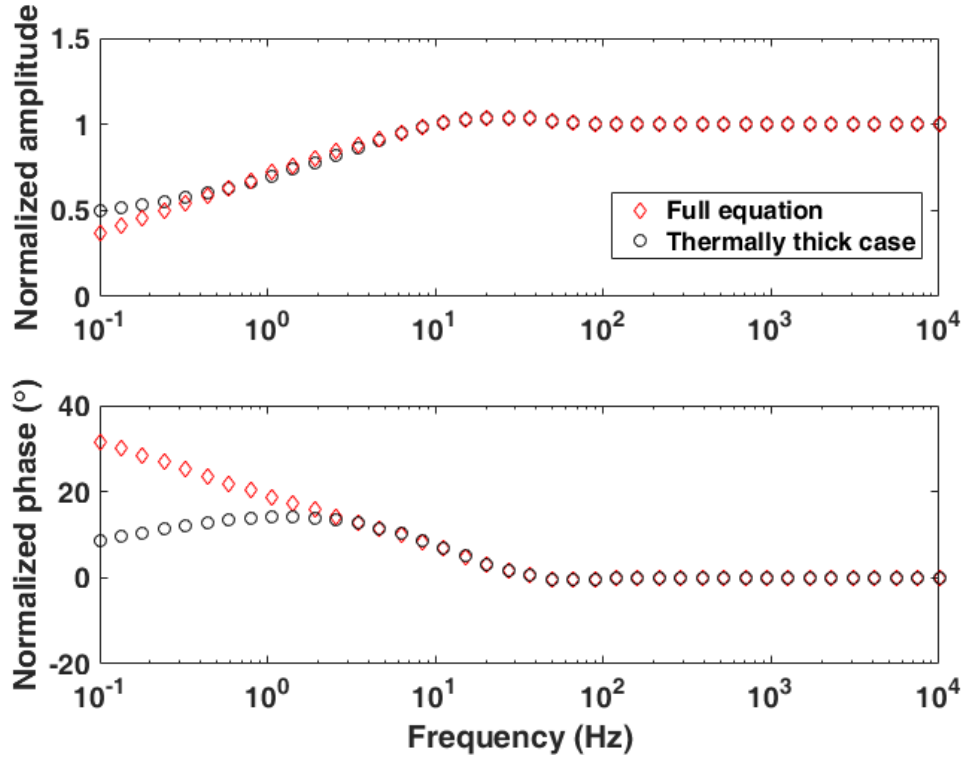


Figure 2.7 – Simulation of normalized amplitude and phase using 2.30 (red  $\diamond$ ) (full equation) and 2.31 (black  $\circ$ ) (thermally thick pyroelectric sensor) for  $300 \mu\text{m LiTaO}_3$  for FPPE model

## 2.4 Determination of Thermal Parameters at Ambient Temperature

A simple way to obtain simultaneously the thermal diffusivity and effusivity is by fitting the normalized signal using the corresponding model. In both models, if the thermal parameters of the sample are known then we can determine the parameters of sensor and vice versa. Although PPE can be used for solids, liquids and gases, we focused only on liquids. To begin with, we have to characterize the pyroelectric sensors. This can be done with any standardizing material, provided we must know its thermal effusivity and diffusivity. The best choice for us is pure water. Once the parameters of sensor are determined we can use them for the study of thermal parameters of different CPAs and their aqueous solutions.

The expression for the normalized amplitude and phase of the signal from both models can be solved analytically to find the thermal parameters. We discuss them individually in the following subsections.

### 2.4.1 FPPE Configuration with Semi Transparent Sensor

Instead of using the fitting method, a simple analytical method [107] can offer information about the thermal parameters of pyroelectric materials. This can be done from the phase of the PPE signal by finding the frequency at which the phase crosses zero. Information can also be gathered from amplitude by finding the frequency at which the amplitude attains a maximum.

From the figure 2.5, we can observe that the normalized amplitude attains a maximum and the normalized phase crosses zero at some frequency. From the expression 2.27, the lowest frequency ( $f_0$ ) at which the phase becomes zero is given by  $l_p/\mu_p = \frac{\pi}{2}$ . By substituting the expression for  $\mu$  (2.7), the diffusivity of the pyroelectric sensor is given by:

$$\alpha_p = \frac{4 f_0 l_p^2}{\pi} \quad (2.32)$$

Once the detector diffusivity is known, the reflection coefficient of the thermal wave  $R_{sp}$  can be calculated. From the known sample effusivity, the effusivity of the sensor can be calculated using the equation:

$$\frac{e_s}{e_p} = \frac{1 + R_{sp}}{1 - R_{sp}} \quad (2.33)$$

Similarly, the amplitude reaches a maximum at a particular frequency ( $f_1$ ).  $f_1$  is the frequency where the derivative of the amplitude as function of  $l_p/\mu_p$  equals zero. This happens at  $l_p/\mu_p = \frac{3\pi}{8}$  in the expression 2.27. Diffusivity,  $\alpha_p$  can be determined from the amplitude of the normalized signal by using the following equation:

$$\alpha_p = \frac{64 l_p^2 f_1}{9 \pi} \quad (2.34)$$

### 2.4.2 FPPE Configuration with Opaque Sensor

In a similar way, we can find the frequency at which the normalized amplitude attains a maximum and the normalized phase crosses zero from the FPPE simulation as shown in the figure 2.7. From the expression 2.31, the lowest frequency ( $f_0$ ) at which the phase becomes zero is given by  $l_p/\mu_p = \pi$ .

Diffusivity,  $\alpha_p$  can be determined from the phase of the normalized signal by using the following equation:

$$\alpha_p = \frac{f_0 l_p^2}{\pi} \quad (2.35)$$

Once  $\alpha_p$  is known and using  $R_{sp}$ , one can calculate the effusivity using the equation:

$$\frac{e_s}{e_p} = \frac{1 + R_{sp}}{1 - R_{sp}} \quad (2.36)$$

Similarly, the frequency ( $f_1$ ) at which the amplitude reaches a maximum can be found. This is where the derivative of the amplitude as function of  $l_p/\mu_p$  equals zero which happens at  $l_p/\mu_p = \frac{3\pi}{4}$  in expression 2.31. Diffusivity,  $\alpha_p$  can be determined from the amplitude of the normalized signal by using the following equation:

$$\alpha_p = \frac{16 l_p^2 f_1}{9 \pi} \quad (2.37)$$

Also there is a relation between these two frequencies given by  $f_0 = (16/9) f_1$ .

Thus the analytical approach gives simple expressions to obtain the thermal parameters and provides a double check to minimize experimental and calculation errors.

## 2.5 Summary

Starting from heat diffusion equation, this chapter explains the temperature fields in each layer of a multi-layer stacked arrangement. Here we focus on the theory behind the determination of thermal parameters of the sensor and sample from a multilayer PPE configuration. Also the normalization process and approximations for special cases are discussed. This chapter ends by briefing the extraction of thermal parameters from the PPE signal using simple analytical method. Details about the PPE experimental setup and ambient temperature measurements are discussed in the next chapter.



---

# Experimental Setup and Photo Pyroelectric Measurements at Ambient Temperature

---

### **Introduction**

The main objective of our study was to understand the thermal properties of cryoprotectants at low temperature mainly near the glass transition temperature. So it was necessary to have a robust instrumental setup with precise temperature control. The aim was to conduct some tests in room temperature with some known samples to calibrate the instrument and then to extend the studies to low temperature range. As the glass forming liquids have the typical characteristics of having a frequency dependence on its specific heat capacity [72, 114] it was necessary to study the temperature and frequency dependence of thermal effusivity.

This chapter discusses about the construction of a new PPE instrument in the UDSMM laboratory which is capable of working at low temperature (till  $-180\text{ }^{\circ}\text{C}$ ) and the challenges faced and their solutions. Also it says about the different sensors used and their characterization and sample preparation. The chapter ends by discussing the results of the effusivity measurements at ambient temperature for pure samples and the molecular association in the binary solutions of glycerol and 1,2 propanediol.

### **3.1 Experimental Setup**

Since the setup was newly built many models and designs were tried and the best possible was chosen. The whole setup can be divided into three categories:

- 1) PPE cell
- 2) Illumination and temperature controller
- 3) Data acquisition

Figure 3.1 shows a simple cross section of our PPE instrumentation.

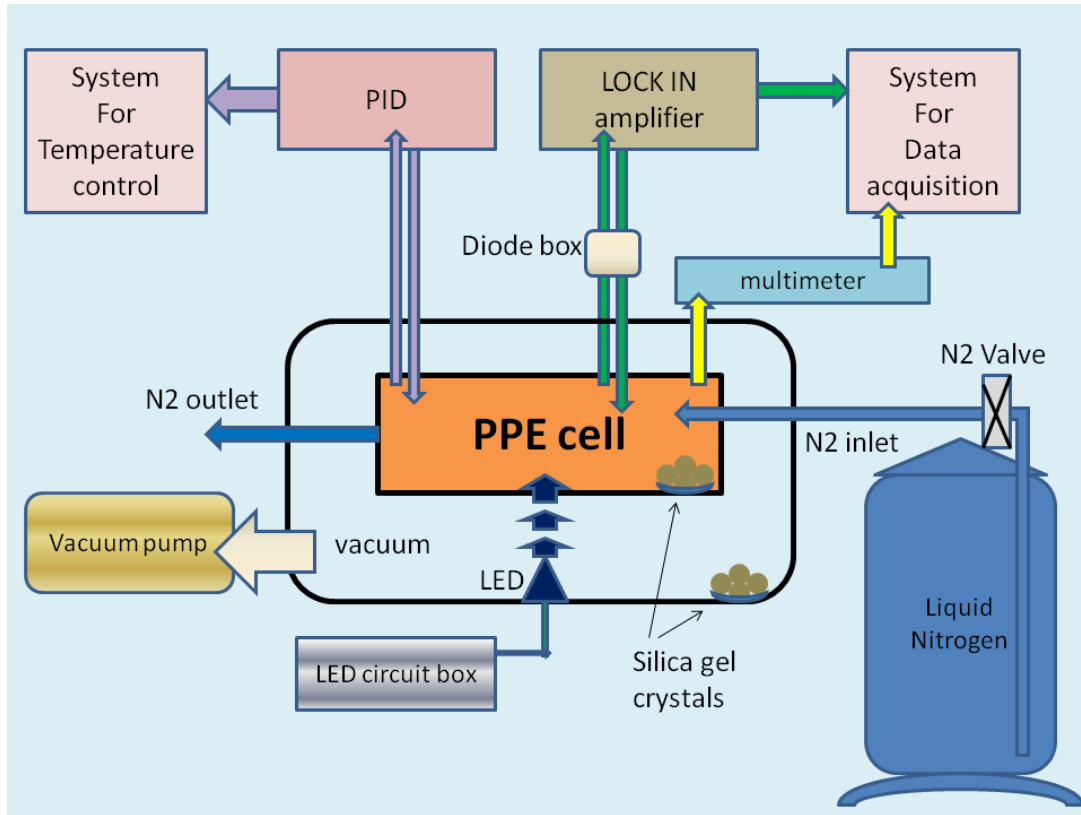


Figure 3.1 – A simple cross section of our PPE setup and the arrangement of the temperature control and data acquisition system.

### 3.1.1 PPE Cell

#### 3.1.1.1 Cell Design

A cell was designed which was adapted to different PPE configurations to study the different thermal parameters precisely at various temperatures. Liquid nitrogen was used for cooling the cell till  $-180\text{ }^{\circ}\text{C}$ . Pyroelectric materials are piezoelectric also [116]. Therefore, in addition to the pyroelectric signal, they generate a piezoelectric signal as a response to mechanical stress. The piezoelectric effect dominates due to the mechanical stress generated by the flow of liquid nitrogen when it comes in direct contact with pyroelectric sensor. So it was very necessary to isolate the sensor from the nitrogen flow. Basically the cell was made in aluminum with two chambers, A and B, shown in figure 3.2. Chamber A was to hold the pyroelectric sensor and the sample and chamber B was where the liquid nitrogen was circulated. Inlet and outlet valves for liquid nitrogen are connected to chamber B. The chamber A was fixed inside the chamber B. It was necessary to have two separate chambers in order to isolate the sensor and sample from the liquid nitrogen flow.

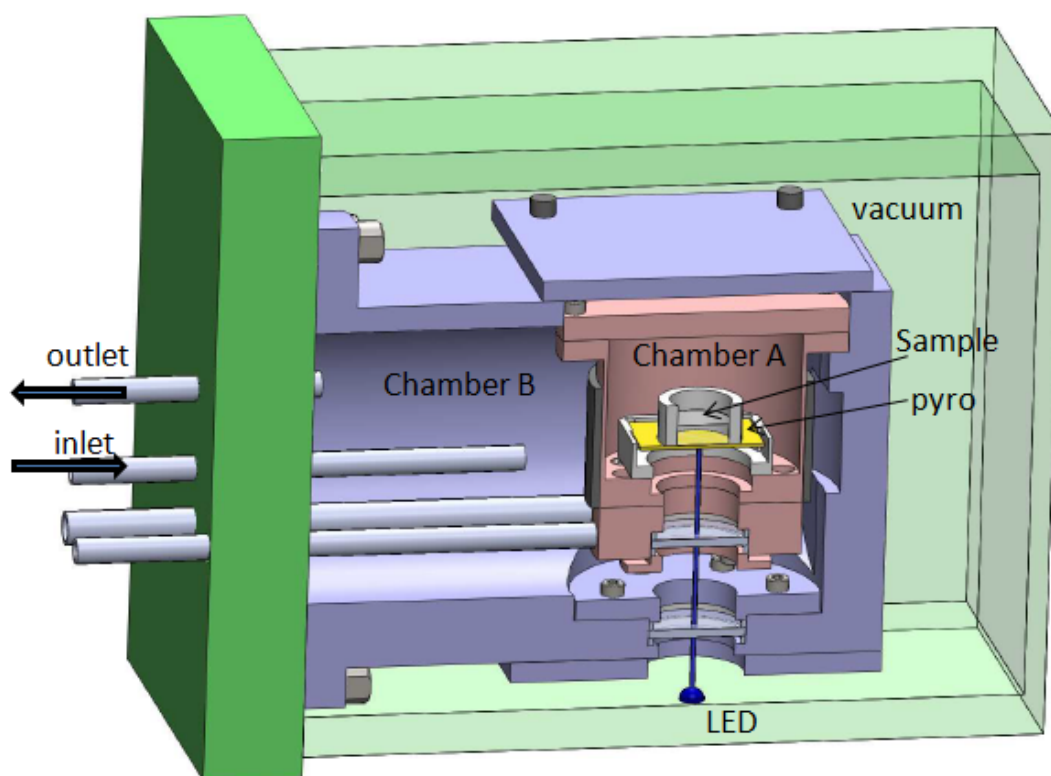


Figure 3.2 – Schematic representation of the PPE cell

The chamber A was adapted for all PPE configurations. We used a structure made from polytetrafluoroethylene (PTFE), commonly known as Teflon, to hold the sample in contact with the pyroelectric sensor. The sample was placed above the sensor as shown in figure 3.2 so that the sample could maintain a better contact with the sensor throughout the low temperature experiments. The structure has provision to add sample without displacing the sensor. This was because each measurement was a set of two experiments, first without sample and the second with sample. A normalization was done with signal measured with sample to the one without sample thereby nullifying the dependence of the electronic and illumination contributions. Maintaining atmospheric pressure inside the chamber A was very important and this was done by introducing an opening to the surroundings without affecting the nitrogen flow. To maintain a homogeneous temperature inside this chamber, a slight flow of gaseous nitrogen was always given inside the chamber A around the sensor and sample. The flow was optimized to get a clear signal and to avoid the vaporization of sample. The normalized flow was set at a maximum of  $35 \text{ ml min}^{-1}$ .

The illumination was given from bottom of the cell because when the sample became opaque during freezing the radiation couldn't reach the pyro sensor. Glass windows were used for the light entrance. The glass was fixed with PTFE O-rings between aluminum. The whole cell was isolated from the surroundings by keeping it in vacuum. Cold leaks were detected by checking the vacuum level. Cryogenic vacuum grease was used at all the contacts to avoid leaks when cooled to low temperature.

### 3.1.1.2 Pyroelectric Sensors Used for Measurement

Most commonly used pyroelectric sensors are Lithium Tantalate ( $LiTaO_3$ ) monocrystal, Polyvinylidene difluoride (PVDF) and Lead Zirconate Titanate (PZT). We didn't use PVDF because of its polymer nature and its glass transition temperature of  $-40\text{ }^\circ\text{C}$  which is in our working range (till  $-180\text{ }^\circ\text{C}$ ). First we worked with PZT because of its cost efficiency and a higher pyroelectric coefficient when compared to  $LiTaO_3$  [116]. A circular PZT (CTS corporation) having a dimension of 20 mm diameter and  $500\text{ }\mu\text{m}$  thickness was used in FPPE configuration. We obtained very accurate effusivity values for samples from room temperature measurements that will be discussed in the section 3.2. But to attain sub-zero temperature liquid nitrogen was circulated around the cell. Although there was no direct contact between PZT and nitrogen flow, the vibration induced by this flow was enough for PZT to generate a piezoelectric contribution to the signal because of its higher piezoelectric coefficient [116]. Moreover, at ambient temperature we had some problems when water was used as sample which might be due to the current leakage under high humidity condition [117] and from the porosity [118] of PZT. So we chose to work with  $LiTaO_3$  because it has a lower piezoelectric co-efficient [116] and is a better choice for thermal measurements [116] and has no issues reported when in contact with water.

A square shaped  $LiTaO_3$  sensor (OPTON LASER INTERNATIONAL) with a dimension of  $300\text{ }\mu\text{m}$  and  $30\times 30\text{ mm}^2$  surface area with gold coated on both sides was used for the effusivity measurements at room temperature. This sensor was used in FPPE configuration for the room temperature measurements. For the low temperature measurements, we started with the FPPE configuration but the thickness of the sensor limited our working frequency range because the heat wave has to traverse the whole thickness of the pyro sensor to reach the sample which is on the other side. To overcome this limitation, we introduced the semi transparent pyro sensor where the sample-sensor interface was illuminated. A semi-transparent  $LiTaO_3$  with one side coated with indium tin oxide (ITO) and other side with gold was used for low temperature measurements. The ITO was deposited by SOLEMS (ITO sol 30) on a  $LiTaO_3$  from OPTON LASER INTERNATIONAL. The  $LiTaO_3$  dimensions were  $500\text{ }\mu\text{m}$  in thickness and  $30\times 30\text{ mm}^2$  surface area. Connections were made with silver paint (Agar scientific).

### 3.1.1.3 Temperature Measurement

Temperature measurements were done using sensors Pt1000 in four wire connection using two multimeters: Keithley 3706 and Keithley 2700. Four wire connection offers better reliability and accuracy. For low temperature measurements, Pt1000 (Class Y) sensors were used. Multimeter K2700 was dedicated for the temperature measurements inside chamber A. All other temperatures were measured using K3706. The reason for a dedicated multimeter for measurements inside the chamber A was due to the generation of noise in the LOCK-IN am-

plifier signal because of the near proximity of pyro sensor with the Pt1000 sensor. The signal from the LOCK-IN amplifier was disturbed when all Pt1000 sensors were triggered using the multimeter K3706. So the temperature inside the chamber A was acquired using K2700 after the acquisition of the LOCK-IN signal.

Temperature of the chamber A was maintained by using a heating coil wrapped around it and controlled by a PID. Power delivered to the PID was always the same AC line voltage (220-240V). This PID setup consisted of a step down transformer (220 (AC) V to 32 (DC) V) to power a MODBUS communication interface and a solid state relay. Sensors were fixed on the outer surface of the chamber A. The LABVIEW program controlled the solid state relay via MODBUS communication and delivered the line voltage to the heating ring around the cell. The heating ring has a resistance of 220 ohms and a power rating of 220 W. It is worth mentioning that the flow of AC didn't induce any noise in the signal. The temperature of the cell was controlled with a precision of +/-0.01 °C.

It is always a problem to measure the sample temperature accurately because the sensor cannot be in contact with the sample because this induces noise. Here we introduced two sensors to reduce the error. One sensor ( $T_1$ ) was freely suspended in air in close proximity to the sample-sensor combination and the second sensor ( $T_2$ ) was immersed in a small container filled with the same quantity of sample which was kept near the main sample. Comparing the two temperatures resulted in reducing the error in temperature measurement. The figure 3.3 shows the temperature profile of both sensors while cooling and heating.

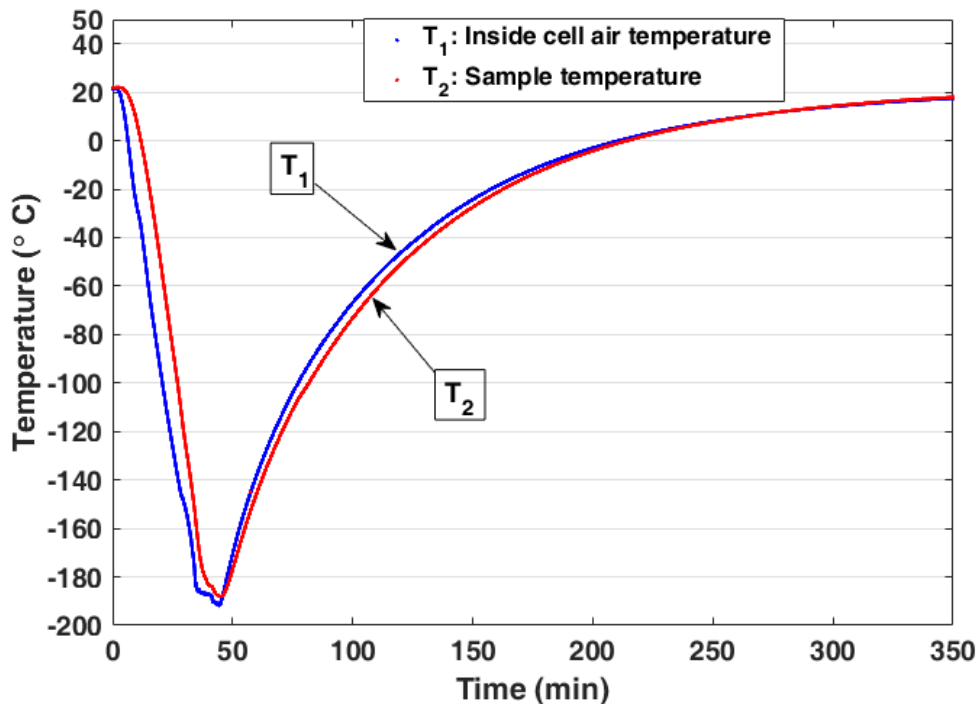


Figure 3.3 – Comparison between two sensors inside the PPE cell (chamber A).

The two temperature profiles show that there was a delay for the sample to follow the cell

air temperature. To allow the sample to reach the same temperature, the cell was maintained at  $-196\text{ }^{\circ}\text{C}$  for 10 minutes with the flow of liquid nitrogen. There was a difference between the two temperatures while heating and is given by  $\Delta T = T_1 - T_2$  (figure 3.4). Therefore the temperature of the sample was corrected using  $\Delta T$  and is given by  $T_2 = T_1 - \Delta T$ .

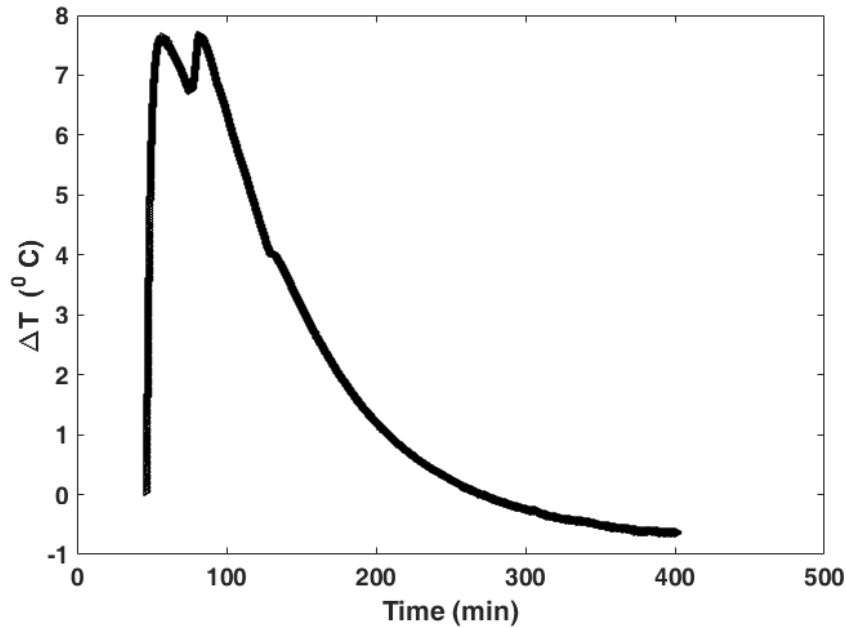


Figure 3.4 – Values used to adjust the cell air temperature to the sample temperature during heating

### 3.1.2 Illumination and Temperature Controller

A periodic heating is necessary for the pyroelectric sensor to generate a signal. This is done by using an illumination source. Generally, a laser is used for this purpose. But in our setup it was difficult to introduce a laser. So we used an LED, which is very cost efficient compared to a laser. To light the LED, a driving circuit was used which took input from a power supply and the LOCK-IN amplifier provided the reference frequency for a periodic illumination. We have observed that the heat generated in the transistor in the driving circuit resulted in a change in the phase of the signal from the pyro sensor. To avoid this, we had to set up a PID to regulate the temperature of the transistor. We called it "Circuit PID". A peltier was used here. One side of the peltier was fixed to the transistor, which should be controlled at a fixed temperature and other side to a heat sink. The peltier was powered by a TTI CPX200D power supply. LXI interfacing was used between the TTI power supply and computer. Controlling and interfacing were done with LABVIEW program. Then the best possible Ziegler Nichols parameters were found to set the PID. We were able to set it to a maximum deviation of  $T \pm 0.01\text{ }^{\circ}\text{C}$ .

The main disadvantage of LED was the influence of its junction temperature on the intensity of the light. The amplitude of the signal kept decreasing as the junction temperature

increased. Only way to avoid this problem was to control the junction temperature perfectly. Many attempts were tried and finally a perfect heat sink was attached to the cathode terminal of the LED and the temperature was controlled using a PID just like the same mentioned earlier. This PID was called as the "LED PID". This was also set to a precision of  $T \pm 0.01$  °C. Comparison of PPE amplitude with and without the LED PID is shown in the figure 3.5. The LED PID reduced the decrease of the PPE amplitude from 7.2 percent to 0.2 percent. The TTI CPX200D power supply offered master and slave terminals. Master was used for the Circuit PID and slave was for the LED PID.

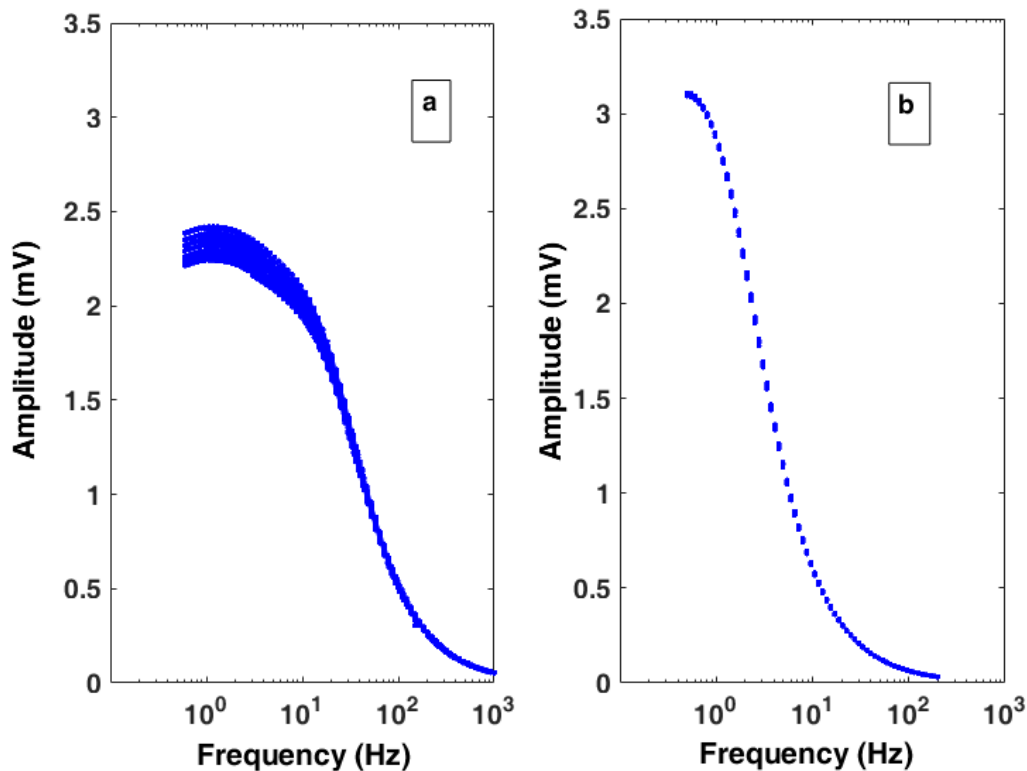


Figure 3.5 – Comparison of PPE amplitude at ambient temperature from 0.5 Hz to 1 kHz for 10 scans. a: without LED PID (bad reproducibility) b: with LED PID (good reproducibility)

### 3.1.3 Data Acquisition

The pyroelectric signal was measured by the LOCK-IN amplifier from Signal Recovery (model 7124). All room temperature measurements were done in voltage mode with auto settings for sensitivity, AC gain and time constant. The low temperature measurements were done in current mode with manual settings for those parameters. This LOCK-IN was specially designed for the low temperature measurements. It consisted of two units connected by optic fibers to avoid all sorts of noise issues that can happen at low temperature measurements like switching noise. The data was sent to a computer and all interfacing were done using LAB-

VIEW programming. The length of the connectors were optimized to avoid noise and protected from electromagnetic interference using faraday protection.

When heating or cooling any pyroelectric crystals, they become electrically charged and can produce electric fields at their surfaces of up to  $10^6 \text{ Vcm}^{-1}$  [119]. This is because of the production of uncompensated charges. This may be either the polarization charge that is inside the crystal surface or the compensation charge that is on the surface [120]. Therefore, to protect the LOCK-IN amplifier from any high DC current peaks which could happen due to fast change in temperature due to the liquid nitrogen flow, a diode combination was used to limit the value, as shown in figure 3.6. Two diodes, 1N4148 (fast responsive), one in forward biasing and other

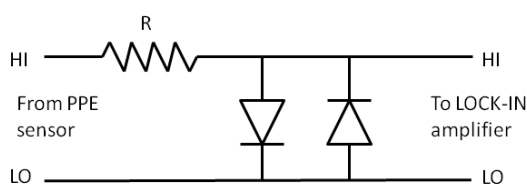


Figure 3.6 – Overload protection circuit

in reverse biasing were connected in parallel with a 100 ohms resistor in series and this could limit the maximum voltage to 600 mV so that the LOCK-IN was protected. The temperature variation of these diodes also had an effect on the amplitude of the signal. The amplitude increased when temperature of the diodes increased. This problem was solved using "Diode PID" which was the same kind of LED PID. The diodes were enclosed in a metal box which served as faraday cage and the temperature of this box was controlled using the PID. A second TTi CPX200D power supply in LXi interface was used to power the resistors used to heat the box. It also gave a precision of  $T \pm 0.01^\circ\text{C}$ . All experiments which were a set of two, with and without sample, were always performed by regulating the same temperature on all PIDs.

### 3.1.4 Ground Loop

All electrical systems are equipped with wiring design which has multiple exits for the electricity to flow to ground. But these paths can form a loop which can pick up stray current and this is a serious pick up contributor. We faced this problem which was solved by careful separation of the functional earth ground, the power ground and the analog ground. The noise and pick up were always tested after each modification was made on the instrument.

### 3.1.5 Sample Preparation

Since we were building a new instrument our primary objective was its calibration with some known samples. We chose glycerol (ALFA AESAR, 99+) and 1,2 propanediol (ACROS ORGANICS, 99) which are well known glass formers. As cryoprotectants always encounter

with water in the living cell we were interested to study the glassy behavior of the binary mixtures of these samples with water. So we prepared some samples by varying the percentage of water content. Both were kept overnight in an oven at 40 °C to remove any moisture prior to prepare the mixtures. Ultra pure water from the purifier, ELGA (model PF1XXXXM1) was used for mixture preparation.

### 3.1.6 Low Temperature Experiments

To study the glass transition and fragility of the samples we performed measurements at low temperature. For low temperature experiments, we chose the FPPE configuration with a semitransparent  $LiTaO_3$ , coated with ITO on one face and gold on other, was in contact with the sample. The light entered through the transparent ITO and heated the sensor-sample interface. The system was cooled from ambient temperature to -196 °C at a rate of 6 °C min<sup>-1</sup> by circulating liquid nitrogen and hold at this temperature for 10 min to avoid any temperature gradient in the sample. The flow was stopped and the cell was allowed to heat to ambient temperature at a rate around 1 °C min<sup>-1</sup>. Data acquisition was done from -180 °C to 20 °C. Fast cooling of  $LiTaO_3$  results in building up of surface charges on it and one should be careful when establishing a connection to the LOCK-IN amplifier. We used a shorting BNC to discharge the connection leads before connecting to our LOCK-IN amplifier.

Experiments we have conducted were temperature scans at a fixed frequency. It was possible to observe the temperature range where the heat capacity undergoes a relaxation. This relaxation has been seen as a drop in the amplitude and a maximum in the phase of the signal. As observed by other researchers [114] we have also observed that the temperature range, where the relaxation happened, was shifting to higher values when the modulation frequency was increased. Our frequency range was from 1 Hz to 1 kHz. For each sample, temperature scans were performed at different modulated frequencies.

## 3.2 Effusivity Measurements at Ambient Temperature

### 3.2.1 Characterization of Pyro Electric Sensors (Effusivity and Diffusivity)

To determine the effusivity of a sample, it was necessary to find firstly the thermal parameters of the pyroelectric sensors. Pyroelectric sensors used for the experiments were PZT and  $LiTaO_3$ . Ultra pure water was used as the standardizing sample to characterize the sensors. The aim was to determine the thermal effusivity and diffusivity of the sensors at ambient temperature. Once these parameters were known for our sensors, we could apply them for the thermal study of different CPAs.

FPPE configuration was chosen for the characterization of all sensors. From the equations 2.30 and 2.31, we can determine the effusivity and diffusivity of the sensor just by knowing the effusivity of water and the thickness of the sensor. Two experiments were performed for normalization, first, without sample, second, with sample. Special care was taken while adding the sample in order to avoid any displacement of the sensor so that the illuminated area of the sensor remained the same. The normalized amplitude and phase have been fitted simultaneously to obtain the effusivity and diffusivity of the sensor.

At room temperature, the effusivity of pure water is  $1581 \text{ W s}^{1/2} \text{ m}^{-2} \text{ K}^{-1}$  [107, 110] and we determined the effusivity for the gold-gold  $\text{LiTaO}_3$  as  $4214 \text{ W s}^{1/2} \text{ m}^{-2} \text{ K}^{-1}$  and the diffusivity as  $13.83 \text{ e-7 m}^2 \text{ s}^{-1}$ . Figure 3.7 shows the fitting of the experimental data with equation 2.31.

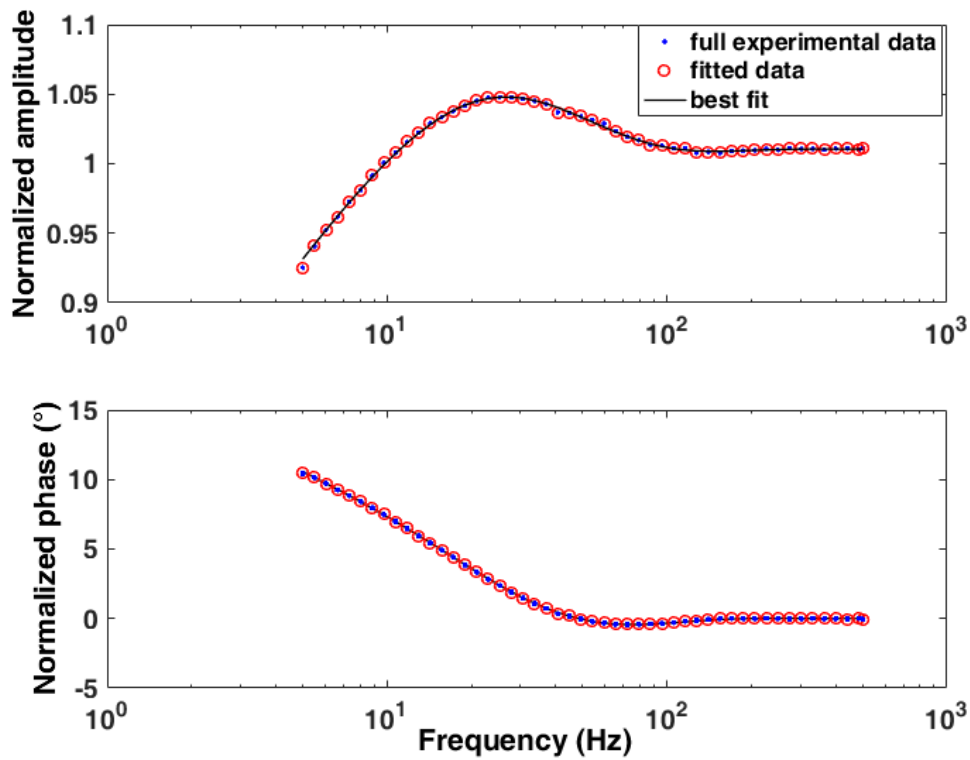


Figure 3.7 – Normalized amplitude and phase of the PPE signal for 300  $\mu\text{m}$  Gold-Gold  $\text{LiTaO}_3$

For the ITO-gold  $\text{LiTaO}_3$ , the effusivity and diffusivity were determined as  $3857 \text{ W s}^{1/2} \text{ m}^{-2} \text{ K}^{-1}$  and  $14.66 \text{ e-7 m}^2 \text{ s}^{-1}$  respectively. Figure 3.8 shows the fitting of the experimental data with equation 2.30.

Also we determined the effusivity and diffusivity for the PZT sensor as  $1710 \text{ W s}^{1/2} \text{ m}^{-2} \text{ K}^{-1}$  and  $4.36 \text{ e-7 m}^2 \text{ s}^{-1}$  respectively. Figure 3.9 shows the fitting of the experimental data with equation 2.31.

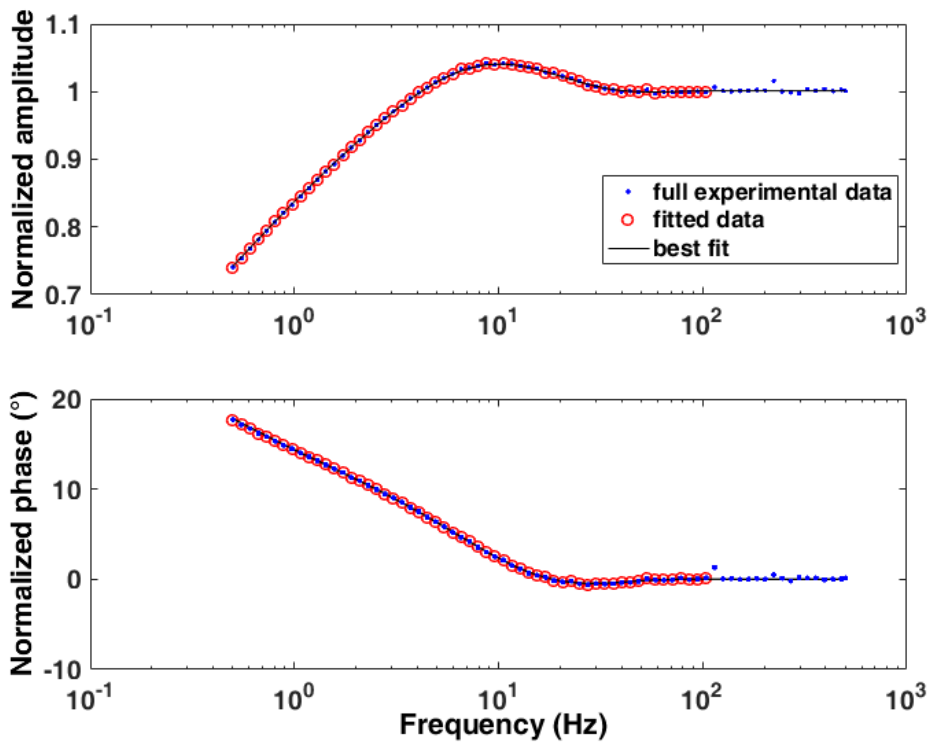


Figure 3.8 – Normalized amplitude and phase of the PPE signal for 500  $\mu\text{m}$  ITO-Gold  $\text{LiTaO}_3$

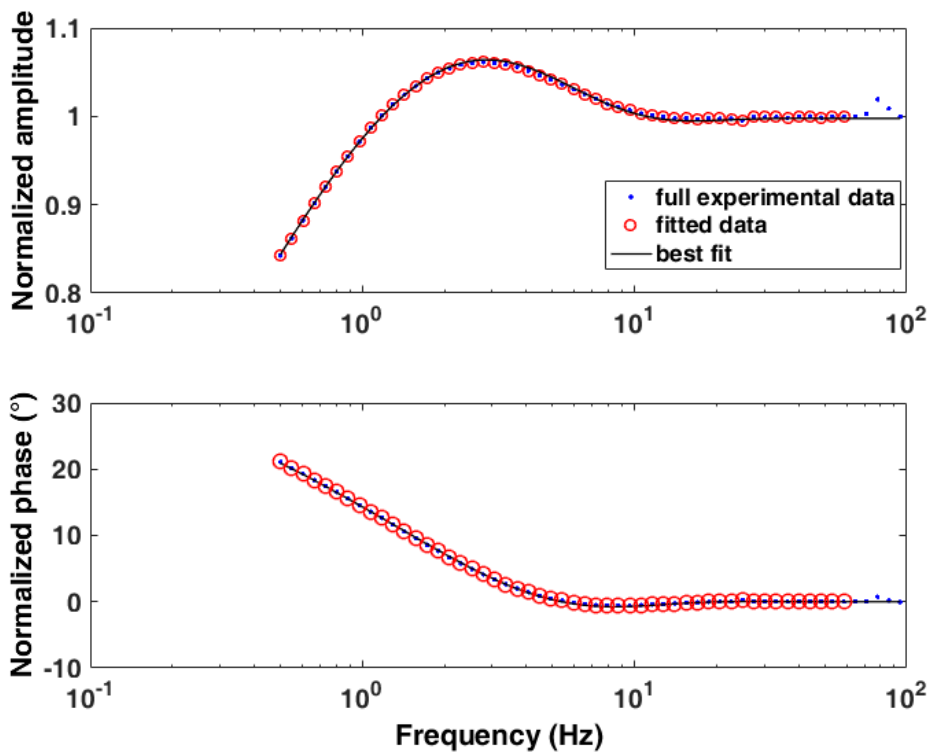


Figure 3.9 – Normalized amplitude and phase of the PPE signal for 500  $\mu\text{m}$  PZT

For the sake of easy understanding, the obtained values are given in tables. Tables 3.1 and 3.2 show the effusivity and diffusivity of different sensors determined from the fit respectively and their comparison with literature data. The fitted values are in good agreement with the literature data.

| Effusivity ( $W s^{1/2} m^{-2} K^{-1}$ ) |               |                         |
|--|---------------|-------------------------|
| Material (room T)                        | This work     | literature              |
| $LiTaO_3$ (300 $\mu m$ )                 | $4214 \pm 11$ | 3777 [103], 3743 [107], |
| $LiTaO_3$ (500 $\mu m$ )                 | $3857 \pm 8$  | 3750 [110], 3575 [112]  |
| PZT (500 $\mu m$ )                       | $1710 \pm 8$  | $1733 \pm 42$ [101]     |

Table 3.1 – Best fitted effusivity for different sensors by using pure water as standarizing sample

| Diffusivity ( $m^2 s^{-1}$ ) |                        |                                       |
|------------------------------|------------------------|---------------------------------------|
| Material (room T)            | This work              | literature                            |
| $LiTaO_3$ (300 $\mu m$ )     | $(13.83 \pm 0.04) e-7$ | $12.46 e-7$ [107], $12.47 e-7$ [110], |
| $LiTaO_3$ (500 $\mu m$ )     | $(14.66 \pm 0.03) e-7$ | $13.67 e-7$ [112]                     |
| PZT (500 $\mu m$ )           | $(4.36 \pm 0.02) e-7$  | $(3.51 \pm 0.15) e-7$ [101]           |

Table 3.2 – Best fitted diffusivity for different sensors by using pure water as standarizing sample

### 3.2.2 Pure Samples

To measure the effusivity at room temperature we used the 300  $\mu m$  thick  $LiTaO_3$  and the 500  $\mu m$  thick PZT. The samples we studied were pure glycerol and 1,2 propanediol. The effusivity was studied using the FPPE configuration mentioned earlier.

The effusivity of the pure glycerol was determined using PZT as  $935 \pm 6 W s^{1/2} m^{-2} K^{-1}$ . The fitted experimental curve is shown in figure 3.10. Also we did the same with 300  $\mu m$   $LiTaO_3$  and the effusivity was determined as  $958 \pm 7 W s^{1/2} m^{-2} K^{-1}$  which is shown in figure 3.11. Both values are in good agreement with the literature data. A comparison of effusivity of glycerol is shown in figure 3.12.

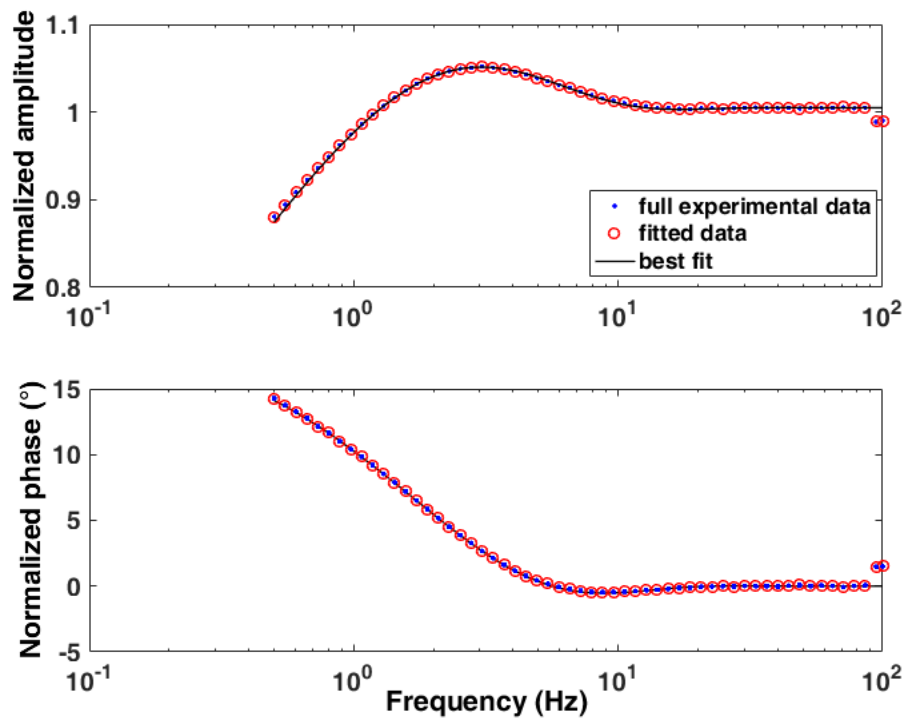


Figure 3.10 – Fitted normalized amplitude and phase of the PPE signal from 500  $\mu\text{m}$  PZT for pure glycerol

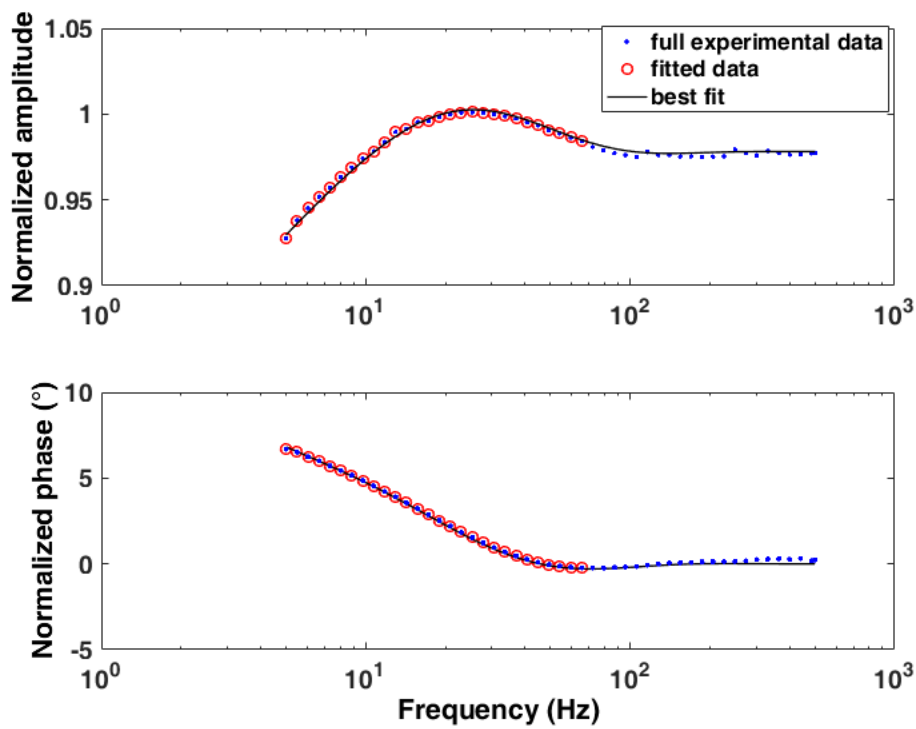


Figure 3.11 – Fitted normalized amplitude and phase of the PPE signal from 300  $\mu\text{m}$   $\text{LiTaO}_3$  for pure glycerol

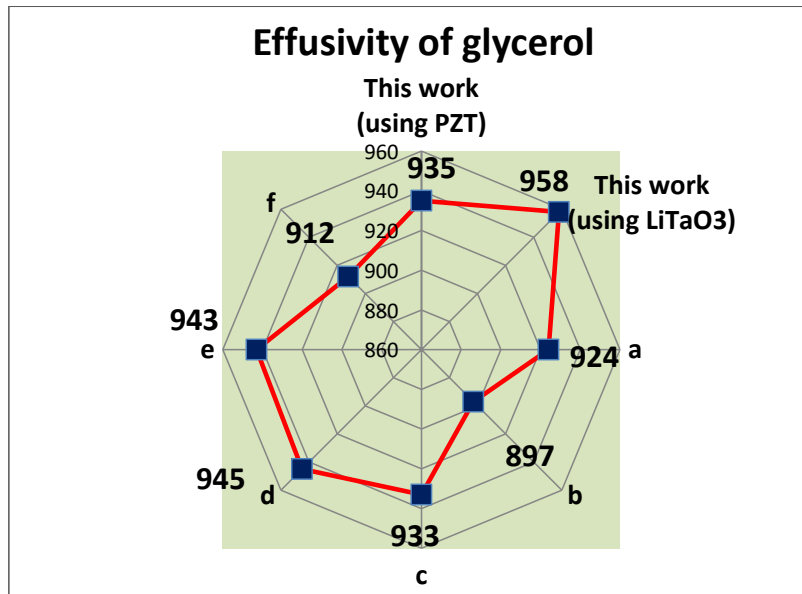


Figure 3.12 – Comparison of determined effusivity value of pure glycerol with literatures, a: [121], b: [107], c: [112], d: [122], e: [93], f: [123]

Similarly, the effusivity of 1,2 propanediol was determined using the same  $LiTaO_3$  as  $768 \pm 5 W s^{1/2} m^{-2} K^{-1}$  and the fitted experimental curve is shown in figure 3.13.

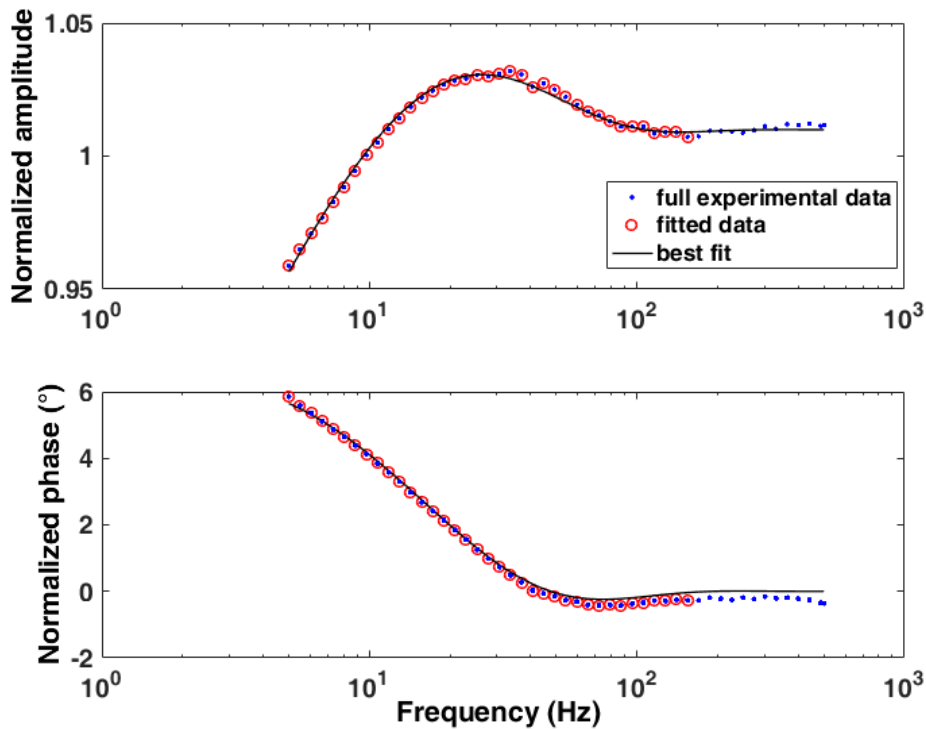


Figure 3.13 – Fitted normalized amplitude and phase of the PPE signal from  $300 \mu m LiTaO_3$  for pure 1,2 propanediol

Table 3.3 shows the comparison of the obtained effusivity of 1,2 propanediol with literatures. Results are in good agreement with literatures.

| Effusivity ( $W s^{1/2} m^{-2} K^{-1}$ ) |              |
|--|--------------|
| This work                                | $768 \pm 5$  |
| a  | $732 \pm 51$ |
| b  | 721          |

Table 3.3 – Comparison of effusivity of 1,2 propanediol with literature, a: [123], b: [121]

### 3.2.3 Binary Mixtures and Molecular Association

Thermal effusivity can be used to study the strength in the molecular interaction in mixtures [124]. Liquids can be divided into two classes, normal liquids and associated liquids. Both have widely different properties. This difference in properties is due to the association forces due to the lone-pair electrons, which play an important role in determining the internal properties of molecules such as shape and electron distribution. The associated liquids have high melting and boiling points, high viscosities, high dielectric constants and have strong ionizing capability. Examples of associated liquids are mixtures of water and alcohols. Molecular association happens in two ways, first type is by binding the molecules together into small groups such as rings or chains by the Van der Waals forces and the second type is by forming a network of bonds extending throughout the whole liquid due to large number of intermolecular bonds formed per molecule. An example of the former case is hydrogen fluoride, which forms ring or chain polymer and carboxylic acid, which are held together in pairs by hydrogen bonds. Best example for the second case is water.

Dadarlat et al. have studied the molecular association in water-ethanol and water-ethylene glycol mixtures [124]. They studied thermal effusivity using FPPE technique to detect molecular association in these mixtures. A. O. Guimaraes et al. [111] also studied the same samples and mixtures of biodiesel-diesel by determining their thermal effusivity using FPPE technique. The sensitivity of thermal effusivity to molecular association is weaker than that of thermal conductivity [111] and thermal diffusivity [124]. N. Houriez [125] had studied the molecular association in water-1,2 propanediol mixtures and water-DMSO mixtures from the diffusivity measurements. We couldn't find any literature data about the effusivity measurements on molecular association in water-glycerol mixtures. Our goal was to use the PPE setup to study the water-glycerol mixtures and also water-1,2 propanediol mixtures to understand their molecular interaction.

Aqueous solutions of both CPAs were prepared in different concentrations ranging from 10 wt% to 90 wt%. The effusivity ( $e$ ) of each binary mixture was determined by running a frequency scan from 5 Hz to 500 Hz in the FPPE configuration. The molecular association was studied by calculating the quantity,  $\Delta e/e$ , named as "excess value" and which is defined

as [124]:

$$\Delta e/e = \frac{e_{exp} - e_{theor}}{e_{theor}} \quad (3.1)$$

where  $e_{theor}$  represents the effusivity value when a perfect additivity law for the mixtures is respected and is calculated by using the equation:

$$e_{theor} = (molepercent_{CPA})(e_{CPA}) + (molepercent_{water})(e_{water}) \quad (3.2)$$

The excess value is a dimensionless quantity and it is a measure of deviation of effusivity from linearity.

### Effusivity Results of Binary Mixtures from PPE

Once the mixtures were prepared the effusivity was determined using the same  $LiTaO_3$  used for the pure samples. The effusivity of glycerol mixtures versus mole concentration of glycerol is shown in figure 3.14. A graph is plotted with the excess value, mentioned earlier, against mole concentration of glycerol to study the molecular association in the liquid mixture as shown in figure 3.15

In a similar way, the effusivity of the binary solutions of 1,2 propanediol with water were determined. Figures 3.16 and 3.17 show the effusivity and the excess value curves versus mole concentration of 1,2 propanediol respectively.

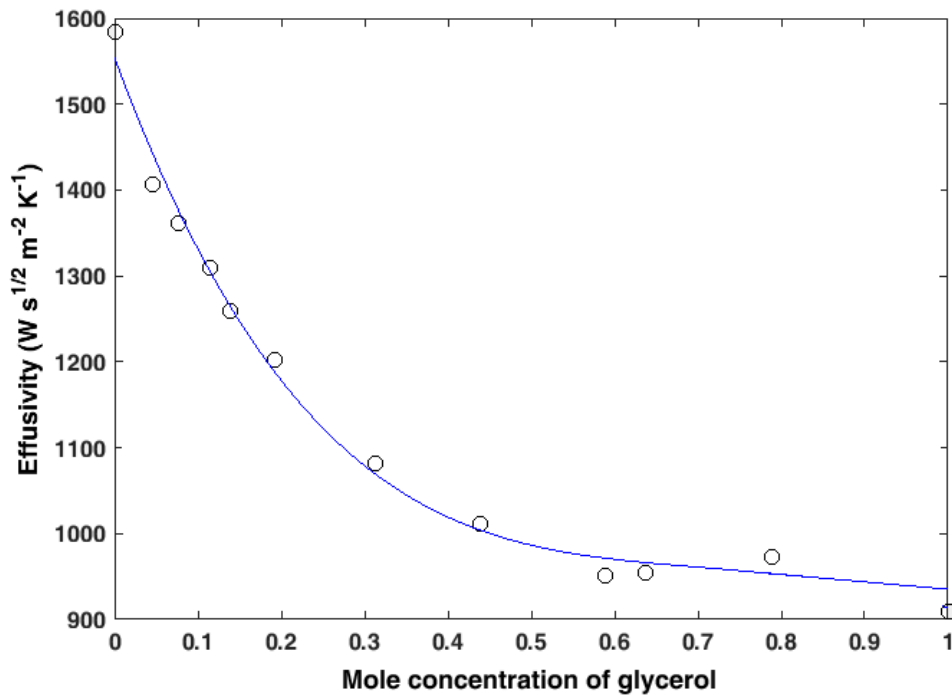


Figure 3.14 – Effusivity of binary solutions of glycerol-water

### 3.2. Effusivity Measurements at Ambient Temperature

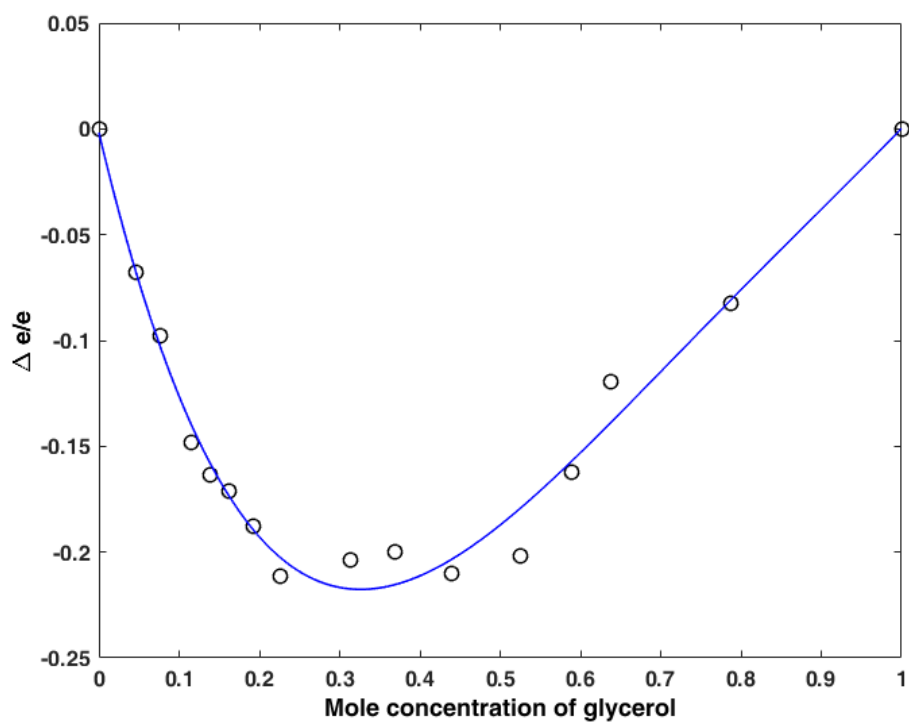


Figure 3.15 – Relative difference in effusivity (excess value) of binary solutions of glycerol-water

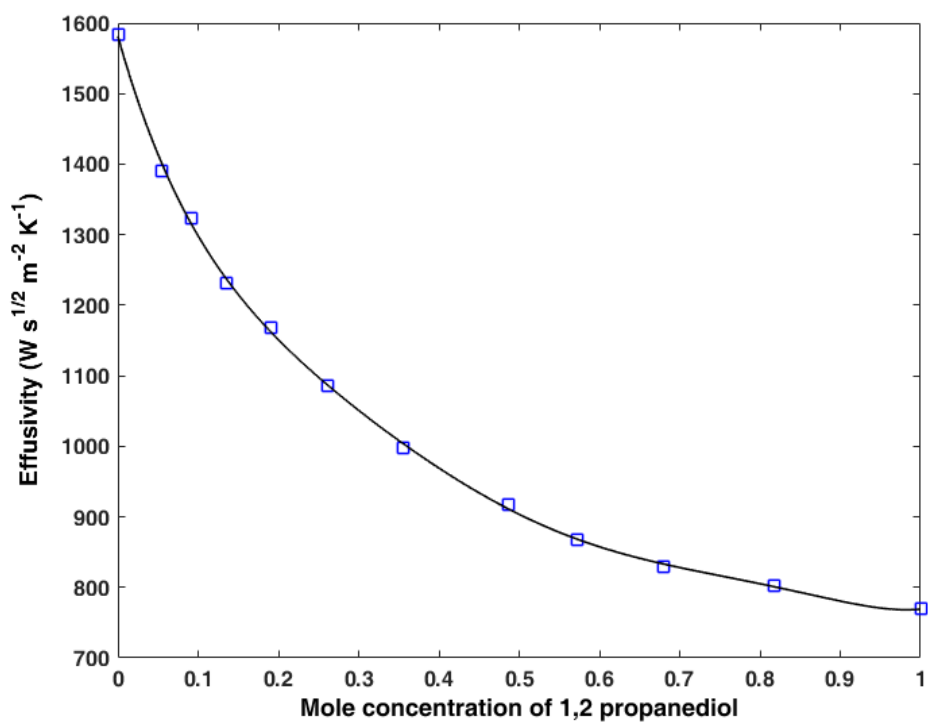


Figure 3.16 – Effusivity of binary solutions of 1,2 propanediol-water

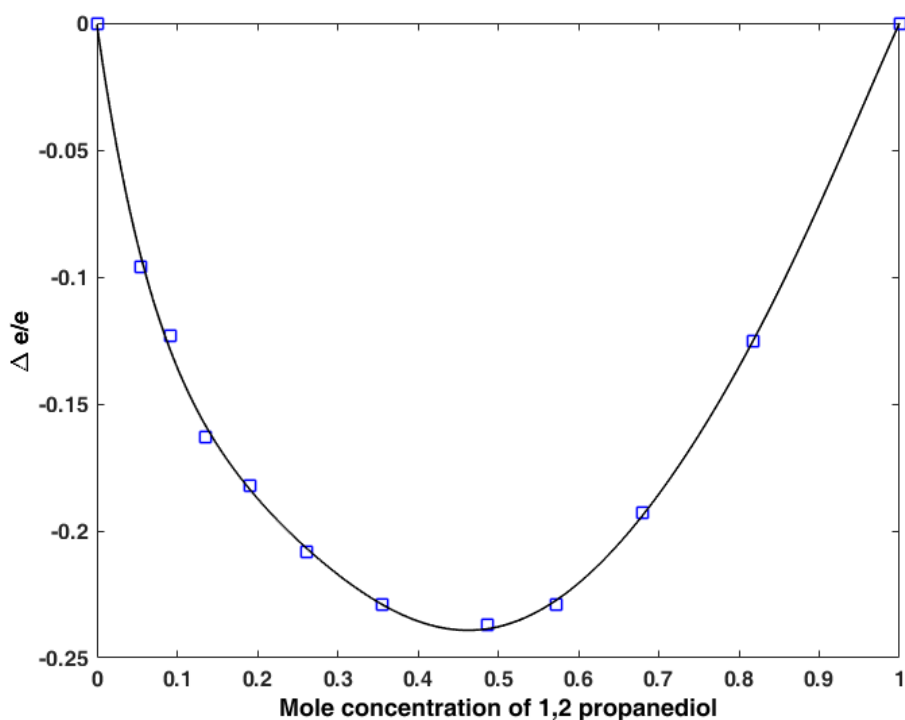


Figure 3.17 – Relative difference in effusivity (excess value) of binary solutions of 1,2 propanediol-water

For non associative binary mixtures, the excess value shows a linear behavior when represented as a function of concentration [124]. The deviation from linearity shows molecular association. Both figures (3.15 and 3.17) show that process of molecular association happened in both binary mixtures of glycerol and 1,2 propanediol. Therefore, we conclude that studying thermal effusivity using PPE technique is a suitable tool for detecting molecular association in binary liquids.

### 3.3 Summary

This chapter gives a detailed description of the instrumentation of our PPE setup and the problems of a home made setup and rectification of those issues. It explains the structure of our PPE cell, temperature regulation using different PID controllers and data acquisition. Also it has given an overview of our pyroelectric sensors and samples and their characterization. The chapter ends with results and discussions about the effusivity measurements at ambient temperature of different mixtures of glycerol and 1,2 propanediol and the presence of molecular association in their binary solutions with water. Results obtained for the effusivity were compared with literature and found to be in good agreement. Results of the low temperature experiments are given in the next chapter.

---

# Low Temperature Photo Pyroelectric Measurements: Results and Discussion

---

### **Introduction**

We have discussed in the first chapter that the survival of biological cells depends strongly on the cooling and warming rates and these depend on their thermal properties. Therefore, the study of thermal parameters of the CPAs is of great relevance. This chapter explains the theoretical aspects of the modelization of effusivity square using PPE when  $\alpha$  relaxation occurs at low temperature and how to extract information about  $T_g$ , activation energy, Dyre-Olsen Index and fragility parameter of the CPAs and their mixtures. It is followed by the application of this protocol on different samples to determine their parameters. Other sections of this chapter gives a description about the low temperature viscosity measurements and DSC measurements and a comparison with the PPE results.

## **4.1 Low Temperature PPE: Theory**

### **4.1.1 Simulation of PPE Signal in the $\alpha$ Relaxation Region**

The quantity in which relaxation occurs is the dynamic heat capacity ( $c$ ). It was reported in literature that frequency dependence of the thermal conductivity ( $k$ ) is negligible in comparison with that of heat capacity [114]. The frequency dependence of heat capacity of glassy liquids is complex. This can be described by the Havriliak-Negami (HN) empirical model [76] and is

given by the expression:

$$c(\omega, T) = c_{\infty} + \left[ \frac{c_0 - c_{\infty}}{\left(1 + (i\omega\tau)^{\alpha}\right)^{\beta}} \right] \quad (4.1)$$

Where  $\omega$  is the angular frequency and is given by  $\omega = 2\pi\nu$ , where  $\nu$  is the frequency.  $c_0$  and  $c_{\infty}$  are constants.  $\alpha$  and  $\beta$  are always in the range  $0 \leq \alpha \leq 1$  and  $0 \leq \beta \leq 1$  respectively.

Generally, the HN equation is used in frequency domain to study the relaxation mechanism, as in the case of dielectric spectroscopy [95]. In our case, we used HN equation (4.1) in temperature domain to study relaxation. Here  $\tau$  is the only temperature dependent parameter.  $\omega$  is fixed because a temperature scan is performed at fixed frequency and  $\tau$  varies with temperature. The dependence of  $\tau$  on temperature has been defined using various theoretical models like VFT, Bässler-Avramov (BA), Waterton-Mauro (WM or MYEGA), Critical-like (Crit) etc.

In VFT model [57, 69],  $\tau$  is given by the equation:

$$\tau(T) = \tau_{\infty} \exp\left(\frac{DT_0}{T - T_0}\right) \quad \text{where } D = B/T_0 \quad (4.2)$$

In BA model [63, 64],  $\tau$  is given by the equation:

$$\tau(T) = \tau_{\infty} \exp\left(\frac{A}{T^n}\right) \quad (4.3)$$

In MYEGA(WM) model [65, 66],  $\tau$  is given by the equation:

$$\tau(T) = \tau_{\infty} \exp\left(\frac{K}{T} \exp\left(\frac{C}{T}\right)\right) \quad (4.4)$$

In Critical-like model [67, 68],  $\tau$  is given by the equation:

$$\tau(T) = \tau_C \left(\frac{T - T_C}{T_C}\right)^{-\phi} \quad (4.5)$$

A simulation of the temperature evolution of real and imaginary parts of the heat capacity (c) using the HN equation is shown in figure 4.1, where the temperature dependence of  $\tau$  is defined by VFT model. The relaxation happens in c can be observed in both real and imaginary parts. By incorporating the evolution of  $c(\omega, T)$  in equation 2.28, we can simulate the PPE signal as shown in figure 4.2.

The importance of the PPE experiment is that the  $\alpha$  relaxation can be directly observed in both amplitude and phase of the PPE signal as shown in the simulation. We can observe that when the modulating frequency increases the region of relaxation moves to higher temperature.

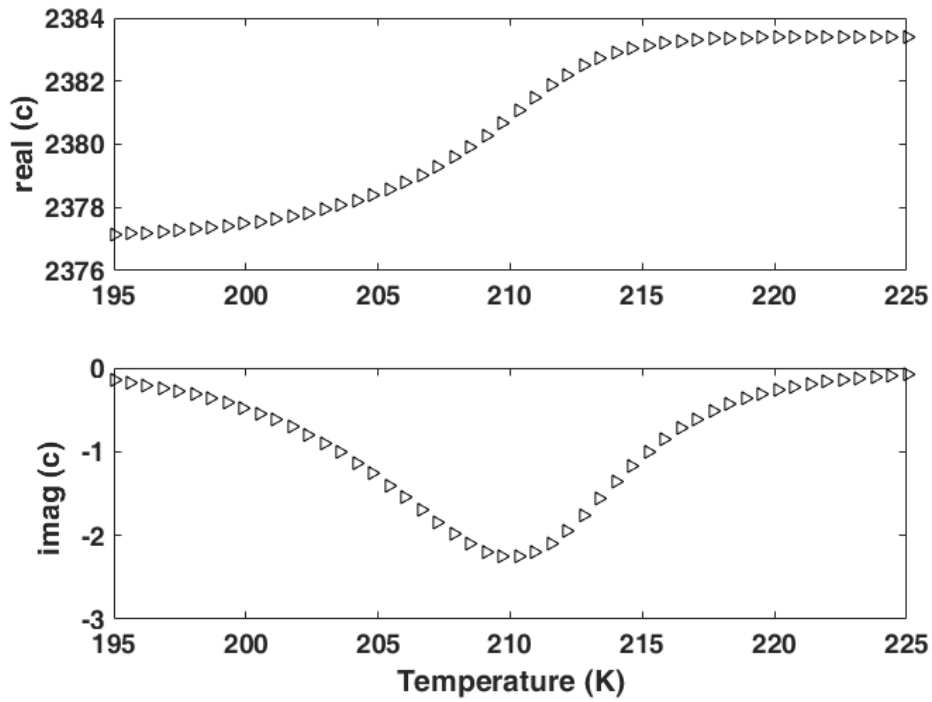


Figure 4.1 – Simulation of real and imaginary parts of heat capacity using HN equation in temperature domain for pure glycerol at a modulating frequency,  $f= 22\text{Hz}$ .

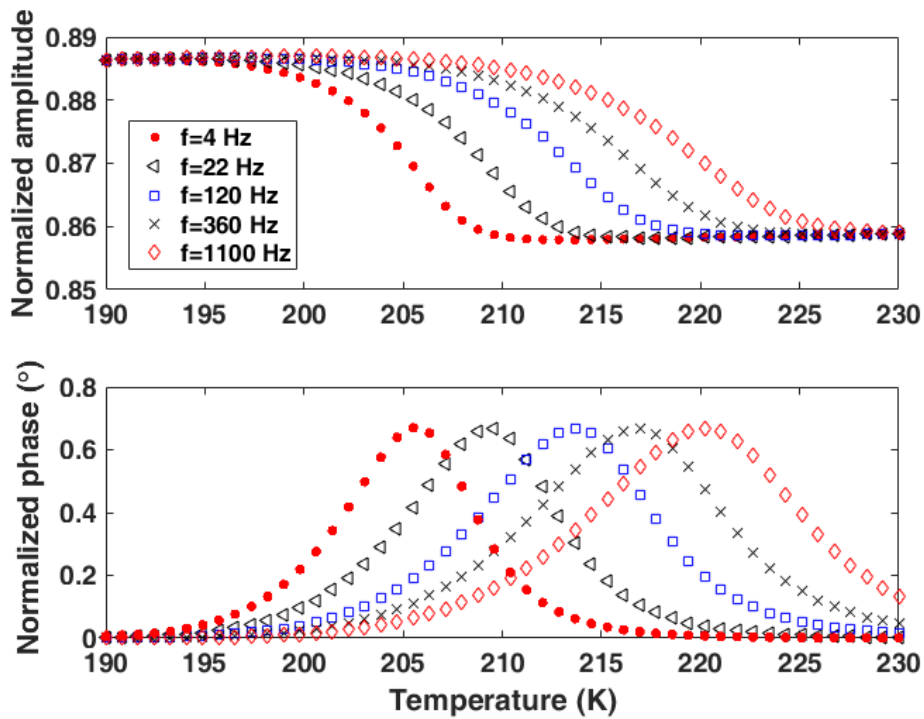


Figure 4.2 – Simulation of temperature evolution of amplitude and phase of the PPE signal using the equation 2.28 for pure glycerol at different modulating frequencies. Here VFT model is used to define the temperature dependence of  $\tau$ .

## 4.1.2 Determination of Effusivity from PPE Signal

In this section we explain how we exploit the PPE signal to study the temperature evolution of thermal parameters of samples in the vicinity of  $\alpha$  relaxation. From the amplitude and phase of the PPE signal we can calculate the effusivity ( $e$ ) of the sample by using the equation 2.28, provided we must know the effusivity of the pyroelectric sensor ( $LiTaO_3$  in our case). The dependence of effusivity on temperature for  $LiTaO_3$  was reported by Oleaga et al [103]. Then, the effusivity square ( $e^2$ ) of the sample is calculated. From equation 2.5, it is evident that the dynamic heat capacity can be studied directly from the squared effusivity. Therefore, equation 4.1 can be modified as:

$$e^2(\omega, T) = e_\infty^2 + \left[ \frac{e_0^2 - e_\infty^2}{(1 + (i\omega\tau)^\alpha)^\beta} \right] \quad (4.6)$$

Figure 4.3 shows a simulation of the temperature evolution of real and imaginary parts of squared effusivity for different modulating frequencies derived from the PPE signal shown in the figure 4.2.

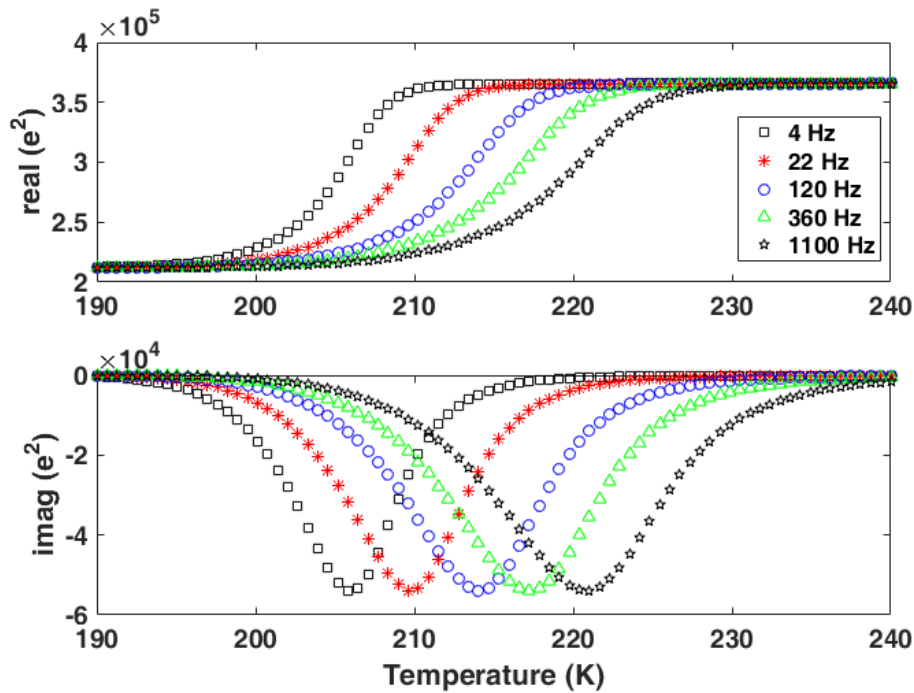


Figure 4.3 – Simulation of temperature evolution of real and imaginary parts of squared effusivity for pure glycerol at different modulating frequencies

## 4.1.3 Determination of the Relaxation Time

In the case of our samples, glycerol and 1,2 propanediol, literatures reported that their  $\tau$  follows VFT law [126, 127]. So  $\tau$  in the HN equation was represented using the VFT equation (4.2). But in the case of a new sample, when we don't know the dependence of  $\tau$ , we have to

use all the aforementioned models for  $\tau$  in the HN equation to find the correct one, which is a tedious task when dealing with plenty of samples. Therefore, we have used a protocol to find the exact model for defining the temperature dependence of  $\tau$ . Here we explain the protocol to determine  $\tau(T)$  from  $e^2(T)$ .

For simplification, we replace  $e^2$  by  $E$ . Therefore, equation 4.6 can be modified as:

$$E(\omega, T) = E_{\infty} + \left[ \frac{E_0 - E_{\infty}}{(1 + (i\omega\tau)^{\alpha})^{\beta}} \right] \quad (4.7)$$

From equation 4.7,  $\tau$  can be calculated using the following equation [128]. We call this method as ‘Direct method’.

$$\tau(T) = -i \frac{\exp(\ln(\exp(\ln((E_0 - E_{\infty})/(E(\omega, T) - E_{\infty}))/\beta) - 1)/\alpha)}{\omega} \quad (4.8)$$

Parameters  $\alpha$ ,  $\beta$ ,  $E_{\infty}$  and  $(E_0 - E_{\infty})$  denoted as  $\Delta E$  are obtained by analysing  $E(\omega, T)$  in a complex plane where the shape is independent of the model of relaxation time. This complex plane representation can be done by using a Cole-Cole plot or a Wicket plot [128].

The complex effusivity square can be written as  $E(\omega, T) = E' + iE''$  ( $E'$  is the real part of  $e^2$  and  $E''$  is the imaginary part of  $e^2$ ). The real part ( $E'$ ) is called storage modulus and the imaginary part ( $E''$ ) is called loss modulus. The Cole-Cole plot is the one in which the loss modulus is plotted against the storage modulus, ( $E''$  vs  $E'$ ). For the Wicket plot, we consider another quantity, called loss factor, defined as  $\tan \delta = \frac{E''}{E'}$ . In Wicket plot, the loss factor is plotted against storage modulus, ( $\frac{E''}{E'}$  vs  $E'$ ).

Therefore, from the Wicket plot or Cole-Cole plot, the four parameters,  $\alpha$ ,  $\beta$ ,  $E_0$ ,  $E_{\infty}$  can be solved by fitting the plot with HN model and then as a second step, the  $\tau$  for different temperature can be calculated easily using the equation 4.8.

### 4.1.3.1 Choosing the Model For Relaxation Time

The general super-Arrhenius equation [53] has defined the relaxation time as:

$$\tau(T) = \tau_{\infty} \exp\left(\frac{\Delta E_a(T)}{RT}\right) \quad (4.9)$$

where,  $\Delta E_a(T)$  is the activation energy (AE). AE can be calculated from equation 4.9 as:

$$\Delta E_a(T) = RT \ln\left(\frac{\tau(T)}{\tau_{\infty}}\right) \quad (4.10)$$

For the calculation of AE, the value of the  $\tau_{\infty}$  is most often chosen to be  $10^{-14}$  s [52, 129, 130]. Substituting equation 4.8 in 4.10, we can study the temperature evolution of the activation energy.

From the AE, the Dyre-Olsen index  $I_{DO}$  [129] can be determined using the equation:

$$I_{DO}(T) = -\frac{d \ln \Delta E_a(T)}{d(\ln T)} \quad (4.11)$$

Linking the super-Arrhenius equation 4.9 and 4.11 directly yields [53]:

$$I_{DO}(T) = \frac{\Delta H_a(T)}{\Delta E_a(T)} - 1 \quad (4.12)$$

where  $\Delta H_a(T)$  is the apparent activation enthalpy (AAH) [131] which is given by:

$$\Delta H_a(T) = R \left( \frac{d \ln \tau}{d(1/T)} \right) \quad (4.13)$$

Analysis of  $I_{DO}$  is an important tool for testing the validity of different models for defining the temperature dependence of  $\tau$  in low-molecular weight glass-forming ultraviscous liquids [130]. The  $I_{DO}$  for different models are given by:

$$I_{DO}^{VFT}(T) = \frac{T_0}{T - T_0} \quad (4.14)$$

$$I_{DO}^{BA}(T) = D - 1 = \text{constant} \quad (4.15)$$

$$I_{DO}^{WM}(T) = \frac{C}{T} \quad (4.16)$$

$$I_{DO}^{Crit}(T) \approx \frac{\phi}{T - T_C} \quad (4.17)$$

The inverse DO ( $I_{DO}^{-1}$ ) index for each model can be calculated as follows.

$$\frac{1}{I_{DO}} = \begin{cases} \left(\frac{1}{T_0}\right) T - 1 & \text{for VFT} \\ \frac{1}{D-1} & \text{for BA} \\ \left(\frac{1}{C}\right) T & \text{for WM} \\ \left(\frac{1}{\phi}\right) T - \frac{T_C}{\phi} & \text{for Crit} \end{cases} \quad (4.18)$$

From equation 4.18, we can find that the inverse DO index shows a linear profile [132] of the form,  $I_{DO}^{-1} = mT + c$ . The value of "c" defines the model for  $\tau$ , ie,  $c=1$  for VFT model,  $c=0$  for WM (MYEGA) model and  $c=-T_C/\phi$  for Critical-like model. The BA model attains a constant value of  $1/(D-1)$ . Therefore, instead of assuming one of these models for defining the temperature dependence of  $\tau$ , we can determine the correct model from the temperature evolution of  $I_{DO}^{-1}$ .

A simulation of the temperature evolution of  $I_{DO}$  and  $I_{DO}^{-1}$  for different models is shown in figure 4.4 [132].

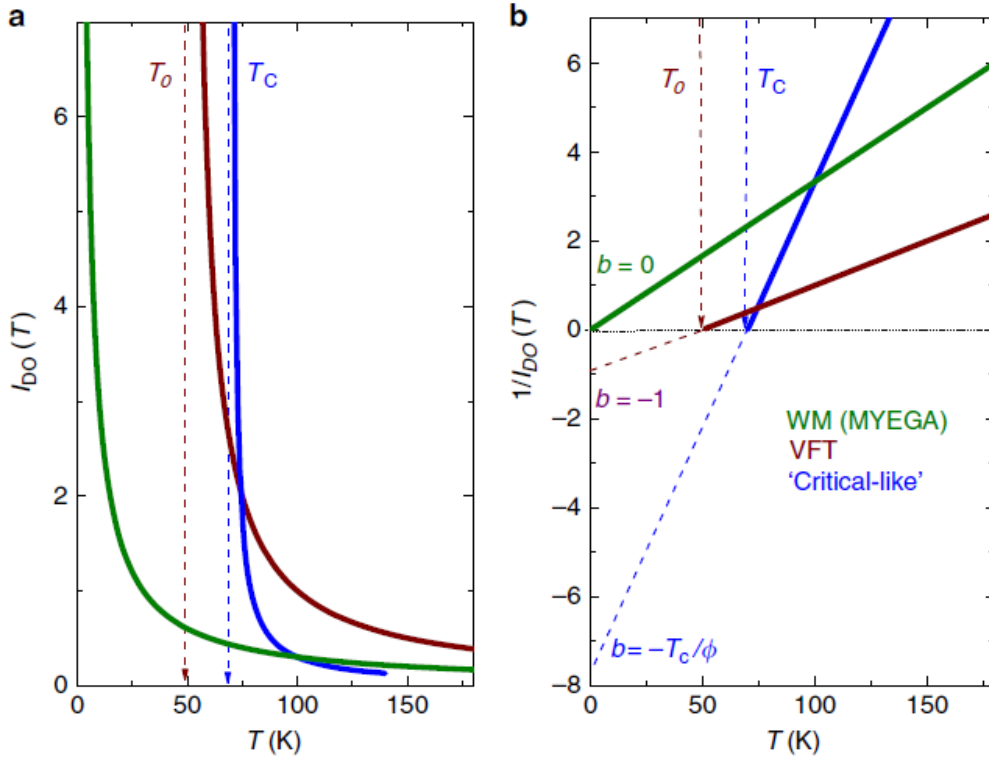


Figure 4.4 – Evolution of  $I_{DO}$  (a) and  $I_{DO}^{-1}$  (b) for different equations for showing the  $\tau(T)$  behavior. The BA equation yields a horizontal line which is omitted here. Figure reproduced from literature [132].

#### 4.1.3.2 Estimation of Model Parameters for Relaxation Time

Once we have determined the correct model for  $\tau$ , we can use the method proposed by Stickel et al. [133] to determine the parameters of that model. A linearized derivative based analysis can be used to present the experimental data. This representation helps to find the valid temperature domain of different theoretical models.

For VFT law, this is done by plotting the factor  $\left[\sqrt{H'_a(T)}\right]^{-1}$  as a function of temperature, where  $H'_a(T)$  is called normalized apparent enthalpy [132] which is given by  $H'_a(T) = \frac{\Delta H_a(T)}{R}$ , where  $\Delta H_a(T)$  is the apparent activation enthalpy (AAH) given in the previous section.

For VFT law, the factor  $\left[\sqrt{H'_a(T)}\right]^{-1}$  is given by the equation [132]:

$$\left[\sqrt{H'_a(T)}\right]^{-1} = \left[\frac{d \ln \tau}{d(1/T)}\right]^{-1/2} = \frac{1}{\sqrt{DT_0}} - \frac{T_0}{T \sqrt{DT_0}} = b - \frac{a}{T} \quad (4.19)$$

Figure 4.5 shows the simulation of the evolution of  $\left[\sqrt{H'_a(T)}\right]^{-1}$  with respect to  $1/T$ . Value of  $T_0$  and B can be calculated from the graph and is given by  $T_0 = a/b$  and  $B = 1/b^2$ .

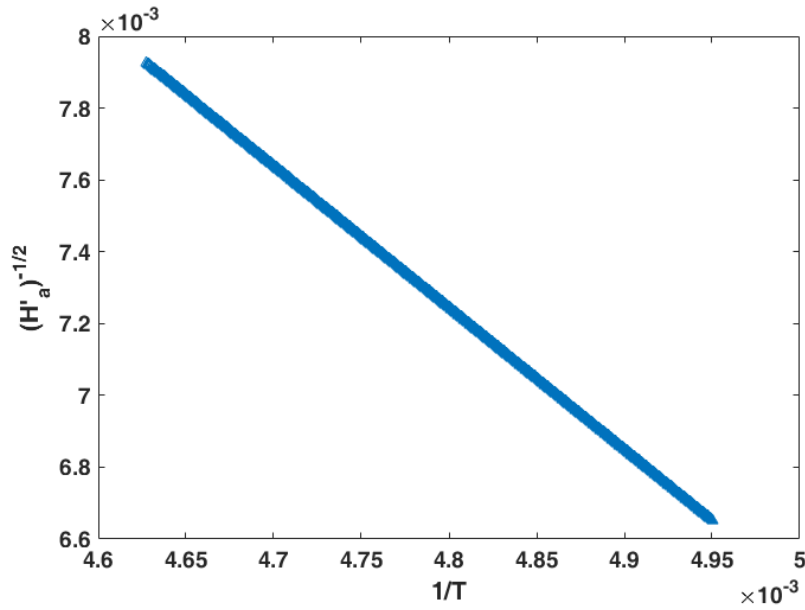


Figure 4.5 – Simulated plot for the evolution of  $\left[\sqrt{H'_a(T)}\right]^{-1}$  with respect to  $1/T$

Similarly, linearized representation can be done for other models also [132]. To improve the precision of the modelization, we can use all the parameters determined using the Wicket fit and the Stickel method as starting values for the "7-parameter fit" which is explained in later sections.

#### 4.1.4 Fragility

Fragility ( $m$ ) is the sensitivity of liquid structure to temperature change and is a dimensionless quantity, given by the expression:

$$m = \left( \frac{d \log(\tau)}{d(T_g/T)} \right)_{T=T_g} \quad (4.20)$$

Once  $T_g$  is determined, we can plot the OLU (Oldekop-Laughlin-Uhlmann-Angell) diagram [134], with  $\log(\tau)$  against  $T_g/T$ . Similarly, OLU diagram can be plotted using viscosity with  $\log(\eta)$  against  $T_g/T$ . An example of OLU plot is shown in figure 4.6.

$m$  is actually the slope of the OLU plot near  $T_g$ . The OLU diagram shows the profile of strong and fragile liquids. Those liquids that obey Arrhenius equation are classified as strong glass formers and those having a stronger deviation from Arrhenius equation (super-Arrhenius) are classified as fragile glass formers.

Using the VFT parameters and  $T_g$ ,  $m$  can be calculated from the following equation which is obtained by taking the derivative of the VFT equation 4.2.

$$m = \left( \frac{D}{\ln 10} \right) \left( \frac{T_0}{T_g} \right) \left( 1 - \frac{T_0}{T_g} \right)^{-2} \quad (4.21)$$

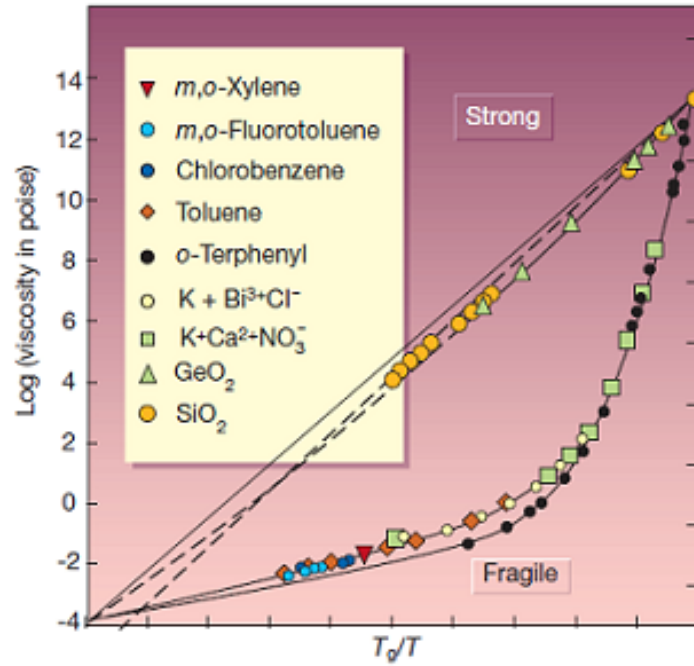


Figure 4.6 – OLU diagram showing strong and fragile liquid profiles from viscosity data, reproduced from literature [50]

Equation 4.21 can be written as:

$$m = \frac{B T_g}{\ln 10 (T_g - T_0)^2} \quad (4.22)$$

The fragility of CPAs like glycerol and 1,2 propanediol are found to be 53 and 52 respectively from literature [69]. It was shown in the literature [135] that value of  $m$  can vary between 16 and 175. But Simon et al. [136] indicated the upper limit for  $m$  as 214. Silica has a fragility value of 28 while poly vinyl chloride has 191. Hence glass formers can be classified according to their  $m$  value [69].

The  $m$  we discussed can be called as the classical fragility. A new fragility parameter,  $M$  has been proposed by Martinez-Garcia et al. [53, 132] which is the ratio between the fundamental process energies at  $T_g$ , given by:

$$M = I_{DO}(T_g) = \left. \frac{d \ln \Delta E_a(T)}{d(T_g/T)} \right|_{T=T_g} = \frac{\Delta H_a(T_g)}{\Delta E_a(T_g)} - 1 \quad (4.23)$$

Hecksher et al. [130] have also reported the relation between  $m$  and  $I_{DO}(T_g)$ . Using equations 4.11, 4.22 and 4.23, they found the relation between the classical fragility,  $m$  and the new one,  $M$  as given by the equation:

$$m = C(1 + M) = C(1 + I_{DO}(T_g)) = C \frac{\Delta H_a(T_g)}{\Delta E_a(T_g)} \quad (4.24)$$

where  $C$  is a constant:  $C = 2 - \log(\tau_\infty)$  and can take values in the range  $13 \leq C \leq 18$ . Temperature evolution of the ratio of apparent activation energy and enthalpy can be studied alongside the OLU plot. This provides a comparison between the classical fragility,  $m$  and the new fragility,  $M$  metrics. An example is shown in figure 4.7.

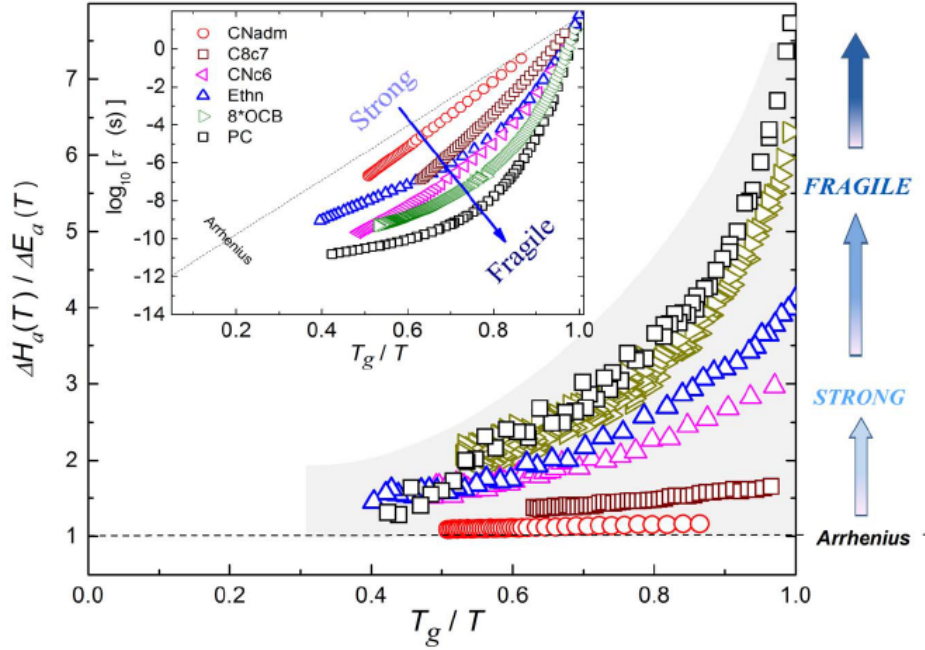


Figure 4.7 – The evolution of the ratio between the apparent activation enthalpy and energy for selected glass forming systems. Figure reproduced from literature [53].

The coming sections discuss the analysis of the PPE experimental data from different samples using the protocol described above.

## 4.2 Low Temperature PPE: Results and Discussion

In this section we discuss about analysis of PPE experimental data for different samples using the protocol presented above. We have used the FPPE configuration with a semi transparent sensor, where the sensor/sample (p-s) interface was illuminated and the modulating frequency for LED and the thickness of both sensor and sample were chosen to satisfy thermally thick condition as given in equation 2.28. Since it was important to validate the accuracy and precision of our experimental results we started with pure samples whose information are already reported in many literatures. For low temperature PPE experiments, the quantity of sample used was  $600\mu l$  which gave a thickness of 5mm to the sample and satisfied the thermally thick sample condition.

## 4.2.1 Pure Glycerol

Glycerol is a well known CPA which has been studied widely and still a material of interests among cryo scientists and glass scientists [17, 23, 24, 27, 137]. Pure glycerol was placed in the sample compartment and cooled to  $-196\text{ }^{\circ}\text{C}$  at a rate of  $6\text{ }^{\circ}\text{C min}^{-1}$  and heated at a rate of approximately  $1\text{ }^{\circ}\text{C min}^{-1}$ . Data acquisition was done at every second while heating. No data acquisition was done while cooling. For normalization, it was important to perform an experiment without sample and this must be performed prior to the one with sample so that sample could be added without displacing the sensor.

### 4.2.1.1 Results at 22Hz

Although it is known that  $\tau$  for glycerol is defined by VFT, we use glycerol to explain the protocol for finding the exact model for defining the temperature dependence of  $\tau$ . We consider the experiment done at a fixed frequency of 22 Hz for explaining the protocol. The normalized amplitude and phase of pure glycerol at a frequency of 22 Hz is shown in figure 4.8.

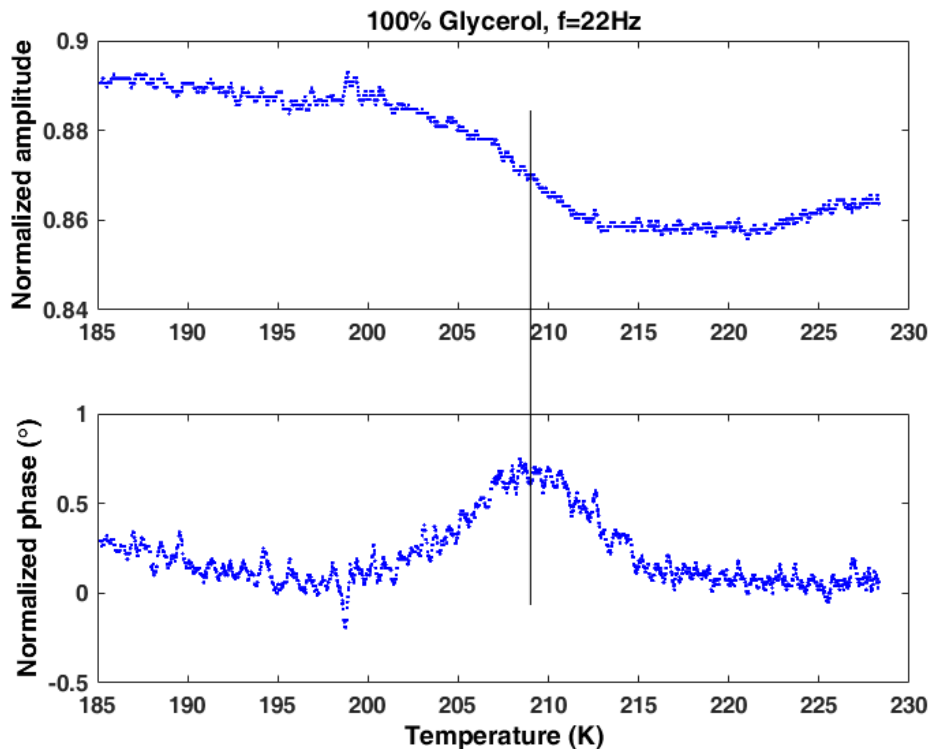


Figure 4.8 – Normalized amplitude and phase of pure glycerol during a temperature scan at a fixed frequency of 22 Hz using a  $500\text{ }\mu\text{m LiTaO}_3$  as sensor

The relaxation was observed in both amplitude and phase of the signal as explained earlier. The amplitude suffered a drop and phase attained a peak and relaxed during the  $\alpha$  relaxation. The temperature at the point of inflection in the amplitude and maximum of the phase corresponded.

Using equation 2.28, the squared effusivity of pure glycerol as a function of temperature was calculated. The temperature evolution of its real and imaginary parts is shown in figure 4.9. The relaxation of heat capacity can be observed in this graph in both real and imaginary parts.

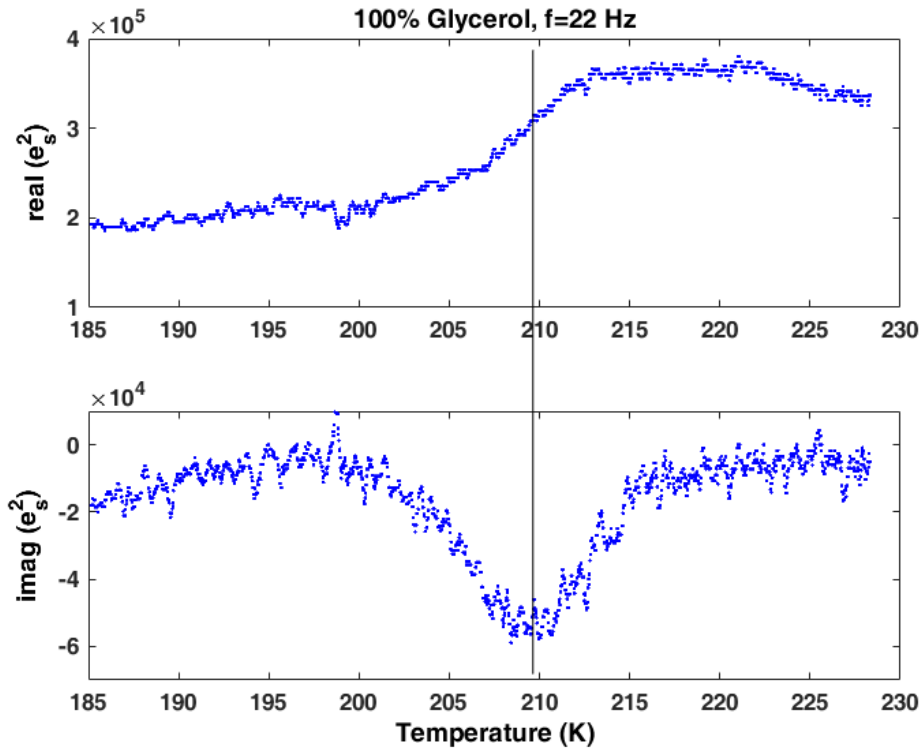


Figure 4.9 – Real and imaginary parts of squared effusivity versus temperature for pure glycerol

#### 4.2.1.1.1 Estimation of Parameters: $\alpha, \beta, E_\infty, \Delta E$

Using real and imaginary parts of  $e^2$ , we plotted the Wicket plot. Fitting the Wicket plot facilitated the determination of the HN parameters. Fitting was done using the "trust region reflective" algorithm in Matlab software. The figure 4.10 shows the fitted Wicket plot for pure glycerol at 22 Hz frequency. The best fitted curve is visible in the figure. Although experimental data was noisy, the program was able to find the best fitted parameters which are presented in table 4.1.

| frequency (Hz) | $\alpha$ | $\beta$ | $E_\infty$ | $\Delta E$ |
|----------------|----------|---------|------------|------------|
| 22             | 1        | 0.52    | 212920     | 146570     |

Table 4.1 – Best fitted data from Wicket plot for pure glycerol using Havriliak-Negami model

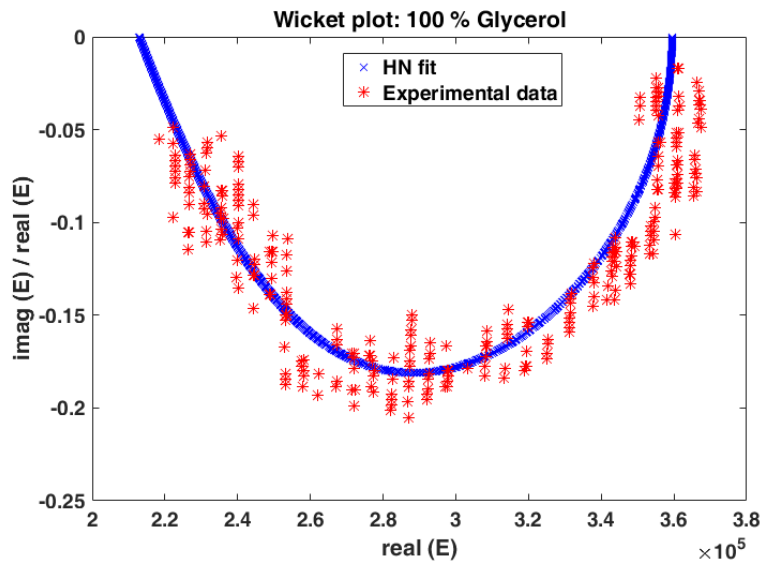


Figure 4.10 – Fitted Wicket plot for pure glycerol at frequency of 22 Hz

#### 4.2.1.1.2 Choosing the Model for Relaxation Time

Using the fitted parameters in the table 4.1, the relaxation time  $\tau$  was calculated from equation 4.8 (Direct method) and is shown in figure 4.11. Raw data has been used for determining  $\tau$ . The calculated value was complex in nature. The imaginary part was negligible. This shows that  $\tau$  was real as expected. Therefore, only the real part is considered here.

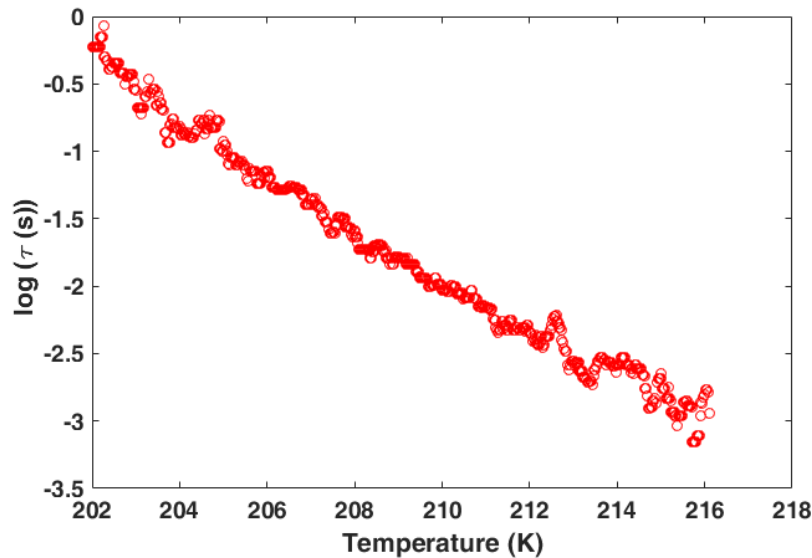


Figure 4.11 – Relaxation time for pure glycerol at frequency 22 Hz calculated using Direct method (equation 4.8) (from HN equation using the  $\alpha$ ,  $\beta$ ,  $E_0$ ,  $E_\infty$  and complex modulus( $E^*$ ))

AE was calculated from the determined  $\tau$  by using the equation 4.10 and is shown in figure 4.12. The value of  $\tau_\infty$  used was  $10^{-14}$  s, which is often considered as the universal value [132].

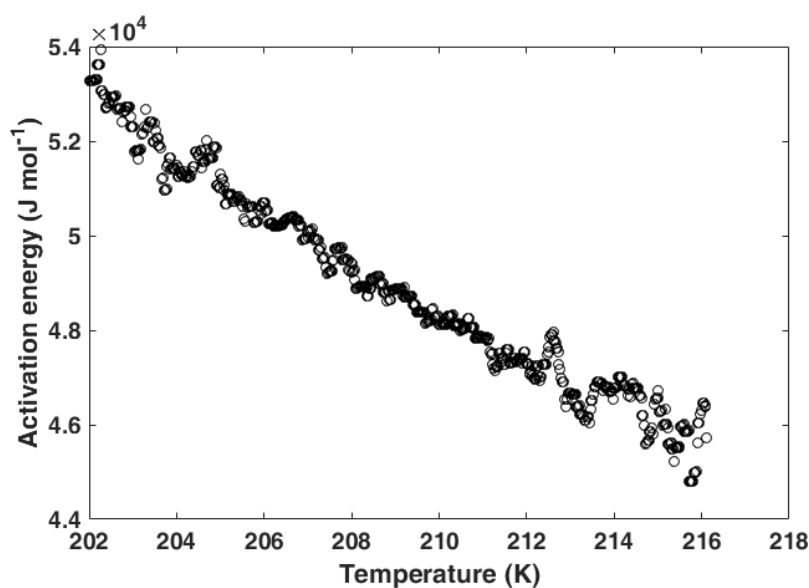


Figure 4.12 – AE for pure glycerol at frequency 22 Hz

The Dyre-Olsen index ( $I_{DO}$ ) was calculated from equation 4.11. The derivative taken from the raw data was so noisy that we couldn't obtain the information. So we used Savitzky-Golay (SG) filter for smoothing the data. The SG filter provides a better signal to noise ratio without greatly distorting the signal and is widely applied in data analysis. Figure 4.13 shows the comparison between the raw data and smooth data using SG filter. It can be observed that SG filter provides efficient smoothing of the raw data which was used for the calculation of  $I_{DO}$  index.

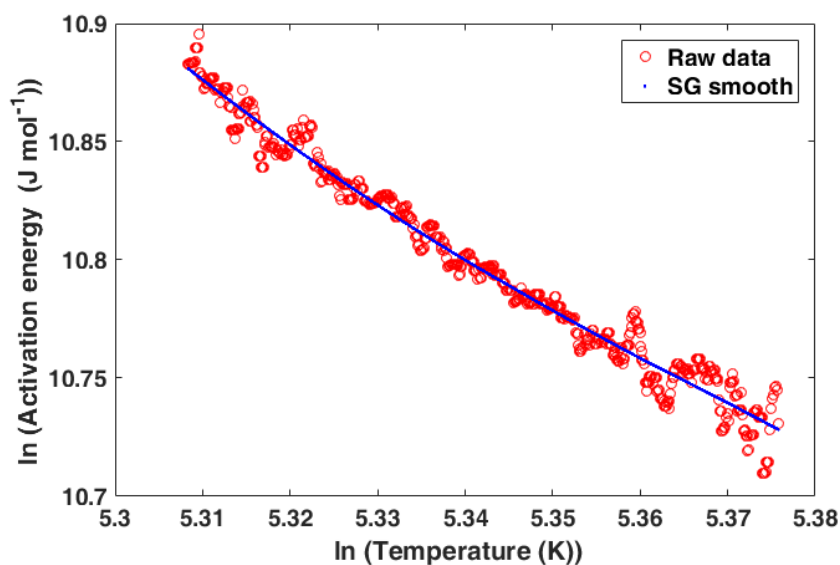


Figure 4.13 – Comparison between raw data and SG filtered data in log scale

Temperature evolution of the  $I_{DO}^{-1}$  is plotted which is shown in figure 4.14. This graph helps to determine the model for the temperature dependence of  $\tau$ .

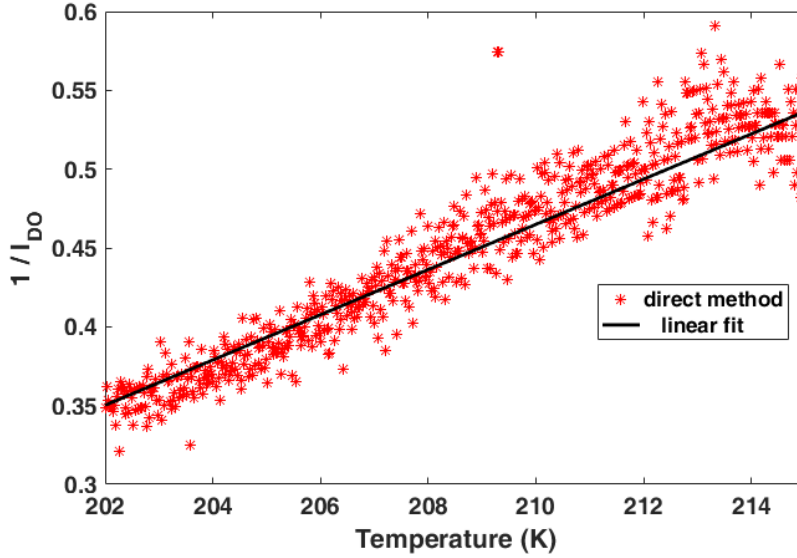


Figure 4.14 – Temperature evolution of the  $I_{DO}^{-1}$  for pure glycerol. Equation of the linear regression is given by  $I_{DO}^{-1} = 0.01434 T - 2.547$

From the linear representation,  $I_{DO}^{-1} = mT + c$ , we obtained the value of  $c = -2.5$ . We can eliminate the possibility of MYEGA model which requires  $c=0$  and BA which gives a horizontal line at a constant  $(1/(D-1))$ . The other possibilities are VFT or Critical-like model. To check if it matches with the Critical-like model, we calculated  $T_C$  and  $\phi$  and found to be 177K and 70 respectively. The value of  $\phi$  was reported as 9-15 [132] which clearly states that pure glycerol doesn't follow Critical-like model. However, we tried to fit the real and imaginary raw data with the Critical-like model using the calculated  $T_C$  and  $\phi$  as starting parameters. The fit was impossible as expected. Therefore, the model to be considered is the VFT model which requires  $c = -1$  and approximately matches with our result. Thus, we can use this method as a standard protocol to find the exact model for the temperature dependence of  $\tau$  for different samples.

#### 4.2.1.1.3 Estimation of Model Parameters for Relaxation Time

For the VFT parameters, we can obtain  $B$  and  $T_0$  from the apparent activation enthalpy (AAH) via the linearized derivative based analysis [133]. AAH was calculated from the relaxation time  $\tau$  using equation 4.13. The quantity  $1/\sqrt{H'_a}$ , calculated directly from  $\tau$  using the HN parameters from the Wicket fit is plotted against  $1/T$  as shown in figure 4.15. A deviation from a linear profile happened due to experimental noise but could be still fitted with a line as shown in the same figure. The value of  $B$  and  $T_0$  were determined from the linear equation,  $\sqrt{H'_a}^{-1/2} 10^3 = -3932/T + 25.945$  and was obtained as  $B = 1485.56$  K and  $T_0 = 151.55$  K.

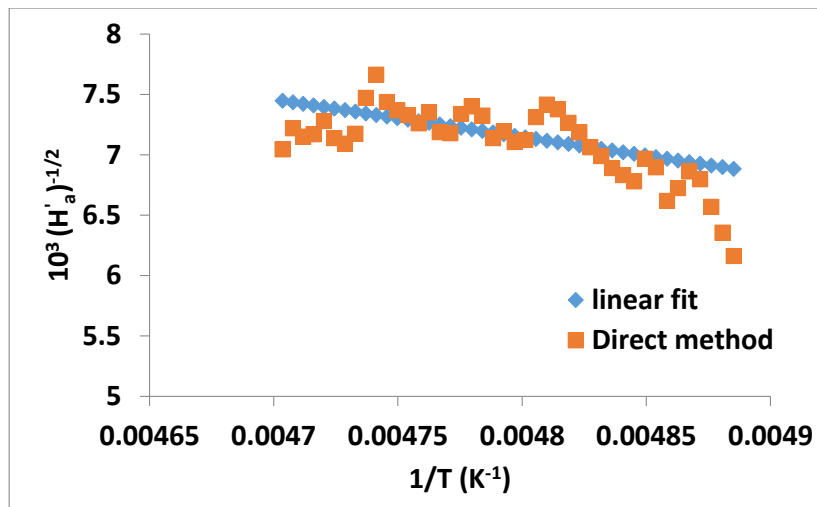


Figure 4.15 – The inverse of the square root of AAH ( $1/\sqrt{H'_a}$ ) plotted against  $1/T$  for pure glycerol

#### 4.2.1.1.4 7-Parameter Fit

The protocol explained earlier can find the correct model for  $\tau$ . One can use that model for defining the temperature dependence of  $\tau$  in the HN equation (4.7). In our case, we used VFT equation for  $\tau$  in the HN equation and fitted the temperature evolution of real and imaginary parts of  $e^2$  for determining 7 parameters (4 HN and 3 VFT parameters). The fit is called as "7-parameter fit". But for the program to find the best fit values, it was very important to set proper initial parameters.

Generally in the VFT equation, the value of  $\tau_\infty$  is chosen between  $10^{-11}$  s and  $10^{-16}$  s [64]. But a wrong assumption can seriously affect the end result. During 7-parameter fit, we didn't fix the value of  $\tau_\infty$ . Instead, we freely fitted  $\tau_\infty$  just like other parameters. Therefore, the parameters we fitted were  $\alpha$ ,  $\beta$ ,  $E_0$ ,  $\Delta E$ ,  $B$ ,  $T_0$  and  $\tau_\infty$ .

The initial values used are shown in table 4.2:

| -             | $\alpha$ | $\beta$ | $E_\infty$ | $\Delta E$ | B (K) | $T_0$ (K) | $\tau_\infty$ (s) |
|---------------|----------|---------|------------|------------|-------|-----------|-------------------|
| Initial value | 0.8      | 0.6     | 200000     | 150000     | 1485  | 151       | $10^{-14}$        |

Table 4.2 – Initial values used for HN and VFT parameters for 7-parameter fit

For the fit, only the  $\alpha$  relaxation region was considered. Figure 4.16 shows the best fitted real and imaginary parts of  $e^2$ . The circular legend represents the experimental data and the smooth one represents the best fitted curve.

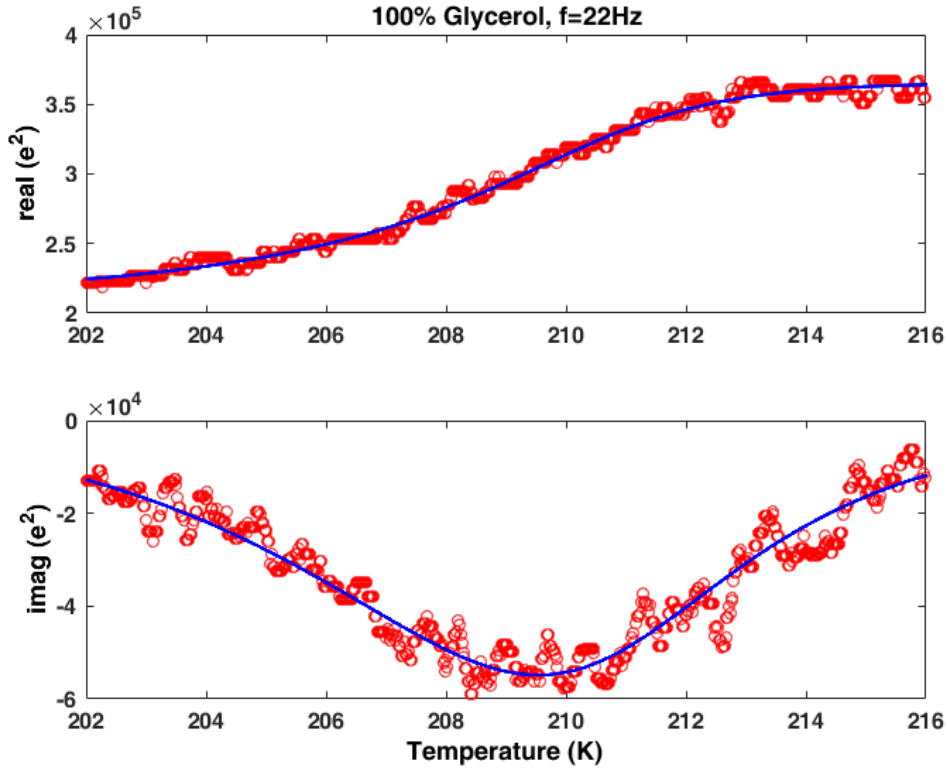


Figure 4.16 – Fitting done on the real and imaginary parts of squared effusivity versus temperature for pure glycerol using Havriliak-Negami model and 7-parameter fit

The best fitted values are shown in table 4.3:

| method          | $\alpha$ | $\beta$ | $E_{\infty}$ | $\Delta E$ | B (K) | $T_0$ (K) | $\tau_{\infty}$ (s) |
|-----------------|----------|---------|--------------|------------|-------|-----------|---------------------|
| Wicket fit      | 1        | 0.52    | 212920       | 146570     | -     | -         | -                   |
| 7-parameter fit | 0.98     | 0.52    | 212178       | 153545     | 1457  | 151       | $10^{-12.6735}$     |

Table 4.3 – Fitted HN and VFT parameters from 7-parameter fit and comparison of HN parameters with Wicket fit

The results from 7-parameter fit are in good agreement with the Wicket fit. Also the VFT parameters, especially  $\tau_{\infty}$ , can be determined.

Figure 4.17 shows the comparison of AE calculated using different values for  $\tau_{\infty}$ . The black curve denotes the AE corresponds to  $\tau_{\infty} = 10^{-14}$  s while the red curve corresponds to  $\tau_{\infty} = 10^{-12.6735}$  s, which is the fitted value from 7-parameter fit. The blue curve is simulated using VFT equation. It is very important to use the exact value for  $\tau_{\infty}$  instead of a rounded value because the rounding error can affect the AE. Therefore, we can say that the 7-parameter fit gives a better and precise result for the value of  $\tau_{\infty}$ .

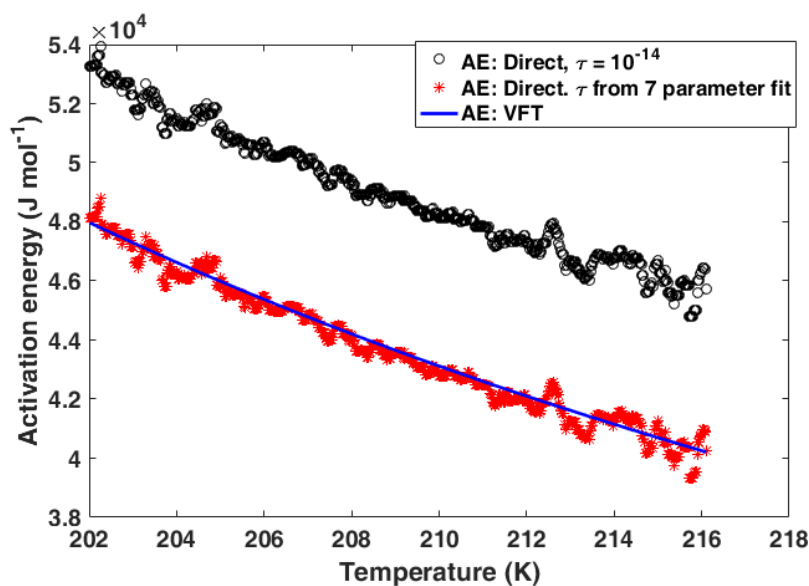


Figure 4.17 – Comparison of AE for pure glycerol calculated from different methods

The  $I_{DO}$  index was calculated using the AE from VFT.  $I_{DO}$  serves as the alternative metric of fragility [132]. Figure 4.18 shows the temperature evolution of  $I_{DO}$  index.

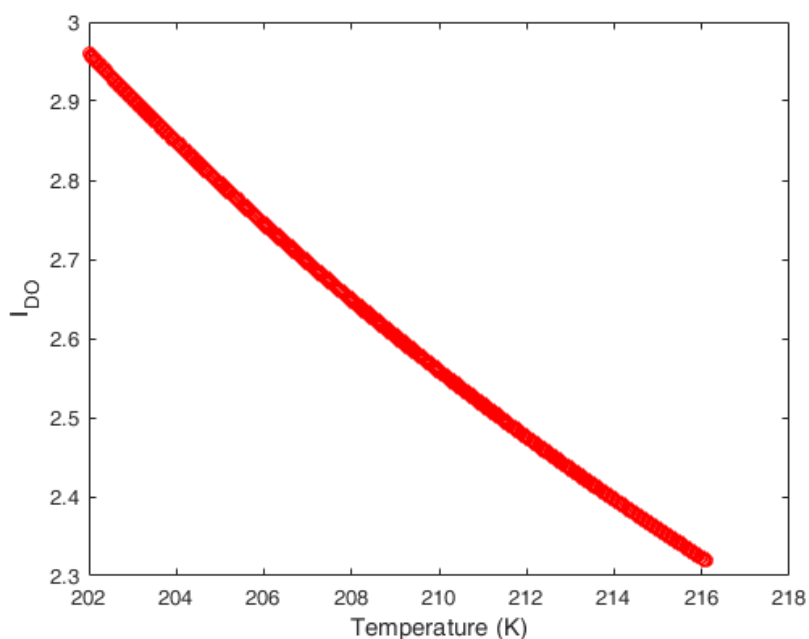


Figure 4.18 –  $I_{DO}$  index calculated using the AE from VFT parameters for pure glycerol

The Wicket plot and the Cole-Cole plot were plotted from the experimental data at 22 Hz frequency as shown in figure 4.19 and 4.20 respectively. To verify our fit, these plots were simulated with the 7-parameter fitted HN parameters given in the table 4.3 and compared with the experimental data. It can be observed clearly that the simulated curve followed the experimental data stating our fit was good despite the noisy experimental data .

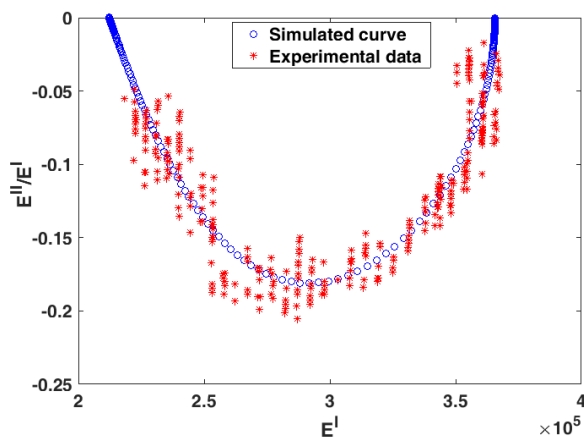


Figure 4.19 – Wicket plot for pure glycerol at frequency of 22 Hz

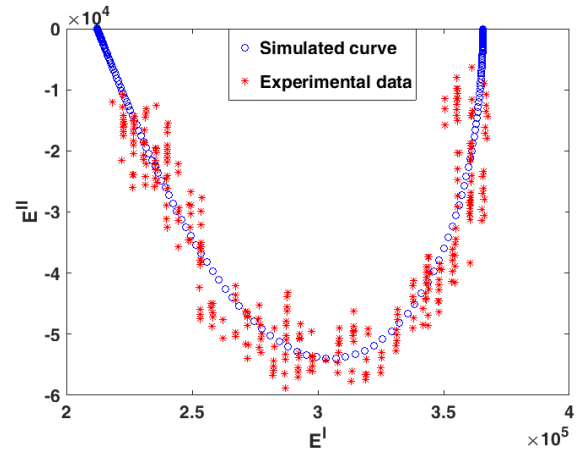


Figure 4.20 – Cole-Cole plot for pure glycerol at frequency of 22 Hz

#### 4.2.1.1.5 Fragility and Dyre-Olsen Index

Using the VFT parameters,  $T_g$  can be calculated using the glass transition convention  $T = T_g$  when  $\tau=100$  s and  $m$  using the equation 4.22. The  $I_{DO}$  at  $T = T_g$  gives the new fragility,  $M$ . We can also determine  $m$  from  $M$  using the equation 4.24. Table 4.4 shows the  $T_g$ ,  $m$  and  $M$  for pure glycerol from the PPE experiment at 22 Hz.

| $T_g$ (K) | $m$   | $M$  |
|-----------|-------|------|
| 193.80    | 65.98 | 3.49 |

Table 4.4 –  $T_g$ ,  $m$  and  $M$  for pure glycerol from the PPE experiment at 22 Hz

Thus the relationship between the classical and new fragility parameters was studied from this analysis. The relationship between apparent activation enthalpy and apparent activation energy was also studied from  $I_{DO}$  using equation 4.12. Figure 4.21 shows the evolution of the ratio between these two quantities.

#### 4.2.1.2 Other Frequencies

The same procedure was applied for the experimental data from other frequencies. In a similar fashion, temperature scans at different fixed frequencies, say, 120 Hz, 360 Hz and 1100Hz were performed. The normalized amplitude and phase of temperature scans at different frequencies (22Hz, 120Hz, 360Hz, 1100Hz) performed are shown in figure 4.22. Considering the easiness of representation, all normalized amplitude curves are moved to 1 and all normalized phase curves are moved to 0 at 235 K.

Relaxation happened during temperature scans at different frequencies can be observed in figure 4.22. It is evident that the peak in the phase moves to higher temperature as the scanning frequency is increased, as observed by other researchers [114] and in the simulation shown in figure 4.2.

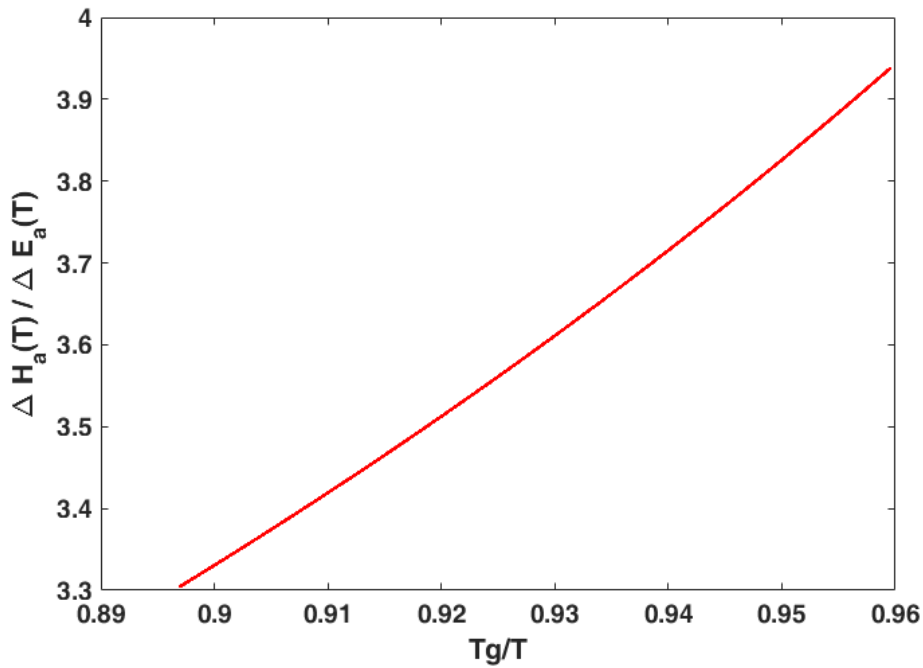


Figure 4.21 – Evolution of the ratio between the apparent activation enthalpy and energy for pure glycerol

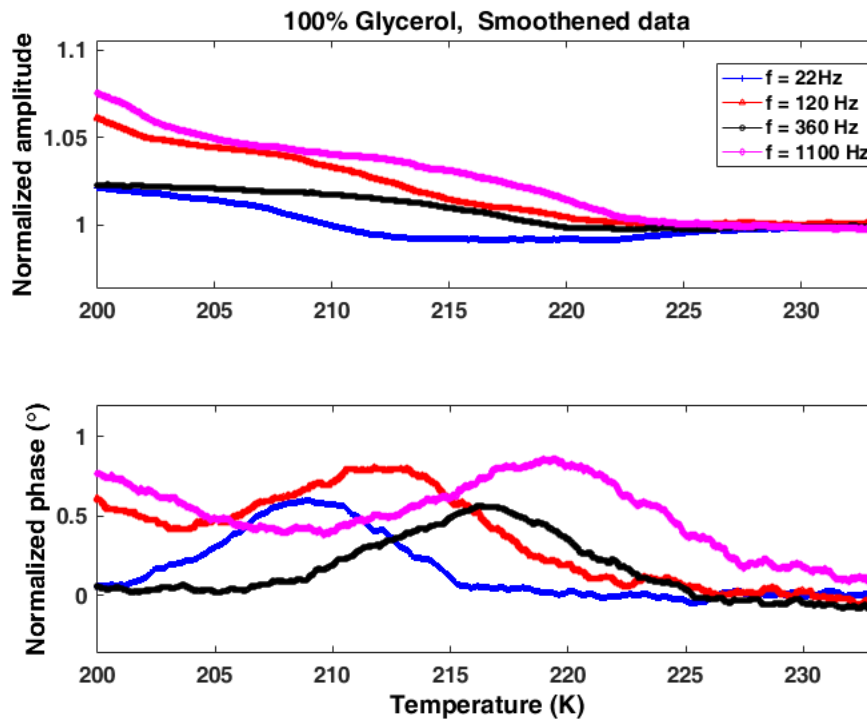


Figure 4.22 – Normalized amplitude and phase of pure glycerol during a temperature scan at different frequencies using a  $500 \mu\text{m}$   $\text{LiTaO}_3$  as sensor

From each frequency data, it was found from the temperature evolution of  $I_{DO}^{-1}$  that glycerol followed VFT model. We have performed the 7-parameter fit on each frequency data and the

best fitted parameters are given in table 4.5.

| Frequency (Hz) | $\alpha$ | $\beta$ | $E_\infty$ | $\Delta E$ | B (K) | $T_0$ (K) | $\tau_\infty$ (s) |
|----------------|----------|---------|------------|------------|-------|-----------|-------------------|
| 120            | 1.00     | 0.27    | 242098     | 295508     | 1855  | 151       | $10^{-15.3081}$   |
| 360            | 1.00     | 0.41    | 137347     | 100673     | 1775  | 138       | $10^{-12.8297}$   |
| 1100           | 0.96     | 0.29    | 245387     | 326958     | 1205  | 169       | $10^{-13.5382}$   |

Table 4.5 – 7-parameter best fitted HN and VFT parameters from different frequency data for pure glycerol

Using the fitted VFT parameters in equation 4.19, the factor  $\left[\sqrt{H'_a(T)}\right]^{-1}$  was calculated for each frequencies. Average value of B and  $T_0$  was determined from the slope of the evolution of mean  $\left[\sqrt{H'_a(T)}\right]^{-1}$  with respect to inverse temperature. Also the average value of  $\tau_\infty$  was calculated from all frequencies. Using these average values,  $\tau$  was calculated for pure glycerol using VFT equation 4.2. The figure 4.23 shows the temperature evolution of  $\tau$  for pure glycerol. This result is in good agreement with results from Hecksher et al. [130].

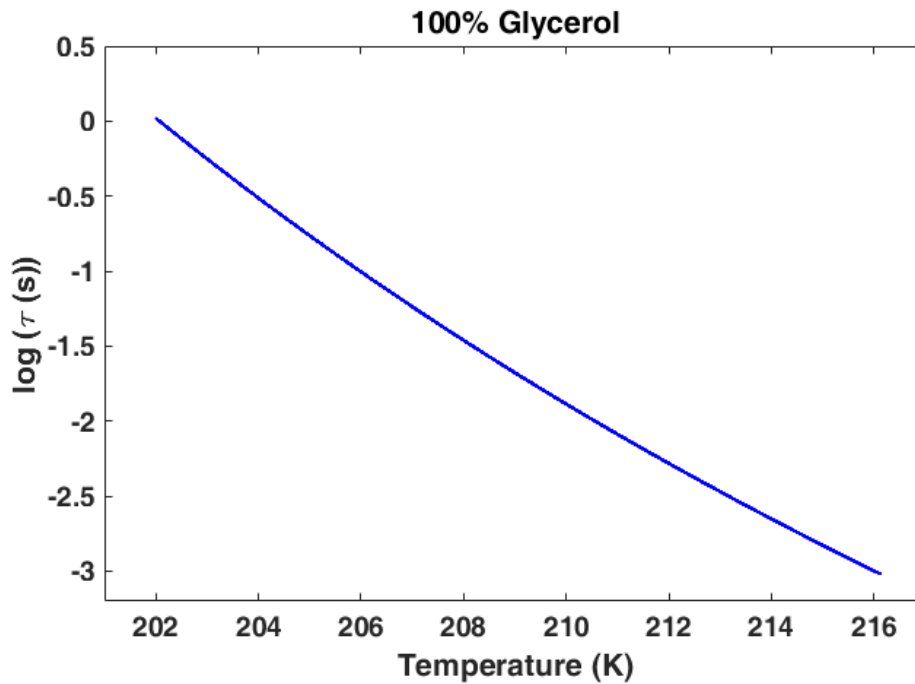


Figure 4.23 – Relaxation time as a function of temperature for pure glycerol

Likewise, average AE was calculated using mean B and  $T_0$ . The uncertainty of result has been determined as  $\pm 17\%$ . We have also determined the AE using B and  $T_0$  from some literatures and all the results are within our error limit. The figure 4.24 shows the mean AE alongside the AE from other frequencies and literatures.

Average values of m, M and  $T_g$  were determined from the mean B and  $T_0$ . Table 4.6 shows the  $T_g$ , m and M for pure glycerol and their reported literature data. The reported value of  $T_g$  has 3% error from the calculated value, which is within the error limit of the experiment. Reported value of m is also within the error limit of our experimental result.

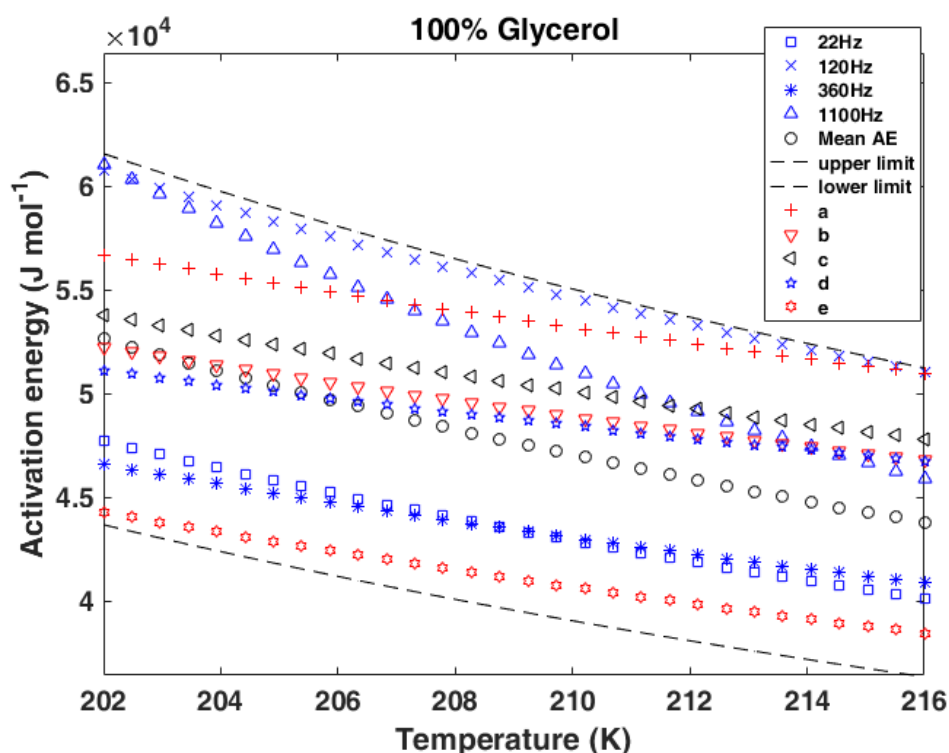


Figure 4.24 – Activation energy as a function of temperature for pure glycerol. AE from all frequencies are plotted with the upper and lower uncertainty limit. AE calculated from literatures are plotted for comparison. a: [114], b: [138], c: [73], d: [127], e: [74]

| $T_g$ (K) mean (PPE) | $T_g$ (K) (literature)   | m (PPE) mean | m (literature)   | M    |
|----------------------|--|--------------|--|------|
| 195 +/- 6            | 190 <sup>a</sup> , 191 <sup>b</sup> , 183.4 <sup>c</sup><br>191.4 <sup>d</sup> , 187 <sup>e</sup> , 195.4 $\pm$ 0.2 <sup>f</sup> | 71 +/- 20    | 53 <sup>a</sup> , 78 <sup>b</sup><br>52.3 <sup>e</sup> | 3.56 |

Table 4.6 –  $T_g$ , m and M of pure glycerol and their comparison with literature data, a:[69], b:[139], c:[127], d: [97], e: [99], f: [137]

## 4.2.2 Pure 1,2 Propanediol

Alike glycerol, we have studied pure 1,2 propanediol to understand the  $\alpha$  relaxation process during cooling to subzero temperature. It is also a well known CPA [24] which is widely used in industries. The procedures followed for pure glycerol were used to analyse the data for 1,2 propanediol. The normalized amplitude and phase of the PPE signal for a temperature scan at fixed frequency of 360 Hz is shown in figure 4.25. The amplitude and phase showed the relaxation in a range of temperature. The temperature at the point of inflection in amplitude and peak in the phase matched, like we have seen earlier in glycerol.

Using equation 2.28, the effusivity of 1,2 propanediol as a function of temperature was calculated from experimental data. The real and imaginary parts of squared effusivity was taken and the Wicket plot was fitted to find the HN parameters.  $\tau$  and AE were calculated using equations 4.8 and 4.10 respectively. To determine the dependence of  $\tau$ , temperature evolution of  $I_{DO}^{-1}$  was studied which is shown in the figure 4.26.

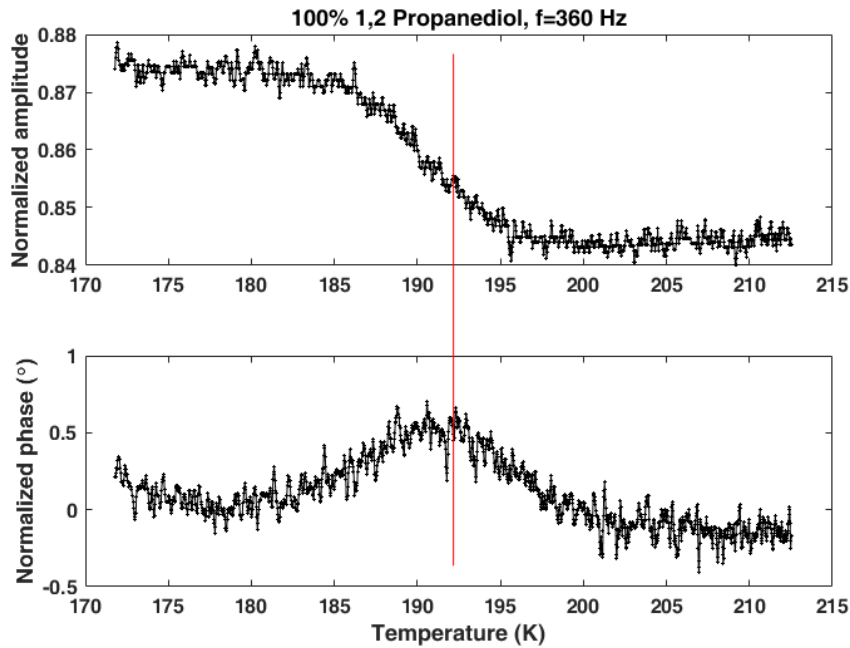


Figure 4.25 – Normalized amplitude and phase of pure 1,2 propanediol during a temperature scan at a fixed frequency of 360 Hz using a  $500 \mu m$   $LiTaO_3$  as sensor

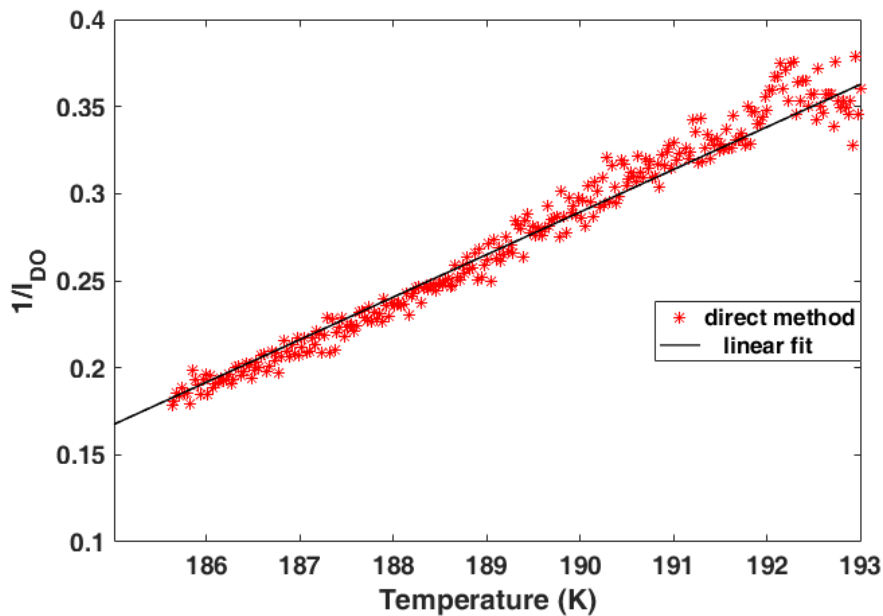


Figure 4.26 – Temperature evolution of the  $I_{DO}^{-1}$  for pure 1,2 propanediol. Equation of the linear regression is given by  $I_{DO}^{-1} = 0.02443 T - 4.3523$

From the linear representation,  $I_{DO}^{-1} = mT + c$ , we obtained the value of  $c = -4.352$ . We could eliminate the possibility of MYEGA model which requires  $c=0$  and BA which should give a horizontal line at a constant ( $1/(D-1)$ ). The other possibilities were VFT or Critical-like model. From the analysis of  $T_C$  and  $\phi$ , we could eliminate the possibility of Critical-like model. Therefore, we found that  $\tau$  for pure 1,2 propanediol followed VFT model, as expected [127].

To calculate  $T_g$  and  $m$ , the VFT parameters must be determined. This was done using the 7-parameter fit. The region of  $\alpha$  relaxation was chosen for the fit. The initial values needed for obtaining the best fit parameters were taken from the Wicket fit and from the linearized derivative based analysis ( $[\sqrt{H'_a(T)}]^{-1}$  vs  $1/T$ ). The VFT equation was used for  $\tau$  in HN equation and the real and imaginary parts were fitted using the 7-parameter fit which is shown in figure 4.27.

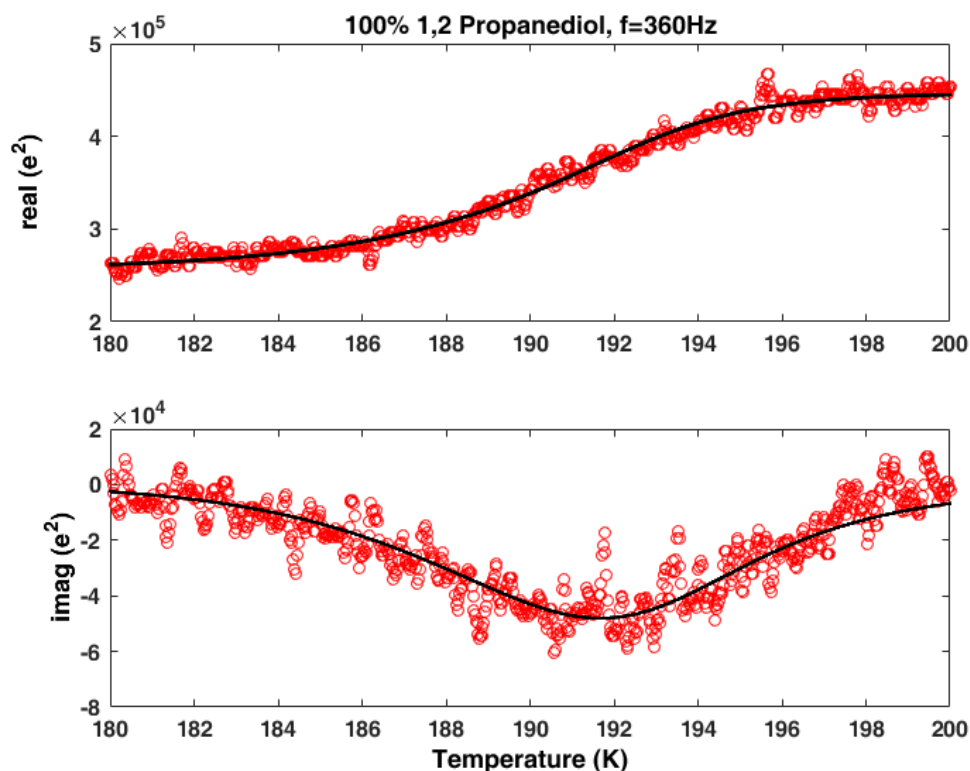


Figure 4.27 – Fitting done on the real and imaginary parts of squared effusivity versus temperature for pure 1,2 propanediol using Havriliak-Negami model

Table 4.7 shows the best fitted HN and VFT parameters from all the frequencies.

| frequency (Hz) | $\alpha$ | $\beta$ | $N_\infty$ | $\Delta N$ | B (K) | $T_0$ (K) | $\tau_\infty$ (s) |
|----------------|----------|---------|------------|------------|-------|-----------|-------------------|
| 22             | 1        | 0.41    | 243708     | 90313      | 1166  | 138       | $10^{-12.2849}$   |
| 120            | 1        | 0.393   | 302333     | 167683     | 1548  | 129       | $10^{-13.6382}$   |
| 360            | 0.778    | 0.483   | 258093     | 189905     | 1142  | 147       | $10^{-14.1308}$   |
| 1100           | 0.974    | 0.40    | 528614     | 277929     | 1540  | 128       | $10^{-13.4385}$   |

Table 4.7 – Best fitted HN and VFT parameters of pure 1,2 propanediol

Goodness of the 7-parameter fit was verified using simulated Wicket and Cole-Cole plot alongside the experimental data which is shown in figures 4.28 and 4.29 respectively. The simulated curve followed the same trend as the experimental curve showing that the best fit parameters are good.  $T_g$ ,  $m$  and  $M$  values were calculated from mean B and  $T_0$  and is compared with literatures which are presented in table 4.8.

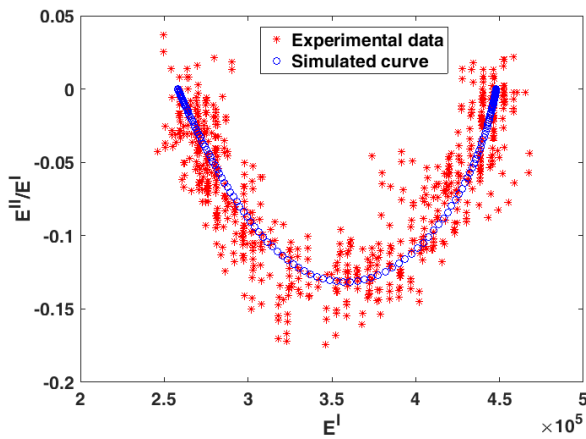


Figure 4.28 – Wicket plot for pure 1,2 propanediol at frequency of 360 Hz

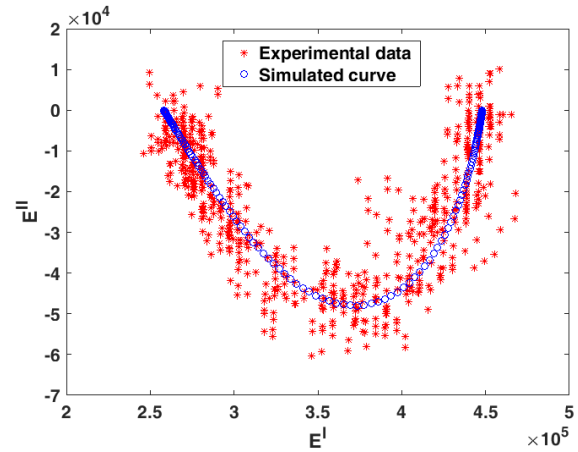


Figure 4.29 – Cole-Cole plot for pure 1,2 propanediol at frequency of 360 Hz

| $T_g$ (K) (PPE) | $T_g$ (K) (literature)  | m (PPE)   | m (literature)                    | M   |
|-----------------|---|-----------|-----------------------------------|-----|
| 173 +/- 3       | 167 <sup>a</sup> , 164 <sup>b</sup><br>162.4 <sup>c</sup> , 166.01 <sup>d</sup> | 71 +/- 16 | 52 <sup>a</sup> , 45 <sup>b</sup> | 3.6 |

Table 4.8 –  $T_g$ , m and M of pure 1,2 propanediol and their comparison with literature data, a: [69], b: [139], c: [127], d: [98]

### 4.2.3 Binary Mixtures

Studying the aqueous solutions of CPA is very important to understand their actions in cryopreservation because of the presence of water in living cells. Some literatures reported the study on aqueous solutions of glycerol [26] and 1,2 propanediol [96], mainly about their  $T_g$  [97, 98] but only one has reported on their fragility [99]. These studies were performed using DSC and dielectric techniques and no PPE results were found on these samples. Therefore, we have done PPE measurements on some of the aqueous solutions of glycerol and 1,2 propanediol at low temperature to understand the effect of water concentration in their glass forming property.

The mixtures were prepared as mentioned in chapter three. Once prepared, they were kept on a vibrator to keep them agitated to avoid any separation into individual liquid.

Binary mixtures of glycerol-water and 1,2 propanediol-water were studied using low temperature PPE technique. The samples we have studied were 90 wt%, 80 wt% and 70 wt% glycerol-water binary solutions and 93.13 wt% and 70 wt% 1,2 propanediol-water binary solutions. The choice of these concentrations can be explained from the phase diagrams. Figure 4.30 shows the phase diagram of glycerol-water system. Freezing curve starts just below 70 wt% glycerol, i.e, crystallization of water starts below this concentration.

Similarly, figure 4.31 shows the phase diagram of 1,2 propanediol-water system. It can be observed that crystallization starts near 50 wt% 1,2 propanediol. Therefore, we have chosen mixtures in higher concentrations for the study.

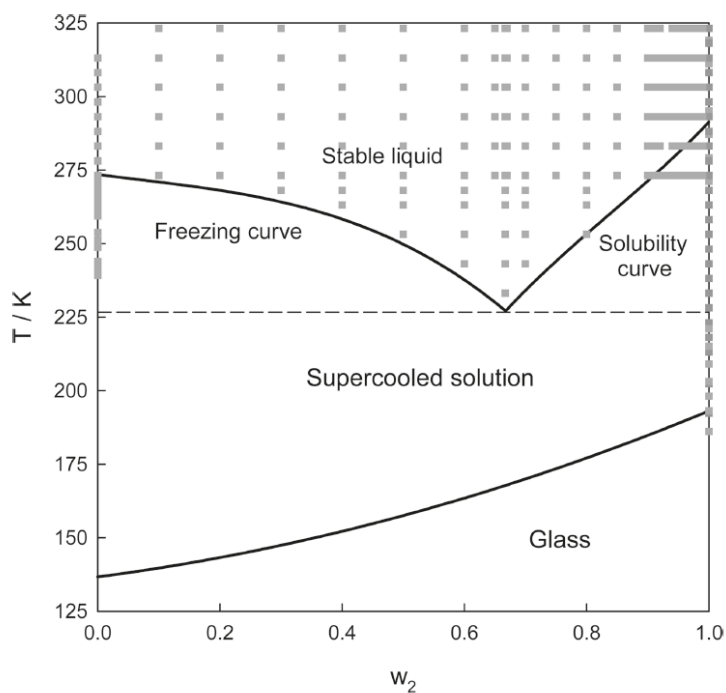


Figure 4.30 – Phase diagram of the glycerol-water system, reproduced from literature [137]

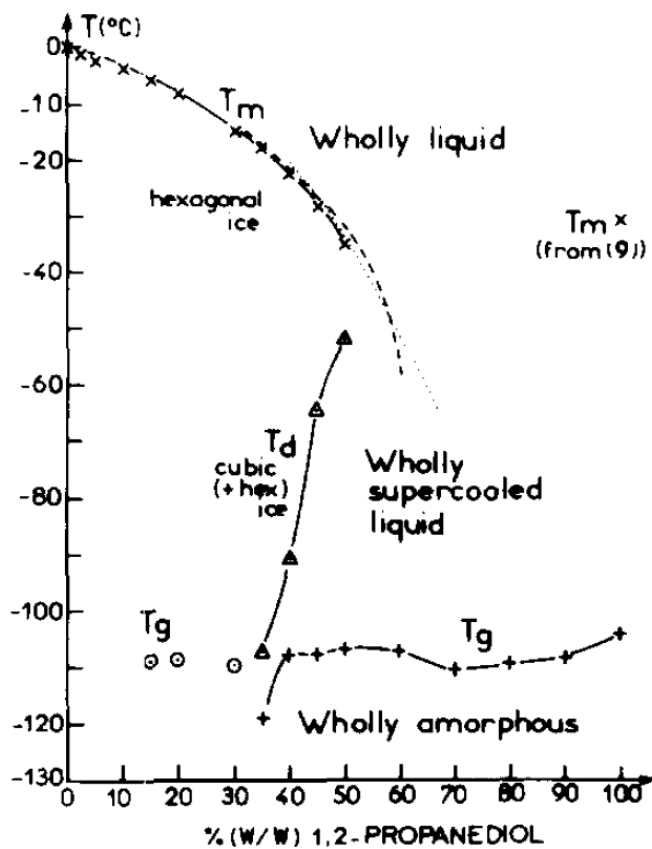


Figure 4.31 – Phase diagram of the system 1,2 propanediol-water, reproduced from literature [96]

The following subsections show the PPE experimental data of studied samples and treatment of data using 7-parameter fit. The fitted parameters and the results obtained for  $T_g$  and  $m$  and their comparison with literature are given in separate tables.

#### 4.2.3.1 90 wt% Glycerol-Water Mixture

The first binary solution we have studied was 90 wt% glycerol-water mixture. The preparation of binary solution has been discussed in chapter 3. The measured quantity of sample was placed in the PPE cell and a temperature scan was performed at a fixed frequency. Figure 4.32 shows the temperature scan of 90 wt% glycerol-water binary mixture at 360 Hz frequency. The relaxation was observed in both amplitude and phase of the signal. The amplitude suffered a drop and phase attained a peak and relaxed during the glass transition as we have seen in pure glycerol. The temperature at the point of inflection in the amplitude and maximum of the phase corresponded.

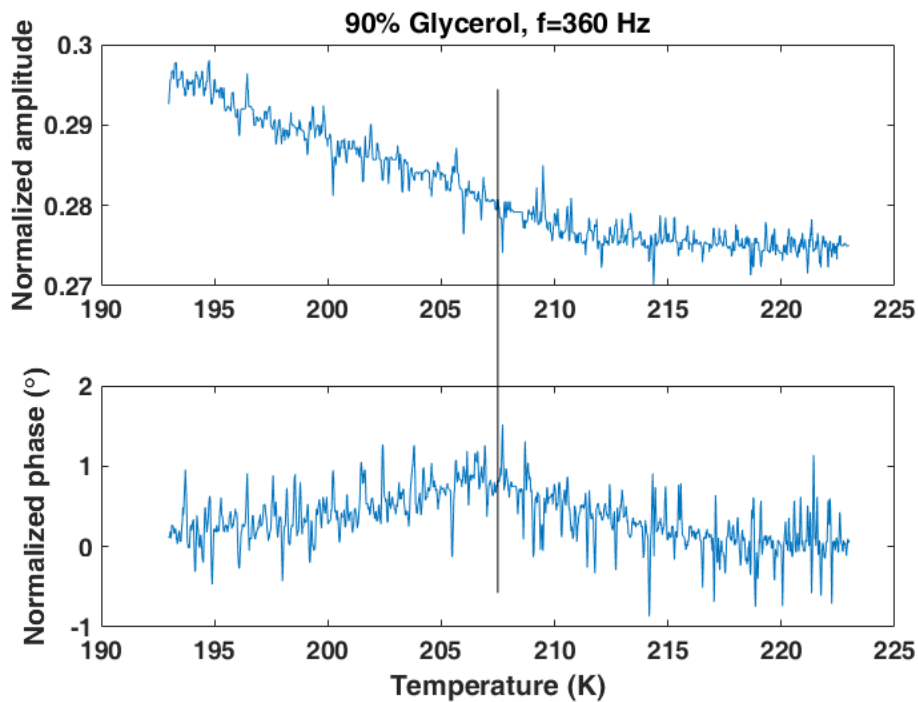


Figure 4.32 – Normalized amplitude and phase of 90 wt% glycerol-water binary solution during a temperature scan at a fixed frequency of 360 Hz using a  $500 \mu\text{m LiTaO}_3$  as sensor

Effusivity of sample was calculated from experimental data using equation 2.28, Temperature evolution of real and imaginary parts of squared effusivity is shown in figure 4.33.

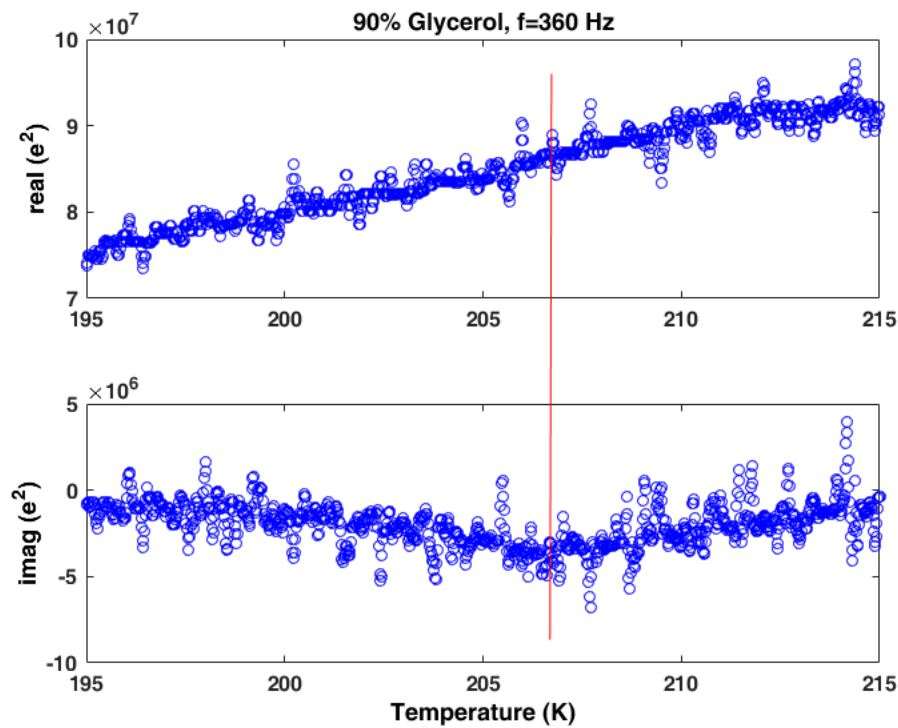


Figure 4.33 – Real and imaginary parts of squared effusivity versus temperature for 90 wt% glycerol-water binary solution at  $f=360$  Hz

We applied the same procedure used for pure glycerol to analyse the experimental data to extract information about the  $\tau$ ,  $AE$ ,  $I_{DO}$ ,  $T_g$  and  $m$ .

#### 4.2.3.1.1 Estimation of Parameters: $\alpha$ , $\beta$ , $E_\infty$ , $\Delta E$

Wicket plot was plotted from the real and imaginary parts of  $e^2$  and fitted to find HN parameters. Figure 4.34 shows the fitted Wicket plot for 90 wt% glycerol-water binary solution at 360 Hz frequency. The experimental data was noisy but Matlab software was able to find the best fitted curve.

Table 4.9 shows the best fitted parameters for the sample.

| frequency (Hz) | $\alpha$ | $\beta$ | $E_\infty$ | $\Delta E$ |
|----------------|----------|---------|------------|------------|
| 360            | 0.85     | 0.19    | 7.3807 e7  | 1.8694 e7  |

Table 4.9 – Best fitted parameters from Wicket plot for 90 wt% glycerol-water binary solution using HN model

#### 4.2.3.1.2 Choosing the Model for Relaxation Time

Using the fitted parameters in table 4.9, the relaxation time,  $\tau$  can be calculated from equation 4.8 and is shown in figure 4.35. Raw data has been used for determining  $\tau$ .

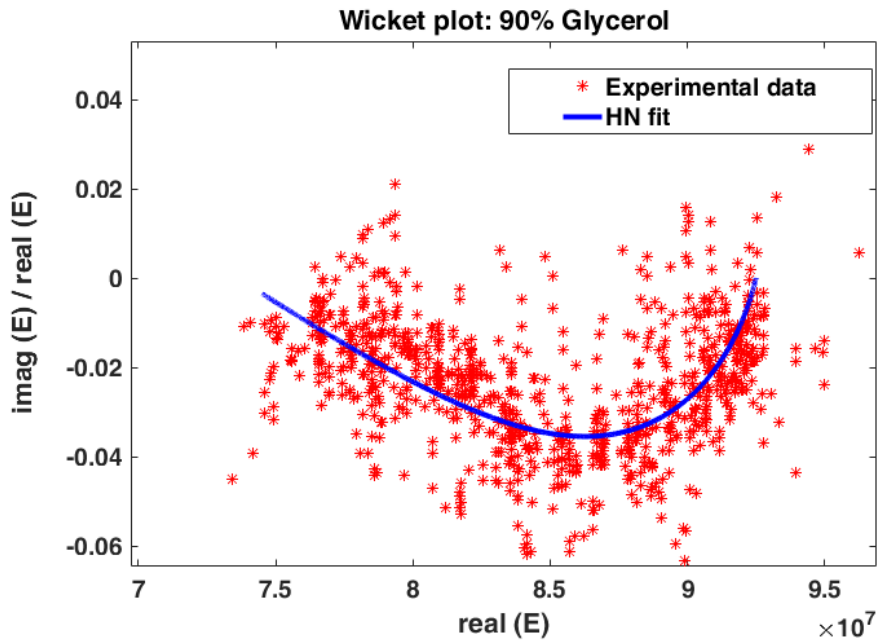


Figure 4.34 – Fitted Wicket plot for 90 wt% glycerol-water binary solution using HN model

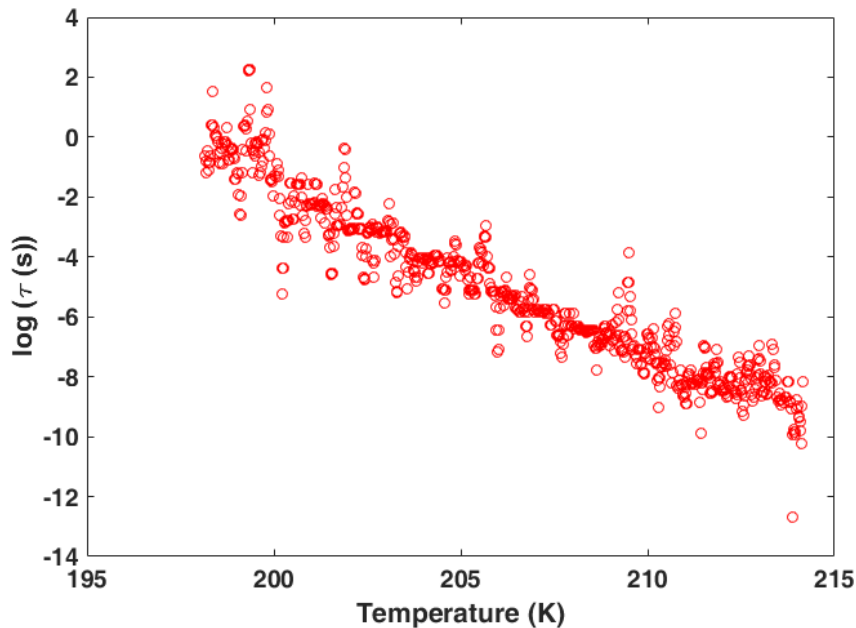


Figure 4.35 – Relaxation time for 90 wt% glycerol at frequency 360 Hz calculated from Direct method (equation 4.8) (from HN equation using the  $\alpha$ ,  $\beta$ ,  $E_0$ ,  $E_\infty$  and complex  $e^2(E(\omega, T))$ )

AE was calculated from the determined  $\tau$  by using the equation 4.10 and is shown in figure 4.36. The value of  $\tau_\infty$  used was  $10^{-14}$  s, which is often considered as the universal value [132].

Using AE,  $I_{DO}$  was determined by using equation 4.11. The data was smoothed using SG filtering before taking the derivative. The figure 4.37 shows the comparison between raw data and SG filtered data.

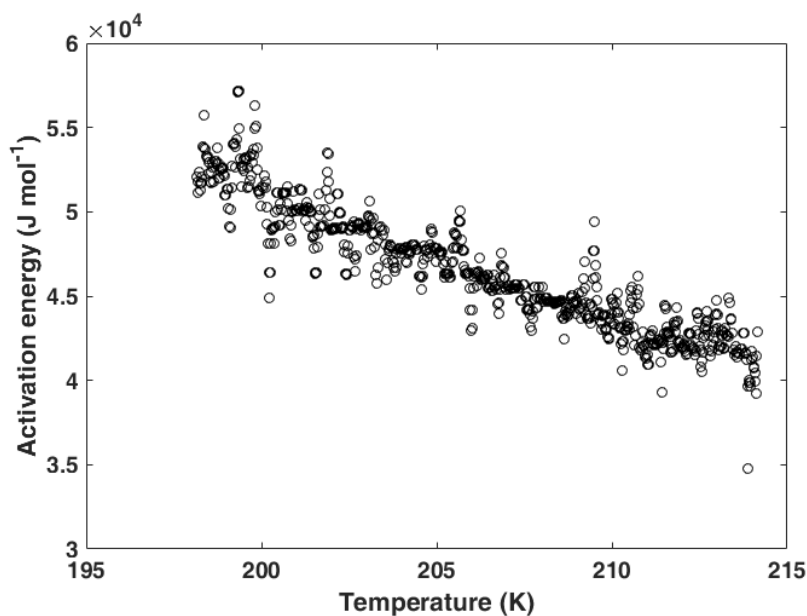


Figure 4.36 – AE for 90 wt% glycerol at frequency 360 Hz

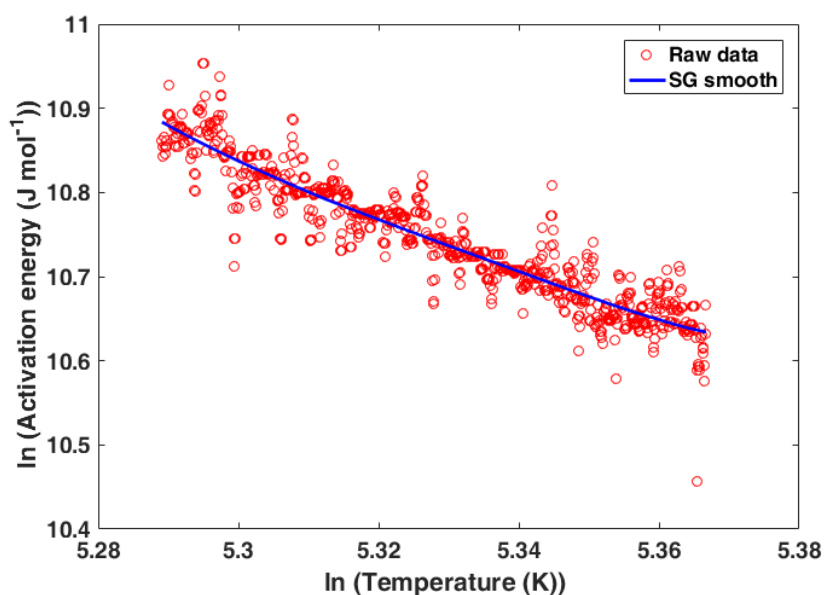


Figure 4.37 – Comparison between raw data and SG filtered data in log scale

As we have done for pure glycerol, temperature evolution of  $I_{DO}^{-1}$  was studied to find the correct model for the temperature dependence of  $\tau$  which is shown in figure 4.38.

From the linear representation,  $I_{DO}^{-1} = mT + c$ , we have obtained the value of  $c = -0.628$ . The condition for VFT model is  $c = -1$  and matched with our result. The possibility of Critical-like model was checked but failed. Therefore,  $\tau$  for 90 wt% glycerol-water mixture follows VFT model so we used VFT equation for  $\tau$  in HN equation and the real and imaginary parts was fitted using the 7-parameter fit.

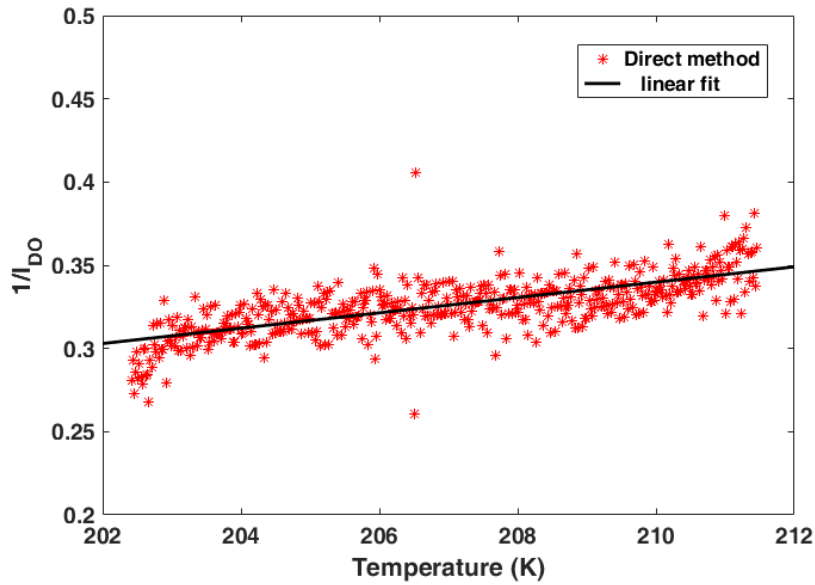


Figure 4.38 – Temperature evolution of the  $I_{DO}^{-1}$  for 90 wt% glycerol. Equation of the linear regression is given by  $I_{DO}^{-1} = 0.0046 T - 0.628$

#### 4.2.3.1.3 Estimation of Model Parameters for Relaxation Time

To initiate the 7-parameter fit, we need to know the initial parameters for the program to find the best fit result. This was done via the linearized derivative based analysis. Using the equation 4.19, we have determined the factor  $\left[\sqrt{H'_a(T)}\right]^{-1}$  for the VFT model. Parameters B and  $T_0$  were obtained from the evolution of  $\left[\sqrt{H'_a(T)}\right]^{-1}$  with respect to  $1/T$  which is shown in the figure 4.39.

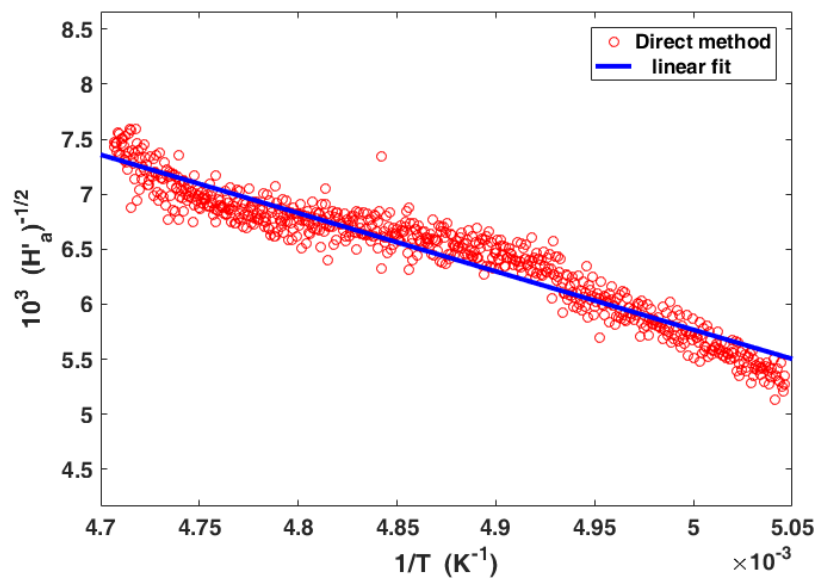


Figure 4.39 – Inverse of the square root of AAH ( $1/\sqrt{H'_a}$ ) plotted against  $1/T$  for 90 wt% glycerol

The linear equation is given by  $\sqrt{H'_a}^{-1/2} 10^3 = -5305/T + 32.296$ . Calculated values of B and  $T_0$  from the equation are 937.7 K and 164.7 K respectively.

#### 4.2.3.1.4 7-Parameter Fit

The initial parameters were known for performing the 7-parameter fit which are shown in table 4.10.

| -             | $\alpha$ | $\beta$ | $E_\infty$ | $\Delta E$ | B (K) | $T_0$ (K) | $\tau_\infty$ (s) |
|---------------|----------|---------|------------|------------|-------|-----------|-------------------|
| Initial value | 0.8      | 0.5     | 7.25000 e7 | 2.00000 e7 | 938   | 165       | $10^{-14}$        |

Table 4.10 – Initial values used for HN and VFT parameters for 7-parameter fit

Figure 4.40 shows the best fitted real and imaginary parts of  $e^2$ .

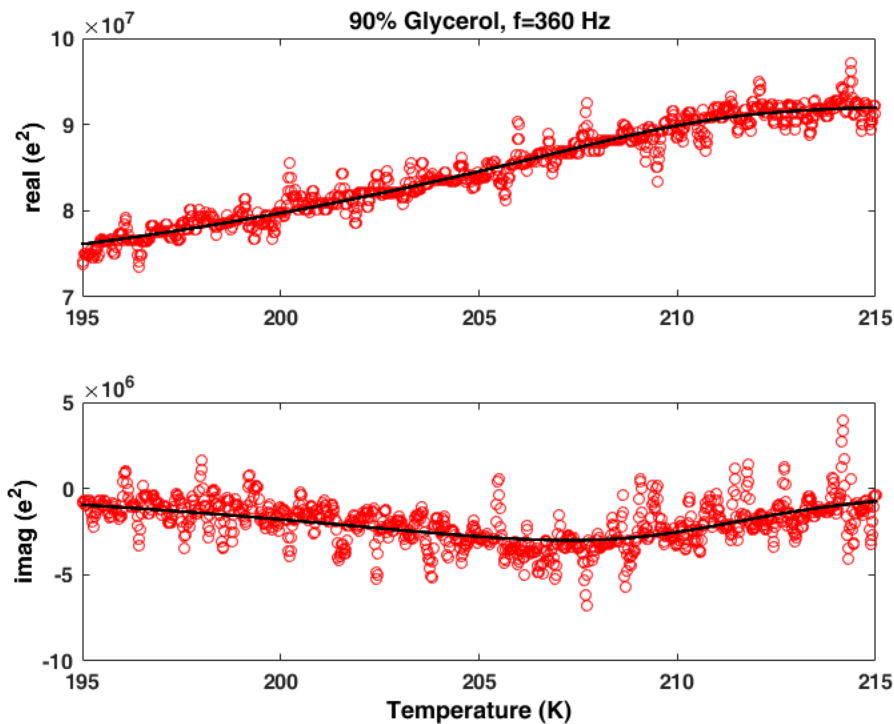


Figure 4.40 – Fitting done on the real and imaginary parts of squared effusivity 90 wt% glycerol-water binary solution using HN and VFT model

Table 4.11 shows the best fitted values of HN and VFT parameter.

| method          | $\alpha$ | $\beta$ | $E_\infty$ | $\Delta E$ | B (K) | $T_0$ (K) | $\tau_\infty$ (s) |
|-----------------|----------|---------|------------|------------|-------|-----------|-------------------|
| Wicket fit      | 0.85     | 0.19    | 7.38070 e7 | 1.86940 e7 | -     | -         | -                 |
| 7-parameter fit | 0.85     | 0.17    | 7.21424 e7 | 2.01031 e7 | 1061  | 162.5     | $10^{-12.8660}$   |

Table 4.11 – Fitted HN and VFT parameters from 7-parameter fit and comparison of HN parameters with Wicket fit for 90 wt% glycerol-water mixture

It was observed from the result that the 7-parameter fit was in good agreement with the Wicket fit. The parameter  $\tau_\infty$  was also fitted in this process.

The commonly used value for  $\tau_\infty$  is  $10^{-14}$  s while we have obtained  $\tau_\infty = 10^{-12.8660}$  s. As already said, it was very important to use the exact value of  $\tau_\infty$  instead of a rounded value. A comparison of AE calculated using these two values and from the VFT law is shown in figure 4.41.

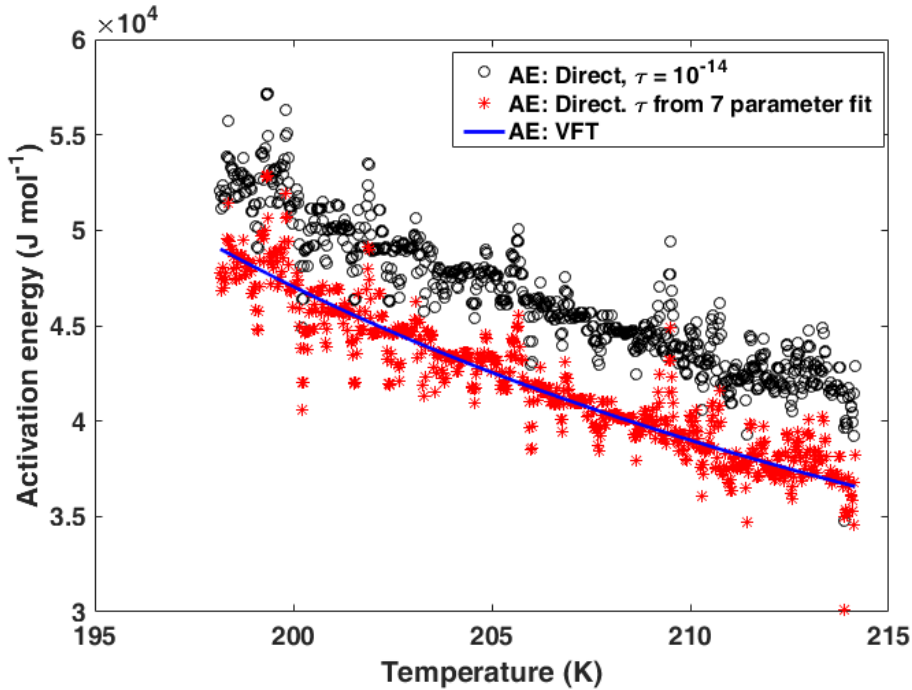


Figure 4.41 – Comparison of AE for 90 wt% glycerol calculated from different methods

To check the goodness of 7-parameter fit, we have used the fitted HN parameters to simulate the Wicket and Cole-Cole plot alongside the experimental data and compared as shown in figure 4.42 and 4.43 respectively.

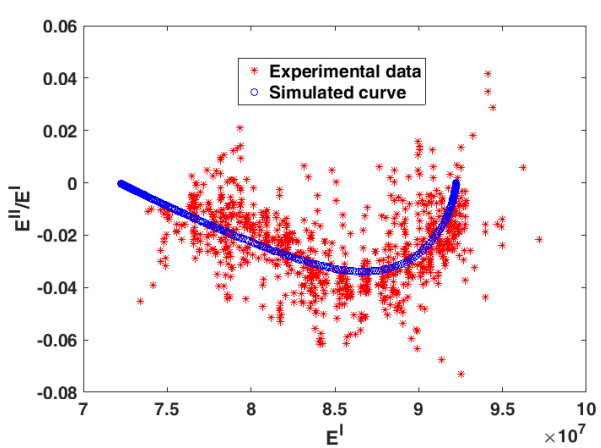


Figure 4.42 – Wicket plot for 90 wt% glycerol at frequency of 360 Hz

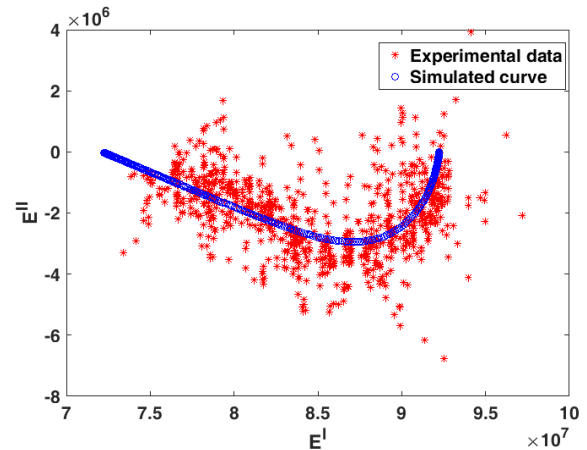


Figure 4.43 – Cole-Cole plot for 90 wt% glycerol at frequency of 360 Hz

From the figure, it was observed that the simulated curve followed the same trend as the experimental curve despite a noisy experimental data, showing that the best fitted parameters are good.

#### 4.2.3.1.5 Fragility and Dyre-Olsen Index

As we have already discussed, using the VFT parameters,  $T_g$  can be calculated using the glass transition convention  $T = T_g$  when  $\tau=100$  s and  $m$  using the equation 4.22. The  $I_{DO}$  at  $T = T_g$  gives the new fragility,  $M$ .  $m$  can also be determined from  $M$  using equation 4.24. Table 4.12 shows the  $T_g$ ,  $m$  and  $M$  for 90 wt% glycerol-water mixture.

| $T_g$ (K) (PPE) | $T_g$ (K) (literature)                            | $m$ (PPE) | $m$ (literature) | $M$ |
|-----------------|---|-----------|------------------|-----|
| 193.4           | 181.5 <sup>a</sup> , 186.0 $\pm$ 0.1 <sup>b</sup> | 92.0      | -                | 5.2 |

Table 4.12 –  $T_g$  and  $m$  of binary mixture of 90 wt% glycerol-water and their comparison with literature data, a: [97], b: [137]

The same procedure was applied to study other samples. Instead of repeating the same procedure, only their results are given in next sections.

#### 4.2.3.2 80 wt% Glycerol-Water Mixture

Figure 4.44 shows the temperature scan of 80 wt% glycerol-water binary mixture at 66 Hz frequency. The relaxation could be observed in both amplitude and phase of the signal.

Figure 4.45 shows the 7-parameter fitted real and imaginary parts of squared effusivity for 80 wt% glycerol-water mixture.

Table 4.13 shows the best fitted values of HN and VFT parameters. Using these parameters, we obtained the  $T_g$ ,  $m$  and  $M$  values which are shown in table 4.14.

| frequency (Hz) | $\alpha$ | $\beta$ | $N_\infty$ | $\Delta N$ | $B$ (K) | $T_0$ (K) | $\tau_\infty$ (s)      |
|----------------|----------|---------|------------|------------|---------|-----------|------------------------|
| 66             | 0.57     | 0.75    | 648214     | 641355     | 977     | 156       | 10 <sup>-13.1422</sup> |
| 120            | 0.88     | 0.36    | 774300     | 656476     | 1358    | 138       | 10 <sup>-12.3328</sup> |
| 360            | 0.48     | 1.0     | 824602     | 832053     | 607     | 166       | 10 <sup>-11.7974</sup> |

Table 4.13 – Fitted HN and VFT parameters of binary mixture of 80 wt% glycerol and water

| $T_g$ (K) (PPE) | $T_g$ (K) (literature)   | $m$ (PPE) | $m$ (literature)  | $M$ |
|-----------------|--|-----------|-------------------|-----|
| 180 +/- 3       | 174.0 <sup>a</sup> , 170 <sup>b</sup> , 177.9 $\pm$ 0.2 <sup>c</sup> | 98 +/- 35 | 54.4 <sup>b</sup> | 6.0 |

Table 4.14 –  $T_g$  and  $m$  of binary mixture of 80 wt% glycerol-water and their comparison with literature data, a: [97], b: [99], c: [137]

Wicket and Cole-Cole plot were simulated alongside the experimental data to check the goodness of fit and compared as shown in figure 4.46 and 4.47 respectively.

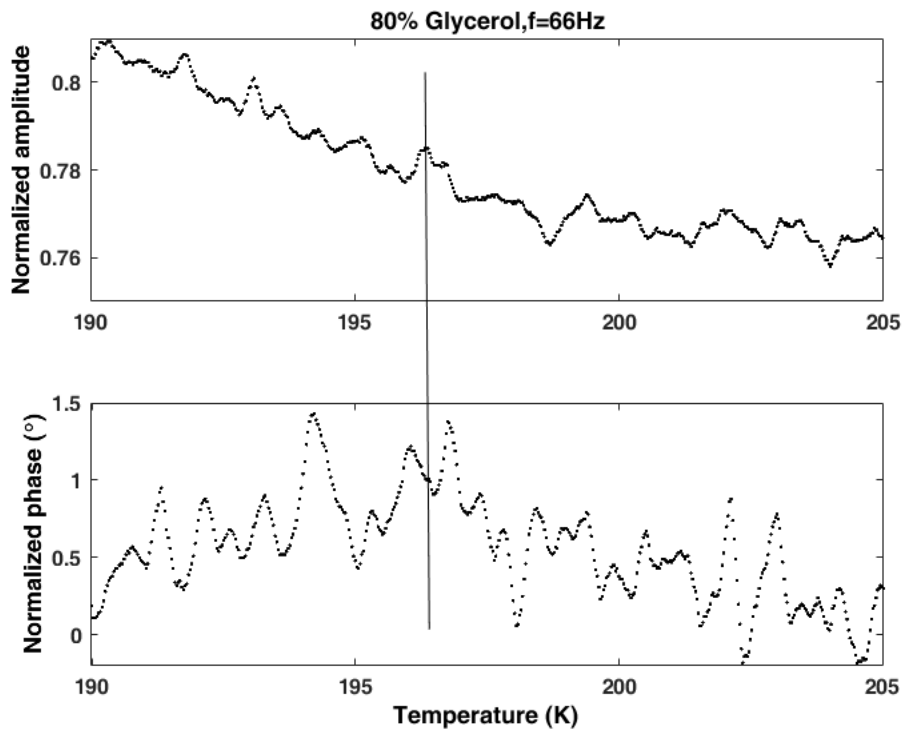


Figure 4.44 – Normalized amplitude and phase of 80 wt% glycerol-water binary solution during a temperature scan at a fixed frequency of 66 Hz using a  $500 \mu\text{m}$   $\text{LiTaO}_3$  as sensor

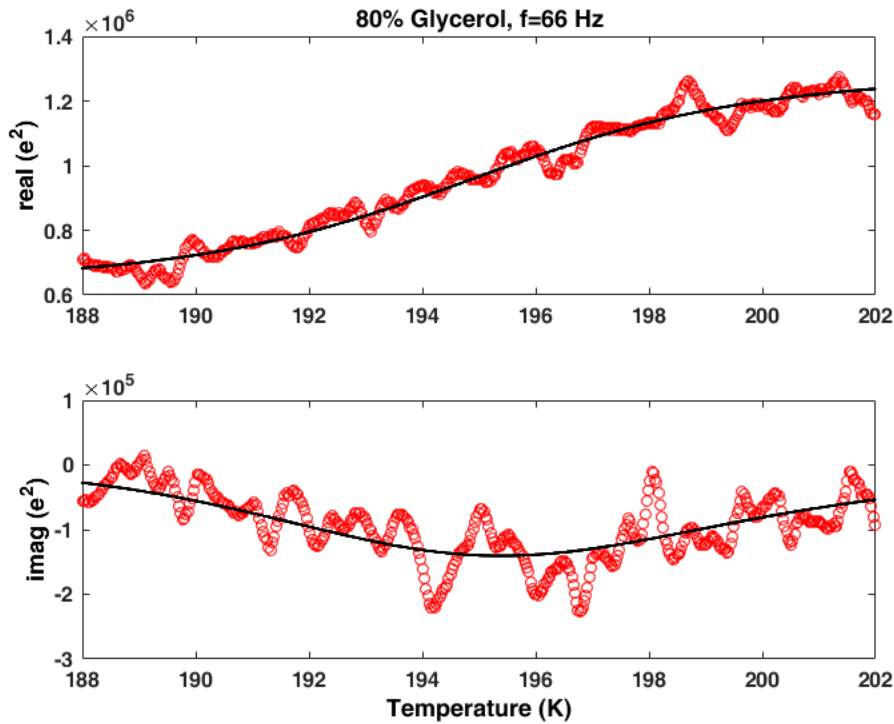


Figure 4.45 – Fitting done on the real and imaginary parts of squared effusivity versus temperature for 80 wt% glycerol-water binary solution using Havriliak-Negami model

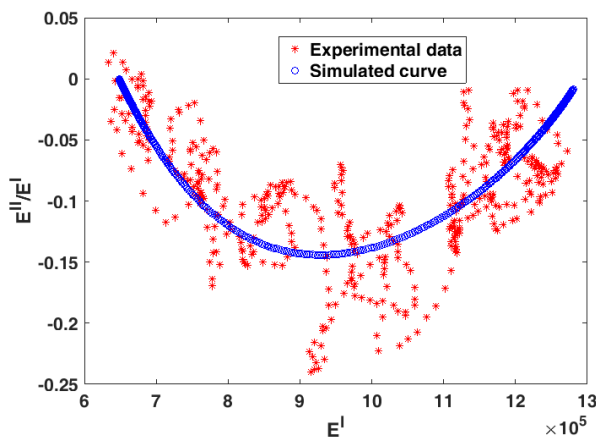


Figure 4.46 – Wicket plot for 80 wt% glycerol at frequency of 66 Hz

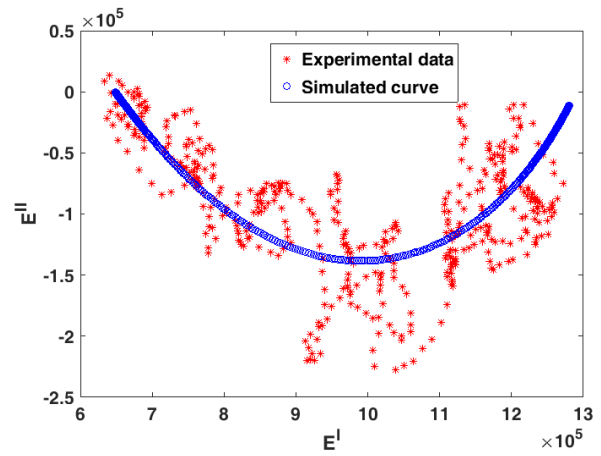


Figure 4.47 – Cole-Cole plot for 80 wt% glycerol at frequency of 66 Hz

The simulated curve followed the same trend as the experimental curve showing that the best fitted parameters are good.

### 4.2.3.3 70 wt% Glycerol-Water Mixture

Figure 4.48 shows the temperature scan of 70 wt% glycerol-water binary mixture at 1100 Hz frequency.

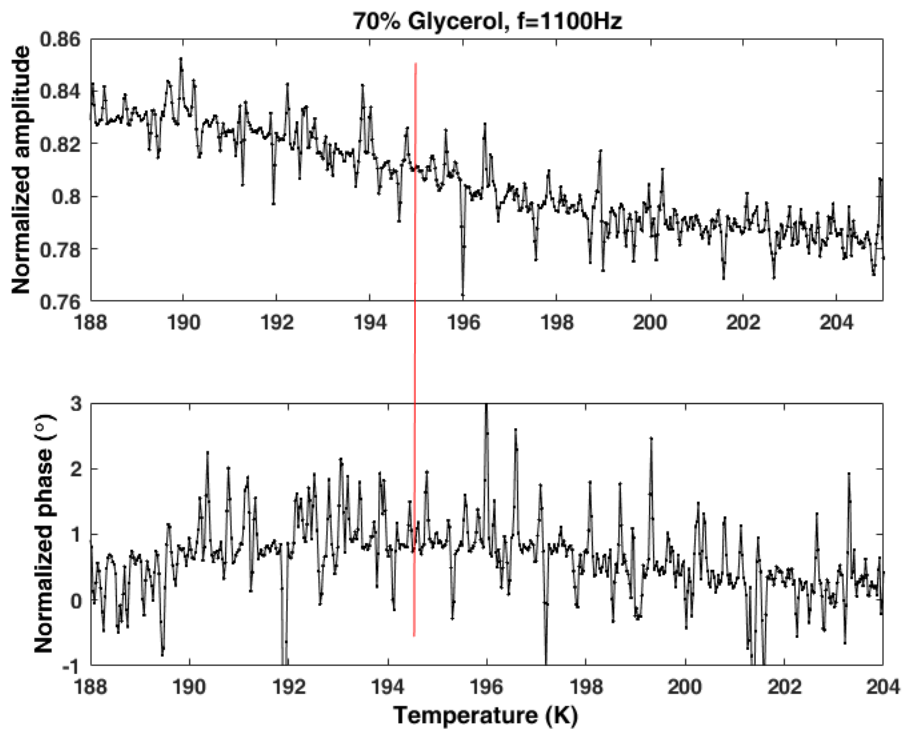


Figure 4.48 – Normalized amplitude and phase of 70 wt% glycerol-water binary solution during a temperature scan at a fixed frequency of 1100 Hz using a 500  $\mu\text{m}$   $\text{LiTaO}_3$  as sensor

Figure 4.49 shows the 7-parameter fitted real and imaginary parts of squared effusivity for 70 wt% glycerol-water mixture.

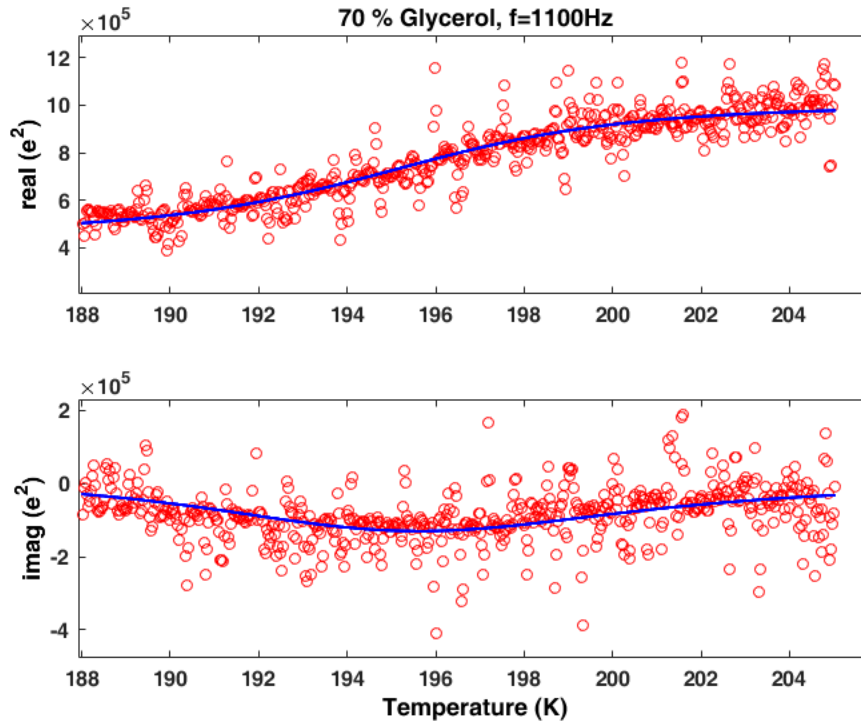


Figure 4.49 – Fitting done on the real and imaginary parts of squared effusivity versus temperature for 70 wt% glycerol-water binary solution using Havriliak-Negami model

Table 4.15 shows the best fitted values of HN and VFT parameters.

| frequency (Hz) | $\alpha$ | $\beta$ | $N_{\infty}$ | $\Delta N$ | B (K) | $T_0$ (K) | $\tau_{\infty}$ (s) |
|----------------|----------|---------|--------------|------------|-------|-----------|---------------------|
| 360            | 0.77     | 0.21    | 381297       | 753276     | 712   | 167       | $10^{-12.7876}$     |
| 1100           | 0.64     | 0.73    | 471038       | 530158     | 880   | 154       | $10^{-12.9151}$     |

Table 4.15 – Fitted HN and VFT parameters of binary mixture of 70 wt% glycerol and water

Using these parameters, values of  $T_g$ , m and M were calculated which are given in table 4.16 .

| $T_g$ (K) (PPE) | $T_g$ (K) (literature)   | m (PPE) | m (literature)    | M   |
|-----------------|--|---------|-------------------|-----|
| 183 +/- 5       | 168.3 <sup>a</sup> , 162.9 <sup>b</sup> , 171.0 $\pm$ 0.2 <sup>c</sup> | 118.0   | 56.5 <sup>b</sup> | 6.9 |

Table 4.16 –  $T_g$  and m of binary mixture of 70 wt% glycerol-water and their comparison with literature data, a: [97], b: [99], c: [137]

Goodness of 7-parameter fit was verified by simulating Wicket and Cole-Cole plot alongside the experimental data and compared as shown in figure 4.50 and 4.51 respectively. The simulated curve followed the same trend as the experimental curve showing that the best fit parameters are good. Here, it was observed that the experimental data was more distorted. It might be due to the increased concentration of water compared to previous samples.

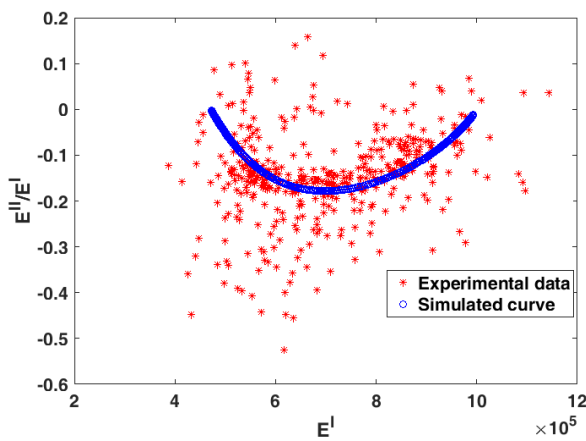


Figure 4.50 – Wicket plot for 70 wt% glycerol at frequency of 1100 Hz

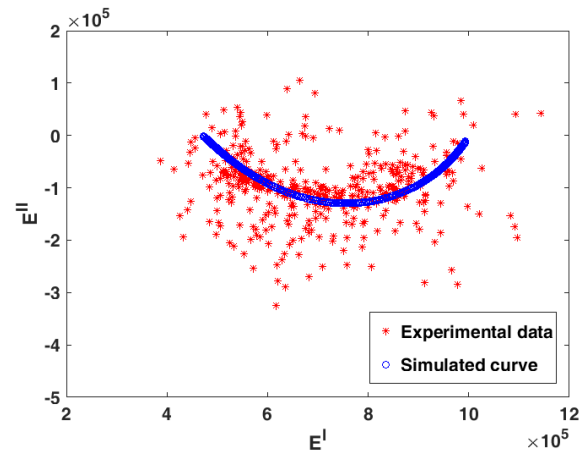


Figure 4.51 – Cole-Cole plot for 70 wt% glycerol at frequency of 1100 Hz

#### 4.2.3.4 93.13 wt% 1,2 Propanediol-Water Mixture

Mixtures of 1,2 propanediol were also studied using this protocol. The first binary sample studied was 93.13 wt% 1,2 propanediol-water binary solution. Figure 4.52 shows the temperature scan of 93.13 wt% 1,2 propanediol-water binary mixture at 120 Hz frequency.

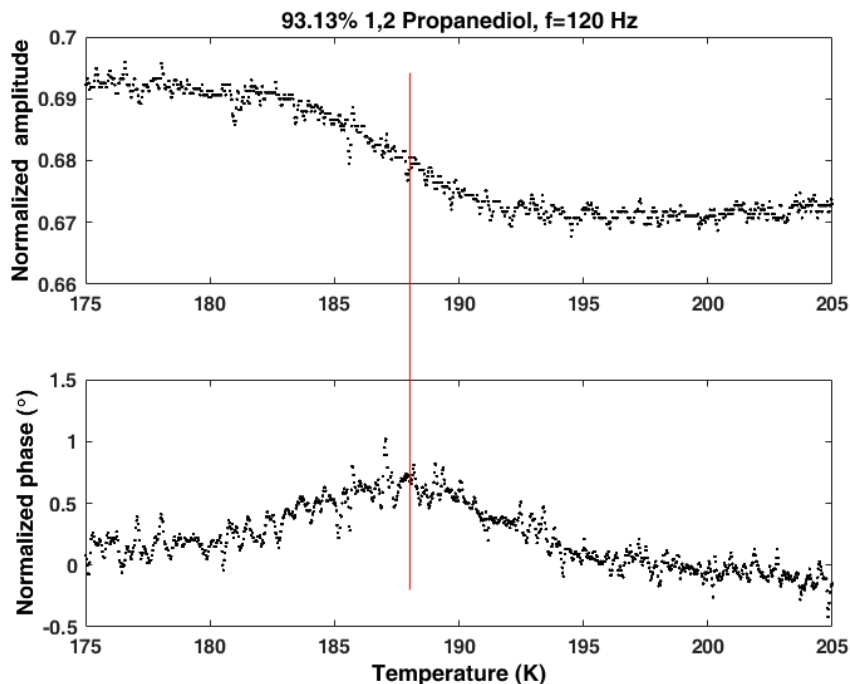


Figure 4.52 – Normalized amplitude and phase of 93.13 wt% 1,2 propanediol-water binary solution during a temperature scan at a fixed frequency of 120 Hz using a 500  $\mu\text{m}$   $\text{LiTaO}_3$  as sensor

Figure 4.53 shows the 7-parameter fitted real and imaginary parts of squared effusivity for 93.13 wt% 1,2 propanediol-water mixture.

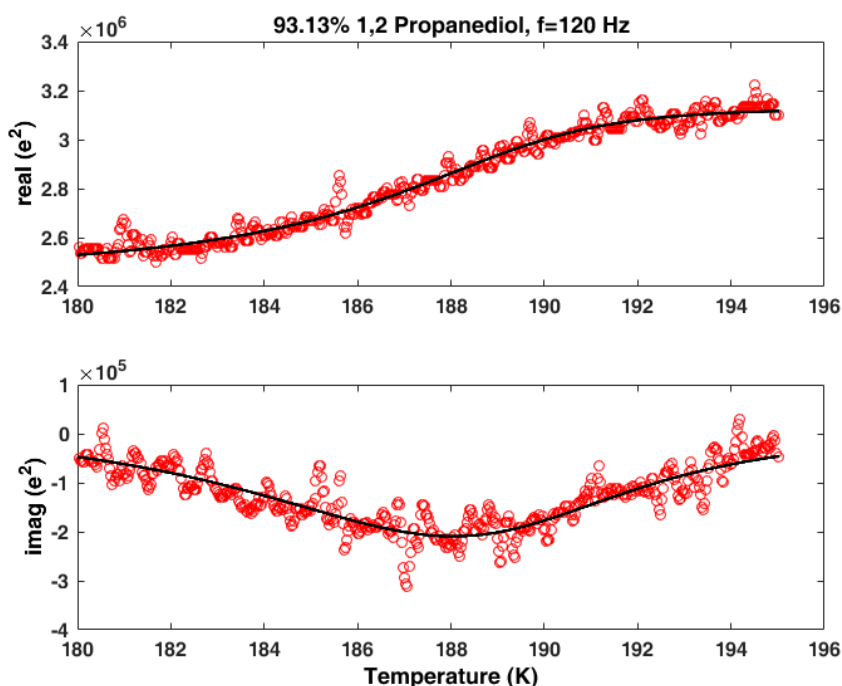


Figure 4.53 – Fitting done on the real and imaginary parts of squared effusivity versus temperature for 93.13 wt% 1,2 propanediol-water binary solution using HN and VFT model

Table 4.17 shows the fitted values of HN and VFT parameters for the  $\alpha$  relaxation occurred during temperature scans at different frequencies.

| frequency(Hz) | $\alpha$ | $\beta$ | $N_{\infty}$ | $\Delta N$ | B (K) | $T_0$ (K) | $\tau_{\infty}$ (s) |
|---------------|----------|---------|--------------|------------|-------|-----------|---------------------|
| 22            | 0.88     | 0.21    | 602680       | 411354     | 1015  | 146       | $10^{-13.0126}$     |
| 120           | 0.90     | 0.53    | 2.4788 e6    | 649288     | 1652  | 127       | $10^{-14.2957}$     |
| 360           | 0.91     | 0.40    | 1.0627 e6    | 456563     | 1143  | 142       | $10^{-13.0000}$     |
| 1100          | 0.87     | 0.69    | 629674       | 297210     | 1201  | 134       | $10^{-12.5017}$     |

Table 4.17 – Fitted HN and VFT parameters of binary mixture of 93.13 wt% 1,2 propanediol-water

Using these parameters, we obtained the  $T_g$ , m and M values which are shown in table 4.18.

| $T_g$ (K) (PPE) | $T_g$ (K) (literature) | m (PPE)   | m (literature) | M   |
|-----------------|------------------------|-----------|----------------|-----|
| 172 +/- 3       | 165 <sup>a</sup>       | 75 +/- 12 | -              | 3.9 |

Table 4.18 –  $T_g$ , m and M of binary mixture of 93.13 wt% 1,2 propanediol-water.  $T_g$  for comparison is taken from phase diagram shown in the figure 4.31.

Goodness of 7-parameter fit was verified by simulating Wicket and Cole-Cole plot alongside the experimental data and compared as shown in figure 4.54 and 4.55 respectively. The simulated curve followed the same trend as the experimental curve showing that the best fit parameters are good.

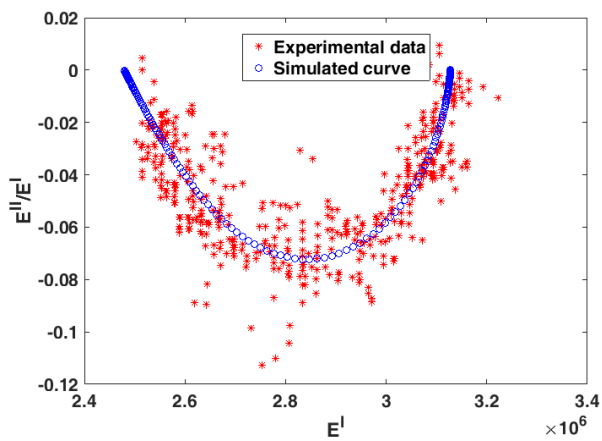


Figure 4.54 – Wicket plot for 93.13 wt% 1,2 propanediol at frequency of 120 Hz

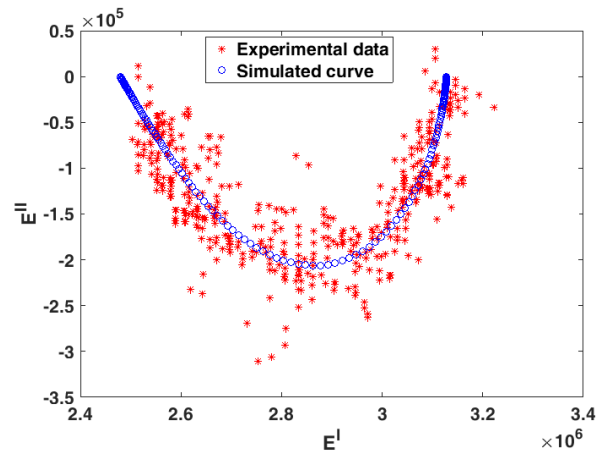


Figure 4.55 – Cole-Cole plot for 93.13 wt% 1,2 propanediol at frequency of 120 Hz

### 4.2.3.5 70 wt% 1,2 Propanediol-Water Mixture

Figure 4.56 shows the temperature scan of 70 wt% 1,2 propanediol-water binary mixture at 360 Hz frequency.

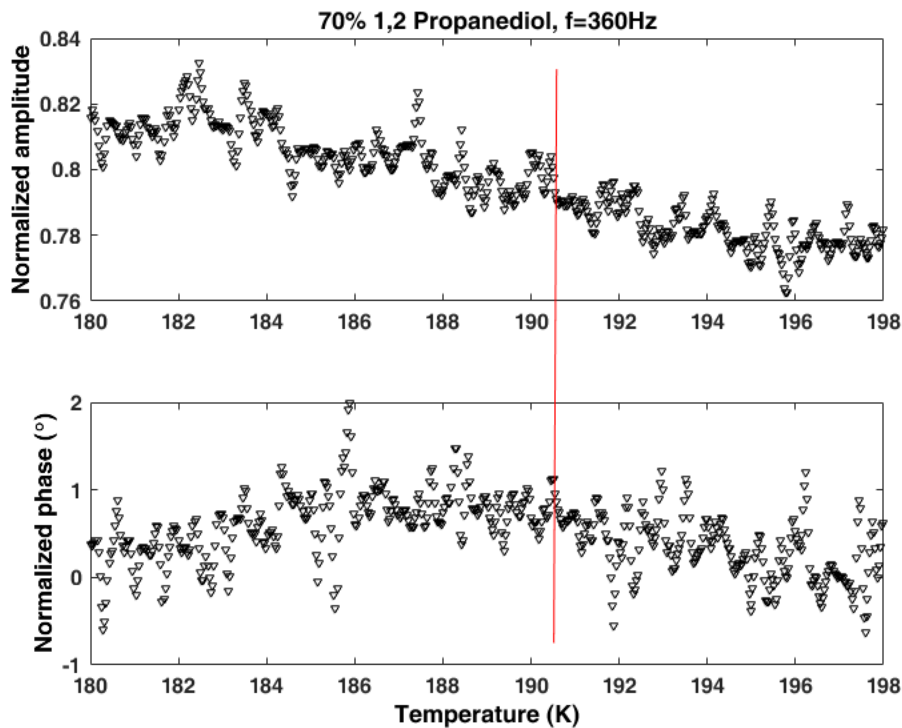


Figure 4.56 – Normalized amplitude and phase of 70 wt% 1,2 propanediol-water binary solution during a temperature scan at a fixed frequency of 360 Hz using a  $500 \mu\text{m}$   $\text{LiTaO}_3$  as sensor

Figure 4.57 shows the 7-parameter fitted real and imaginary parts of squared effusivity for 70 wt% 1,2 propanediol-water mixture.

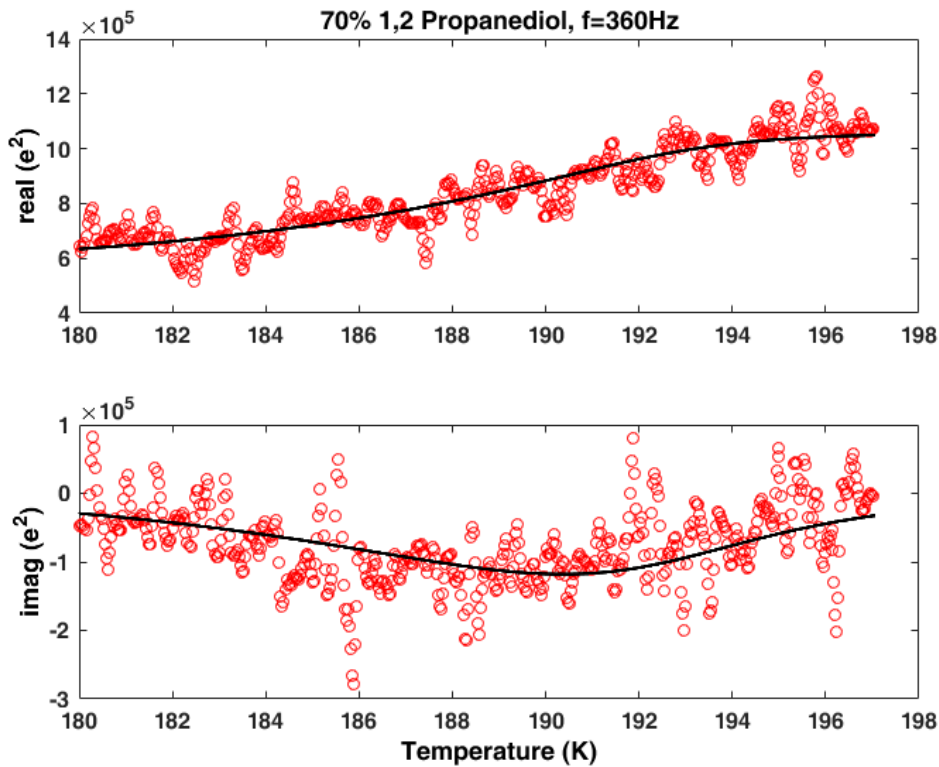


Figure 4.57 – Fitting done on the real and imaginary parts of squared effusivity versus temperature for 70 wt% 1,2 propanediol-water binary solution using Havriliak-Negami model

Table 4.19 shows the fitted values of HN and VFT parameters for the  $\alpha$  relaxation occurred during temperature scans at different frequencies.

| frequency(Hz) | $\alpha$ | $\beta$ | $N_{\infty}$ | $\Delta N$ | B (K) | $T_0$ (K) | $\tau_{\infty}$ (s) |
|---------------|----------|---------|--------------|------------|-------|-----------|---------------------|
| 13            | 0.70     | 0.53    | 650562       | 309726     | 902   | 147       | $10^{-13.4043}$     |
| 360           | 0.92     | 0.31    | 574976       | 483131     | 1280  | 137       | $10^{-13.2922}$     |

Table 4.19 – Fitted HN and VFT parameters of binary mixture of 70 wt% 1,2 propanediol-water

Using the average value of B and  $T_0$ , parameters like  $T_g$ , m and M were determined which are shown in table 4.20.

| $T_g$ (K) (PPE) | $T_g$ (K) (literature) | m (PPE)   | m (literature) | M   |
|-----------------|------------------------|-----------|----------------|-----|
| 173 +/- 1       | 160.45 <sup>c</sup>    | 87 +/- 16 | -              | 4.7 |

Table 4.20 –  $T_g$  and m of binary mixture of 70 wt% 1,2 propanediol-water and their comparison with literature data, c: [98]

The Wicket and Cole-Cole plot were plotted from the experimental data. Using the fitted HN parameters the same were simulated and compared as shown in figure 4.58 and 4.59 respectively. The simulated curve followed the same trend as the experimental curve showing that the best fit parameters are good.

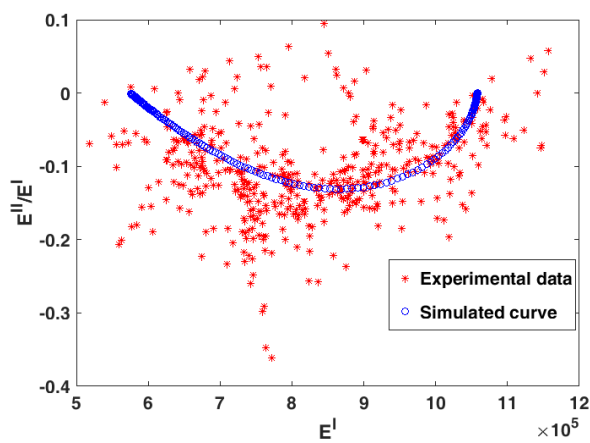


Figure 4.58 – Wicket plot for 70 wt% 1,2 propanediol at frequency of 360 Hz

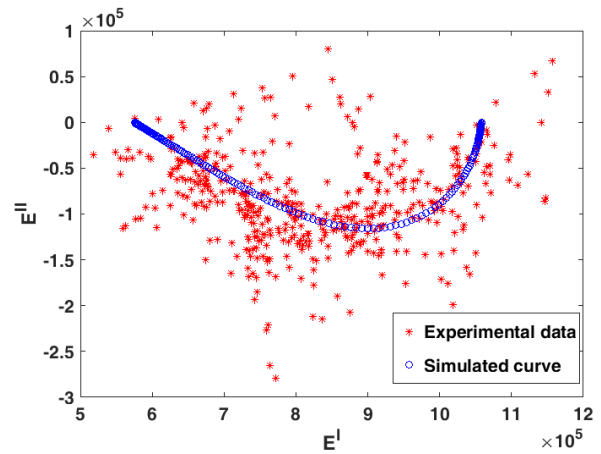


Figure 4.59 – Cole-Cole plot for 70 wt% 1,2 propanediol at frequency of 360 Hz

It was not feasible to extend the low temperature PPE experiments on other binary solutions with higher concentration of water because of the inevitable crystallization. Some experiments were conducted for such mixtures but the relaxation was beyond the scope of our analysis. The experimental data were unable to be fitted using HN model. More complex analysis must be employed to examine the relaxation behavior of such systems.

#### 4.2.4 Classical and New Fragility

The fragility can be described as the extend to which a material deviates from the Arrhenius behavior which was shown in the OLU diagram (figure 4.6). OLU diagram for the studied samples has been plotted together to examine their nature which is shown in figure 4.60.

The trend of strong to fragile nature is shown in the figure 4.60 along with the Arrhenius behavior. Pure samples were found to be in the stronger region which showed lesser deviation from Arrhenius behavior. As the water content was increased the samples became more fragile and started deviating more from Arrhenius behavior.

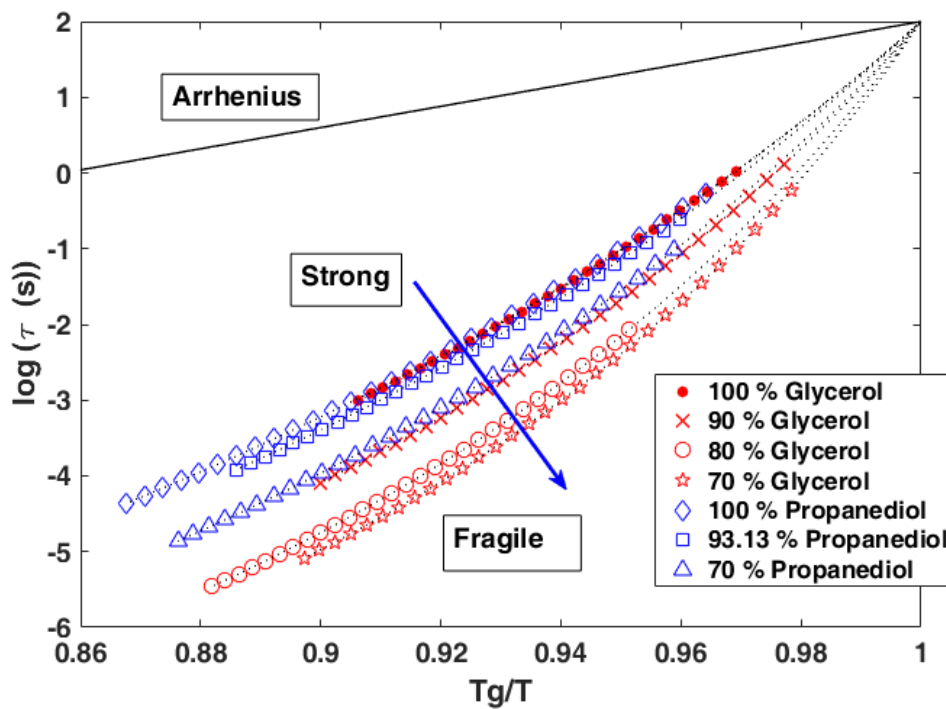


Figure 4.60 – OLU diagram to classify the studied samples according to their fragility

The evolution of ratio between the apparent activation enthalpy and energy with respect to  $T_g/T$  was also studied which is shown in figure 4.61. This representation also provided a classification for fragility. Arrhenius behavior is shown as a horizontal line in the figure 4.61. Comparing both figures, it can be observed that an increase in curvature demonstrates an increase in fragility. It was observed from both figures that the fragility of the glass formers increased as the concentration of water was increased.

The relation between the classical fragility ( $m$ ) and new fragility ( $M$ ) for all the samples were also studied which is shown in figure 4.62.

The figure 4.62 gives the experimental verification of the behavior predicted by the equation 4.24. The  $\tau_\infty$  obtained from 7-parameter fit was used for each sample in this calculation. The slope of the line given by  $C$  was obtained as 15.17 which is within the expected range.

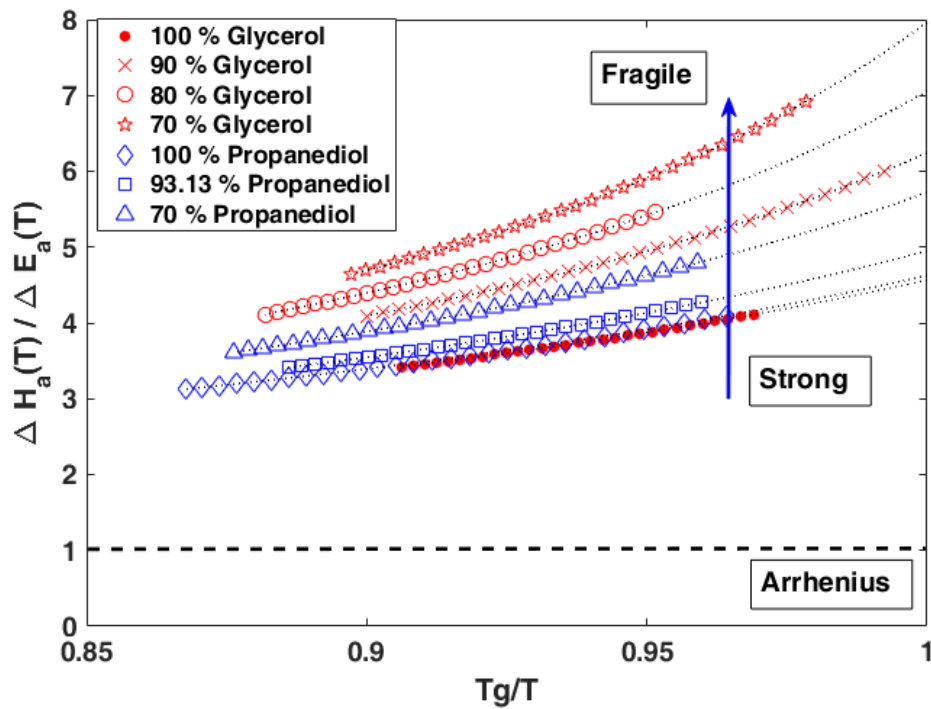


Figure 4.61 – Evolution of the ratio between the apparent activation enthalpy and energy for all the studied samples

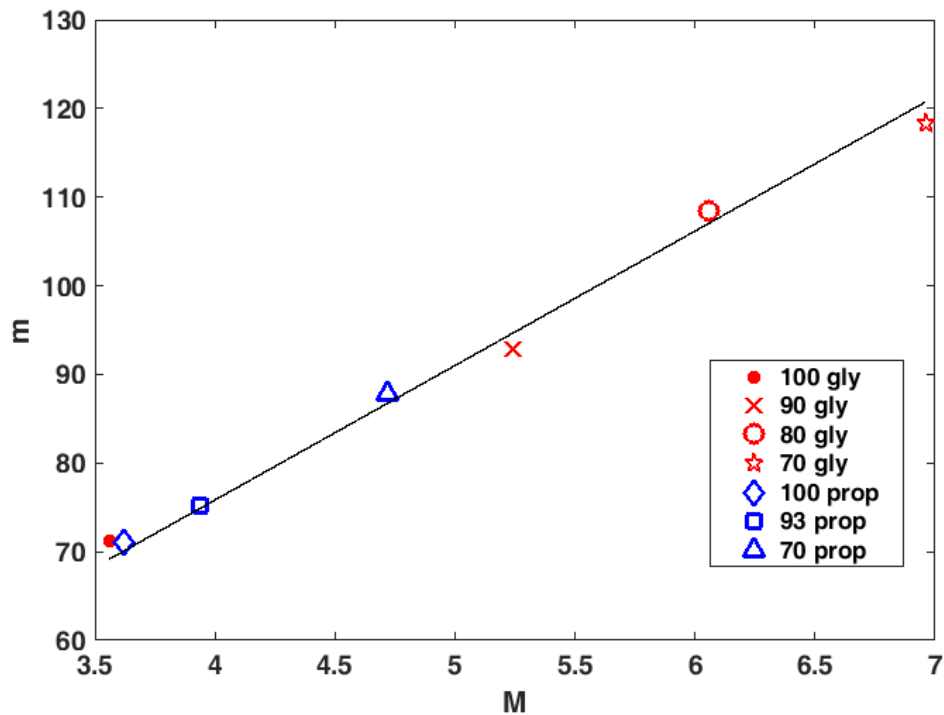


Figure 4.62 – Relationship between the classical fragility,  $m$  and new fragility,  $M$  for all samples. Equation of the line is given by:  $m = 15.17(M + 1)$

## 4.2.5 Individual Frequency Relaxation

In the previous section we have explained a detailed protocol to determine  $\tau$  using the HN equation. Experimental data were fitted using Wicket and 7-parameter methods to obtain the parameters. Here we present another approach to directly obtain  $\tau$  from the  $\alpha$  relaxation peak position during a temperature or frequency scan.

Simulations in figures 4.63 and 4.64 show that the position of the peak in the imaginary part remains the same during a temperature scan at fixed frequency or during a frequency scan at fixed temperature respectively. The previous case was adopted for our experiments in which we could observe the relaxation corresponding to a particular frequency and we called it "individual frequency relaxation" (IFR). From IFR, the temperature at the position of the peak could be obtained.

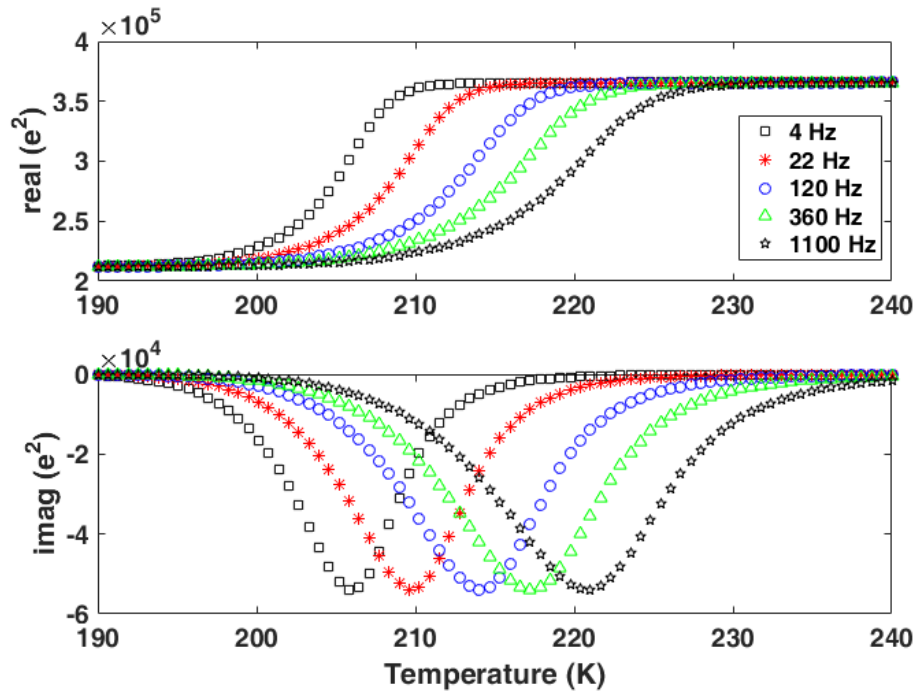


Figure 4.63 – Simulation of real and imaginary parts of squared effusivity during a temperature scan at different fixed frequencies

In IFR analysis, a set of temperature scans is performed at different frequencies. During each scan it is possible to observe the  $\alpha$  relaxation as in figure 4.63 and during each scan the relaxation occurs when  $\tau_{MAX} = \left(\frac{1}{2\pi f}\right) \left(\tan\left(\frac{\pi}{2(\beta+1)}\right)\right)^{1/\alpha}$  [140], where  $f$  is the modulating frequency. From each scan, the  $\tau_{MAX}$  and the temperature at which the  $\alpha$  peak becomes maximum are noted. By performing a series of temperature scans at different frequencies we can obtain a set of  $\tau_{MAX}$  and corresponding temperature. A graph is plotted with  $\log(\tau_{MAX})$  versus inverse temperature. Fitting this curve with a suitable model, for example, VFT model, we can determine the  $T_g$  and  $m$  of the sample. The protocol described in subsection 4.1.3 can be used to find the best model and the starting values required for the fit.

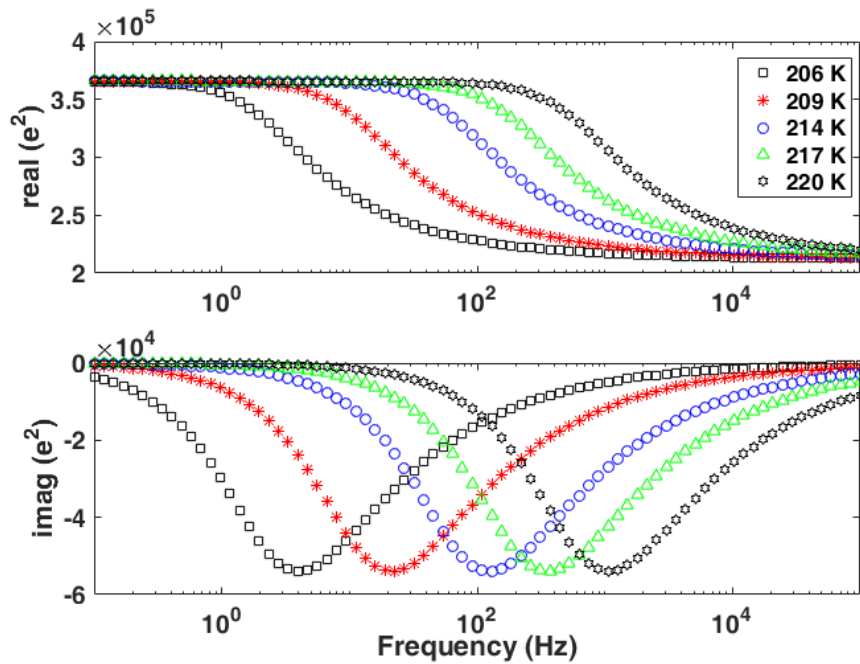


Figure 4.64 – Simulation of real and imaginary parts of squared effusivity during a frequency scan at different constant temperatures

Similarly, if a frequency scan is performed at fixed temperature as in figure 4.64, the same procedure can be used to obtain  $\tau_{MAX}$  by finding  $f_{MAX}$  from each scan, where  $f_{MAX} = \left( \frac{1}{2\pi\tau_{MAX}} \right) \left( \tan\left(\frac{\pi}{2(\beta+1)}\right) \right)^{1/\alpha}$ . A comparison of  $\tau_{MAX}$  calculated from both scans is shown in figure 4.65.  $\tau_{MAX}$  is found to be the same in both cases.

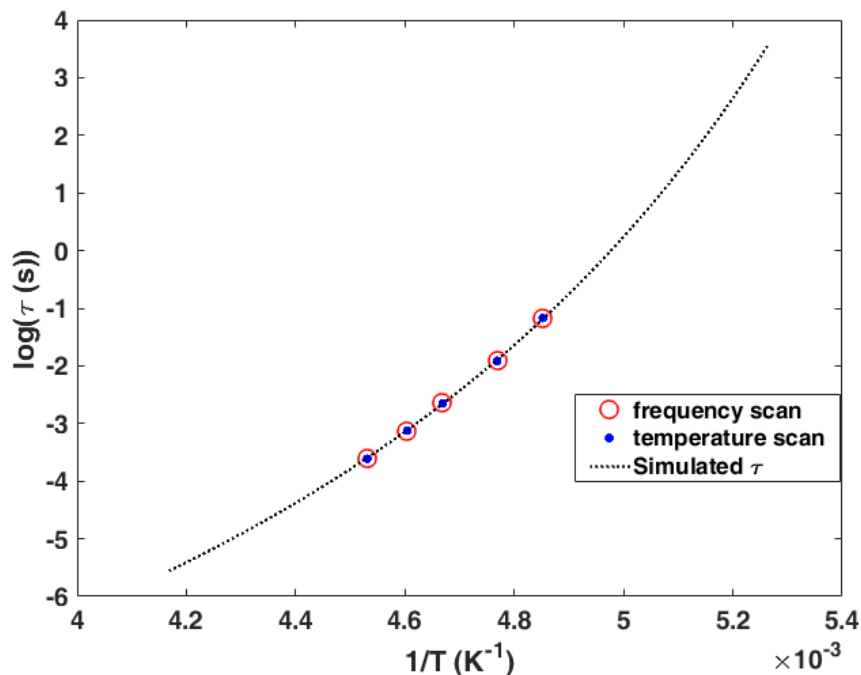


Figure 4.65 – Comparison of  $\tau$  obtained from simulated temperature scans and frequency scans

We have done the IFR analysis for some samples namely, 100 wt%, 90 wt% glycerol and 100 wt%, 93.13 wt% 1,2 propanediol. A series of experiments consisting of temperature scans at six different frequencies (1, 4, 22, 120, 360 and 1100 Hz) were performed for each sample.  $\tau_{MAX}$  and temperature of the peak for  $\alpha$  relaxation from each experiment were noted. As we have already found that the samples follow VFT law, the temperature evolution of  $\log(\tau_{MAX})$  was fitted using VFT equation. While performing the fit, the value of  $T_0$  was fixed at the mean value from 7-parameter fit. Only B and  $\tau_\infty$  were fitted. This was because the fitting program was unable to fit all three parameters at the same time due to very less data. Using the best fitted VFT parameters,  $\tau$  was simulated and compared with the mean  $\tau$  obtained from HN method. Figure 4.66 shows the comparison for glycerol.

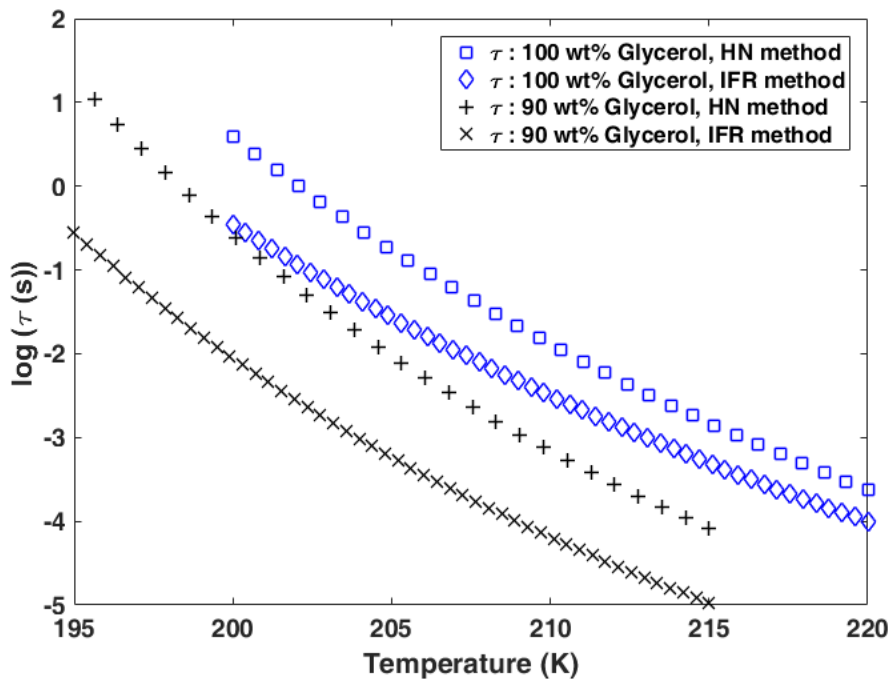


Figure 4.66 – Comparison of  $\tau$  for glycerol calculated using IFR method and HN method

Similarly, figure 4.67 shows the comparison for 1,2 propanediol.

From all studied samples, it was observed that  $\tau$  from IFR model was always lower than that from HN model. It was because of the difference in VFT parameters obtained from both analysis. HN fit could provide better results for the VFT parameters because of the higher number of fitted data while in IFR only six data were available. A limitation of the IFR method is that it requires numerous experiments to have more data for obtaining better VFT parameters.

From the VFT parameters,  $T_g$  was calculated from the glass transition convention and m using equation 4.22. Tables 4.21 and 4.22 show the value of  $T_g$  and m respectively.

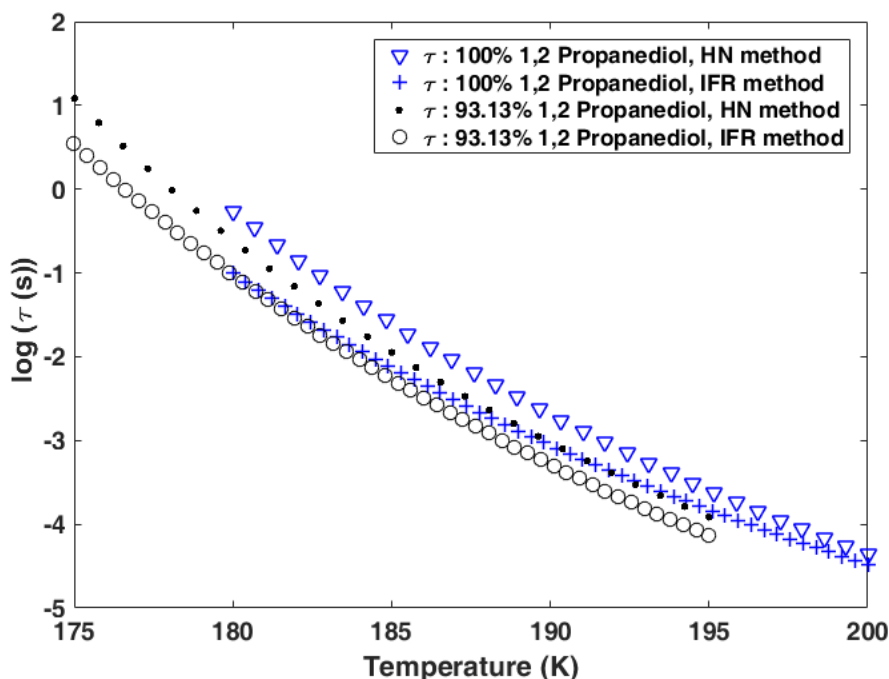


Figure 4.67 – Comparison of  $\tau$  for 1,2 propanediol calculated using IFR method and HN method

| Sample                    | $T_g$ (K) (IFR) | $T_g$ (K) (HN) | $T_g$ (K) (lit) |
|---------------------------|-----------------|----------------|-----------------|
| 100 wt% glycerol          | 191.4           | $195 \pm 6$    | $190^a, 191^b$  |
| 90 wt% glycerol           | 188.7           | 193.4          | $181.5^c$       |
| 100 wt% 1,2 propanediol   | 170.5           | $173 \pm 3$    | $167^a, 164^b$  |
| 93.13 wt% 1,2 propanediol | 171.2           | $172 \pm 3$    | -               |

Table 4.21 – Comparison of  $T_g$  from IFR with HN method and literature, a: [69], b: [139], c: [97]

| Sample                    | m (IFR) | m (HN)      | m (lit)      |
|---------------------------|---------|-------------|--------------|
| 100 wt% glycerol          | 64.9    | $71 \pm 20$ | $53^a, 78^b$ |
| 90 wt% glycerol           | 92.9    | 92.0        | -            |
| 100 wt% 1,2 propanediol   | 68.6    | $71 \pm 16$ | $52^a, 45^b$ |
| 93.13 wt% 1,2 propanediol | 73.2    | $75 \pm 12$ | -            |

Table 4.22 – Comparison of m from IFR with HN method and literature, a: [69], b: [139]

Results obtained with the IFR method are in good agreement with HN method and literature. The slight difference in  $T_g$  and m might be from the discrepancy in the VFT parameters due to less number of available data. Therefore, more temperature scans at different frequencies must be done in order to perform a better fit to find VFT parameters. However, IFR method is a valid approach to study  $\alpha$  relaxation peaks directly from temperature or frequency scan.

## 4.3 Viscosity Measurements

Viscosity measurements were performed at low temperature, till  $-20\text{ }^{\circ}\text{C}$ , lower limit of the rheometer used for measurements. Measurements were done using the rheometer MCR 301 from Anton Paar. This is an air bearing rheometer equipped with the C-PTD 200 chamber which is a peltier thermostated temperature device for concentric-cylinder systems. The samples were cooled to  $-20\text{ }^{\circ}\text{C}$ , maintained at this temperature for 16 min and reheated at  $0.05\text{ }^{\circ}\text{C min}^{-1}$ . The data acquisition was done in every 5.33 minutes.

Once the viscosity ( $\eta$ ) is measured for different temperature, the data can be fitted using VFT law to determine the VFT parameters like  $\eta_{\infty}$ ,  $B$  and  $T_0$ .

$$\eta(T) = \eta_{\infty} \exp\left(\frac{B}{T - T_0}\right) \quad (4.25)$$

For the VFT law to give a satisfactory result, a temperature range between  $T_g$  and  $T_g+100$  should be considered [141]. For PPE data, we were always within this range. But when we worked with the viscosity data, we have considered only the data from  $T_g+100$ , where the  $T_g$  was determined from PPE.

Therefore, from the selected range of data,  $T_g$  can be calculated from the VFT parameters using the glass transition convention,  $T = T_g$  when  $\eta = 10^{12}$  Pa.s or  $10^{13}$  poise.

The fragility ( $m$ ) using viscosity is given by the expression:

$$m = \left(\frac{d \log(\eta)}{d(T_g/T)}\right)_{T=T_g} \quad (4.26)$$

which leads to equation 4.22. The fragility can be calculated as we have done using PPE data. This helps to compare our PPE results and provides a double check.

### 4.3.1 Viscosity Study on Glycerol and Binary Solutions

Viscosity of glycerol and its binary solutions with water were studied by varying their temperature. Figure 4.68 shows the variation of viscosity with respect to temperature for pure glycerol. We observed that the viscosity increased as the temperature was lowered. Since the rheometer used has a lower limit of  $-20\text{ }^{\circ}\text{C}$ , the drastic increase in viscosity near the  $T_g$  couldn't be observed.

In a similar fashion, viscosity variation with respect to temperature for the binary solutions were also studied. When water was added to pure glycerol its viscosity was lowered. This trend followed as the water concentration was increased.

It was interesting to observe that the viscosity profile has a sharp variation for solutions with glycerol concentration 40% (figure 4.69) and lesser. This is because of the crystallization of water during cooling.

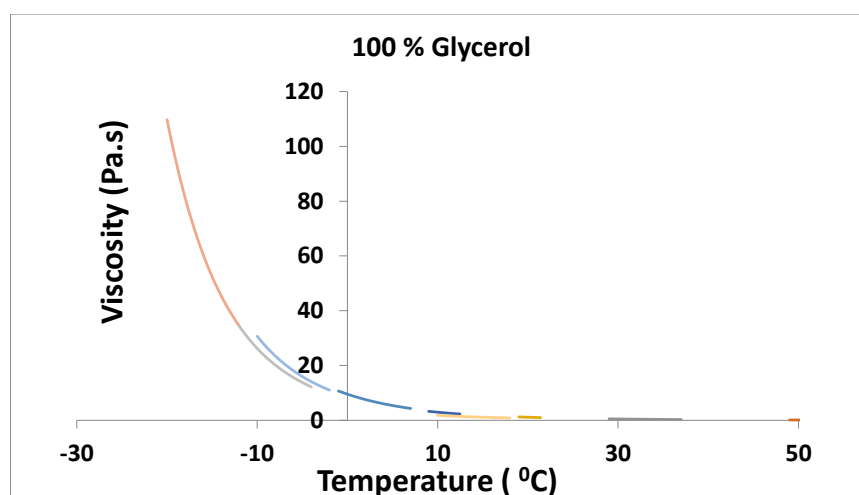


Figure 4.68 – Variation of viscosity with respect to temperature for pure glycerol

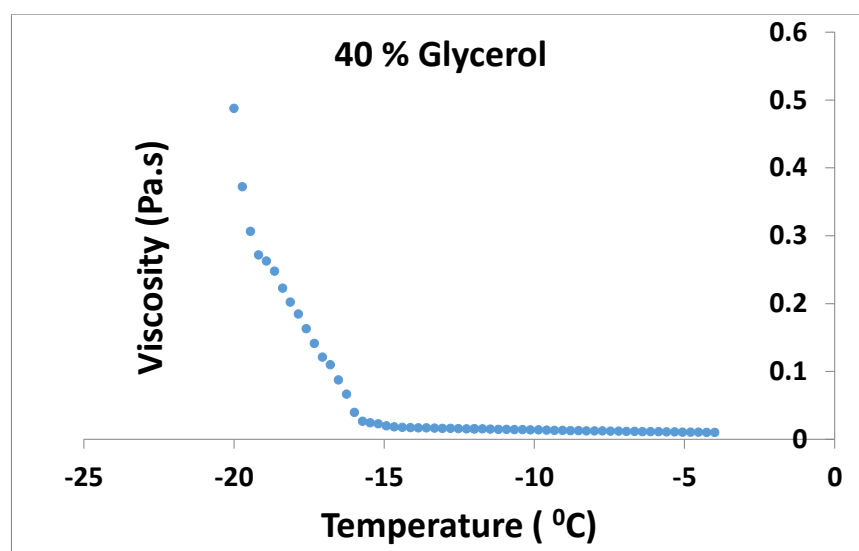


Figure 4.69 – Variation of viscosity with respect to temperature for 40 wt% glycerol-water binary solution

Figure 4.70 shows the behavior of viscosity of different concentrations as a function of temperature. 20% glycerol-water mixture showed a similar behavior like 40% because of the higher concentration of water which led to crystallization while cooling.

The  $\log(\eta)$  was plotted against  $1/T$  (Arrhenius plot) in the range  $T_g < T < (T_g + 100)$  as shown in figure 4.71 and fitted using the VFT law to determine the VFT parameters. From the VFT parameters,  $T_g$  was calculated using the glass transition convention  $T = T_g$  when  $\eta = 10^{12}$  Pa.s and  $m$  using equation 4.22. Parameters for mixtures with glycerol concentration below 50% were unable to be determined due to crystallization of water.

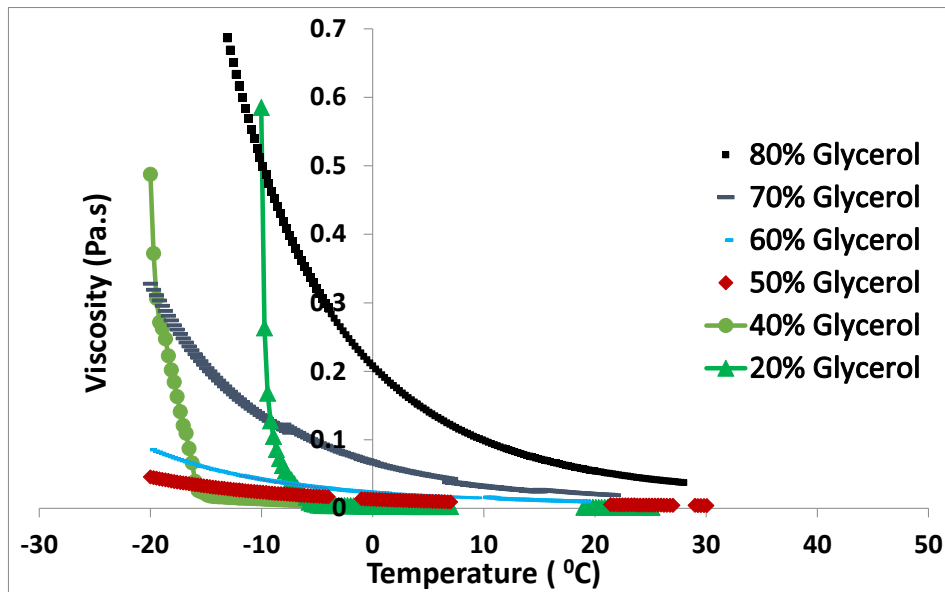


Figure 4.70 – Variation of viscosity with respect to temperature for 80 wt%, 70 wt%, 60 wt%, 50 wt%, 40 wt% and 20 wt% glycerol-water binary solution

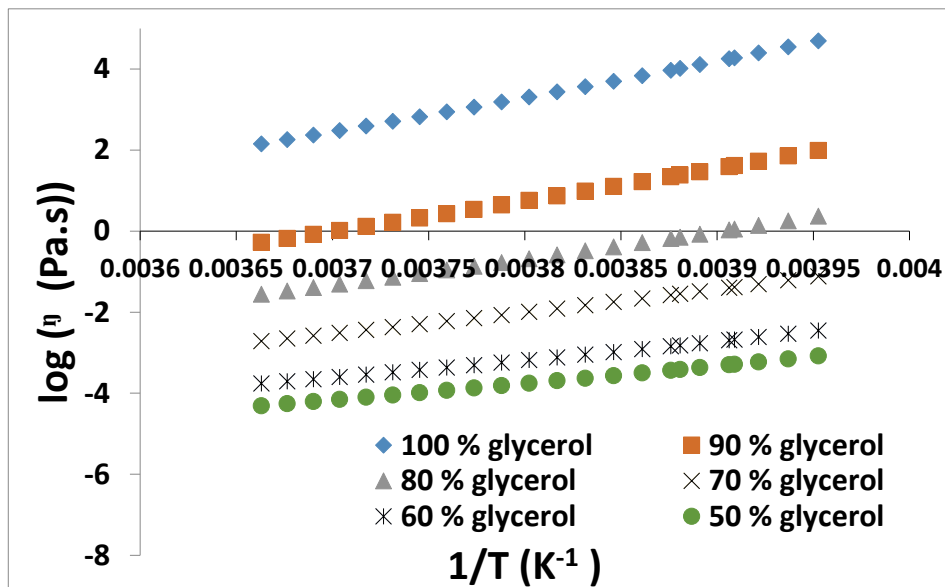


Figure 4.71 – OLU plot for pure glycerol and the binary solution of glycerol-water

The table 4.23 shows the  $T_g$  of binary solutions of glycerol and water which were calculated from PPE and viscosity experiments and the values taken from literature data. Using these values, figure 4.72 was plotted for comparison. The effect of concentration of water on  $T_g$  was observed in the comparison which showed that the  $T_g$  of aqueous solutions decreased as the concentration of water was increased except from the result of 70 wt% glycerol-water sample. This deviation of behavior might be due to experimental uncertainty which should be improved by doing further experiments.

| Sample           | $T_g$ (K) (Viscosity) | $T_g$ (K) (PPE) | $T_g$ (K) (literature)   |
|------------------|-----------------------|-----------------|--|
| 100 wt% glycerol | 182.5                 | $195 \pm 6$     | $190^a$ , $191^b$ , $183.4^c$<br>$191.4^d$ , $187^e$ , $195.4 \pm 0.2^f$ |
| 90 wt% glycerol  | 174.1                 | 193.4           | $181.5^d$ , $186.0 \pm 0.1^f$  |
| 80 wt% glycerol  | 173.6                 | $180 \pm 3$     | $174.0^d$ , $170^e$ , $177.9 \pm 0.2^f$                                  |
| 70 wt% glycerol  | 177.7                 | $183 \pm 5$     | $168.3^d$ , $162.9^e$ , $171.0 \pm 0.2^f$                                |
| 60 wt% glycerol  | 168.9                 | -               | $162.1^d$ , $156.6 \pm 0.8^e$ , $165.1 \pm 0.1^f$                        |
| 50 wt% glycerol  | 166.0                 | -               | $160.0 \pm 0.1^f$  |

Table 4.23 –  $T_g$  of pure glycerol and binary mixtures of glycerol-water and their comparison with PPE and literature data, a: [69], b: [139], c: [127], d: [97], e: [99], f: [137]

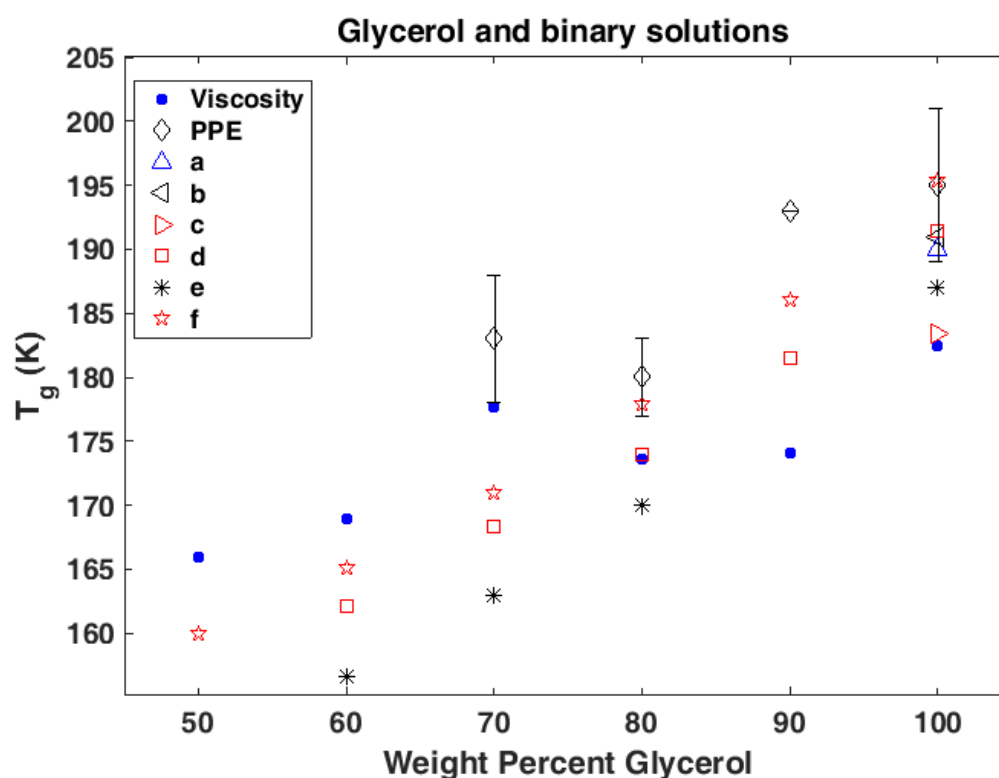


Figure 4.72 –  $T_g$  obtained from different methods and their comparison with literature data, a: [69], b: [139], c: [127], d: [97], e: [99], f: [137]

Similarly, the  $m$  values are shown in the table 4.24 and using these values, figure 4.73 was plotted for comparison among PPE, viscosity and literature data. It is possible to observe that fragility of binary solution increased as the concentration of water was increased. The same trend was observed in the literature [99] which was a dielectric measurement. To the best of our knowledge, only this literature data was available for comparison. This lack of information was the motivation for conducting parallel studies with PPE and viscosity methods. From all the obtained results, we have observed that as the water concentration increases, the fragility of aqueous solutions of glycerol increases which makes them less resistant to the change in temperature which results in a decrease in their cryoprotective nature.

| Sample           | m (Viscosity) | m (PPE)     | m (literature)       |
|------------------|---------------|-------------|----------------------|
| 100 wt% glycerol | 54.5          | $71 \pm 20$ | $53^a, 78^b, 52.3^c$ |
| 90 wt% glycerol  | 60.5          | 92.0        | -                    |
| 80 wt% glycerol  | 78.6          | $98 \pm 35$ | $54.4^c$             |
| 70 wt% glycerol  | 115.2         | 118         | $56.5^c$             |
| 60 wt% glycerol  | 119.5         | -           | $57.3^c$             |
| 50 wt% glycerol  | 124.3         | -           | -                    |

Table 4.24 – Fragility of pure glycerol and binary mixtures of glycerol-water and their comparison with PPE and literature data, a: [69], b: [139], c: [99]

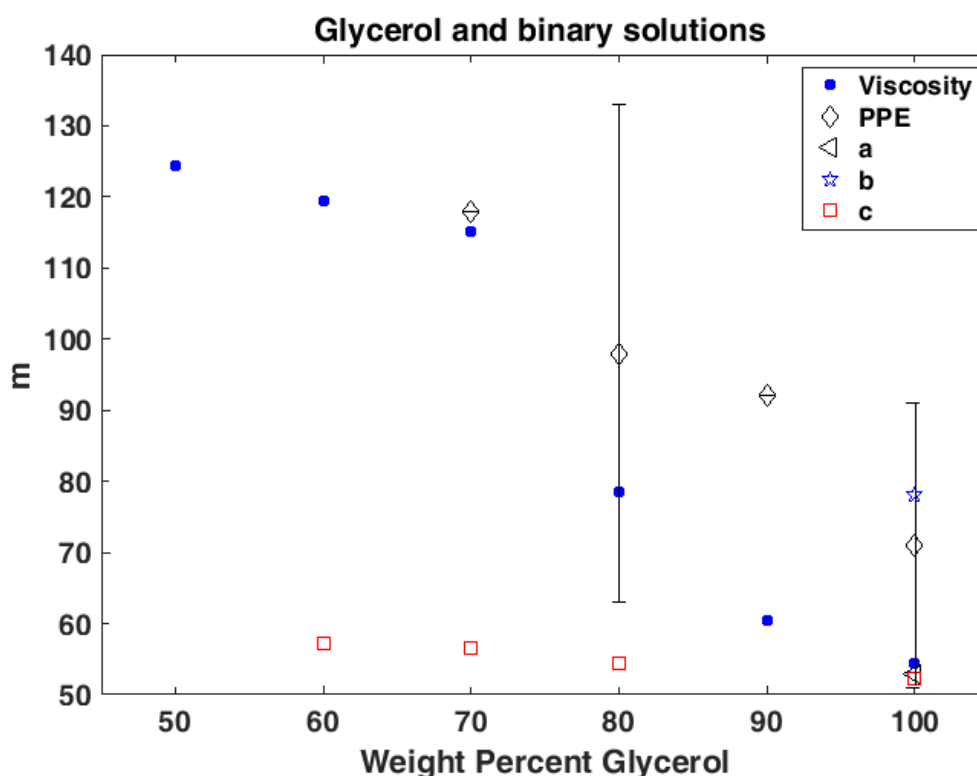


Figure 4.73 – Fragility (m) obtained from different methods and their comparison with literature data, a: [69], b: [139], c: [99]

### 4.3.2 Viscosity Study on 1,2 Propanediol and Binary Solutions

Viscosity of 1,2 propanediol and its binary solutions with water were studied with respect to their temperature. Figure 4.74 shows the variation of their viscosity according to temperature. Alike glycerol, 1,2 propanediol and its binary solutions with water also showed an increase in viscosity as their temperature was lowered. A drastic increase in viscosity could be observed if the rheometer could reach the temperature near  $T_g$ .

A sharp variation in the viscosity was observed for the 35 wt% mixture and also in lower concentrations. This was due to the crystallization of water while cooling.

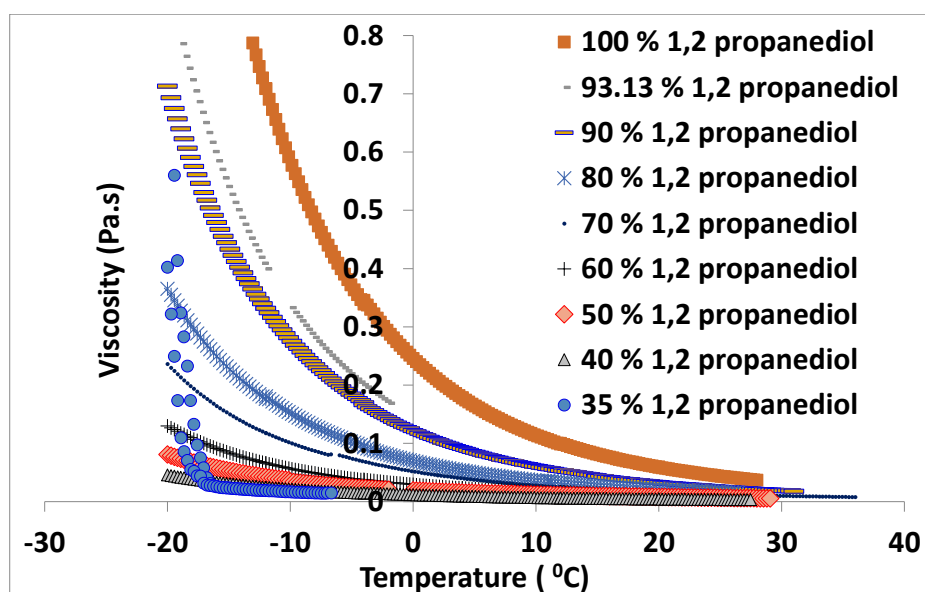


Figure 4.74 – Variation of viscosity with respect to temperature for 100wt%, 93.13wt%, 90wt%, 80wt%, 70wt%, 60wt%, 50wt%, 40wt% and 35wt% 1,2 propanediol-water binary solution

The  $\log(\eta)$  was plotted against  $1/T$  in the range  $T_g < T < (T_g + 100)$  as shown in figure 4.75 (also known as Arrhenius plot) and fitted using the VFT law to determine the VFT parameters. From the VFT parameters, the  $T_g$  was calculated using the glass transition convention  $T = T_g$  when  $\eta = 10^{12}$  Pa.s and  $m$  using equation 4.22.

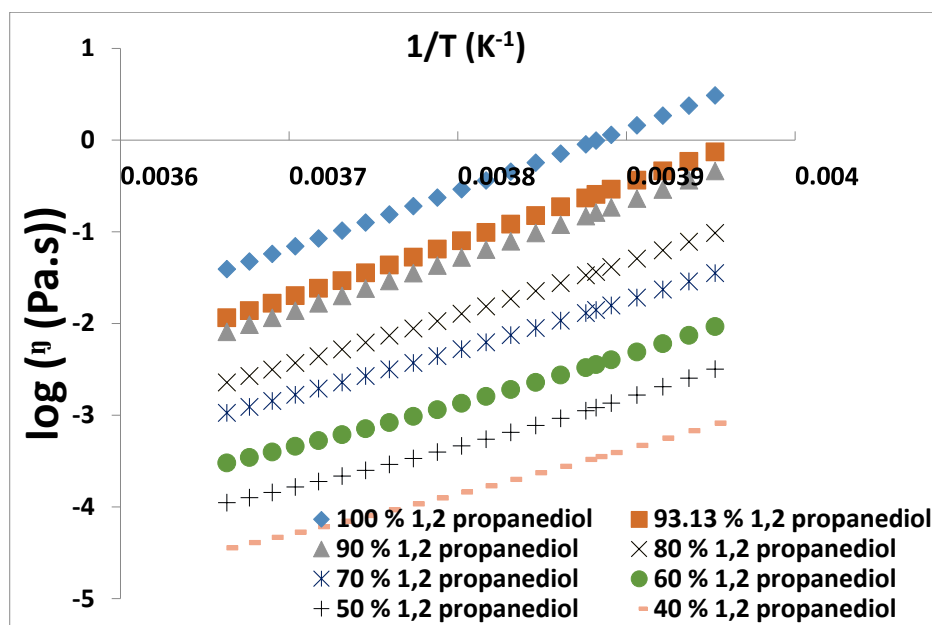


Figure 4.75 – OLUA plot for pure 1,2 propanediol and the binary solution of 1,2 propanediol-water

### 4.3. Viscosity Measurements

$T_g$  (table 4.25) of pure 1,2 propanediol and its binary solutions with water were determined and compared with PPE and literature data. Figure 4.76 shows the variation of  $T_g$  of pure 1,2 propanediol with respect to water concentration. It was observed that the  $T_g$  of aqueous solutions of 1,2 propanediol obtained from viscosity increased as the water concentration was increased while PPE and literature results tend to remain same or slightly decreasing. The discrepancy for viscosity result might be due to the fact that the temperature range of experimental data was far from the  $T_g$ . The lowest temperature that the rheometer could reach was  $-20\text{ }^\circ\text{C}$  and that is much higher than the  $T_g$  of the samples.

| Sample                    | $T_g$ (K) (Viscosity) | $T_g$ (K) (PPE) | $T_g$ (K) (literature)                                |
|---------------------------|-----------------------|-----------------|---|
| 100 wt% 1,2 propanediol   | 167.9                 | $173 \pm 3$     | $167^a$ , $164^b$<br>$162.4^c$ , $166.01^d$ , $169^e$ |
| 93.13 wt% 1,2 propanediol | 167.4                 | $172 \pm 3$     | -   |
| 90 wt% 1,2 propanediol    | 174.4                 | -               | $162.47^d$ , $165^e$                                  |
| 80 wt% 1,2 propanediol    | 185.8                 | -               | $160.78^d$ , $164^e$                                  |
| 70 wt% 1,2 propanediol    | 185.2                 | $173 \pm 1$     | $160.45^d$ , $163^e$                                  |
| 60 wt% 1,2 propanediol    | 182.2                 | -               | $161.00^d$ , $166^e$                                  |

Table 4.25 –  $T_g$  of pure 1,2 propanediol and binary mixtures of 1,2 propanediol-water and their comparison with PPE and literature data, a: [69], b: [139], c: [127], d: [98], e: [96]

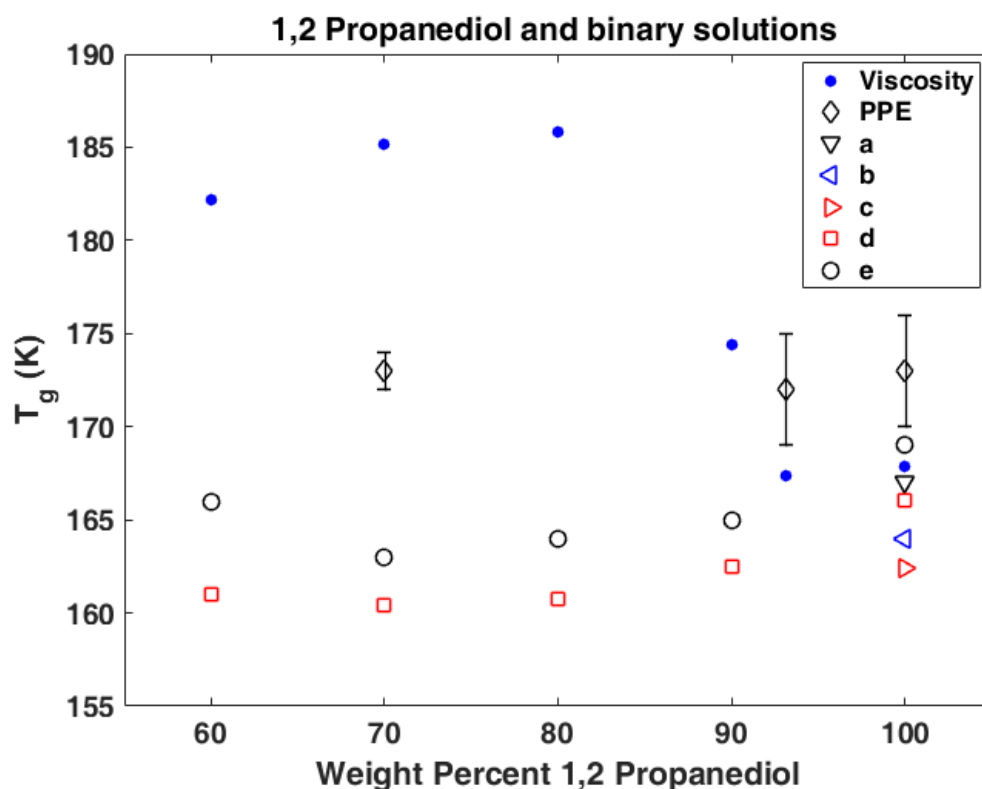


Figure 4.76 – Variation of  $T_g$  with respect to weight percent of 1,2 propanediol. PPE and viscosity results are compared with literature data, a: [69], b: [139], c: [127], d: [98], e: [96]

Table 4.26 shows the fragility of aqueous solutions of 1,2 propanediol determined from viscosity and PPE techniques and their comparison with literature.

| Sample                    | m (Viscosity) | m (PPE)     | m (literature) |
|---------------------------|---------------|-------------|----------------|
| 100 wt% 1,2 propanediol   | 67.4          | $71 \pm 16$ | $52^a, 45^b$   |
| 93.13 wt% 1,2 propanediol | 73.0          | $75 \pm 12$ | -              |
| 90 wt% 1,2 propanediol    | 93.4          | -           | -              |
| 80 wt% 1,2 propanediol    | 149.9         | -           | -              |
| 70 wt% 1,2 propanediol    | 156.1         | $87 \pm 16$ | -              |
| 60 wt% 1,2 propanediol    | 150.9         | -           | -              |

Table 4.26 – Fragility of pure 1,2 propanediol and binary mixtures of 1,2 propanediol-water and their comparison with PPE and literature data: a: [69], b: [139]

Figure 4.77 shows the variation of m of pure 1,2 propanediol with respect to water concentration.

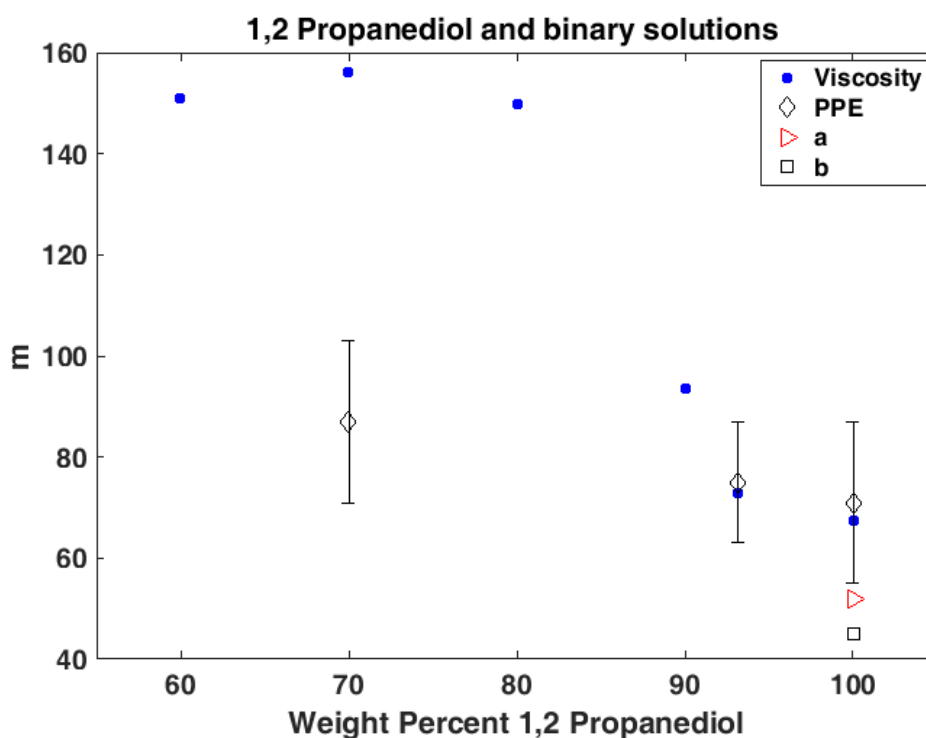


Figure 4.77 – Variation of fragility (m) with respect to weight percent of 1,2 propanediol. Results from PPE and viscosity data are compared with literature data., a: [69], b: [139]

It was observed that fragility of aqueous solutions of 1,2 propanediol increased as the water concentration was increased. PPE results also show the same trend. To the best of our knowledge, no literatures were found to do a comparison for the fragility results. As the fragility increases the cryoprotective action reduces. Therefore, from viscosity and PPE results we have observed that the cryoprotective nature of 1,2 propanediol decreased as it went towards more aqueous phase. 60 wt% sample showed a slight decrease in m and it might be due to the experimental uncertainty for the measurement of this sample.

## 4.4 Differential Scanning Calorimetry Measurement

DSC measurements were performed on some samples to study  $m$  and  $T_g$  using a power compensation Differential Scanning Calorimeter (Diamond DSC, Perkin-Elmer). The samples studied were 100 wt% glycerol, 90 wt% glycerol-water, 100 wt% 1,2 propanediol and 93.13 wt% 1,2 propanediol-water binary solutions. Weight of the samples used was between 4mg and 11mg. Measurements were based on the fictive temperature ( $T_f$ ) [142]. Fictive temperature is the temperature at which the structure of the glass and its configurational entropy would be the same than those of the equilibrium liquid [7]. This temperature depends on the previous cooling rate [143] and is expected to decrease with increased aging time [7] due to a decrease in enthalpy when the sample approaches equilibrium.  $T_f$  can be found using the so-called “equal areas” procedure depicted in the figure 4.78 on a DSC heat capacity curve.

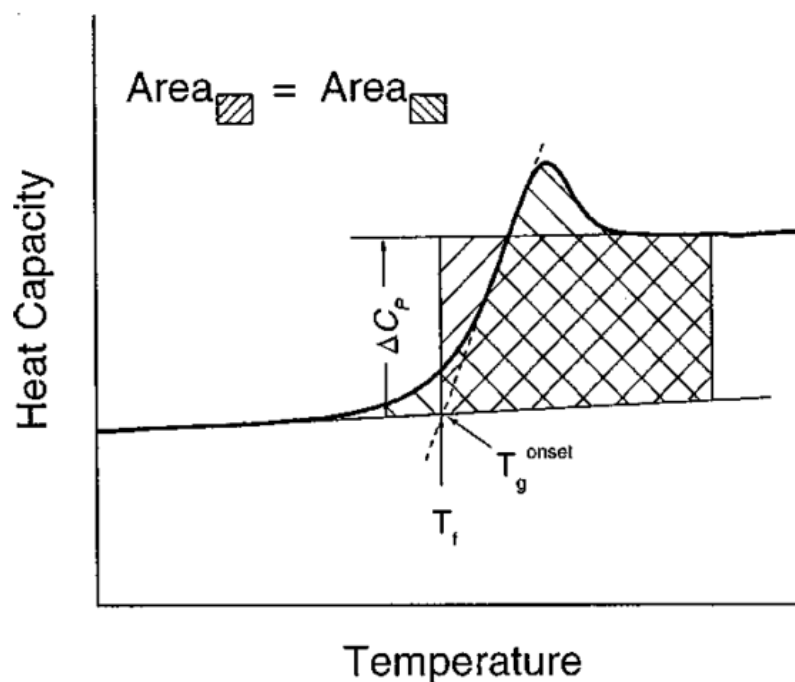


Figure 4.78 – The definition of the fictive temperature of the glassforming liquid from the upscan heat capacity vs temperature curve, reproduced from literature [92]

For calculating  $m$ , series of cooling and heating were performed [92, 144]. At first, the holding time between each cooling and heating stage was set to 5 minutes. The full procedure of cooling, heating and holding time used for pure glycerol is shown in figure 4.79 for a better understanding. Heating was always carried out at a rate of  $20\text{ }^{\circ}\text{C min}^{-1}$ , cooling was done at different rates varying from  $2.5$  to  $100\text{ }^{\circ}\text{C min}^{-1}$  and  $T_f$  corresponding to each cooling rate was determined. The cooling rates are denoted as  $Q$ . A standard cooling rate was chosen as  $20\text{ }^{\circ}\text{C min}^{-1}$ , denoted as  $Q^S$ . Fictive temperature for a heating and cooling rate at  $20\text{ }^{\circ}\text{C min}^{-1}$  is expressed as  $T_f^S$ .

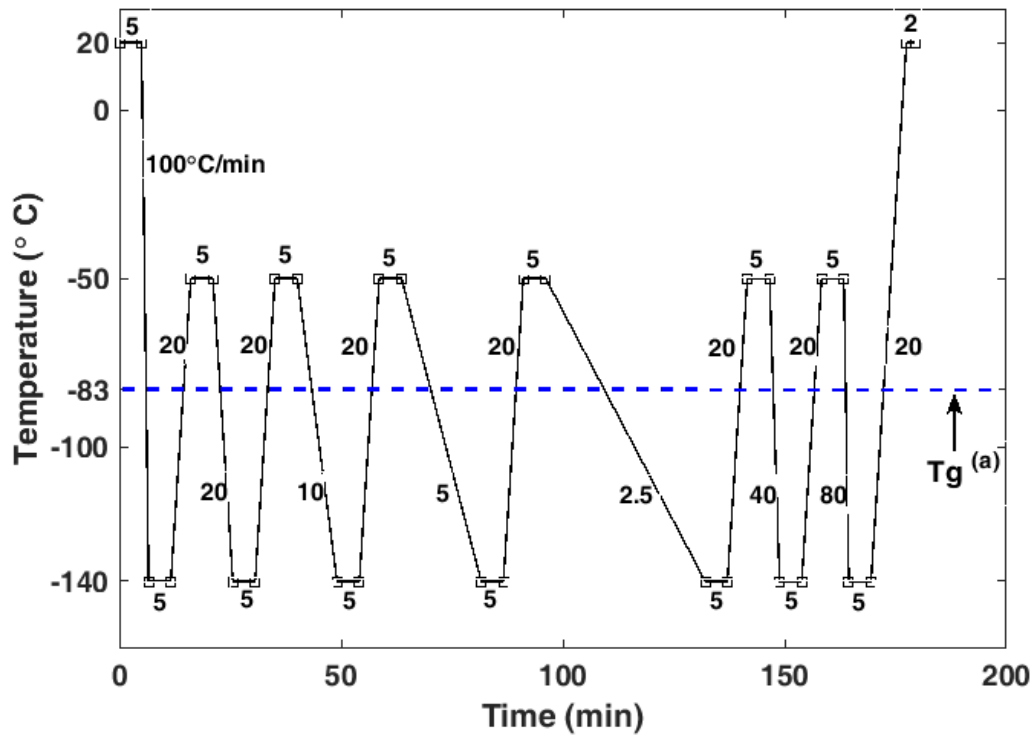


Figure 4.79 – Different stages of cooling, heating and holding followed during DSC measurement of pure glycerol (a: [92])

A graph can be plotted with  $\log(Q/Q^S)$  against  $T_f^S/T_f$ . The graph follows a linear profile. Equation of the line is given by [92]:

$$\log\left(\frac{Q}{Q^S}\right) = m - m\left(\frac{T_f^S}{T_f}\right) \quad (4.27)$$

The slope of this plot, or the intercept, gives the fragility index of the studied sample directly.

Specific heat determination was made according to the traditional 2-curves method (DSC Perkin-Elmer) using the same sample pan to record the base line and to test the sample under interest. Pure aluminum pans were used as sample holder for these measurements. For the baseline run, the pan was empty, then the same pan was filled with the sample and measurements were repeated in the exact same conditions. These curves provided the temperature evolution of heat capacity with around 1.5% accuracy [145]. The software associated with the DSC was used to determine the fictive temperature for each cooling rate.

We have studied the samples using the procedure explained above. The graph obtained for 100 wt% glycerol is shown in figure 4.80. Its fragility was determined directly from the slope of the plot using the equation 4.27.

Similarly, other sample were studied using the same procedure and their results were compared and found to be in agreement with other techniques which are given in table 4.27.

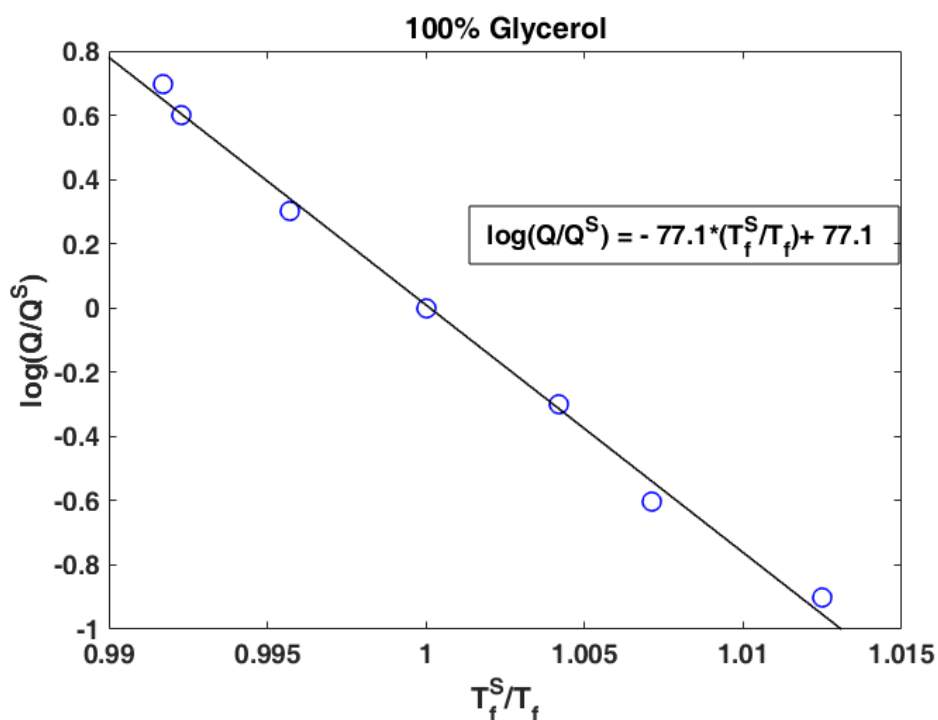


Figure 4.80 – Graph plotted for 100 wt% glycerol from the cooling rates and the corresponding fictive temperature. The slope gives its fragility which is equal to 77.1.

| Sample                    | m (DSC) | m (PPE) | m (Viscosity) | m (literature)  |
|---------------------------|---------|---------|---------------|---|
| 100 wt% glycerol          | 77.1    | 71 ± 20 | 54.5          | 53 <sup>a</sup> , 78 <sup>b</sup> , 52.3 <sup>c</sup> |
| 90 wt% glycerol           | 63.3    | 92      | 60.5          | -   |
| 100 wt% 1,2 propanediol   | 74.5    | 71 ± 16 | 67.4          | 52 <sup>a</sup> , 45 <sup>b</sup>                     |
| 93.13 wt% 1,2 propanediol | 82.9    | 75 ± 12 | 73.0          | -   |

Table 4.27 – Fragility of studied samples and their comparison with PPE, viscosity and literature data, a: [69], b: [139], c: [99]

$T_f$  is equal to  $T_g$  when the cooling rate is the same as the heating rate [92]. In our case, this rate was 20 °C min<sup>-1</sup>. The  $T_g$  was determined from the heating part of the thermograms.

The table 4.28 shows the comparison of  $T_g$  determined from DSC with those from PPE, viscosity and literature. Results show good correspondence with the other techniques.

| Sample                    | $T_g$ (DSC) | $T_g$ (PPE) | $T_g$ (Viscosity) | $T_g$ (literature) |
|---------------------------|-------------|-------------|-------------------|--------------------|
| 100 wt% glycerol          | 191.7       | 195.7       | 182.5             | 190.0              |
| 90 wt% glycerol           | 182.2       | 193.4       | 174.1             | 181.5              |
| 100 wt% 1,2 propanediol   | 169.5       | 173.5       | 167.9             | 166.0              |
| 93.13 wt% 1,2 propanediol | 167.8       | 172.7       | 167.4             | -                  |

Table 4.28 – Comparison of  $T_g$  (K) from DSC measurements with other techniques

In the above case we hold the temperature for 5 minutes between each stages. To find the impact of holding time on  $m$ , we have performed new cycles of cooling and heating using different holding time such as 1, 3, 5, 10 and 20 minutes. In this case, every cooling / reheating cycle was tested independently of the others with a new pan for each cooling rate. The warming rate was fixed to  $20\text{ }^{\circ}\text{C min}^{-1}$ , and the cooling rate was 2.5, 5, 10, 20, 40 or  $80\text{ }^{\circ}\text{C min}^{-1}$ . For each measurement, the cooling started from  $20\text{ }^{\circ}\text{C}$  to reach  $-140\text{ }^{\circ}\text{C}$ . After holding at  $-140\text{ }^{\circ}\text{C}$ , pure glycerol sample was rewarmed to  $-50\text{ }^{\circ}\text{C}$  at  $20\text{ }^{\circ}\text{C min}^{-1}$ . For each cycle, we tested the empty pan before testing immediately pure glycerol in the same pan. Next, from the DSC curve, we calculated fragility by the determination of  $T_f$ , from the specific heat capacity using the 2-curves method. The table 4.29 shows the holding time and the corresponding calculated fragility of pure glycerol from the DSC measurements.

| Holding time (min) | $m$  |
|--------------------|------|
| 1                  | 71.7 |
| 3                  | 78.9 |
| 5                  | 71.5 |
| 10                 | 64.4 |
| 20                 | 66.6 |

Table 4.29 – Variation of fragility of pure glycerol for different holding time between cooling and heating stages

Results didn't show any specific dependence of  $m$  with holding time. The variation in  $m$  might be due to the uncertainty of DSC measurements. More accurate measurements could be obtained using an additional measurement in a sapphire disk as a reference material to evaluate the specific heat. A statistical study should also be realized to study the reproducibility of  $m$  for a given holding time, since fragility is not directly obtained by a measurement, but deduced from successive calculations based on raw DSC results. The mean value of fragility from all DSC measurements for pure glycerol was calculated and compared with other techniques which is shown in table 4.30.

| Sample           | $m$ (DSC)  | $m$ (PPE)   | $m$ (Viscosity) | $m$ (literature)     |
|------------------|------------|-------------|-----------------|----------------------|
| 100 wt% glycerol | $71 \pm 8$ | $71 \pm 20$ | 54.5            | $53^a, 78^b, 52.3^c$ |

Table 4.30 – Fragility of studied samples and their comparison with PPE, viscosity and literature data, a: [69], b: [139], c: [99]

Results of DSC technique are in good agreement with PPE technique. Viscosity result differs from the other two techniques and that could result from the limited working range of the rheometer. Considering the variation of  $m$  with the holding time, a modulated DSC (MDSC) may yield a better result than DSC. The current DSC was not adapted to work in modulation mode. Therefore, it will be more desirable to continue measurements using MDSC to get a better understanding of  $m$ .

## 4.5 Summary

In this chapter, we have given a comprehensive picture of the low temperature measurements. The first section shows the simulation of PPE experimental data, effusivity square and the protocol used to extract information about the  $\alpha$  relaxation using HN equation. This protocol explains about the selection of model for the temperature dependence of  $\tau$  using the inverse Dyre-Olsen index from the activation energy. The second section explains the application of the protocol on the experimental data for pure glycerol at 22 Hz. Results of all samples are also discussed using the same protocol. The OLU diagram and the ratio of basic process energies for all the studied samples were plotted to understand their fragility behavior. A direct way of studying the  $\alpha$  relaxation peaks using the IFR method is discussed and applied for some samples. Results obtained from IFR were compared with HN method and found to be in good agreement. Samples were studied using viscosity and DSC methods to determine their  $T_g$  and  $m$  to compare with PPE and literature data. The agreement among the results are discussed.



---

## Discussion, General Conclusion and Future Outlook

---

The previous chapters have discussed about the theoretical and experimental aspects of this thesis and the results obtained from the new PPE experimental setup which was the main focus of this thesis. Results obtained from PPE were compared with the literature data. We have studied the samples using rheometer and DSC to make a comparison with PPE results. This section discusses some of the new ideas for the improvement in the experimental setup. It ends with a general conclusion and future outlook.

### 4.6 Discussion

#### New Cell

One of the main discussions about the experimental setup is the way we performed our experiments. PPE experiments are normally done in two ways, firstly, frequency scan at a constant temperature, secondly, temperature scan at a fixed frequency. We chose the former case for ambient temperature experiments. But the latter case was chosen for the  $\alpha$  relaxation study at low temperature. The chamber A shown in figure 3.2 was made with aluminum. Plastic tubes were used as inlets for temperature sensors and pyroelectric sensors and the joints between chamber A and plastic tubes were susceptible to leak at very low temperature, especially below  $-180\text{ }^{\circ}\text{C}$  which could disturb the sensor-sample area. To maintain a constant temperature for performing a frequency scan or to have a controlled and precise heating rate, liquid nitrogen must be flown during the experiment which results in a noisy signal. In order to obtain a clear signal, a new cell was made with stainless steel where plastic inlets were replaced with stainless steel pipes with all joints welded to avoid leaks. But we didn't have sufficient time to install this new cell. With this new cell we will be able to maintain a constant temperature below zero to perform frequency scans. Also the new cell enables to control the heating rate precisely.

The importance of this cell arises when it comes to the data analysis using HN equation.

Researchers have used the HN equation to work on the data in frequency domain. Some researchers worked in PPE method where they obtained data in temperature domain and converted their data to frequency domain [146]. But here we have worked directly in temperature domain using the 7-parameter fit. The new cell will directly provide data in frequency domain because it is designed to perform frequency scans at constant temperature. Therefore, one of our important prospect is to install the new cell and continue the study of more complex CPAs directly in frequency domain.

Another important prospect is the determination of thermal diffusivity at sub zero temperature. The new cell is adapted with special installations for this study. Combination of effusivity and diffusivity gives a comprehensive idea about the thermal behavior of materials.

### Dependance of Cooling Rate

Effect of cooling rate on the PPE signal has been studied by changing the rate of cooling and running temperature scans. Figure 4.81 shows the profile of normalized amplitude and phase for two different cooling rates. It was observed that the rate of cooling didn't affect the position of the relaxation during a temperature scan.

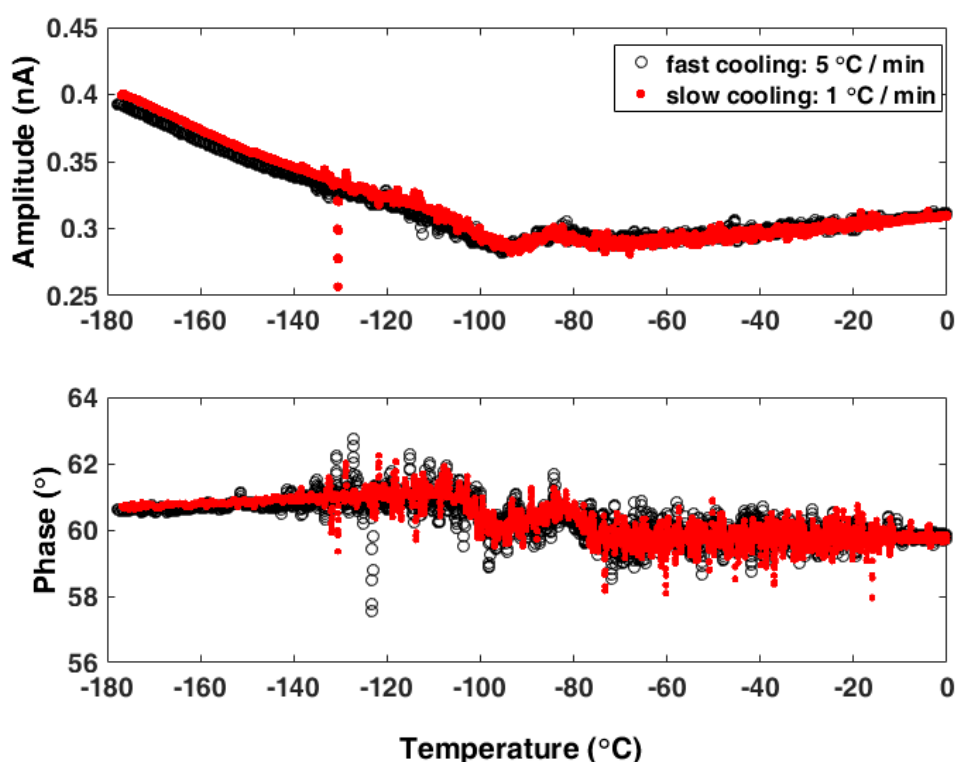


Figure 4.81 – Comparison of PPE signal from two different cooling rates for 70 wt% 1,2 propanediol-water mixture during 360 Hz experiments

### Experimental Uncertainty

J.P Szabo and I.A. Keough [128] have used a single frequency DMTA (Dynamic Mechanical Thermal Analysis) data to predict the complex modulus over a range of frequencies and temperatures. But the HN parameters fitted from our experimental data using both Wicket and 7-parameter method have shown a dependency on frequency. For example: the table 4.5 shows different values of  $E$  and  $\Delta E$  for different frequency experiments for pure glycerol. A similar difference was observed for 1,2 propanediol (table 4.7) and other samples. This difference was due to experimental uncertainties. Some experiments were repeated to verify reproducibility of results. Figures 4.82 and 4.83 show the results from reproducibility tests performed for pure 1,2 propanediol at 120 Hz and 360 Hz respectively.

Analysing these figures, it was observed from the normalized phase that the position of  $\alpha$  relaxation peak remained the same. The amplitude showed an uncertainty of  $+/- 0.03$  at 120 Hz which means that the relaxation step in amplitude (0.06 at 120 Hz) is very small in comparison with the uncertainty. For the amplitude at 360 Hz, the situation was poor with a relaxation step of 0.03. The reason for the determined HN parameters, especially  $\Delta E$  and  $E_\infty$  were different from each scan emerged from the uncertainty in the amplitude.

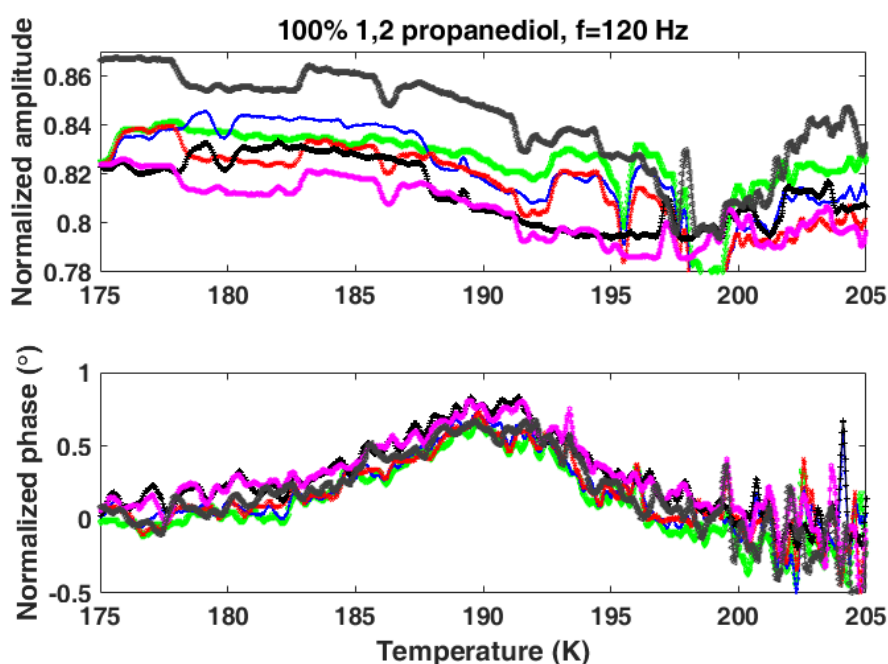


Figure 4.82 – Reproducibility tests performed for pure 1,2 propanediol at 120 Hz

We have determined the HN and VFT parameters from these experiments and analysed the temperature variation of the factor  $\left[\sqrt{H'_a(T)}\right]^{-1}$  and compared with earlier experiments which is shown in figure 4.84.

It was observed that results from all frequencies were under the uncertainty limit. This justifies the validity of taking the mean of VFT parameters from different frequency scans.

The current low temperature experimental setup is a preliminary setup which is not very

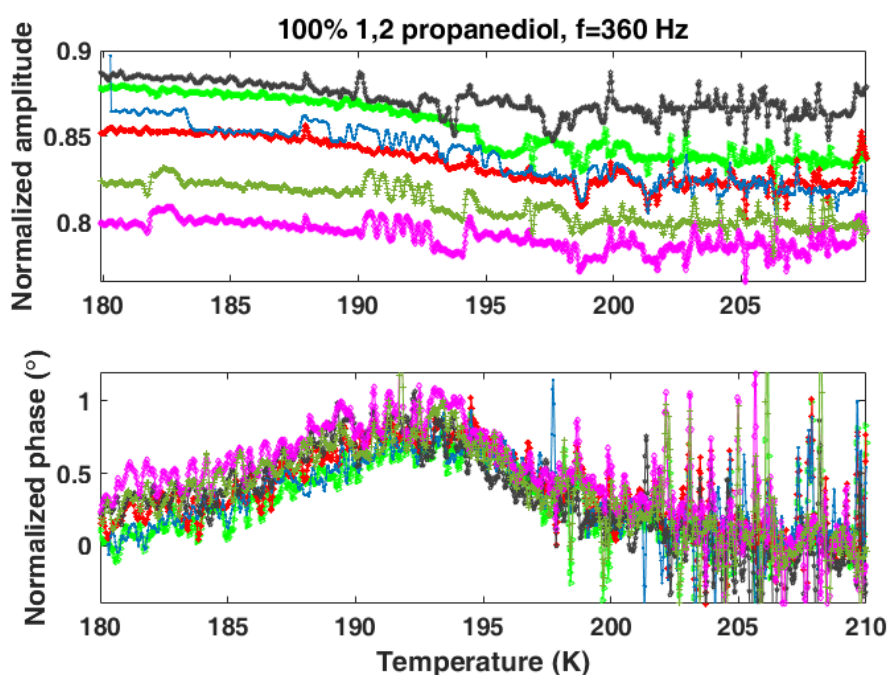


Figure 4.83 – Reproducibility tests performed for pure 1,2 propanediol at 360 Hz

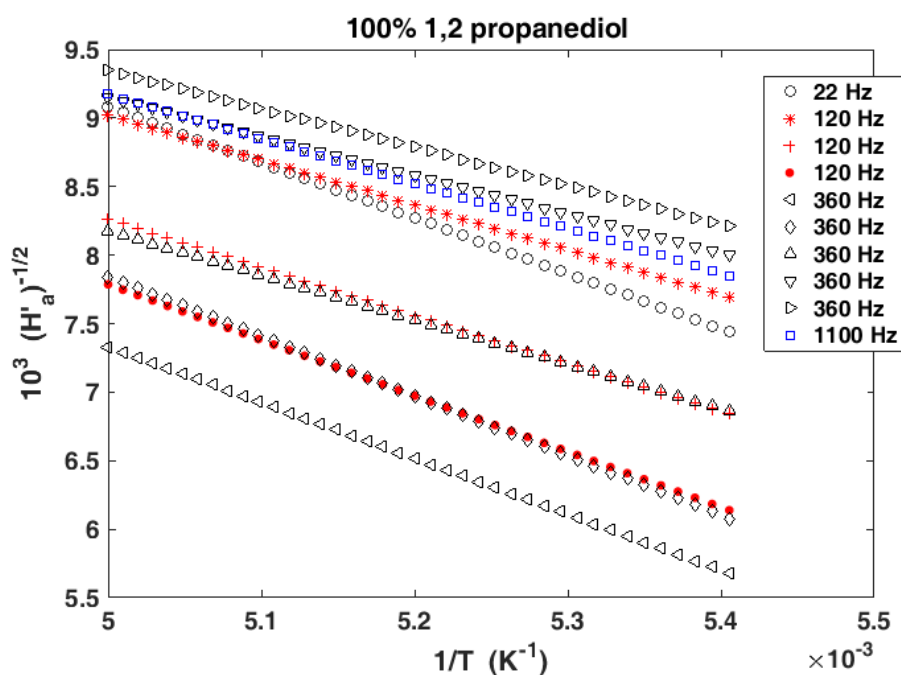


Figure 4.84 – Comparison of  $\left[\sqrt{H'_a(T)}\right]^{-1}$  for pure 1,2 propanediol calculated from repeated experiments at different frequencies

sophisticated to have a very clean signal. Otherwise, only a single temperature scan at a fixed frequency is required to determine the VFT parameters for a sample. Improvements must be done to have a better immunity to noise. One of the improvements is the installation of the new cell. Nevertheless, this variation in these parameters has a negligible impact on the mean value of  $\tau$  and AE.

## 4.7 Conclusion

This thesis work was intended to investigate the thermal effusivity of materials at low temperature using PPE technique. As our laboratory was focused mainly at ambient and higher temperature measurements, this work was aimed to develop a new low temperature PPE instrument to study the thermal effusivity of different samples especially cryoprotectants (CPAs). The instrumentation part was first done for ambient temperature measurements and then it was extended to low temperature measurements, till  $-180\text{ }^{\circ}\text{C}$ .

PPE technique was adopted because of its ability to characterize a wide range of materials from solids to liquids to gases in a wide range of temperature. PPE technique can provide high sensitivity, large bandwidth and higher signal to noise ratio. One of its main advantage is the simple installation. In this work, the PPE technique was implemented successfully to study the  $\alpha$  relaxation in the samples by studying their thermal effusivity at subzero temperature.

The materials we wanted to study using our setup were CPAs. CPAs are essential materials used in cryopreservation. CPAs play an important role in limiting the formation of ice crystals in the cells and forming a glassy state while cooling to subzero temperature. Studying their thermal properties and the effect of addition of water gives information about their performance in cryoprotection.

As we were developing a new instrument, it was very important to calibrate and optimize the setup. Due to these reasons, we used the well known CPAs like glycerol and 1,2 propanediol as samples. Both these materials show  $\alpha$  relaxation while cooling to subzero temperature. The thermal effusivity study enabled to observe the  $\alpha$  relaxation directly from the PPE signal. We have investigated the relaxation curve by Havriliak-Negami model. The aqueous solutions of glycerol and 1,2 propanediol were also studied in this work. This is important to understand their behavior in the presence of water. There was a lack of information on the glass properties of these aqueous solutions. As the result of this study we were successfully able to determine the glass parameters like glass transition temperature ( $T_g$ ) and fragility ( $m$ ) of these CPAs and their aqueous solutions.

In PPE technique, the most common illumination source used for providing a modulated heating is laser. In this work we have successfully installed an LED thereby replacing the costly lasers to build our setup in a cost efficient way. PIDs controllers were successfully built to control the LED temperature to maintain their working efficiency. We successfully built a PPE setup which can reach a working temperature of  $-180\text{ }^{\circ}\text{C}$ . Characterization of pyroelectric sensors used in different experiments were done using pure water as standardizing sample. Once these pyro sensors were characterized, they were used to find the thermal effusivity of pure glycerol, 1,2 propanediol and their binary solutions with water. Effusivity result was used to study molecular associations in binary liquids. Although thermal diffusivity and conductivity have higher sensitivity to study molecular associations, thermal effusivity was efficiently used to study molecular association in the aqueous solutions of glycerol and 1,2 propanediol.

Havriliak-Negami equation was used to analyse the squared effusivity curve to study  $\alpha$  relaxation in the samples. A successful protocol comprising of Wicket plot, Dyre-Olsen Index and 7-parameter fit was adopted to study the samples which has been discussed in chapter four. This protocol explains how to find the correct model to define the temperature dependence of  $\tau$  and to extract  $T_g$  and  $m$  from PPE experimental data.

We have presented a direct method of obtaining the relaxation time from each temperature scan at a fixed frequency called IFR method. This method has been successfully applied to determine  $T_g$  and  $m$ . Unlike other researchers, this thesis directly applied the data in temperature domain to determine the parameters. For a better comparison we have performed viscosity and DSC measurements on pure and binary samples. Results of all samples obtained from PPE were compared with viscosity, DSC and literature data. PPE results were in good agreement with other techniques. Using all these techniques, we have successfully conducted an effective study on the thermal behavior of glycerol, 1,2 propanediol and their binary solutions with water.

## **4.8 Future Outlook**

Talking about future outlook, it will be the installation of the new cell made of stainless steel to run frequency scans at isothermal conditions. This will make possible to use the HN equation directly in frequency domain and provide a comparison to our existing results. New cell will be adapted for thermal diffusivity measurements also.

Presently, we use our instrument to study liquid samples only, mainly two CPAs. It will be possible to extend this study to more complex CPAs and solid samples.

One of the main advantage of this newly constructed PPE instrument is the use of LED for modulated heating. It will be possible to extend the studies to a wide range of wavelength in a cost efficient manner.

The current rheometer used for the viscosity measurements has a lower working temperature range of  $-20$  °C. This limited our study far away from the  $T_g$ . When the rheometer will be adapted with further low temperature capability it will be possible to do measurements near  $T_g$  and obtain better information about the  $T_g$  and  $m$ .

Application of modulated DSC (MDSC) to study the fragility will provide an additional approach to verify and compare the results obtained from PPE.

Therefore, with the new cell, improved rheometer and MDSC, we look forward to study more complex CPAs with better precision and accuracy.

---

## Bibliography

---

- [1] K. B. Storey and J. Zhang. Cell cycle regulation in the freeze tolerant wood frog, *Rana sylvatica*. *Cell Cycle*, 11(9):1727–1742, 2012.
- [2] L. Sømme. Anhydrobiosis and cold tolerance in tardigrades. *European Journal of Entomology*, 93(3):349–357, 1996.
- [3] B. Wowk, E. Leidl, C. M. Rasch, N. Mesbah-Karimi, S. B. Harris, and G. M. Fahy. Vitrification enhancement by synthetic ice blocking agents. *Cryobiology*, 40(3):228–236, 2000.
- [4] D. E. Pegg. Principles of cryopreservation. In *Cryopreservation and Freeze-Drying Protocols*, pages 39–57. Humana Press, New Jersey, 2007.
- [5] G. M. Fahy, D. R. Macfarlane, C. A. Angell, and H. T. Meryman. Vitrification as an approach to cryopreservation. *Cryobiology*, 21(4):407–426, 1984.
- [6] B. J. Luyet and P. M. Gehenio. *Life and death at low temperatures*. Biodynamica, Normandy, Missouri, 1940.
- [7] B. Wowk. Thermodynamic aspects of vitrification. *Cryobiology*, 60(1):11–22, 2010.
- [8] J. Aussedat, P. Boutron, P. Coquilhat, J. L. Descotes, G. Faure, M. Ferrari, L. Kay, J. Mazuer, P. Monod, J. Odin, and A. Ray. Organ preservation at low temperature: A physical and biological problem. *journal of physics I France*, 3:515–531, 1993.
- [9] S. P. Leibo, J. Farrant, P. Mazur, M. G. Hanna JR., and L. H. Smith. Effects of freezing on marrow stem cell suspensions: Interactions of cooling and warming rates in the presence of PVP, sucrose, or glycerol. *Cryobiology*, 6(4):315–332, 1970.
- [10] C. James, G. Purnell, and S. J. James. A review of novel and innovative food freezing technologies. *Food Bioprocess Technol*, 8(8):1616–1634, 2015.
- [11] H. T. Meryman. Cryopreservation of living cells: principles and practice. *Transfusion*, 47(5):935–945, 2007.
- [12] A. R. V. Morais, E. N. Alencar, F. H. Xavier-Junior, C. M. Oliveira, H. R. Marcelino, G. Barratt, H. Fessi, E. S. T. Egito, and A. Elaissari. Freeze-drying of emulsified systems: A review. *International Journal of Pharmaceutics*, 503(1-2):102–114, 2016.

- [13] W. Block. Water or ice?—the challenge for invertebrate cold survival. *Science Progress*, 86(1-2):77–101, 2003.
- [14] R. A. Ring and D. Tesar. Adaptations to cold in Canadian arctic insects. *Cryobiology*, 18(2):199–211, 1981.
- [15] K. B. Storey, J. G. Baust, and P. Buescher. Determination of water "bound" by soluble subcellular components during low-temperature acclimation in the gall fly larva, *Eurosta solidagensis*. *Cryobiology*, 18(3):315–321, 1981.
- [16] P. L. Davies and B. D. Sykes. Antifreeze proteins. *Current opinion in structural biology*, 7(6):828–834, 1997.
- [17] B. J. Fuller. Cryoprotectants: The essential antifreezes to protect life in the frozen state. *CryoLetters*, 25(6):375–388, 2004.
- [18] A. L. DeVries. The use of antifreeze proteins in cryopreservation: Facts and realities. *Cryobiology*, 29:780–781, 1992.
- [19] D. K. Hinch, A. L. DeVries, and J. L. Schmitt. Cryotoxicity of antifreeze proteins and glycoproteins to spinach thylakoid membranes—comparison with cryotoxic sugar acids. *Biochim Biophys Acta*, 1146(2):258–264, 1993.
- [20] N. A. Maximow. *Berichte der Deutschen Botanischen Gesellschaft*. 30:52–65, 1912.
- [21] E. V. D. Abbeel, J. V. D. Elst, L. V. Waesberghe, M. Camus, P. Devroey, I. Khan, J. Smits, and C. Staessen. Hyperstimulation : the need for cryopreservation of embryos. *Human Reproduction*, 3(2):53–57, 1988.
- [22] Z. Hubálek. Protectants used in the cryopreservation of microorganisms. *Cryobiology*, 46(3):205–229, 2003.
- [23] G. M. Fahy, B. Wowk, J. Wu, J. Phan, C. Rasch, A. Chang, and E. Zendejas. Cryopreservation of organs by vitrification: Perspectives and recent advances. *Cryobiology*, 48(2):157–178, 2004.
- [24] G. J. Morris, M. Goodrich, E. Acton, and F. Fonseca. The high viscosity encountered during freezing in glycerol solutions: effects on cryopreservation. *Cryobiology*, 52(3):323–334, 2006.
- [25] K. E. Zachariassen. The mechanism of the cryoprotective effect of glycerol in beetles tolerant to freezing. *Journal of Insect Physiology*, 25(1):29–32, 1979.
- [26] P. Boutron and A. Kaufmann. Stability of the amorphous state in the system water-glycerol-dimethylsulfoxide. *Cryobiology*, 15(1):93–108, 1978.
- [27] A. Abazari, N. M. Jomha, J. A. W. Elliott, and L. E. McGann. Cryopreservation of articular cartilage. *Cryobiology*, 66(3):201–209, 2013.
- [28] V. Berejnov, N. S. Husseini, O. A. Alsaied, and R. E. Thorne. Effects of cryoprotectant concentration and cooling rate on vitrification of aqueous solutions. *Journal of Applied Crystallography*, 39:244–251, 2006.

- [29] W. J. Armitage. Preservation of viable tissues for transplantation. In B. J. Fuller and B. W. W. Grout, editors, *Clinical Applications of Cryobiology*, pages 169–190. CRC press, 1991.
- [30] O. Mishima and Y. Suzuki. Vitrification of emulsified liquid water under pressure. *Journal of Chemical Physics*, 115(9):4199–4202, 2001.
- [31] J. Dubochet and A. W. McDowell. Vitrification of pure water for electron microscopy. *Journal of Microscopy*, 124(3):3–4, 1981.
- [32] E. Mayer and P. Bruggeller. Vitrification of pure liquid water by high pressure jet freezing. *Nature*, 298:715–718, 1982.
- [33] J. Farrant. Mechanism of cell damage during freezing and thawing and its prevention. *Nature*, 205:1284–1287, 1965.
- [34] W. F. Rall and G. M. Fahy. Ice-free cryopreservation of mouse embryos at -196 degree C by vitrification. *Nature*, 313:573–575, 1985.
- [35] E. E. Benson. *Plant conservation technology*. Taylor & Francis, London, 1999.
- [36] B. J. Luyect. On the amount of liquid water remaining amorphous in frozen aqueous solutions. *Biodynamica*, 10:277–291, 1969.
- [37] B. J. Luyect and D. Rasmussen. Study by differential thermal analysis of the temperature of instability of rapidly cooled solutions of glycerol, ethylene glycol, sucrose and glucose. *Biodynamica*, 10(211):167–191, 1968.
- [38] D. Rasmussen and B. J. Luyect. Complimentary study of some non-equilibrium phase transitions in frozen solutions of glycerol, ethylene glycol, glucose and sucrose. *Biodynamica*, 10:321–331, 1969.
- [39] A. Baudot, B. Courbiere, V. Odagescu, B. Salle, C. Mazoyer, J. Massardier, and J. Lornage. Towards whole sheep ovary cryopreservation. *Cryobiology*, 55(3):236–248, 2007.
- [40] G. M. Fahy, N. Guan, I. A. M. de Graaf, Y. Tan, L. Graffin, and G. M. M. Groothuis. Cryopreservation of precision-cut tissue slices. *Xenobiotica*, 43(1):113–132, 2013.
- [41] A. Arav, A. Revel, Y. Nathan, A. Bor, H. Gacitua, S. Yavin, Z. Gavish, M. Uri, and A. Elami. Oocyte recovery, embryo development and ovarian function after cryopreservation and transplantation of whole sheep ovary. *Human Reproduction*, 20(12):3554–3559, 2005.
- [42] F. Marco-Jiménez, X. Garcia-Dominguez, E. Jimenez-Trigos, C. D. Vera-Donoso, and J. S. Vicente. Vitrification of kidney precursors as a new source for organ transplantation. *Cryobiology*, 70(3):278–282, 2015.
- [43] R. L. Bohon and W. T. Conway. DTA studies on the glycerol-water system. *Thermochimica Acta*, 4(3-5):321–341, 1972.
- [44] G. Vigier and R. Vassoille. Ice nucleation and crystallization in water-glycerol mixtures. *Cryobiology*, 24(4):345–354, 1987.

- [45] U. Buchenau. E9 Glass Transition. 33, 2012.
- [46] W. Kauzmann. The nature of the glassy state and the behavior of liquids at low temperatures. *Chemical reviews*, 43(2):219–256, 1948.
- [47] W. Götze and L. Sjogren. Relaxation processes in supercooled liquids. *Reports on Progress in Physics*, 55(3):241–376, 1992.
- [48] L. Sjögren and W. Götze. Alpha relaxation near the glass transition. *Journal of Non-Crystalline Solids*, 131-133:153–160, 1991.
- [49] W. Götze and L. Sjögren. Beta relaxation near glass transition singularities. *Journal of Physics: Condensed Matter*, 1(26):4183–4202, 1989.
- [50] P. G. Debenedetti and F. H. Stillinger. Supercooled liquids and the glass transition. *Nature*, 410:259–267, 2001.
- [51] S. A. Brawer. Theory of relaxation in viscous liquids and glasses. *The Journal of chemical physics*, 81(2):954–975, 1984.
- [52] K. L. Ngai. *Relaxation and diffusion in complex systems*. Springer, Berlin, 2011.
- [53] J. C. Martinez-Garcia, S. J. Rzoska, A. Drozd-Rzoska, S. Starzonek, and J. C. Mauro. Fragility and basic process energies in vitrifying systems. *Scientific Reports*, 5(2):8314, 2015.
- [54] H. Vogel. Temperaturabhängigkeit gesetz der Viskosität von Flüssigkeiten. *Phys, Zeit*, 22:645–646, 1921.
- [55] G. S. Fulcher. Analysis of recent measurements of the viscosity of glasses. *Journal of the American Ceramic Society*, 75(5):1043–1055, 1992.
- [56] G. Tammann. Glasses are supercooled liquids. *J. Soc. Glass Technol*, 9:166–185, 1925.
- [57] F. Stickel, E. W. Fischer, and R. Richert. Dynamics of glass-forming liquids. I. Temperature-derivative analysis of dielectric relaxation data. *The Journal of Chemical Physics*, 102(15):6251–6257, 1995.
- [58] D. Turnbull and M. H. Cohen. Free-volume model of the amorphous phase: Glass transition. *The Journal of Chemical Physics*, 34(1):120–125, 1961.
- [59] D. Turnbull and M. H. Cohen. On the free-volume model of the liquid-glass transition. *The Journal of Chemical Physics*, 52(6):3038–3041, 1970.
- [60] M. H. Cohen and G. S. Grest. Liquid-glass transition, a free-volume approach. *Physical Review B*, 20(3):1077–1098, 1979.
- [61] G. Adam and J. H. Gibbs. On the temperature dependence of cooperative relaxation properties in glass - forming liquids. *The Journal of chemical physics*, 43(1):139–146, 1965.
- [62] E. Donth. *The Glass transition. Relaxation dynamics in liquids and disordered materials*. Springer Series in Materials Sci. II, Springer, Berlin, 1998.

- [63] H. Bassler. Viscous flow in supercooled liquids analyzed in terms of transport theory for random media with energetic disorder. *Physical Review Letters*, 58(8):767–770, 1987.
- [64] I. Avramov. Viscosity in disordered media. *Journal of Non-Crystalline Solids*, 351(40-42):3163–3173, 2005.
- [65] J. C. Mauro, Y. Yue, A. J. Ellison, P. K. Gupta, and D. C. Allan. Viscosity of glass-forming liquids. *Proceedings of the National Academy of Sciences*, 106(47):19780–19784, 2009.
- [66] J. C. Mauro. Through a glass, darkly: Dispelling three common misconceptions in glass science. *International Journal of Applied Glass Science*, 2(4):245–261, 2011.
- [67] A. Drozd-Rzoska, S. J. Rzoska, and M. Paluch. Universal critical-like scaling of dynamic properties in symmetry-selected glass formers. *Journal of Chemical Physics*, 129(18):184509, 2008.
- [68] A. Drozd-Rzoska, S. J. Rzoska, S. Pawlus, J. C. Martinez-Garcia, and J. L. Tamarit. Evidence for critical-like behavior in ultraslowing glass-forming systems. *Physical Review E - Statistical, Nonlinear, and Soft Matter Physics*, 82(3):031501, 2010.
- [69] R. Böhmer, K. L. Ngai, C. A. Angell, and D. J. Plazek. Nonexponential relaxations in strong and fragile glass formers. *The Journal of chemical physics*, 99(5):4201–4209, 1993.
- [70] S. Magazù, F. Migliardo, C. Mondelli, and M. Vadalà. Correlation between bioprotective effectiveness and dynamic properties of trehalose-water, maltose-water and sucrose-water mixtures. *Carbohydrate Research*, 340(18):2796–2801, 2005.
- [71] S. Koda, T. Shibata, I. S. Park, and S. Kojima. Relaxation dynamics and fragility during liquid-glass transitions of poly(propylene glycol)s. *Current Applied Physics*, 15(7):805–810, 2015.
- [72] N. O. Birge and S. R. Nagel. Specific-heat spectroscopy of the glass transition. *Physical Review Letters*, 54(25):2674–2677, 1985.
- [73] K. L. Ngai and R. W. Rendell. Comparison between frequency-dependent specific heat and dielectric relaxation of glycerol and propylene glycol. *Physical Review B - Condensed Matter*, 41(1):754–756, 1990.
- [74] E. H. Bentefour. *Development of dynamic calorimetry using pyroelectric detector for investigating complex system: Application to glass forming super-cooled liquids*. PhD thesis, University of Leuven, 2002.
- [75] C. J. F. Böttcher and P. Bordewijk. *Theory of electric polarization*. Elsevier, Amsterdam, second edition, 1978.
- [76] S. Havriliak and S. Negami. A complex plane representation of dielectric and mechanical relaxation processes in some polymers. *Polymer*, 8:161–210, 1967.
- [77] A. A. Pronin, K. Trachenko, M. V. Kondrin, A. G. Lyapin, and V. V. Brazhkin. Nonlocal dielectric relaxation in glycerol. *Physical Review B - Condensed Matter and Materials Physics*, 84(1):012201, 2011.

- [78] D. Stefan and H. L. Williams. Molecular motions in bisphenol A polycarbonates as measured by pulsed NMR techniques. I. Homopolymers and copolymers. *Journal of Applied Polymer Science*, 18(5):1279–1293, 1974.
- [79] E. A. Friedman, A. J. Ritger, and R. D. Andrews. Brillouin scattering near the glass transition of polymethyl methacrylate. *Journal of Applied Physics*, 40(11):4243–4247, 1969.
- [80] Y. Wada and K. Yamamoto. Temperature dependence of velocity and attenuation of ultrasonic waves in high polymers. *Journal of the Physical Society of Japan*, 11:887–892, 1956.
- [81] Perkin Elmer. Differential Scanning Calorimetry ( DSC ) A Beginner ' s Guide. Technical report.
- [82] P. S. Gill, S. R. Sauerbrunn, and M. Reading. Modulated differential scanning calorimetry. *Journal Of Thermal Analysis*, 40(3):931–939, 1993.
- [83] M. Reading, A. Luget, and R. Wilson. Modulated differential scanning calorimetry. *Thermochimica Acta*, 238:295–307, 1994.
- [84] S. Pittois, B. V. Roie, C. Glorieux, and J. Thoen. Static and dynamic thermal quantities near the consolute point of the binary liquid mixture aniline–cyclohexane studied with a photopyroelectric technique and adiabatic scanning calorimetry. *The Journal of chemical physics*, 122(2):024504, 2005.
- [85] H. Yao, K. Ema, and C. W. Garland. Nonadiabatic scanning calorimeter. *Review of Scientific Instruments*, 69(1):172–178, 1998.
- [86] D. Dadarlat, V. Surducun, K. J. Riezebos, and D. Bicanic. A new photopyroelectric cell for thermal characterization of foodstuffs; Application to sugar systems. *Instrumentation Science & Technology*, 26(2-3):125–131, 1998.
- [87] J. Mura, L. C.M. Miranda, M. L. Baesso, A. C. Bento, and A. F. Rubira. Piezo- and pyroelectric photothermal characterization of polymers as a function of temperature. *Journal of Applied Polymer Science*, 82(11):2607–2867, 2001.
- [88] E. H. Bentefour, C. Glorieux, M. Chirtoc, and J. Thoen. Broadband photopyroelectric thermal spectroscopy of a supercooled liquid near the glass transition. *Journal of Applied Physics*, 93(12):9610–9614, 2003.
- [89] G. S. Parks and W. A. Gilkey. Studies on glass. IV. Some viscosity data on liquid glucose and glucose-glycerol solutions. *Journal of Physical Chemistry*, 33(9):1428–1437, 1929.
- [90] X. He, A. Fowler, and M. Toner. Water activity and mobility in solutions of glycerol and small molecular weight sugars: Implication for cryo- and lyopreservation. *Journal of Applied Physics*, 100(7):074702, 2006.
- [91] P. K. Dixon and S. R. Nagel. Frequency-dependent specific heat and thermal conductivity at the glass transition in o-Terphenyl mixtures. *Physical Review Letters*, 61(3):341–344, 1988.

- [92] L. M. Wang, V. Velikov, and C. A. Angell. Direct determination of kinetic fragility indices of glassforming liquids by differential scanning calorimetry: Kinetic versus thermodynamic fragilities. *Journal of Chemical Physics*, 117(22):10184–10192, 2002.
- [93] J. A. Balderas-Lopez, D. Acosta-Avalos, J. J. Alvarado, O. Zelaya-Angel, F. Sanchez-Sinencio, C. Falcony, A. Cruz-Orea, and H. Vargas. Photoacoustic measurements of transparent liquid samples: Thermal effusivity. *Measurement Science and Technology*, 6(8):1163–1168, 1995.
- [94] C. A. Angell. Liquid fragility and the glass transition in water and aqueous solutions. *Chemical Reviews*, 102(8):2627–2650, 2002.
- [95] P. Dixon, L. Wu, S. R. Nagel, B. D. Williams, and J. Carini. Scaling of the relaxation of supercooled liquids. *Physical Review Letters*, 65(9):1108–1111, 1990.
- [96] P. Boutron and A. Kaufmann. Stability of the amorphous state in the system water-1,2-Propanediol. *Cryobiology*, 16(6):557–568, 1979.
- [97] C. Gao and G. Zhou. Phenomenological study of structure relaxation of glycerol aqueous glass. *Acta Physico - Chimica Sinica*, 21(8):909–914, 2005.
- [98] C. Gao, T. Wang, G. Zhou, and Z. Hua. Glass transition and structure relaxation of 1,2-propanediol aqueous solutions. *Acta Physico - Chimica Sinica*, 23(2):206–211, 2007.
- [99] S. Sudo, M. Shimomura, N. Shinyashiki, and S. Yagihara. Broadband dielectric study of  $\alpha$ - $\beta$  separation for supercooled glycerol-water mixtures. *Journal of Non-Crystalline Solids*, 307-310:356–363, 2002.
- [100] D. Dadarlat, M. Nicolae, M. Streza, S. Longuemart, M. Depriester, and A. H. Sahraoui. Combined FPPE – PTR calorimetry involving TWRC technique II . Experimental : application to thermal effusivity measurements of solids. *International Journal of Thermophysics*, 32(10):2092–2101, 2011.
- [101] P. C. Menon, R. N. Rajesh, and C. Glorieux. High accuracy, self-calibrating photopyroelectric device for the absolute determination of thermal conductivity and thermal effusivity of liquids. *The Review of scientific instruments*, 80(5):54904, 2009.
- [102] J. Caerels, C. Glorieux, and J. Thoen. Photopyroelectric thermal wave setup for the absolute measurement of the thermal conductivity of low density gases. *Review of Scientific Instruments*, 71(9):3506–3512, 2000.
- [103] A. Oleaga, V. Shvalya, A. S. Sefat, and A. Salazar. Transport thermal properties of LiTaO<sub>3</sub> pyroelectric sensor from 15 K to 400 K and its application to the study of critical behavior in EuCo<sub>2</sub>As<sub>2</sub>. *International Journal of Thermophysics*, 37:4, 2016.
- [104] A. Mandelis and M. M. Zver. Theory of photopyroelectric spectroscopy of solids. *Journal of Applied Physics*, 57(9):4421–4430, 1985.
- [105] M. Chirtoc and G. Mihailescu. Theory of the photopyroelectric method for investigation of optical and thermal materials properties. *Physical Review B - Condensed Matter*, 40(14):9606–9617, 1989.

- [106] J. F. Power and M. C. Prystay. Nondestructive optical depth profiling in thin films through robust inversion of the laser photopyroelectric effect impulse response. *Applied spectroscopy*, 49(6):725–745, 1995.
- [107] A. H. Sahraoui, S. Longuemart, D. Dadarlat, S. Delenclos, C. Kolinsky, and J. M. Buisine. The application of the photopyroelectric method for measuring the thermal parameters of pyroelectric materials. *Review of Scientific Instruments*, 73(7):2766–2772, 2002.
- [108] A. H. Sahraoui, S. Longuemart, D. Dadarlat, S. Delenclos, C. Kolinsky, and J. M. Buisine. Analysis of the photopyroelectric signal for investigating thermal parameters of pyroelectric materials. *Review of Scientific Instruments*, 74(1):618–620, 2003.
- [109] S. Delenclos, D. Dadarlat, N. Houriez, S. Longuemart, C. Kolinsky, and A. H. Sahraoui. On the accurate determination of thermal diffusivity of liquids by using the photopyroelectric thickness scanning method. *Review of Scientific Instruments*, 78(2):024902, 2007.
- [110] S. Delenclos, M. Chirtoc, A. H. Sahraoui, C. Kolinsky, and J. M. Buisine. Assessment of calibration procedures for accurate determination of thermal parameters of liquids and their temperature dependence using the photopyroelectric method. *Review of Scientific Instruments*, 73(7):2773, 2002.
- [111] A. O. Guimarães, F. A. L. Machado, E. C. da Silva, and A. M. Mansanares. Thermal effusivity and thermal conductivity of biodiesel/diesel and alcohol/water mixtures. *International Journal of Thermophysics*, 33(10-11):1842–1847, 2012.
- [112] M. Chirtoc, E. H. Bentefour, C. Glorieux, and J. Thoen. Development of the front-detection photopyroelectric (FPPE) configuration for thermophysical study of glass-forming liquids. *Thermochimica Acta*, 377(1):105–112, 2001.
- [113] D. Dadarlat, A. Frandas, M. Marinelli, F. Mercuri, and D. Bicanic. New photopyroelectric scheme suitable for phase-transition investigations: The front configuration with semitransparent sensor. *Applied Physics A: Materials Science and Processing*, 61(2):183–186, 1995.
- [114] N. O. Birge. Specific Heat Spectroscopy of glycerol and propylene glycol near glass transition. *Physical Review B*, 34(3):1631–1642, 1986.
- [115] D. Dadarlat, H. Visser, and D. Bicanic. An improved inverse photopyroelectric cell for measurement of thermal effusivity : application to fatty acids and triglycerides. *Measurement Science and Technology*, 6:1215–1219, 1995.
- [116] A. Salazar and A. Oleaga. On the piezoelectric contribution to the photopyroelectric signal. *Review of Scientific Instruments*, 76(3):034901, 2005.
- [117] D. Zheng, J. Swingler, and P. Weaver. Current leakage and transients in ferroelectric ceramics under high humidity conditions. *Sensors and Actuators, A: Physical*, 158(1):106–111, 2010.

- [118] P. M. Weaver, M. G. Cain, M. Stewart, A. Anson, J. Franks, I. P. Lipscomb, J. W. McBride, D. Zheng, and J. Swingler. The effects of porosity, electrode and barrier materials on the conductivity of piezoelectric ceramics in high humidity and dc electric field. *Smart Materials and Structures*, 21(4):1–9, 2012.
- [119] J. D. Brownridge and S. M. Shafroth. Self-focused electron beams produced by pyroelectric crystals on heating or cooling in dilute gases. *Applied Physics Letters*, 79(20):3364–3366, 2001.
- [120] J. D. Brownridge and S. M. Shafroth. Using static charge on pyroelectric crystals to produce self-focusing electron and ion beams and transport through tubes. *Journal of electrostatics*, 63(3-4):249–259, 2005.
- [121] D. R. Lide, editor. *CRC handbook of chemistry and physics*. Chemical Rubber, Boca Raton, New York, 78 edition, 1997.
- [122] M. Kuriakose, M. Depriester, D. Dadarlat, and A. H. Sahraoui. Improved methods for measuring thermal parameters of liquid samples using photothermal infrared radiometry. *Measurement Science and Technology*, 24(2):25603, 2013.
- [123] R. Ivanov, E. I. Martínez-Ordóñez, E. Marin, C. Araujo, D. Alaniz, M. E. Araiza, J. Villa, and J. I. de la Rosa-Vargas. Absolute measurements of thermal effusivity using the electropyroelectric technique. *Thermochimica Acta*, 554:59–62, 2013.
- [124] D. Dadarlat and C. Neamtu. Detection of molecular associations in liquids by photopyroelectric measurements of thermal effusivity. *Measurement Science and Technology*, 17(12):3250–3254, 2006.
- [125] N. Houriez. *Etude du transport thermique dans des fluides complexes par calorimétrie photopyroélectrique*. PhD thesis, Université du Littoral-Côte-d’Opale, 2008.
- [126] A. Puzenko, Y. Hayashi, Y. E. Ryabov, I. Balin, Y. Feldman, U. Kaatz, and R. Behrends. Relaxation dynamics in glycerol-water mixtures: I. Glycerol-rich mixtures. *Journal of Physical Chemistry B*, 109(12):6031–6035, 2005.
- [127] M. Cutroni, A. Mandanici, and L. De Francesco. Fragility, stretching parameters and decoupling effect on some supercooled liquids. *Journal of Non-Crystalline Solids*, 307-310:449–454, 2002.
- [128] J. P. Szabo and I. A. Keough. Method for analysis of dynamic mechanical thermal analysis data using the Havriliak-Negami model. *Thermochimica Acta*, 392-393:1–12, 2002.
- [129] J. C. Dyre and N. B. Olsen. Landscape equivalent of the shoving model. *Physical Review E*, 69(4):042501, 2004.
- [130] T. Hecksher, A. I. Nielsen, N. B. Olsen, and J. C. Dyre. Little evidence for dynamic divergences in ultraviscous molecular liquids. *Nature Physics*, 4:737–741, 2008.
- [131] A. Drozd-Rzoska and S. J. Rzoska. Derivative-based analysis for temperature and pressure evolution of dielectric relaxation times in vitrifying liquids. *Physical Review E*, 73(4):041502, 2006.

- [132] J. C. Martinez-Garcia, S. J. Rzoska, A. Drozd-Rzoska, and J. Martinez-Garcia. A universal description of ultraslow glass dynamics. *Nature Communications*, 4(1823):1–9, 2013.
- [133] F. Stickel, E. W. Fischer, and R. Richert. Dynamics of glass-forming liquids. II. Detailed comparison of dielectric relaxation, dc-conductivity, and viscosity data. *The Journal of Chemical Physics*, 104(5):2043–2055, 1996.
- [134] K. L. Ngai. Glass forming substances and systems. In *Relaxation and Diffusion in complex systems*, pages 127–129. Springer, New York, 2011.
- [135] L. M. Wang and J. C. Mauro. An upper limit to kinetic fragility in glass-forming liquids. *Journal of Chemical Physics*, 134(4):044522, 2011.
- [136] S. L. Simon, D. J. Plazek, J. W. Sobieski, and E. T. McGregor. Physical aging of a polyetherimide: Volume recovery and its comparison to Creep and enthalpy measurements. *Journal of Polymer Science Part B: Polymer Physics*, 35(6):929–936, 1997.
- [137] J. A. Trejo González, M. P. Longinotti, and H. R. Corti. The viscosity of glycerol-water mixtures including the supercooled region. *Journal of Chemical and Engineering Data*, 56(4):1397–1406, 2011.
- [138] N. Menon, K. P. O’Brien, P. K. Dixon, L. Wu, S. R. Nagel, B. D. Williams, and J. P. Carini. Wide-frequency dielectric susceptibility measurements in glycerol. *Journal of Non-Crystalline Solids*, 141:61–65, 1992.
- [139] J. C. Martinez-Garcia, S. J. Rzoska, A. Drzozd-Rzoska, J. Martinez-Garcia, and J. C. Mauro. Divergent dynamics and the Kauzmann temperature in glass forming systems. *Scientific Reports*, 4(5160):1–8, 2014.
- [140] F. Alvarez, A. Alegria, and J. Colmenero. Relationship between the time-domain Kohlrausch-Williams-Watts and frequency-domain Havriliak-Negami relaxation functions. *Physical Review B*, 44(14):7306–7312, 1991.
- [141] J. Dudowicz, J. F. Douglas, and K. F. Freed. The meaning of the "universal" WLF parameters of glass-forming polymer liquids. *The Journal of chemical physics*, 142(1):014905, 2015.
- [142] C. T. Moynihan, A. J. Easteal, M. A. De Bolt, and J. Tucker. Dependence of the fictive temperature of glass on cooling rate. *Journal of the American Ceramic Society*, 59(1-2):12–16, 1976.
- [143] R. B. Cassel. Physical aging and fragility of amorphous sucrose by DSC. *Notice TA Instruments 296*, pages 1–7.
- [144] V. Velikov, S. Borick, and C. A. Angell. Molecular glasses with high fictive temperatures for energy landscape evaluations. *Journal of Physical Chemistry B*, 106(5):1069–1080, 2002.
- [145] P. Robinson. Practical specific heat determination by dual furnace DSC. *Application note: Differential Scanning Calorimetry*, pages 1–9.

- [146] E. H. Bentefour, C. Glorieux, M. Chirtoc, and J. Thoen. Thermal relaxation of glycerol and propylene glycol studied by photothermal spectroscopy. *Journal of Chemical Physics*, 120(8):3726–3732, 2004.



# PHOTOTHERMAL STUDIES ON CRYOPROTECTANT MEDIA

## Abstract

The construction, calibration and application of a new low temperature instrument based on a photothermal technique called photo pyroelectricity (PPE) is described in this manuscript. The samples we studied using the new PPE instrument were glycerol, 1,2 propanediol and their binary mixtures with water. These liquids are well known cryoprotectants (CPAs) used in cryopreservation, which is a technique to preserve the living cells and tissues from biological degradation by cooling to sub zero temperatures. The ultimate goal in cryopreservation is to avoid or control the ice formation and attain a glassy or amorphous state. The rate of cooling and heating and the concentration of the CPAs used are the key parameters that determine the ice formation. Therefore, studying the temperature dependent thermal properties especially near their glass transition temperature ( $T_g$ ) of the binary solutions of CPAs with water at different concentrations are highly important to understand their behavior while cooling. The PPE technique was used to study the effusivity and the  $\alpha$  relaxation time near the glass transition phenomenon. The  $T_g$  and fragility ( $m$ ) were determined from the PPE data using the Havriliak Negami model. The glassy state has a characteristic property of very high viscosity, of the order of  $10^{12}$  Pa.s at  $T_g$ . The  $T_g$  and  $m$  can be calculated from the temperature evolution of viscosity or from Differential Scanning Calorimetry (DSC) measurements. Therefore, viscosity and DSC studies were conducted on the samples and were compared with PPE data.

**Keywords:** photo pyroelectricity; cryopreservation; cryoprotectant; vitrification; glass transition temperature; fragility; viscosity; Differential Scanning Calorimetry

## Résumé

La mise en place, l'étalonnage et l'utilisation d'un nouveau banc expérimental basses températures basé sur une technique photothermique appelée photo pyroélectricité (PPE) sont décrits dans ce manuscrit. Les échantillons que nous avons étudiés en utilisant ce nouvel instrument sont le glycérol, le 1,2 propanediol et leurs mélanges binaires avec l'eau. Ce sont des cryoprotecteurs bien connus (CPAs) utilisés dans la cryoconservation, qui est une technique de préservation des cellules et tissus vivants en les refroidissant à des très basses températures. Le but ultime de la cryoconservation est d'éviter ou de maîtriser la formation de glace et d'atteindre un état vitreux ou amorphe. La vitesse de refroidissement, de chauffage et la concentration des CPAs utilisés sont les paramètres clés qui déterminent la formation de la glace. Par conséquent, l'étude des propriétés thermiques, en particulier près de la température de transition vitreuse ( $T_g$ ) des solutions binaires des CPAs avec de l'eau est très importante pour comprendre leur comportement lors du refroidissement. La PPE a été utilisée pour étudier l'effusivité et le temps de relaxation  $\alpha$  caractéristique de la transition vitreuse. Le  $T_g$  et la fragilité ( $m$ ) ont été déterminés à partir des données de la PPE en utilisant le modèle d'Havriliak Negami. L'état vitreux présente une très grande viscosité, de l'ordre de  $10^{12}$  Pa.s au voisinage du  $T_g$ . Le  $T_g$  et  $m$  peuvent être calculés à partir de l'évolution de la viscosité en fonction de la température ou par calorimétrie différentielle à balayage (DSC). Ainsi, des études à l'aide de ces deux techniques ont été menées et les résultats ont été comparés avec les données de la PPE.

**Mots-clés:** photo pyroélectricité; cryoconservation; cryoprotecteur; vitrification; température de transition vitreuse; fragilité; viscosité; calorimétrie différentielle à balayage